HYDROGEN ENTRY IN ZIRCALOY-4 FUEL CLADDING: AN ELECTROCHEMICAL STUDY

by
Jennifer Anne Jarvis

Triple B.S., Nuclear Eng., Mechanical Eng., and French and Francophone Studies (2010)
The Pennsylvania State University

SUBMITTED TO THE DEPARTMENT OF NUCLEAR SCIENCE AND ENGINEERING
IN PARTIAL FULFILLMENT OF THE REQUIREMENTS FOR THE DEGREE OF

DOCTOR OF PHILOSOPHY IN NUCLEAR AND SCIENCE AND ENGINEERING
AT THE
MASSACHUSETTS INSTITUTE OF TECHNOLOGY

June 2015

Signature of Author: Signature redacted
Department of Nuclear Science and Engineering
May 15, 2015

Certified By Signature redacted
Ronald G. Ballinger
Professor of Nuclear Science and Engineering
Professor of Materials Science and Engineering
Thesis Supervisor

Certified By Signature redacted
Ju Li
Battelle Energy Alliance Professor of Nuclear Science and Engineering
Professor of Materials Science and Engineering
Thesis Reader

Accepted by: Signature redacted
Mujid S. Kazimi
TEPCO Professor of Nuclear Engineering
Chair, Department Committee on Graduate Students

Hydrogen Entry in Zircaloy-4 Fuel Cladding: An Electrochemical Study

by
Jennifer Anne Jarvis
Submitted to the Department of Nuclear Science and Engineering
on May 15, 2015 in partial fulfillment of the requirements for the degree of
Doctor of Philosophy in Nuclear Science and Engineering

Abstract

Corrosion and hydrogen pickup of zirconium alloy fuel cladding in water cooled nuclear reactors are life-limiting phenomena for fuel. This thesis studies the fate of hydrogen liberated by waterside corrosion of Zircaloy-4 fuel cladding in Pressurized Water Reactors (PWRs): are the adsorbed protons incorporated into the oxide and eventually the metal, or are they evolved into molecular hydrogen and released into the coolant? Water chemistry modeling was used to understand effects of radiolysis and CRUD. Density functional theory (DFT) was used to investigate the role of oxidized $Zr(Fe,Cr)_2$ second phase particles. Chemical potentials and the electron chemical potential were used to connect these two modeling efforts.

A radiolysis model was developed for the primary loop of a PWR. Dose profiles accounting for fuel burnup, boron addition, axial power profiles, and a CRUD layer were produced. Dose rates to the bulk coolant increased by 21-22% with 12.5-75 μm thick CRUD layers. Radially-averaged core chemistry was compared to single-channel chemistry at individual fuel rods. Calculations showed that local chemistry was more oxidizing at high-power fuel and fuel with CRUD. Local hydrogen peroxide concentrations were up to 2.5 ppb higher than average levels of 5-8 ppb. Radiolysis results were used to compute chemical potentials and the corrosion potential. Marcus theory was applied to compare the band energies of oxides associated with Zircaloy-4 and the energy levels for proton reduction in PWR conditions.

Hydrogen interactions with Cr_2O_3 and Fe_2O_3, both found in oxidized precipitates, were studied with DFT. Atomic adsorption of hydrogen was modeled on the Cr and Fe-terminated (0001) surfaces. Climbing Image-Nudged Elastic Band calculations were used to model the competing pathways of hydrogen migration into the subsurface and molecular hydrogen formation. A two-step mechanism for hydrogen recombination was identified consisting of: reduction of an adsorbed proton (H^+) to a hydride ion (H^-) and H_2 formation from an adjacent adsorbed proton and hydride ion. Overall, results suggest that neither surface will be an easy entrance point for hydrogen ingress and that Cr_2O_3 is more likely to be involved in hydrogen evolution than the Fe_2O_3.

Thesis Advisor: Ronald G. Ballinger
Title: Professor of Nuclear Science and Engineering,
and Materials Science and Engineering

Acknowledgements

I am very grateful to my advisor, Professor Ballinger, for his support and advice throughout my doctoral studies. Your relentless support of your students is remarkable, and I do not think I could have succeeded without it.

I'd like to thank my committee members: Professor Li, Professor Yildiz, and Professor Short, for guidance with this thesis. I was completely new to the modeling and simulation of materials when I started this project, and this thesis would not have been possible without your help.

Many thanks to Dr. Koroush Shirvan for help with MCNP and feedback on the PWR parameters used in the RADICAL model. I'd like to thank Miaomiao Jin for assisting with the input parameters for CRUD. Many thanks as well to Dr. Mostafa Youssef who was a great help with VASP and solid state physics in general. I'd also like to thank my fellow students in the H.H. Uhlig Corrosion group, who have helped make the past few years enjoyable. You have all been great colleagues, and I've benefited greatly from seeing the experimental side of corrosion through your work.

I'd like to thank Al and Mary Jarvis, for sharing their knowledge about water chemistry. Your advice and industry experience was valuable back when I first started with radiolysis modeling and worked on the BWR benchmarking calculations. I was very fortunate to find out that I already had connections in the radiolysis and water chemistry business!

Many thanks to my family: I could not have survived so many years in school without your support. Mom and Dad, thank you for all the encouragement over the years, checking up on me (not to mention my studies and research!). Your dedication is amazing, and I am very grateful to have parents who were both capable and willing to help me with tables and equations for my thesis, during my illness at the very end of my studies. Many thanks to my brothers, Matt and Andy, who have helped and advised me on all sorts of things (especially programing problems) and cheered me all along the way. Most importantly: thank you for laughing with me about the woes of studying engineering and coding in Fortran- it's been a fantastic morale booster.

I would also like to thank all my friends at Sidney-Pacific, who have made the past few years a delight. I'd like to especially acknowledge my fellow 2012-2013 executive officers – Pierre, Steve, George, and Steph. It was a challenging job, and I personally learned a lot from the experience and all of you. I can't imagine a better or more fun group to have worked with and shared so many adventures with.

This research has been funded by the US Department of Energy's Consortium for Advance Simulation of Light Water Reactors.

Table of Contents

List of Figures

List of Tables

Nomenclature

Abbreviations

AOA	Axial Offset Anomaly
AES	Auger Electron Spectroscopy
AVS	Absolute vacuum energy scale
BOC	Beginning of cycle
BWR	Boiling Water Reactor
CI-NEB	Climbing Image Nudged Elastic Band
CILC	CRUD induced localized corrosion
CIPS	CRUD induced local power shift
CRUD	Chalk River Unidentified Deposit
DFT	Density Functional Theory
DOS	Density of States
ECP	Electrochemical Corrosion Potential
EOC	End of Cycle
GGA	Generalized Gradient Approximation
hcp	Hexagonal close packed
HPUF	Hydrogen Pickup Fraction
LDA	Local Density Approximation
LOCA	Loss of Coolant Accident
LWR	Light Water Reactor
MOC	Middle of Cycle
MPM	Mixed Potential Model
MWd	Megawatt-days
NEB	Nudged Elastic Band
PAW	Projector Augmented Wave
PBE	Perdew-Burke-Ernzerhof functional
PDOS	Projected Density of States
PEC	Photoelectrochemical
ppb	Parts per billion
ppm	Parts per million
PW91	Perdew-Wang functional
PWR	Pressurized Water Reactor
scc	Standard cubic centimeter. (At standard pressure and temperature)
SCE	Saturated calomel electrode

SEM	Scanning Electron Microscope
SHE	Standard Hydrogen Electrode
SIMS	Secondary ion mass spectroscopy
SPP	Second Phase Particle
STP	Standard temperature and pressure
TEM	Transmission Electron Microscope
TSS	Terminal Solid Solubility
XANES	X-ray Adsorption Near Edge Structure
XRD	X-ray Diffraction

Symbols

a_i	Activity of species "I"
a_o	Lattice constant
A	Cross sectional area
b_a, b_c	Tafel coefficients
B	Bulk modulus
C_i	Concentration of species i
d	Hydraulic diameter
D_i	Diffusivity of i in water
E	Energy
$E_{10B(\alpha,Li)}$	Effective total energy of the α and $^{7}_{3}Li$ recoil nuclei from the $^{10}B(n,\alpha)$ reaction
E_c	Conduction band energy (the bottom of the conduction band)
E_{cs}	Conduction band at the surface
E_{fb}	Flat band potential
E_g	Band gap energy
E_v	Valence band energy (the top of the valence band)
$\mathbb{E}$	Cell potential (Volts)
$\mathbb{E}^{e}_{R/O}$	Equilibrium potential of (R/O) redox couple
$\mathbb{E}^{o}_{R/O}$	Standard cell potential
$\mathcal{E}_i$	energy deposition per unit mass in i
$\mathcal{E}'$	Energy deposition per unit length
f_{cool}	Fraction of energy deposited in CRUD
$\mathcal{F}$	Faraday's constant
F	Helmholtz free energy

$g(E)$	Density of states
G	Gibbs free energy
$\mathcal{G}_i$	G-value of the given species
h_{fg}	Latent heat of evaporation
H	Nuclear heating
i	Partial current
i^o	Exchange current density
i_l	Limiting current
I	Ionic strength (used in Debye Huckel Theory)
J_c	Cathodic current
k	Rate constant for chemical reactions
k_B	Boltzmann constant
k_{rad}	Conversion factor for g-values from [# / 100 eV]
K	Equilibrium reaction constant
$\mathcal{K}_i$	Henry's law constant for i
m_i	Molality
M_i	Molar mass of i
n(E)	Density of conduction electrons as a function of energy
N	Atom density
N_A	Avagadro's number
$\mathcal{N}$	number of atoms
p(E)	Density of holes as a function of energy
pH_{zpc}	pH at the point of zero charge
P	Partial pressure
P^o	Reference pressure (0.1 MPa)
q'	Linear heat generation rate
q''	Heat flux
Q_i	Dose rate
r_{ion}	Radius of ion
R	Universal gas constant
Re	Reynold's number
$\mathcal{R}$	Distance to mirror image of an ion at an electrode
S	Entropy
Sc	Schmidt number
T	Temperature
T^o	Standard temperature 298 K
V	Fluid velocity
$\mathbb{V}$	Volume

x	Mole fraction of i
w_{cool}	Mass fraction of the coolant in CRUD deposit
$W(E)$	Distribution of energy levels, normalized to 1
z	charge (number of electrons transferred in a reaction, or charge of species)
α	Void fraction
γ_i	Activity Coefficient of i
δ	Crud thickness
ϵ_o	Permittivity of vacuum
$\epsilon_{opt,1}$	Optical dielectric constant
$\epsilon_{s,1}$	Static dielectric constant
Θ	Surface coverage
λ	Reorganization energy
μ	Chemical potential
$\mu_i^{g,l}$	Mass transfer coefficient of species i from liquid to vapor
ν	kinematic viscosity
ρ	Density
σ_a	Absorption cross section
σ_T	total cross section
ϕ	Porosity
Φ	Fluence (particles/cm^2)

Chapter 1: Introduction

1.1 Motivation

Zirconium alloys are used as fuel cladding in current light water reactor (LWR) nuclear power plants. The cladding is exposed to harsh operating conditions: high temperature, high pressure, and large neutron fluxes during the fuel residence in core, which is typically 4-6 years in total. Waterside corrosion of the cladding occurs due to the reaction between the zirconium and water, producing a protective zirconium oxide layer and molecular hydrogen. The majority of the hydrogen produced by the corrosion reaction is released into the coolant. However, a fraction is absorbed by the cladding. Hydrogen generally causes embrittlement in metals. Hydrogen has a relatively low solubility in zirconium and precipitates in zirconium hydrides, which are detrimental to the material strength and ductility. [1] The mechanism of how hydrogen enters the cladding and hence the "hydrogen split," the division between adsorbed and released hydrogen, is not understood but is critical to understanding cladding performance.

Previously, cladding hydrogen entry in Light Water Reactors (LWRs) has been treated empirically through the use of a hydrogen pickup fraction, which is defined as the ratio of hydrogen absorbed by the cladding to the total amount of hydrogen liberated in the corrosion reaction. For example, FRAPCON 3.2 uses a pickup fraction of 0.15 for Zircaloy-4 in PWR (Pressurized Water Reactor) conditions, and a pickup fraction of 0.29 for Zircaloy-2 in BWR (Boiling Water Reactor) conditions, regardless of the material properties. [2] However, hydrogen pickup is experimentally observed to depend on the

manufactured cladding chemical composition and microstructure, the chemistry of the coolant, and fuel burnup. [3–5]

Hydrogen absorption is life limiting for fuel cladding. As fuel is being pushed to higher burnup, corrosion and hydrogen pickup become more important in determining the lifetime of the fuel. Being able to accurately predict these rates is crucial to ensuring that the cladding integrity will be maintained through the life of the fuel and in spent fuel storage.

A diverse number of theories have been proposed to explain the behavior of hydrogen pickup in zirconium alloys:

- Second Phase Particles (SPPs) can short circuit diffusion through the oxide layer [6]
- Metallic SPPs (in the oxide) can trap hydrogen [7]
- Cracks and pores act as the sites for recombination/entry [8]
- Cracks/pores can serve as "hydrogen pumps" through a "steam depletion effect" [9,10]
- Hydrogen atoms or ions enter on the outer surface of the oxide. They diffuse through the oxide layer, most likely along grain boundaries

1.2 The Coolant/CRUD/Oxide/Clad System

We begin by considering the overall system for hydrogen entry, shown in Figure 1-1. In this general case, the system is independent of the alloy composition or coolant chemistry. The metal cladding is covered by an oxide layer, which consists of a dense

inner layer and an outer porous layer. There may also be a layer of CRUD covering the oxide layer. Individual parts of this system will be discussed in greater detail throughout this thesis.

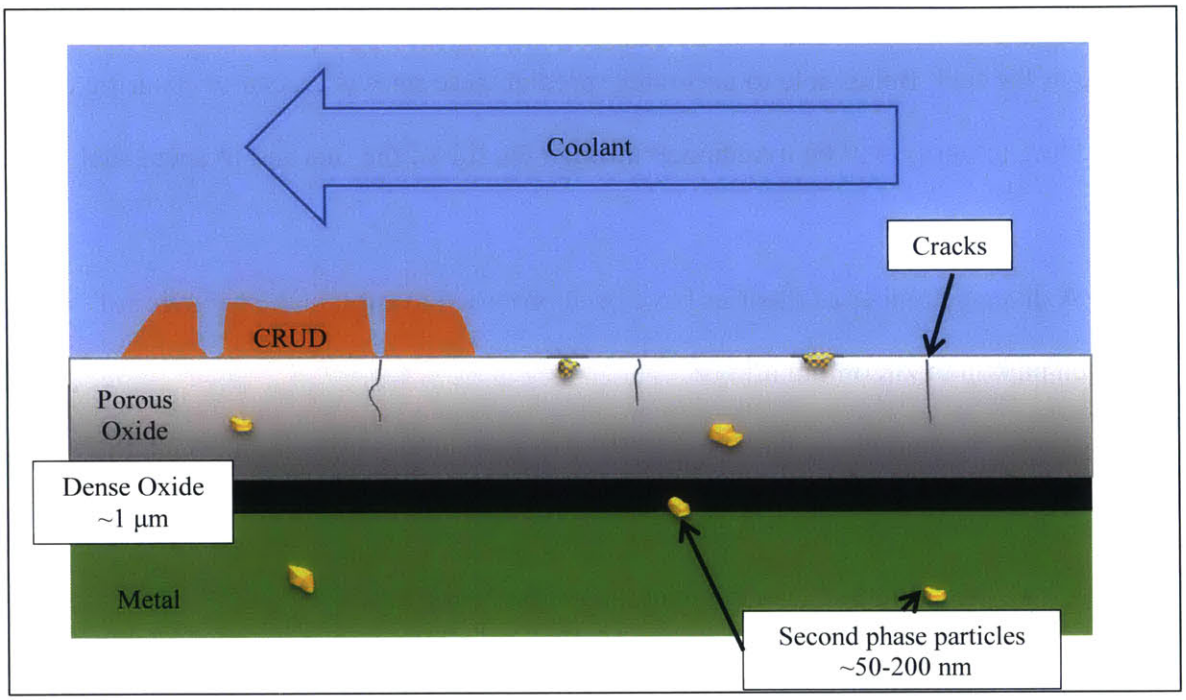

Figure 1-1. Coolant/CRUD/Oxide/Clad System for corrosion and hydrogen entry

1.3 Waterside Corrosion and the "Hydrogen Split"

To put hydrogen pickup into context, we first begin with corrosion. In waterside corrosion, the zirconium metal reacts with water as follows:

$$Zr + 2\,H_2O \rightarrow ZrO_2 + 2H_2$$

The anodic half-cell reaction is:

$$Zr \rightarrow Zr^{4+}\,4e^-$$

And the cathodic half-cell reaction is:

$$2H^+ + e^- \rightarrow H_2$$

The overall corrosion reaction can be broken down into separate steps, beginning with a water molecule dissociating onto the oxide surface:

$$H_2O \rightarrow OH_{ad}^{-} + H_{ad}^{+} \rightarrow O_{ad}^{2-} + 2H_{ad}^{+}$$

The oxygen ion is incorporated into the oxide layer and diffuses to the metal oxide interface. The zirconium ion forms zirconia with the oxygen ions:

$$Zr + 2O^{2-} \rightarrow ZrO_2 + 4e^{-}$$

The electrons migrate across the oxide layer and reduce the adsorbed protons which eventually form molecular hydrogen. However, a fraction of the hydrogen migrates to and is absorbed into the zirconium metal. The chemical potential of hydrogen must be lower (more negative) in the metal than in the coolant for hydrogen absorption to occur. In the case of PWRs, the majority of hydrogen is evolved and released into the coolant, which means that the rate of hydrogen transport rate into the metal is slower than the rate of hydrogen recombination and release. Thus, while hydrogen entry into the cladding is preferred by *thermodynamics*, the rate of hydrogen ingress is limited by *kinetics*.

Returning to the adsorbed protons at the oxide surface, the two possible pathways are:

$$2H_{ad}^{+} + 2e^{-} \rightarrow H_2$$

$$H_{ad}^{+} \rightarrow H_{ab}^{+}$$

In the equations above, hydrogen is incorporated into the oxide in the form of a proton. However, the proton could alternatively be reduced at the surface and absorbed as a neutral hydrogen atom or a hydrogen anion. The recombination reaction will likely

occur by several elementary reactions, such as proton reduction, chemical recombination ($2H \rightarrow H_2$), and/or electrochemical recombination ($H + H^+ + e^- \rightarrow H_2$). The competition between these two pathways, the "hydrogen split," ultimately determines the hydrogen pickup fraction.

Figure 1-2 summarizes the hydrogen split. In this diagram, we make no distinction as to:

1. The location(s) of surface reactions: do they occur within a pore/crack in the oxide, on the outer oxide surface, on a precipitate, at an exposed grain boundary?
2. Diffusion pathways or mechanisms: is it along grain boundaries, through "bulk" crystal)
3. Whether hydrogen absorbs as a proton or neutral hydrogen atom
4. The specific mechanism of recombination: chemical, $2H \rightarrow H_2$ or electrochemical, $H + H^+ + e^- \rightarrow H_2$

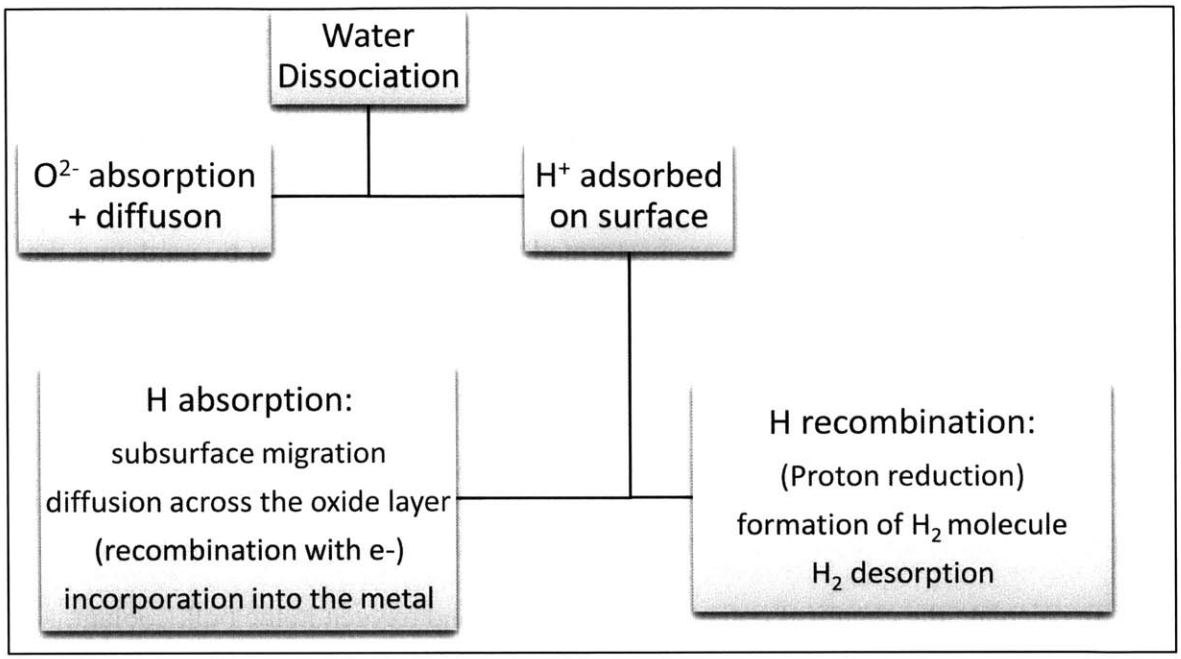

Figure 1-2. The hydrogen split between adsorption and recombination

This brings us to the main point: the hydrogen split is complicated; if we wanted to create a mechanistic model for hydrogen pickup fraction, we would need to identify specific locations and mechanisms of each step, as well as the rate-limiting step for the absorption and recombination pathways. On a more practical note, if we can understand what governs the hydrogen split, we can design alloys, heat treatments, or surface treatments to reduce hydrogen pickup.

1.4 Thesis Objectives

This thesis investigates the effects of water chemistry, radiolysis, and intermetallic precipitates on the hydrogen pickup fraction of Zircaloy-4 fuel cladding in pressurized water reactors. The focus of this research in this thesis will be along two

major paths: (1) the potential effect of radiolysis on bulk and local chemistry, including the effects of CRUD and (2) the energetics of hydrogen reactions on the surface of oxidized precipitates.

The radiolysis calculations are performed on a macroscale level by modeling the entire primary loop of a PWR. The surface reactions are studied at the atomic level with Density Functional Theory. While these two types of calculations may seem quite different, they are closely related. Radiolysis calculations determine the concentrations of hydrogen, oxygen, and hydrogen peroxide in the coolant. These concentrations can be used to calculate the chemical potentials of hydrogen and oxygen in the bulk coolant. Using pH calculations and mixed potential theory, we can estimate the redox potentials of hydrogen, oxygen, and hydrogen peroxide, and the corrosion potential (ECP). We can link the radiolysis calculations and DFT surface reaction calculations thorough thermodynamics. We can also apply electrochemistry to calculate the energy levels of the proton-neutral hydrogen redox couple in solution, and compare these to the band structure of the oxide layer.

1.5 Thesis outline

As mentioned above, the focus of this research in this thesis will be along two major paths: (1) the potential effect of radiolysis on bulk and local chemistry, especially as it relates to CRUD and (2) the energetics of the hydrogen reactions and transport through the oxide layer. This thesis begins with an extensive literature review of zirconium alloys, corrosion, and radiolysis in Chapter 2.

The first part of this thesis addresses the modeling radiolysis and primary water chemistry in a PWR core. In Chapter 3, water reaction sets, g-values, and ECP models are benchmarked against measured data from BWRs. From these results, we can determine the appropriate sets and models to use in the PWR radiolysis model. In Chapter 4, a more advanced and detailed radiolysis model is developed for the primary loop of a pressurized water reactor. Dose rates in the core, bypass, and downcomer are calculated for realistic axial power profiles. In Chapter 5, the PWR model is modified to study the effects of CRUD on bulk water chemistry. Dose rates are explicitly calculated for various crud thicknesses and boron concentration. Within the radiolysis models, we discuss bulk and local water chemistry: bulk chemistry referring to a channel averaged (either over the whole core or a single channel). Local bulk water chemistry designates changes in chemistry that may be found near a high power or high burnup fuel rod. "Local effects" can also occur on a smaller length scale, for example near surfaces or within porous CRUD deposits.

The second part of this thesis studies second phase particles at the oxide/coolant interface in an effort to gain insight into the energetics of the hydrogen disposition processes. Density functional theory calculations are used to investigate Cr_2O_3 and Fe_2O_3, which are found in the oxidized second phase particles (SPPs). In Chapter 6, the chemical potentials of hydrogen and oxygen in the bulk coolant are calculated. The equilibrium potential of the hydrogen evolution reaction is compared to the band structures of oxides which can be found in Zircaloy-4 fuel cladding. In Chapter 7, density functional theory calculations are performed for bulk perfect crystal α-Cr_2O_3 and α-Fe_2O_3. Surface

relaxations are performed for common termination of the (0001) surfaces. In Chapter 8, hydrogen adsorption, recombination, and migration into the surface are studied on the single metal terminated (0001) Cr_2O_3 and Fe_2O_3 surfaces.

Chapter 2: Literature Review

In this chapter, literature related to corrosion and hydrogen pickup of zirconium alloys is reviewed. The chapter begins with a brief introduction to water chemistry in pressurized water reactors (PWRs). Next, we review information on zirconium alloys, including a detailed review of the many factors influencing corrosion and hydrogen pickup. Finally, we examine radiolysis and recent modeling efforts at the atomic level to understand hydrogen pickup and corrosion.

2.1 Core Conditions and Primary Loop Chemistry

The coolant in a PWR is subcooled water at nominally 15.5 MPa and temperatures ranging from 300-350°C. The chemistry of the primary loop is carefully maintained to minimize degradation of reactors components and limit out-of-core radiation levels. [11] Hydrogen is added to the coolant to suppress the effects of radiolysis, maintain reducing conditions, and limit corrosion of the primary loop components. Boric acid is added for reactivity control, and lithium hydroxide is added for pH balance. Figure 2-1 shows a typical boron letdown curve. The boron concentration is greatest in the early part of the cycle, when the core has the most excess reactivity. As the fuel is depleted, less boron is required to maintain criticality. Beginning of cycle (BOC) boron concentrations may be as high as 2000 ppm, and at the end of cycle, no boron is added. Longer fuel cycles required higher initial concentrations of boron; however the required boron addition can be reduced by adding burnable poisons, such as boron,

gadolinium, or erbium to the fuel. Note that the maximum boron addition to the coolant is set by limits on a positive moderator temperature coefficient, which quantifies how reactivity changes with temperature. An increase in coolant temperature decreases the coolant density, which reduces neutron moderation (lowering reactivity) and decreases the amount of boron per unit volume (increasing reactivity). In Figure 2-1, there is a maximum in boron at 2.5 MWd/kgU; this peak is attributed to the depletion of burnable poisons in the fuel.

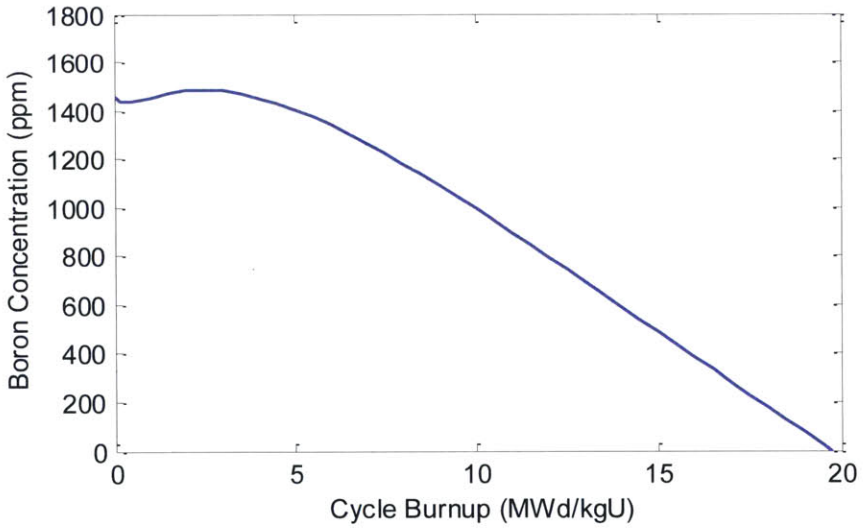

Figure 2-1. Typical boron letdown curve for a PWR [10]

The pH of the primary coolant is typically maintained at 6.9-7.4. The operating pH is bounded by multiple concerns: operating at a higher pH can reduce out of core radiation fields and reduce CRUD deposition, however, the higher lithium concentrations increase the risk of cracking of Alloy 600 components and increase corrosion of the fuel cladding. To balance concerns over pH and lithium, multiple chemistry regimes have been developed: [11]

1. Coordinated Chemistry: Li addition to maintain pH_T of 6.9
2. Elevated Lithium: Target $pH_T = 7.4$, but do not exceed 3.5 ppm Li
3. Modified Chemistry:
    a. Maintain constant $pH_T = 6.9$ while decreasing Li until 2.2 ppm Li
    b. Increase pH with constant Li until $pH_T = 7.2$-7.4
    c. Maintain $pH_T = 7.2$-7.4

Figure 2-2 shows the relationship between boron, lithium, and pH for these regimes.

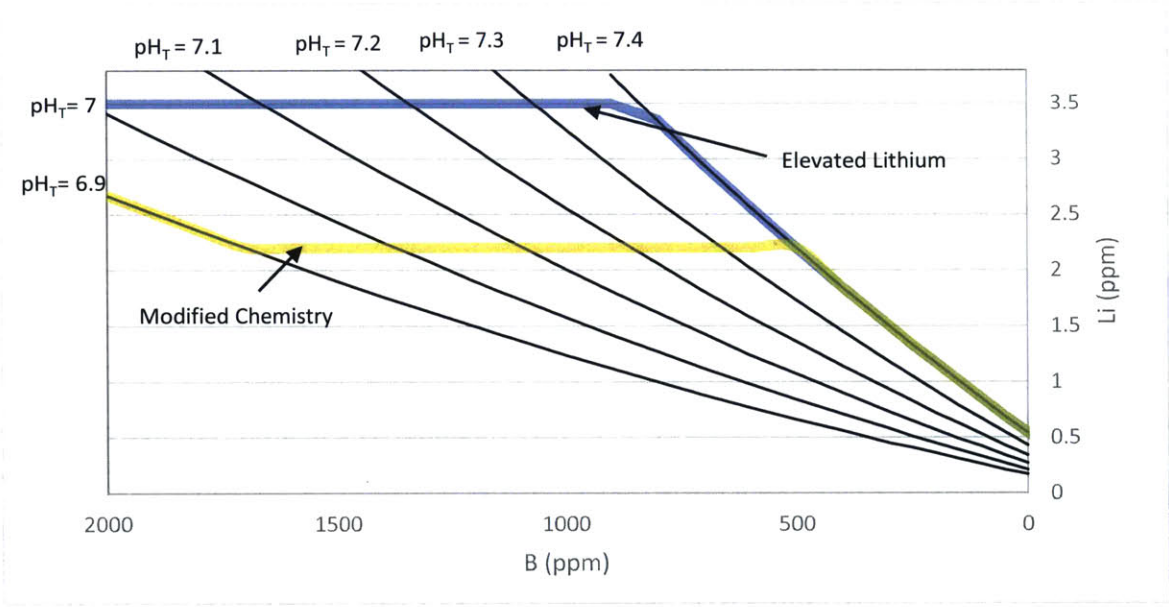

Figure 2-2. B and Li addition for PWR chemistry regimes at 310°C. Adapted from [11]

CRUD (original name: Chalk River Unidentified Deposits) are deposits of corrosion product on the fuel cladding. The different components in the reactor cooling system (steam generators, pipes, pumps, pressurizer, and the reactor pressure vessel) slowly corrode under exposure to the coolant and release corrosion products, namely iron and nickel, in the primary loop. CRUD deposition is associated with subcooled nucleate

boiling; thus most CRUD is found at the top of the core. If boiling occurs in the porous CRUD deposits, then boron and lithium can become concentrated. In cases with significant boron enrichment, the boron will suppress the neutron flux in the top of the core and shift the axial power distribution toward the bottom of the core, resulting in Axial Offset Anomaly (AOA) or a CIPS (CRUD-induced power shift). [12–14]

2.2 Zirconium Alloys

Zirconium alloys were chosen for fuel cladding because of their low thermal neutron cross section, material strength, and relatively good corrosion resistance at high temperatures. Up to temperatures of approximately 865°C, zirconium is in the alpha phase: a hexagonal close packed structure, with a =3.23 A and c=5.15 A. [1]

Boiling water reactors traditionally use Zircaloy-2 for fuel cladding. Pressurized water reactors traditionally use Zircaloy-4 for fuel cladding. The main difference between the two alloys is that Zircaloy-4 has no nickel, as nickel was associated with increased hydrogen pickup. In recent years, new alloys such as ZIRLO and M5 have been developed for improved corrosion resistance and lower hydrogen pickup. [1,15,16] Table 2-1 lists the composition of Zircaloy-2, Zircaloy-4, ZIRLO and M5.

Table 2-1. Composition of common zirconium alloys

	Cr	Fe	Ni	Sn	Nb	Reference
Zircaloy-2	0.05-0.15	0.07-0.2	0.03-0.08	1.2-1.7	-	[1]
Zircaloy-4	0.07-0.113	00.18-0.24	-	1.2-1.7	-	[1]
ZIRLO™	<0.01	0.1-0.11	-	0.9-1	0.9-1	[15,16]
M5®	<0.015	<0.05	-	<0.01	1	[15]

The solubility of Fe, Ni, and Cr in zirconium are very low, and these form intermetallic precipitates of $Zr(Fe,Cr)_2$ and $Zr_2(Fe,Ni)$. $Zr(Fe,Cr)_2$ is a laves phase with either the C14 hexagonal structure or the C15 face centered cubic structure. [1] The size and distribution of these second phase particles depends on the heat treatment of the alloy. [5]

2.2.1 Oxide Microstructure

The solubility of oxygen in alpha zirconium at reactor temperatures has been cited as 28-33 atom percent. [17,18] Once the solubility of oxygen in the metal exceeded, ZrO_2 will precipitate. The oxide film on zirconium alloys has a layered structure; generally consisting of a dense inner layer and a porous outer layer. Near the metal/oxide interface, the oxide is substoichiometric. Suboxides of Zr_2O, ZrO, and Zr_2O_3 have been observed at the inner surface of the oxide layer. These suboxides transform to tetragonal zirconia further away from the interface. [17,19] Monoclinic zirconia is the stable phase at room and reactor temperatures; the monoclinic to tetragonal transition occurs at approximately 1200°C. The Pilling-Bedworth ratio of ZrO_2 is approximately 1.56, which creates high compressive stresses in the oxide. [1] These stresses, along with a small grain size, stabilize the tetragonal phase. As the distance from the metal/oxide interface increases, the compressive stresses decrease. Once the stress is below the critical stress for stabilization of the tetragonal phase, the oxide transforms to monoclinic. This transformation is accompanied by a 5-7% volume increase, and the transition is associated with cracking and or porosity in the oxide. [5,17] The oxide layer is observed

to consist of small equiaxed grains near the oxide/metal interface, and columnar grains further from the interface.

Ni et al. studied porosity in oxide layers on zirconium alloys using TEM (Transmission Electroscope Microscope). They studied four materials which were oxidized in simulated PWR chemistry. Samples of recrystallized Zircaloy-4 sheet and stress relieved Zircaloy-4 tube were exposed at 360°C to produce a pretransition oxide. Zircaloy-2 was exposed at 415°C to produce a 32 μm post-transition oxide. In the pretransition oxide films, the researchers observed small cracks 30-100 nm long and 10 nm wide and pores that were 10-30 nm in diameter and unevenly distributed in the oxide. These were primarily found at the outer part of the oxide. Near the oxide/metal interface, the authors observed denser oxide, with a few small cracks that were parallel to the outside oxide surface, yet remained isolated from this surface. Pores 1-3 nm in size were observed near the oxide-metal interface and along the columnar grain boundaries of the oxide. In the post transition oxide, the pores in the oxide on this sample were almost fully interconnected at boundaries between the monoclinic grains. Noting that the width of these connected pathways are close to the size of the pores in the pre-transition sample, the authors propose that in post transition oxides, the small pores start to connect parallel and perpendicular to the oxide growth direction, forming an easy diffusion path. [20]

Preuss et al. studied the microstructure of oxide layers on ZIRLO that had been exposed in a water environment at 18 MPa and 360°C with 2 ppm LiOH and 1000 ppm boric acid. Samples were exposed to produce an oxide thickness of up to 3 μm. The resulting oxide had a layered structure: the innermost oxide layers, near the metal/oxide interface were "nearly perfectly dense" with isolated pores along the columnar grain

boundaries. At a distance of 300-400 nm from the metal-oxide interface, connected porosity along the grain boundaries was observed. The porosity became well developed at around 700 nm from the metal oxide interface. Additionally, cracks and larger pores are observed near the surface of the oxide. An outer layer was observed consisting of equiaxed grains with high levels of porosity.

Figure 2-3 shows key features of the porosity in the oxide, as observed by Ni et al. and Preuss et al. [16,20] The left side shows the observed features, while the right side shows the degree of the porosity.

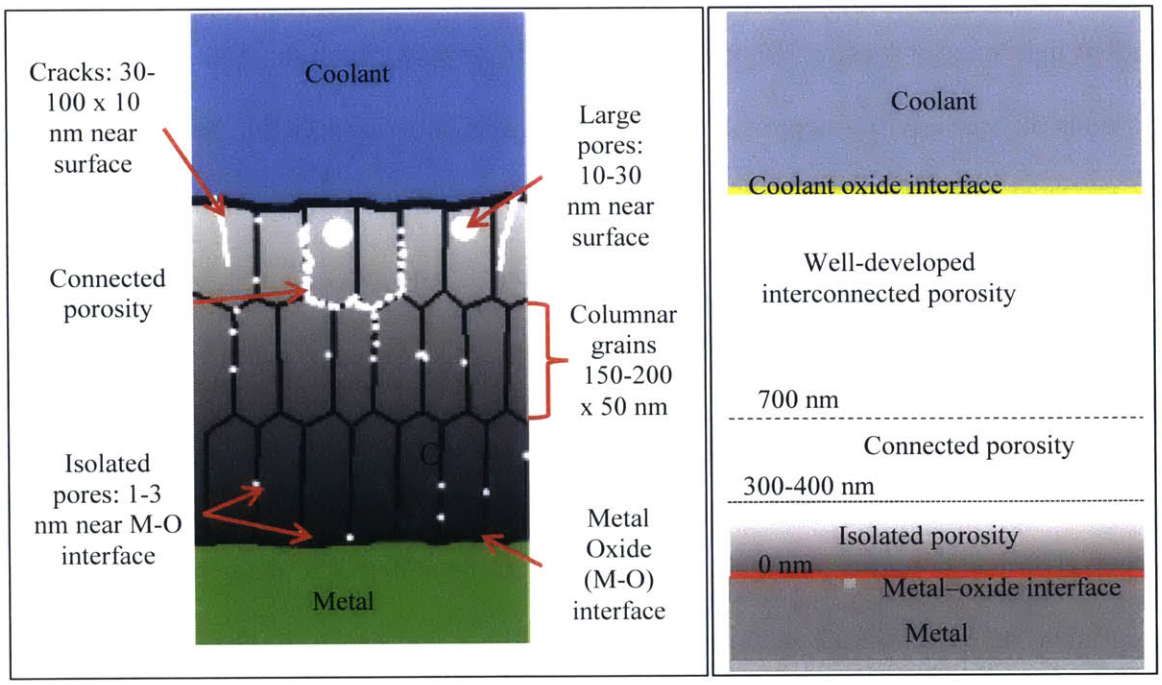

Figure 2-3. Key features of porosity in the oxide layer, findings from [16,20]

2.2.2 Second Phase Particle Microstructure and Behavior

The second phase particles in Zircaloy-4, $Zr(Cr,Fe)_2$, oxidize after the bulk α-zirconium matrix. These precipitates are incorporated into the oxide layer while still metallic, and eventually oxidize. Researchers have used various techniques to study the composition and microstructure of the precipitates in the oxide layer in order to better understand the changes that occur to the oxidizing precipitates and surrounding zirconia matrix both in-pile and out-of-pile.

Photoelectrochemical (PEC) techniques can be used to identify the various phases in the oxide film by comparing the known band gaps to a measured photocurrent vs. incident light energy spectra. Benaboud et al. oxidized pure zirconium and Zircaloy-4 in a gaseous oxygen environment at 470°C. Using x-ray diffraction (XRD), they were only able to observe metallic zirconium and monoclinic zirconia in samples. With macroscopic PEC, they identified monoclinic zirconia (band gap of 5 eV), hematite (band gap of 2.2-2.6 eV), mixed $(Fe_xCr_{x-1})_2O_3$ oxides (band gap 2.6-3.0 eV), and Cr_2O_3 (band gap of 3 eV – 4.0 eV). [21] Dali et al. also used PEC to study oxides on Zircaloy-4 formed in steam at 415°C. They further distinguished between n-type Cr_2O_3 grown at low oxygen chemical potential at 3.0 eV and p-type Cr_2O_3 grown at high oxygen chemical potential at 3.5 eV. Unlike Benaboud et al., they did not find Fe_2O_3 in the oxide layer. In a 0.9 μm pretransition oxide, they observed mixed oxides, and both n and p-type Cr_2O_3. In a 5 μm post-transition oxide, they found no mixed oxides, and noted that the p-type Cr_2O_3 concentration was greater than n-type Cr_2O_3. They note that PEC measurements could only be obtained at depths of up to ~1 μm in from the surface. [22]

Sakamoto et al. studied the oxidation states of Fe and Cr in the oxide layer of a Zr-0.5Sn-1.0Cr-0.5Fe alloy. Samples were exposed in steam at 673K to an oxide thickness of 1.3 μm and 1 M LiOH water at 573K to an oxide thickness of 20μm. XANES (x-ray adsorption near edge structure) was used to determine the fraction of oxidized states of Fe and Cr at different depths in the oxide layer. Results indicated that the fraction of oxidized states increased with distance from the metal-oxide interface and that Cr oxidized twice as fast Fe. [23]

Baek and Keong studied the oxidization of precipitates in Zircaloy-4. They heat treated the samples to make larger precipitates; post treatment, the precipitates were ~3 μm. Prior to oxidation the precipitates had a Fe/Cr ratio 1.2-1.7, and the C14 hcp laves phase structure. Samples were oxidized in steam at 400°C and studied with SIMS (secondary ion mass spectroscopy) and EPMA (electron probe micro-analysis). Both techniques indicated that the iron content in oxidized precipitates was less than the content of the original metallic precipitates, while the chromium content did not significantly change. [24]

Hatano and Sugisaki studied precipitates in oxidized Zircaloy-4 using Auger electron spectroscopy (AES). Samples were oxidized in 0.1 MPa steam at 673 K, to produce 0.9 2.1, and 4.1 μm oxide thicknesses. In the 0.9 μm pretransition oxide, the oxygen concentration was higher in the first new nanometers from the outer oxide surface. The concentration of oxygen was constant from 3 nm from the oxide surface to the metal/oxide interface. This indicates that the Fe and Cr were both metallic; the oxygen concentration would change as either Fe or Cr switched from an oxide form to metallic form. Iron is depleted and the oxide is enriched in Cr_2O_3 near the outer oxide

surface. The authors note that sputtering of 10 nm was required for samples with thicker oxide layers, so they could not obtain AES profiles at the surface. From what they were able to measure, the profiles indicated that the Cr enriched region had not grown, but the Fe depleted region had. Overall, the authors explained their results as follows: Cr_2O_3 formed the top layer of the oxide, and the iron oxidized by dissolution in the ZrO_2 matrix, but remained metallic. Cr has a smaller diffusivity than Fe in in ZrO_2. The overall order of oxidation of the $Zr(Fe,Cr)_2$ precipitates is likely thus: first, Zr oxidized to ZrO_2, then Cr oxidized by dissolution into the ZrO_2 matrix, and finally Fe via dissolution into ZrO_2. The Cr segregates to the oxide surface, while the Fe diffuses into the ZrO_2 matrix. [25]

Iltis et al. studied the effects of oxidation and irradiation on $Zr(Fe,Cr)_2$ precipitates in Zircaloy-4. [26] The diameters of precipitates in the initial unoxidized samples ranged from 50-500 nm. They oxidized samples in steam in an autoclave, and in an experimental PWR. They used EDX (energy dispersive x-ray spectroscopy) to study the composition of the samples. For the autoclave samples, the authors observed that oxidation of the precipitates begins several hundred nanometers away from the metal oxide interface. The oxidized zirconium in the precipitates formed cubic or tetragonal nanoparticles of ZrO_2, and iron was gradually rejected from the precipitate. At 1-2 μm away from the oxide-metal interface, the precipitates have no more major structural or chemical changes. However, the iron which had been rejected from the SPPs continued to diffuse in the ZrO_2 matrix. [26]

The PWR exposed samples were oxidized at a temperature of 320°C to a total fluence of 5.4×10^{24} n/m^2 (estimated to be 10.6 displacements per atom), and the resulting oxide was 6-8 μm thick. The authors did not find precipitates near the oxide/coolant

interface and hypothesized that the precipitates had dissolved nearly entirely. In the middle of the oxide layer, the majority of precipitates had ~100 nm diameters, and very few precipitates were larger than 300 nm in diameter. Typical Fe/Cr ratios were 0.6. The largest precipitates in this part of the oxide had diameters greater than 250 nm, were crystalline in the center, and had an amorphous ring around the edges, as shown in Figure 2-4. The ZrO_2 surrounding these precipitates was enriched in iron and contained a higher proportion of tetragonal zirconia, up to several micrometers from the precipitate. Smaller precipitates, approximately 100 nm in diameter, were amorphous, and there was no iron enrichment in the surrounding ZrO_2, which was mainly monoclinic. Near the metal-oxide interface, the largest precipitates were approximately 100 nm in diameter. The author found relatively few precipitates, which they took as indicating high degrees of precipitate dissolution. The observed precipitates appeared to have delayed oxidation, i.e., there was no discernable oxygen enrichment. The Fe/Cr ratio was ~0.2. [26] Figure 2-5 shows a summary of the precipitate morphology observed in the PWR samples.

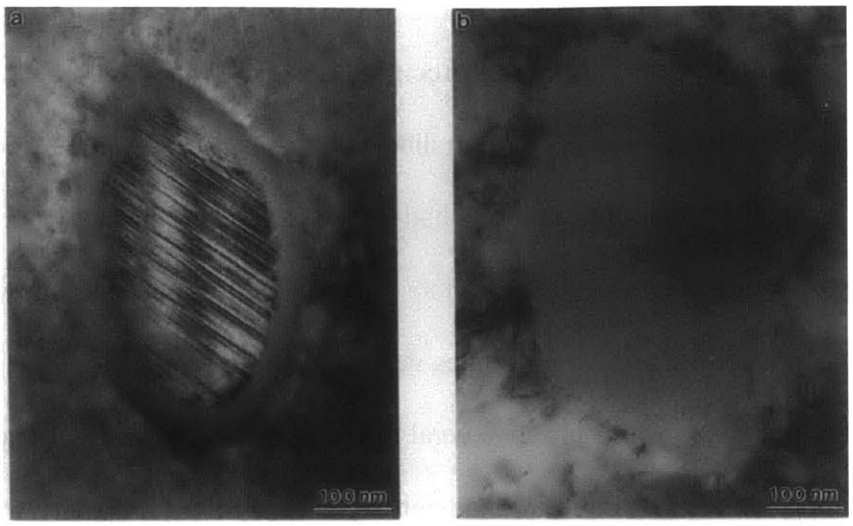

Figure 2-4. Precipitates in the middle of the oxide layer of Zircaloy-4 exposed in PWR. Left: The center is crystalline with Fe/Cr ≈ 1.7. The outer ring is amorphous with Fe/Cr ≈ 0.2. Right: Amorphous precipitate in oxide. Fe/Cr ≈ 0.2 [26]

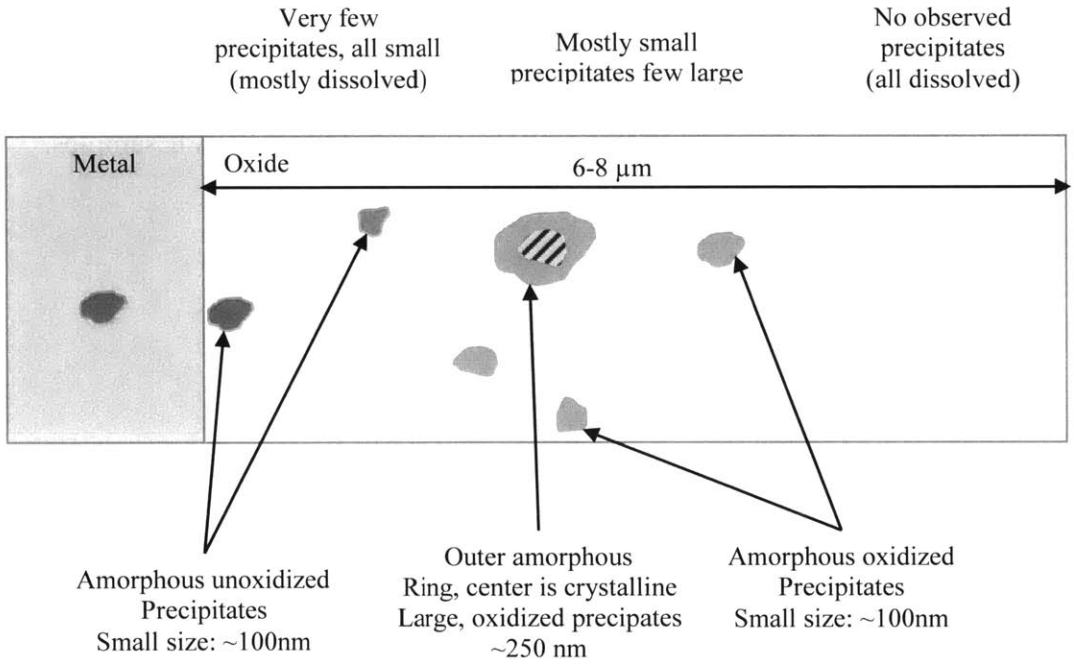

Figure 2-5. Observed precipitates in Zircaloy-4, exposed in PWR at 320°C to a fluence of 5.4×10^{24} n/m^2 , based on results from [26]

Cockeram et al. studied irradiation effects on Zircaloy-2 and Zircaloy-4 using atom probe and TEM methods. The samples were irradiated at 358°C to fluences of 0.058- 29.3 x 10^{24} n/m^2 (E> 1 MeV). Both hexagonal and cubic $Zr(Fe,Cr)_2$ precipitates were found in the Zircaloy-4, and none of the precipitates had become amorphous. EDS scans across the precipitate and surrounding zirconium matrix showed gradients in the composition of the precipitates which indicated that iron and chromium may have diffused out of the precipitates. [27] The researchers noted that their results were consistent with literature results, which indicate that for temperatures greater than 327°C, higher fluences are needed to cause amorphoziation of $Zr(Fe,Cr)_2$ precipitates.

In summary, the following observations have been made about oxidized $Zr(Fe,Cr)_2$ precipitates:

- The precipitates oxidize after the surrounding zirconium matrix.
- Likely phases in the oxidized precipitates include: ZrO_2, Fe_2O_3, Fe_3O_4, Cr_2O_3, and $(Fe_xCr_{x-1})_2O_3$. However, there are some discrepancies among the reported compositions.
- Within the precipitates, zirconium oxidizes first, followed by chromium, and finally iron.
- Oxidation and irradiation cause the precipitates to become depleted in iron, and the surrounding zirconia matrix becomes enriched in iron.
- Under irradiation, precipitates become amorphous and/or dissolve, although the extent will depend on temperature and precipitate size.

2.3 Waterside Corrosion of Zirconium Alloys

Oxide growth occurs via oxygen ion diffusion from the coolant-oxide interface to the metal. Zirconium cations have very low mobility in zirconia, although at high temperatures, for example during a loss-of-coolant accident (LOCA), there may be some zirconium migration in the oxide. [28] The oxide growth kinetics are believed to be governed either by oxygen ion diffusion or electron conduction. [28] Oxygen diffusion in zirconia occurs by migration of oxygen vacancies. Vacancies are generated at the metal/oxide interface and migrate to the outer surface. For diffusion-controlled oxidation, the growth would be expected to follow a parabolic rate law. Instead, a cubic growth law is observed for pre-transition oxide. The deviation in oxide growth kinetics has been attributed to the fact that oxygen anions tend to migrate along grain boundaries. [1,17,28] The oxide structure changes from equiaxed grains to columnar grains further away from the metal/oxide interface, which reduces the available grain boundary area and thus the oxygen migration area. [1]

Oxide growth on zirconium alloys undergoes a transition in kinetics when the oxide layer is approximately 2 μm thick. Prior to this transition, oxide growth generally follows a cubic rate law. Post transition growth tends to follow cyclic behavior, consisting of periods of growth followed by transitions; generally, the growth rate can be approximated as a linear oxidation rate. [1,17,19,28] Figure 2-6 depicts the transitions in oxide growth kinetics. Oxide transitions are associated with a reduction in the protectiveness of the oxide layer. The cause of the transitions is not known, but it is likely related to the development of porosity and cracks in the oxide layer. [22]

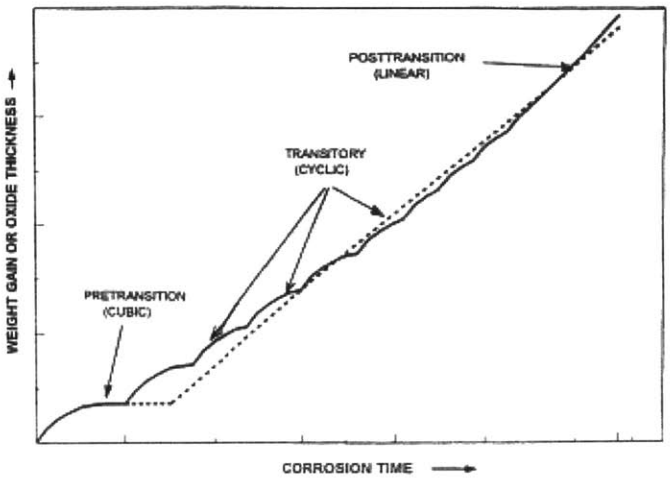

Figure 2-6. Kinetics of zirconium alloy corrosion [29]

The corrosion of zirconium alloys is often discussed in the context of a barrier layer. The barrier layer is the inner protective layer of the oxide film, with higher electric resistivity and is generally impervious. Typical reported thickness of the barrier layer are on the order of 1 μm. [30,31]

2.4 Hydrogen Pickup of Zirconium Alloys

The mechanisms of hydrogen uptake are not well understood; there has been disagreement about the path by which hydrogen enters the metal. It is generally believed that the cathodic half-cell reaction occurs on the coolant side of the oxide film, and the hydrogen diffuses through the oxide layer. [1,4,32,33] Furthermore, it is believed that the "split" of hydrogen occurs on the oxide film surface: adsorbed hydrogen atoms or ions can either recombine to form molecular hydrogen or the hydrogen enters the metal from the surface. [32] The main uncertainty in the process is how hydrogen crosses the oxide from the oxide/coolant interface to the metal: does it diffuse through the bulk oxide

layer, or is it very localized- for example traveling through cracks/porosity, along grain boundaries, or through precipitates?

Early experiments focused on determining by what form hydrogen diffuses through the oxide layer and on measuring the diffusivity of hydrogen in the oxide film, using permeation experiments. However, there were significant variations in the measured diffusivities, and the diffusivity of hydrogen was found to be extremely low. [4,10] These two observations led some researchers to hypothesize that hydrogen entry may be a localized process and does not involve migration through the bulk zirconia. [34]

In 1996, based on the observation that the rate of hydrogen uptake slowed down once the terminal solid solubility (TSS) of the bulk metal was exceeded, Cox proposed that hydrogen uptake is an extremely localized process. When TSS of hydrogen in zirconium is exceeded, zirconium hydrides precipitates in the metal. Cox noted that hydrogen diffusion in the metal matrix is very slow compared to hydrogen ingress rates and hydrides tend to precipitate uniformly in the metal matrix. Consequently, high local hydrogen fluxes would be required for hydrides to precipitate at the metal-oxide interface, and that the precipitation of hydrides at the interface could explain the lower hydrogen uptake rate. [34] He argued that gaseous diffusion experiments, which had been used to measure the diffusivity of hydrogen may not be valid, as oxides exposed to hydrogen gas have been observed to rapidly break down. He further suggested that hydrogen may not enter through the oxide layer, citing a study in which gaseous tritium from the environment was found in the metal but not in the oxide layer. [9],[10]

Cox et al. performed studies on Van Arkel zirconium, Zircaloy-2 and Zr-2.5%Nb to identify the cathodic sites on the oxide. They used cathodic polarization to deposit

small copper balls on pre-oxidized samples. Cathodic sites were located at small cracks or residual scratches on the oxide. After samples were exposed to 400°C steam, the previously identified cathodic sites were no longer active, and new sites had formed. Based on these results, they proposed a steam depletion mechanism: a pore or crack is initially filled with water, and the water reacts with the metal at the bottom of the pore and forms a protective oxide. Hydrogen gas from the cathodic reaction will accumulate at the base of the crack or pore, and eventually the oxide will break down. The hydrogen gas will then be absorbed by the metal, and the metal surface will be repassivated. [9,10]

2.5 Factors Affecting Corrosion and Hydrogen Pickup

The following subsections discuss in detail the many factors that affect the corrosion rate and hydrogen pickup, including alloying elements, precipitates, electrochemical effects, water chemistry, and radiation damage.

2.5.1 Effect of alloying elements

As discussed earlier, zirconium is alloyed with a variety of elements, including Fe, Cr, Sn, Ni. Table 2-1 on page 40 lists the chemical composition of common zirconium alloys. As previously mentioned, nickel is associated with increased hydrogen pickup. [1]

In Zircaloy-2 and Zircaloy-4, tin has been observed to have an effect on corrosion resistance but not on hydrogen pickup. Tin was originally added to zirconium alloys to counteract poor corrosion resistance caused by nitrogen impurities. Takeda and Ananda studied corrosion of Zr-Sn-0.19Fe-0.1Cr alloys with tin content varying from 0.09 to

1.43% (mass percent). The nitrogen content was 40 ppm. The authors exposed samples in 400°C steam for 300 days. They found that oxide growth increased with tin content, and they observed tin segregation at grain boundaries in the oxide. Furthermore, the tetragonal layer of ZrO_2 was thicker in samples with lower tin content and less tin segregation. The authors proposed that the segregated tin degrades the tetragonal ZrO_2 and promotes the tetragonal to monoclinic transition. [35]

Broy et al. studied the effects of increasing iron, chromium, and vanadium content in Zr-Sn alloys on long-term corrosion behavior. [36] Samples were oxidized out of reactor in 350°C pressurized water with and without LiOH additions and in 400°C steam for up to three years. More samples were exposed in a PWR core, at 310-335°C for up to six years. In the out-of-reactor corrosion tests without LiOH present, increasing iron content in the alloys improved corrosion resistance, but chromium and vandium did not. All three elements improved corrosion resistance in the LiOH-containing water and PWR tests. Samples with smaller precipitates exposed in PWRs had higher corrosion rates. The authors also observed that the hydrogen pickup fraction increased with corrosion resistance. [36]

Lim et al. studied hydrogen permeation in standard Zircaloy-4 and two modified Zircaloy-4 alloys. The compositions of the materials are listed in Table 2-2.

Table 2-2. Composition of Zircaloy-4 materials studied by Lim et al. [37]

	Sn	Nb	Fe	Cr	O	Si
Zircaloy-4	1.5	0.01	0.2	0.1	0.1	0
Modified Alloy	1.5	0	0.2	0.1	0.1	0.01
Modified Alloy	0.5	0.1	0.1	0.2	0.2	0

Samples were oxidized in water at 360°C and 18.3 MPa for 150 days. The oxidation behavior (weight gain) was similar for all materials samples, ending with a final oxide thickness of 3.8±0.1 μm. Electrochemical hydrogen permeation tests were performed at room temperature to determine the diffusion coefficient in the oxide. The diffusivity in order of highest to lowest was: Zircaloy-4, followed by the silicon containing alloy, and the niobium containing alloy. The authors correlated the reduction in diffusivity to a higher fraction of tetragonal ZrO_2 in the oxide, and a higher area fraction of precipitates. Note that the precipitate size was approximately 120 nm for all samples. The authors hypothesized that the tetragonal to monoclinic transformation, which is associated with cracking, creates a fast ingress path for hydrogen. [37]

2.5.2 Second Phase Particle/Precipitate Effects

For Zircaloy-2 fuel cladding in BWRs, there is an optimal size for precipitates in the manufactured alloy. [5] Precipitates that are too large will make the cladding susceptible to nodular corrosion. Cladding with small precipitates will generally have good uniform corrosion resistance at the beginning. However, during operation, small precipitates will preferentially dissolve. The dissolution of precipitates coincides with degradation of the barrier layer and a marked increase in both the corrosion rate and hydrogen pickup fraction. Rudling and Wikmark recommended an optimum precipitate diameter of 25-175 nm. [5]

It is generally believed that for thin oxide layers, SPP's can serve as short circuit diffusion pathways for hydrogen, but only while they are metallic and in contact with the metal. Lelièvre et al. studied the role of intermetallic precipitates on hydrogen uptake in

Zircaloy-2 and Zircaloy-4. They oxidized the samples in heavy water stem at 400°C in an autoclave at 15 MPa for 48h and 168 h, which produced oxide thicknesses of 0.7-1.4 μm. The authors analyzed the deuterium distribution using the $^{2}D(^{3}He,p)\alpha$ reaction. In the sample with 0.7 μm oxide, hydrides formed in the zirconium metal near precipitates that were metallic and in the oxide layer but near the metal-oxide interface. The authors did not note any connection between the location of zirconium hydrides and intermetallic precipitates in the sample with 1.4 μm oxide. This was taken as evidence that precipitates can short circuit hydrogen transport through the oxide layer, while precipitates are metallic and in contact with the bulk metal. [6]

Cox argued that although there is an observable correlation between second phase particles and the hydrogen uptake rate, intermetallic particles are not necessarily the path by which hydrogen ingress takes place. He suggested that hydrogen found in intermetallic particles may have been redistributed there by cooling processes; thus the presence of hydrogen may not sufficiently demonstrate that ingress occurs through the intermetallics. Furthermore, in his experiments from 1999, he identified local cathodic sites on zirconium alloys in which all surface precipitates were removed. [9,10]

Murai et al. studied corrosion and hydrogen pickup in iron and chromium containing zirconium alloys. They performed anodic and cathodic polarization experiments on intermetallics $ZrFe_2$, Zr_2Fe, $ZrCr_2$, and $Zr(Fe_{0.66},Cr_{0.33})_2$ at room temperature and 523 K. The chromium containing intermetallics had lower anodic current densities, suggesting better corrosion resistance. The two Zr-Fe intermetallics had lower cathodic resistance, suggesting that they could serve as cathodic sites. [38,39] In later work, Murai et al performed corrosion tests on Zr, Zr-0.2Fe, Zr-0.2Cr, and Zr-0.1Fe-

0.1Cr. Two different heat treatments were used to produce different sized precipitates in the alloys, and samples were oxidized in steam at 633 K. [40] The pickup fractions of the chromium containing alloys were 10-15%, those of Zr-Fe alloys were 80%, and those for crystal bar zirconium were 30%. The samples which had the higher temperature heat treatment and consequently larger precipitate size had slightly smaller pickup fractions than samples of the same alloy but with the lower temperature heat treatment. The Zr-Fe samples had better corrosion resistance than the Zr-Cr samples. The authors attributed the difference in corrosion behavior to anodic protection from the second phase particles: Zr-Fe has higher cathodic efficiencies and serve as more effective cathodes. They attributed the high hydrogen pickup to Zr-Fe second phase particles acting as "windows." The lower pickup fraction with chromium additions was explained by "physical and chemical interactions between the precipitates and hydrogen." [40]

Yao et al. performed steam oxidation tests on Zircaloy-4 and Zircaloy-2 to better understand the relationship between second phase particles and hydrogen uptake. Before oxidation, they applied heat treatments to change the SPP size and distribution. Samples were oxidized at 10.3MPa steam at 400°C for 302 days. Table 2-3 lists the Zircaloy-4 samples designation, the SPP size and area fraction, and the final corrosion and hydrogen measurements after exposure. Figure 2-7 shows the corresponding weight gain and hydrogen content of the samples. For a fixed hydrogen pickup fraction, the weight gain vs. hydrogen content would be a straight line. A higher pickup fraction corresponds to a larger slope and a lower pickup fraction corresponds to a smaller slope. The results in Figure 2-7 show that both the corrosion rate and hydrogen pickup fraction vary with the SPP distribution. The pickup fraction is greatest for samples 12 and 13, which have the

largest precipitate size and area fraction. The pickup fraction is smallest for sample 11 which has the smallest size and area fraction. For samples 12-14, the corrosion rate decreases with precipitate size. [41]

Table 2-3. Zircaloy-4 specimens tested in 400°C/10.3 MPa steam [41]

Sample	SPP mean size (nm)	SPP area fraction (%)	Weight Gain (mg/dm^2)	Hydrogen content (μg/g)
11	35	0.1	267	288
12	280	1.9	238	543
13	216	2.0	147	273
14	180	1.2	132	195

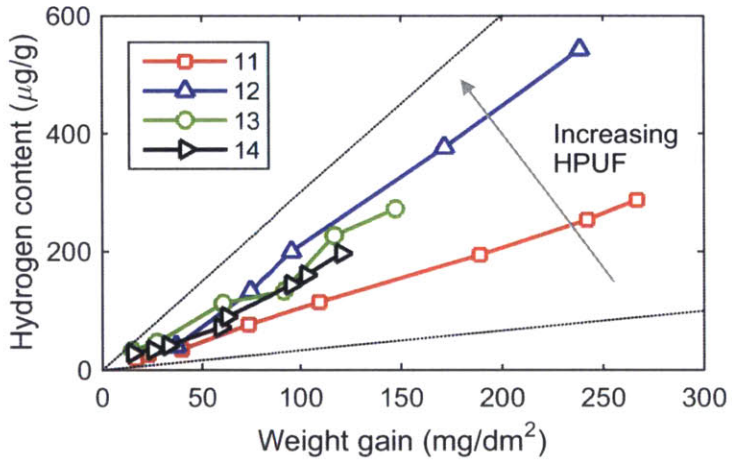

Figure 2-7. Corrosion and hydrogen uptake of Zircaloy-4 specimens tested in steam 400°C/10.3 MPa. Adapted from [41]

Couet et al. studied corrosion and hydrogen pickup in Zircaloy-4, ZIRLO, pure zirconium, two Zr-0.4Fe-0.2Cr model alloys, and Zr-2.5Nb. The two Zr-Fe-Cr model alloys differed in that one had small precipitates (average size 40 nm), and the other had undergone heat treatment to grow precipitates (average size 110 nm). Samples were oxidized in water at 360°C and 18.7 MPa. Prior to oxide transition, the pickup fractions

were: 18% for zirconium, less than 10% for Zircaloy-4, and approximately 10% for both model Zr-Fe-Cr alloys. The pickup fractions for ZIRLO and Zr-Nb were lower. After 375 days of exposure, the total pickup fraction was 25% for Zircaloy-4, and 19% for ZIRLO. The pickup fraction increased from pretransition to first transition, and from the first transition to the second transition.

The two model Zr-Fe-Cr alloys had similar pickup fractions and corrosion rates up until the samples reached an oxide thickness of 3 μm. After this point, the corrosion behavior was the same for both alloys, but the pickup fractions diverged. The sample with larger precipitates had a smaller pickup fraction.

The authors fitted the corrosion data to power laws, Kt^n, and observed an inverse relationship between the exponent "n" and the hydrogen pickup fraction, as shown in Figure 2-8. The samples with the fastest corrosion rates had the lowest pickup fractions. However, note that the total hydrogen amount of absorbed by the cladding depends on both the corrosion rate and the pickup fraction.

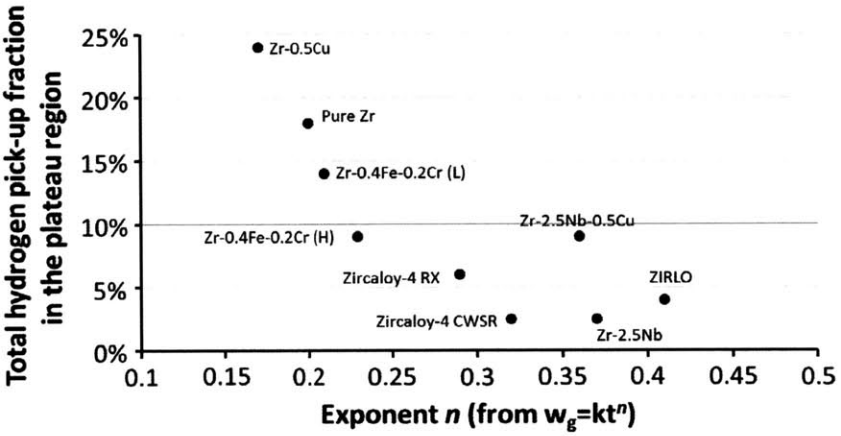

Figure 2-8. Relationship between oxide growth kinetics and hydrogen pickup fraction for various zirconium alloys. [42]

From the instantaneous hydrogen pickup fraction and corrosion data, as shown in Figure 2-9, Couet et al. observed that the pickup fraction is low initially and the corrosion rate is relatively fast. The corrosion rate slows down as the oxide thickens, and the hydrogen pickup fraction increases. The pickup fraction drops at the corrosion transition, when the corrosion rate is relatively fast. The authors hypothesized that this trend can be explained based on charge neutrality. At all times, the net charge transported across the oxide is zero. Thus, there is a balance between oxygen transport, proton transport, and electron transport. For a fixed oxygen current, if the outward electron transport increases (for example due to increased conductivity), then the inward proton transport must decrease. For zirconium alloys, the electron transport decreases as the oxide layer thickens. In order to maintain charge neutrality, the hydrogen pickup fraction increases. [42,43]

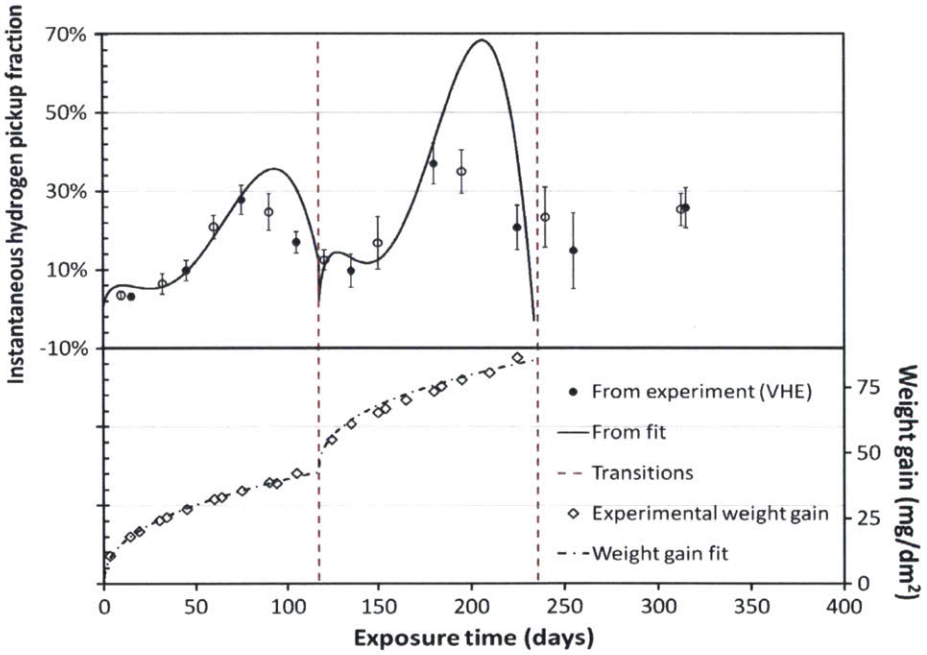

Figure 2-9. Instantaneous hydrogen pickup fraction and weight gain in ZIRLO [42]

approaches of interest: open circuit potential measurements of corroding zirconium alloys, the electrical resistance of the oxide layer (studied through electrochemical impedance spectroscopy), and polarization studies. Open circuit potential measurements in water give the potential of the metal sample (often reference to as the corrosion potential), and include the effects of the potential drops across the oxide layer and electrolyte. Measurements have shown that potential at the metal is negative to the potential in the oxide. [28]

Baur et al. performed electrochemical studies on Zircaloy-4 with varying composition and precipitate size, and Zr-2.5Nb. They performed long term corrosion test in autoclave at 350°C with and without external polarization. The rest (corrosion) potential, which is due to the potential drop across oxide and changes due to hydrogen formation, was greatest as the sample was brought temperature, when the oxide is thin and the corrosion rate high. The potential decreased as the oxide thickened and the corrosion rate slowed down for the rest of the pretransition period. At transition, the rest potential increased. The rest potential was measured in reference to a platinum electrode, and they observed the following trends in the *potential difference* from platinum: it was lowest for Zr-2.5Nb and highest for Zircaloy-4 with the lowest iron content. Zircaloy-4 with large precipitates and higher iron content had lower electrical resistance than Zircaloy-4 with small precipitates and lower iron content. Samples with lower electric resistance had lower hydrogen pickup fractions. Hydrogen pickup was observed to increase under cathodic polarization [47]

On a similar note, Kakiuchi et al. studied the relationship between potential differences across the oxide layer and hydrogen pickup for Zircaloy-2 and HiFi alloy

Anghel et al. studied the effects of intermetallic particles on zirconium alloy oxidation. They measured the ability of different intermetallics to dissociate oxygen molecules. At 400°C, the order in decreasing efficiency was: Pt > Zr_2Fe > Zr_2Ni > $ZrCr_2$ > Zircaloy-2. The authors also coated zirconium samples (one of which was charged with deuterium) with platinum particles and oxidized them in steam. For samples containing deuterium, there was a critical coverage at which platinum decreases the oxidation rate (less than 4 μg Pt/cm^2). Increasing coverage beyond this level increased the oxidation rate. The authors were not able to identify a critical coverage for zirconium samples without deuterium. Based on the oxidation results, Angel et al. proposed that hydrogen may induce/enhance outward zirconium diffusion in the oxide and lead to a self-repairing mechanism. [19,44,45]

Luscher et al. modified the surface of Zircaloy-4 by adding a nickel-zirconium intermetallic. They plated nickel on Zircaloy-4 samples, and applied heat treatments to form an intermetallic layer. They oxidized samples in D_2O steam, at temperatures of 290, 330, and 370°C. The oxidation rates were initially enhanced, but they approached the oxidation rate of Ziraloy-4 as the time progressed. The hydrogen pickup fraction from these tests was ~0.5, which is significantly higher than reported pickup fractions in Zircaloy-4. [46]

2.5.3 Electrochemical Effects

Researchers have studied the relationship between oxidation, hydrogen pickup, and potential of zirconium alloys. Within the electrochemical studies, there are three

(High corrosion resistance and high Fe (iron) zirconium alloy). Autoclave corrosion test were performed on Zircaloy-2 and HiFi samples, some of which had been pickled to remove precipitates from the surface. The weight gains were similar for all samples, but the hydrogen pickup fractions were noticeably different. The HPUF were in decreasing order: picked Zircaloy-2> unpickled Zircaloy-2 > pickled HiFi > unpickled HiFi. The authors determined flat band potentials of the oxides by photoelectrochemical measurements: -0.634 V for HiFi and -0.905 V for Zircaloy-2. Contact potential differences (CPD) were measured against a platinum electrode. The CPD is defined as the difference in work functions of the oxidized samples and the platinum electrode: so a higher CPD corresponds to a more positive potential. The authors note that the CPD is a measurement of the relative potential at the oxide surface. The CPD grew under an oxygen environment, and in order of greatest to lowest were: HiFi > Zircaloy-2 > zirconium. The authors hypothesized that the difference in CPD measurements of the different alloys is associated with the oxygen vacancy concentrations in the oxide: the higher iron content in HiFi increases the number of oxygen vacancies and raises the potential of the oxide at surface. The raised potential reduces the potential gradient across the oxide and slows the ingress of protons, thereby reducing the hydrogen pickup. [48,49]

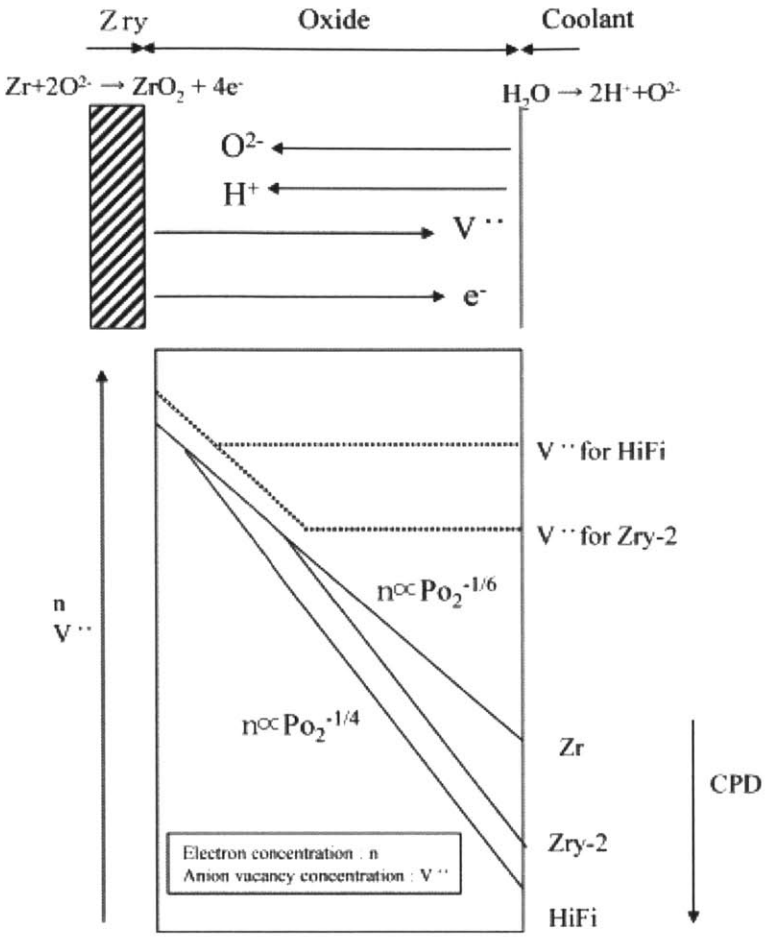

Figure 2-10. Oxide surface potentials and oxygen vacancy concentrations of pure zirconium, Zircaloy-2, and HiFi [49]

Shirvington studied the conductivity of oxide films on Zircaloy-2. If a layer of p-type Fe_3O_4 formed over the ZrO_2, then the conductivity of ZrO_2 increased due to hole injection. An increase in conductivity was not observed with a layer of n-type Fe_2O_3. The conductivity of the Zircaloy-2 oxide film increased with a layer of Fe_2O_3 over Fe_3O_4. [50]

Kim et al studied photoelectrical corrosion effects of Zircaloy-2, Zircaloy-4, GNF-Ziron, and GNF-NSF, as well as 304SS and Alloy X-750. They measured ECP, galvanic

current and impendence with and without UV illumination. [51] ECP measurements showed that at a hydrogen overpressure, water at 300°C with 150 ppb hydrogen addition, corrosion potentials were similar for the various samples. At the same temperature with 1.1 ppm O_2 addition to the water, the ECP was significantly higher for 304 SS. Table 2-4 lists the measured ECP values.

Table 2-4. ECP of Zircaloy-2, 304 SS, and Zirconium in water at 300°C [51]

Sample	ECP with 0.15 ppm H_2 (V SHE)	ECP with 1.1 ppm O_2 (V SHE)
Zircaloy-2	-0.6	-0.12
304 SS	-0.55	+0.1
Zirconium	-0.68	-0.55

Measurements of corrosion potential (25°C, 0.01 M $NaSO_4$ solution) were made with and without UV radiation. The results are summarized as follows:

1. Zircaloy-2: the ECP decreased with UV radiation
2. Alloy X750 and 304SS: ECP increased with UV radiation
3. Zr-Fe-Cr, Zr-Fe-Ni, Zr+Fe+Ni+Si: ECP increased with UV radiation. The authors note that the oxidation status of these intermetallic compounds was unknown

The measurements for Zircaloy-2 and Alloy X750 were repeated in 300°C water with 1.1 ppm O_2, and the same effects of UV irradiation on ECP were observed. The authors suggest that ECP changes under UV radiation could be explained by photoelectric effects. The UV radiation produces electron-hole pairs in the oxide films of the samples. If there is a depletion layer at the oxide/coolant interface, then the electron and hole will separate and migrate according to the electric field. In p-type

semiconductors, the electrons will migrate toward the surface and the holes towards the metal. In n-type semiconductors, the electrons will migrate toward the metal, the holes toward the surface. [51]

Ramasubramanian and collaborators performed several studies on zirconium alloys to understand the mechanisms of corrosion and hydrogen pickup from an electrochemical perspective. Ramasubramanian and Balakrishnan studied the effect of lithium, boron, and hydrogen in Zircaloy-4 and Zr-2.4Nb oxides. They identified hydroxyls in the oxide, and proposed that proton transport occurs via hydroxyls along oxide grain boundaries. In post transition oxides with pores larger than 2 nm in diameter, proton transport occurs via these pores and can be considered in terms of electrochemical double layers. [52] Ramasubramanian, Perovic and Leger studied corrosion and hydrogen pickup of Zr-2.5Nb exposed to heavy water in autoclave and in reactor using SIMS and Fourier transfer infrared spectroscopy (FTIR). They identified the presence of deuterium in the oxide in the form of hydroxyls and adsorbed water. They also examined the exchange between hydrogen and deuterium in the oxide for samples exposed to first light water then heavy water and vice versa. Exchange between the isotopes occurred faster than the corrosion rate. The authors proposed the hydrogen transport in the oxide occurs through hydrated pathways and is relatively rapid. The physical barrier for hydrogen entry from the oxide to the metal is a thin layer of oxide. A positive space charge layer from anion vacancies is the electrical barrier to proton entry. A negative corrosion potential would lower the barrier height for proton entry. [53] Ramasubramanian, Billot and Yagnik investigated the effect of weld regions and palladium coating, as well as under an externally imposed polarization on hydrogen pickup. They performed

experiments both in static autoclave, and in an out-of-reactor loop. [8] They observed that pickup was greatest in weld regions than in the remainder of the clad material, and that palladium reduced the pickup fraction. Based on the observed behavior, the authors argued that hydrogen evolution cannot occur on ZrO_2, because the conduction band energy at 1.4 V (SHE) is too high, compare the energy level for the proton reduction reaction, which had a maximum probability at 0.2 V(SHE). The authors concluded that under PWR conditions, the evolution of hydrogen occurs on (1) semiconducting tin sites and (2) on the metal at the bottom of micropores, and hydrogen pickup occurs at the bottom of pores. The barrier for electron transport is the oxide layer for semiconductor tin sites, and the electrochemical double layer at the metal/solution interface for pores. The authors noted that their findings indicate that there is a minimum cathodic potential for pickup at the bottom of pores and that pickup will depend on the potential at the surface-metal interface at the bottom of the pores. They also noted that the semiconductivity of tin likely results from doping by Sn^{2+}, interstitial tin, and doping by iron and nickel from alloying elements. In Chapter 6 we will apply this energy level comparison to ZrO_2 and other oxides found in Zircaloy-4 oxidized precipitates.

2.5.4 Water Chemistry Effects

Kumar et al. studied the effect of dissolved oxygen on the corrosion and hydrogen pickup of Zircaloy-2 and Zr-Nb . Samples were oxidized in steam at 400°C and 10 MPa, with and without deaeration, For Zircaloy-2, the weight gain under conditions of high dissolved oxygen was slightly larger. The hydrogen content of the samples was lower than the sample oxidized in deaerated steam. The difference can be explained as: at high

dissolved oxygen concentrations, the metal preferentially reacts with dissolved oxygen in addition to water, and corrosion by oxygen will not produce hydrogen. [54]

The addition of LiOH to water increases the corrosion rate of zirconium alloys. Researchers have found LiOH in the porous oxide which is likely adsorbed onto the oxide surfaces. Enhanced corrosion by LiOH is likely related to the degradation of the barrier layer, which has been observed to coincide with a reduction in tetragonal ZrO_2. Pecheur et al. studied the effects of boron and lithium addition on the corrosion of Zircaloy-4 in water at 633 K and 18 MPa. They observed that high concentrations of lithium are required to produce a significant increase in corrosion rate: 10 ppm Li addition had minimal effect whereas 70 and 700 ppm Li did. Lithium decreased the time to transition. They also observed that boron had a beneficial effect on the corrosion rate with 10 and 70 ppm Li. The presence of boron delayed the transition and decreased the post transition rate. Boron decreased the ingress of lithium into the oxide, but this effect was only noticeable in pre-transition oxide. The authors hypothesized that the beneficial effect of boron in post transition oxide is pH related. [55]

Recall from the beginning of this chapter, that typical LiOH addition to PWRs is less than 3.5 ppm, which means there should not be significant corrosion enhancement unless the lithium becomes concentrated at the oxide surface.

2.5.5 Radiation Effects

As previously mentioned, in BWRs there is an increase in the corrosion rate and hydrogen pickup fraction of fuel cladding that is associated with the irradiation dissolution of second phase particles. For Zircaloy-2 cladding in reactors, the hydrogen

pickup fraction has been observed to increase at burnups greater than 50 MWd/kgU. Structural components made from Zircaloy-2 exhibit an accelerated pickup fraction at burnups of 30-40 MWd/kgU. However, there have been no observed instances where the hydrogen pickup fraction of Zircaloy-4 structural components in BWRs increased at high burnup. Zircaloy-2 shadow corrosion at high burnups has also been correlated with accelerated pickup fractions, i.e. higher pickup fractions are observed at regions with thick, porous, shadow corrosion-related oxides. [3] There is also a correlation between accelerated pickup at high burnup and the water chemistry: relatively low pickup fractions were observed at high burnup, with medium copper (5-20 ppb) and low-medium iron content in the coolant, and low-medium room temperature (RT) electrical conductivity (0.11-0.15μS/cm).The same was not observed for plants with low copper content in the coolant and low RT electrical conductivity (<0.1μS/cm).[3]

The hydrogen pickup fraction of Zircaloy-4 does not increase at high burnup. Moreover, measured pickup fractions are not significantly different for autoclave compared to in-reactor exposure. However, corrosion rates are higher in reactor. Bossis et al. studied corrosion and hydrogen pickup of low tin Zircaloy-4 in PWR as water rods and as fuel cladding. They observed high burnup corrosion acceleration of the fuel cladding, which had an acceleration factor of up to five. They report that burnup accelerated corrosion has threshold type behavior, and first occurs at 25-40 MWd/kgU. The acceleration factor for water tubes remains constant after the threshold, however, the acceleration factor for fuel cladding continues to increases with burnup. The authors

report hydrogen pickup fractions of approximately 17.5% for both water rods and fuel cladding. [56,57]

2.6 Radiolysis and Water Chemistry Modeling

Water exposed to ionizing radiation will decompose in the process of radiolysis. The simplified equation is typically written as: [58]

$$H_2O \rightarrow e_{aq}^-, H, H_2, OH, H_2O_2, HO_2, H^+$$

There are three stages of radiolysis:

The first is the *physical stage*, which occurs about 10^{-15}s after the matter-radiation interaction. Ionized water molecules (H_2O^+), excited water molecules, and sub-excitation electrons (e^-) are formed in this stage. [59] The liberated electrons often possess enough energy to ionize other water molecules, leading to the formation of spurs, which are groups of ions along the track of the ionizing radiation. [60] Figure 2-11 shows the formation of spurs along the radiation track.

This is followed by the *physico-chemical stage*, which occurs from 10^{-15} to 10^{-12} s after the initial interaction. [59] In this stage, the liberated electrons lose enough energy to become solvated. By the end of the physicochemical stage, the species are in thermal equilibrium within the bulk medium. [60]

The final stage is the *chemical stage*, which spans 10^{-12} to 10^{-6} s after the initial reactions. In this stage, the species react in the tracts and diffuse in the solution. The species can react with each other and molecules in the surrounding solution. [59] At the beginning of the chemical stage, the species are clustered in spurs, it is during this time

period that they diffuse. Some species react to form secondary products (molecular or radical) and other escape into the homogenized solution. [60]

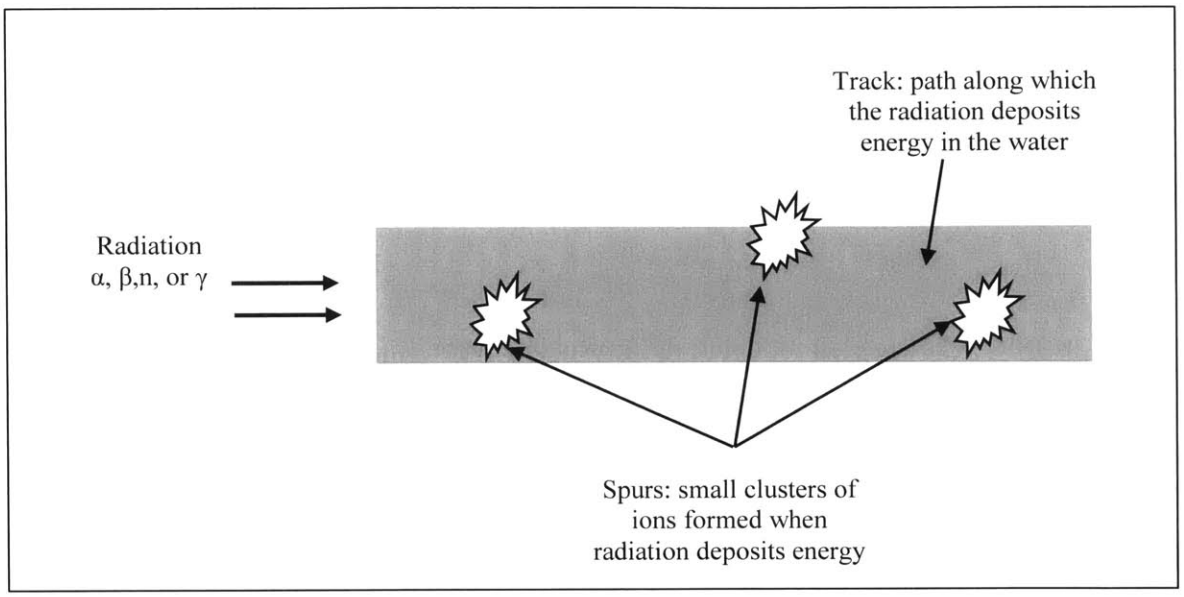

Figure 2-11. Radiolysis of water showing track and spur formation.

The primary yields remain after the conclusion of the chemical stage. These are referred to as "g-values" and give the number of species produced per 100 eV of absorbed radiation. G-values are different for different types of radiation (alpha, beta, gamma, fast neutron) and vary with temperature. Generally, high LET (Linear Energy Transfer) radiation, such α particles and fast neutrons has higher molecular yields. Lower LET radiation, such as gamma rays, have higher radical yields. The difference in yields can be explained by the spur diffusion model. With higher LET radiation, ionization reactions will occur closer together, and the spurs will be more concentrated. This reduces the chances for radiolysis products to escape the spurs, and thus there will be higher molecular yields. [60]

2.6.1 Radiolysis in a PWR

In PWRs, the alpha and Li recoil from the ^{10}B $(n,\alpha)^7Li$ reaction are an additional source of radiolysis. At the beginning of a fuel cycle, when the boron concentration is the highest, there can be up to a 40% increase in the radiolytic species due to this process. [1]

In 1994, Christensen modeled radiolysis in PWRs using the MACKSIMA-CHEMIST program. He studied the effects of changing boron concentration, hydrogen concentration, and the inclusion of Fe^{2+} on oxidant species. His results showed that the inclusion of 5 ppb Fe^{2+} resulted in O_2 and H_2O_2 concentrations of that are 2-3 times higher. He also determined the critical hydrogen concentration, which is the minimum amount of hydrogen required to suppress radiolysis, for varying boron concentrations.

Pastina et al. experimentally studied the effect of mixed radiation (γ and α-radiation resulting from the $^{10}B(n,\alpha)^7Li$ reaction) on the decomposition of water. They performed these experiments at temperatures ranging from 30-200°C. They observed a threshold behavior: there is a critical concentration of boron required to observe a net decomposition of water. Furthermore, they observed that higher temperatures tended to shift the threshold to higher concentrations. They suggested that the temperature effect results from increased diffusion of the species, which increases the ability of radiolysis products to escape the spurs. The authors observed that at 200°C, the threshold is not observed below the solubility limit of boric acid. [61], [62] Further experiments showed that the mechanism by which boron affects radiolysis is purely through the LET, as only the concentration of ^{10}B had an effect on the transition; thus there is no chemical or

catalytic reaction with boron. It was observed that zinc nitrate has no effect on yields, but that iron nitrate reacts with the species, and reduces the recombination of water. Lithium hydroxide was observed to increase decomposition; however the mechanism is not known. The authors suggested that the effect is most likely related to pH. They further noted that for these experiments, the extent of water decomposition depends on the local ratio of $[^{10}B(n,\alpha)^{7}Li$ +fast neutron$]/\gamma$. [63]

Lemaignan suggested that local enhancement of the corrosion rate in zirconium alloys could be explained by β- radiolysis. [64] He noted that several cases of enhanced corrosion: such as in the region near stainless steel components, near platinum inserts, and near copper-rich CRUD. Strong neutron absorbers, such as gadolinia poison rods can also cause local enhancement, as the 8.7 MeV emitted can cause pair production in the cladding. The e^+ is captured in the cladding and results in another gamma photon, while the e^- escapes the cladding. He noted that beta radiolysis is a local phenomenon, as the recoil distances of electrons are on the order of a centimeter, whereas the gamma mean free path is on the order of a meter. He suggested that it is the transient radiolytic species that cause the increase in corrosion, and not the final products, because the coolant velocity is approximately 2-7 m/s. He noted that in PWRs, enhanced corrosion had only been observed with porous oxides, and he suggested that this could be caused by the pores being saturated with hydrogen from reduction of water, thus leading to bubble formation. This would mean that there is two phase flow in the thick oxide. He suggested that the surface/volume ratio is the main parameter controlling the radiolytic species behaviors; the species are trapped by the pores, and thus more oxidizing species are

absorbed on the surface. Furthermore, the concentration of H_2 is much greater in the pores than in the bulk of the coolant. [64]

Lemaignan and Salot further developed the ideas concerning corrosion enhancement due to local radiolysis. They suggested that the effects of localized beta radiolysis are less noticeable in PWRs because of the added contribution from the ^{10}B reaction. They estimated the total energy deposition rate in PWRs is approximately $2x10^{19}$ eV/cm^3-s. In contrast, the rate in BWR's is approximately 10^{18} eV/cm^3-s. The energy deposition from the localized activated materials typically has an order of magnitude of 10^{18} eV/cm^3-s. [65]

2.6.2 Radiolysis Surface Effects

Radiolysis is different for water in the presence of a surface, for example near the cladding surface or for water confined in CRUD or porous oxides. There can be higher local doses to the water from alpha or beta emitting isotopes in the cladding or CRUD. Certain materials, namely some oxides, can change the radiolysis yields, either due to chemical reactions between the surface and radiolysis products, or energy transfer from the solid phase to the adsorbed water. In order to address heterogeneous radiolysis, the following factors must be considered: geometrical dose distribution, the mechanisms and kinetics of reactions between the radiolysis products both in solution and at the solid interface, sorption and dissolution reactions, and the effects of energy deposition in the solid phase. [66]

Computations by Lemaignan and Salot showed that substantially more energy is absorbed by water in the pores of the oxide compared to the bulk coolant, as a result of

localized β radiation. Their calculations were for a PWR gamma spectrum. Using the gamma interaction cross sections and considering three different gamma energies, they determined the induced electron spectrum at the oxide/water interface. These calculations showed that the energy deposition rate was 52 times greater for the water in the oxide than for bulk coolant. [65]

At a water/oxide interface, radiation interacts with both the water and the oxide, and energy transfer can occur between the two. The effect of oxides on radiolysis has typically been studied in the context of H_2 yields. Some oxides increase the H_2 yields, others are neutral, and others decrease the yield. ZrO_2 is among the oxides which increase hydrogen yield. For materials that increase the yields, the difference is usually quantified as an energy transfer process; energy absorbed in the oxide is transferred by some means to the water. For the case of ZrO_2, energy transfer is believed to occur via excitons (a bound state of an electron and hole) migration. [59,67,68] For SiO_2, the proposed transfer mechanism is electron and hole migration. [59]

Petrik et al studied gamma radiolysis of water adsorbed to various oxides. They observed that some oxides decreased the H_2 production, some increased it, and some had no effect. Of particular note, as they may impact Zircaloy-4, are Fe_2O_3, which decreased H_2 production, Cr_2O_3, which had minimal effect, and ZrO_2, which increased H_2. The authors also found the H_2 yield was correlated with the oxide band gap: all oxides that increase hydrogen production have a band gap of 4.5 to 6 eV, as shown below in Figure 2-12.

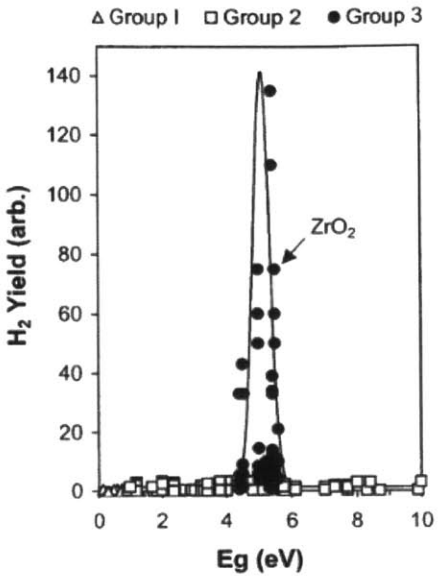

Figure 2-12. Hydrogen radiation chemical yield vs. oxide band gap for radiolysis of H_2O molecules absorbed on the surface of various oxides with coverage 1±4 ML. $G(H_2)$ is calculated relative to the energy of γ rays absorbed by the H_2O. Group 1 oxides inhibit H_2 production relative to bulk water, Group 2 oxides have no effect on H_2 production, and Group 3 oxides promote H_2 production. [67]

The same authors further studied water adsorption and radiolysis on monoclinic ZrO_2 crystals that were 0.05 to 5 mm in diameter. They observed that the hydrogen yields changed with the form of water adsorbed: physiosorbed water had minimal effect on overall yields but chemisorbed water did. By doping the surface of the particles with 0.1% mass Nb^{5+}, the H_2 yield decreased by a factor of 0.2. Doping with 0.1% (mass percent) Li^+ increased H_2 production by a factor of two. Oxygen vacancies are traps for the electrons in ZrO_2. Doping with niobium decreases the anion vacancy concentration, while lithium increases the concentration. These results suggest that the energy

migration does not occur through electrons. The authors noted that parameters such as the oxide band gap, the water absorption form, and energy migration distance contribute to the observed enhanced H_2 yield. Based on their observations, they proposed that the enhanced energy transfer in zirconia occurs by a mechanism of exciton migration to the surface, and resonant coupling with H_2O absorption. The migration distance of excitons in ZrO_2 was estimated to be 5 nm. [67]

LaVerne and Tandon investigated H_2 production from radiolysis of water with ZrO_2 particles. The mean diameter of the particles was 13.4 μm, the density 5.6 g/m^3, and the specific area was 1.99 m^2/g. They measured the weight of samples exposed to a high relative humidity to determine the amount of water adsorbed. They calculated the number of water layers by assuming the coverage for a single layer to be 0.22 mg/m^2. They measured the yield (the G-value) of hydrogen for water adsorbed on the oxide surface, and there was a marked increase relative to the g-value in bulk water of 0.45 molecules/ 100 eV. Figure 2-13 presents the g-value as a function of water layers on the oxide. The hydrogen yield is greatest when there are few layers of adsorbed water. This suggests that if coolant is confined in small areas, such as pores in the oxide, the hydrogen yields may be greatly enhanced.

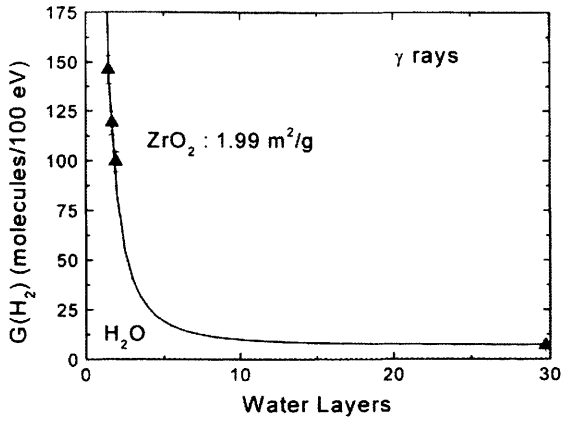

Figure 2-13. H_2 yield relative to the amount of energy deposited direct by γ-rays to water adsorbed on ZrO_2 microparticles. [68]

Laverne et al. also measured the production of molecular hydrogen relative to the total energy absorbed in both the oxide and water. They did this for both gamma rays and for 5 MeV alpha particles. For ZrO_2, they observed that the H_2 production for alpha radiation was smaller than that for gamma radiation. This was not observed for CeO_2, for which the production rate was the same for both gamma and alpha radiation, as shown in Figure 2-14. The authors suggested that the alpha particles irradiation produce Frenkel defects in ZrO_2, which traps excitons, thus limiting energy transfer between the oxide and water. They suggest that the similarity between the results indicated that there may be another minor mode which allows for transfer of energy between the oxide and water. They suggested that it may be due to electron hole escape, and noted that the range of electrons and holes are shorter in comparison to excitons, so it is predominately a near surface effect.

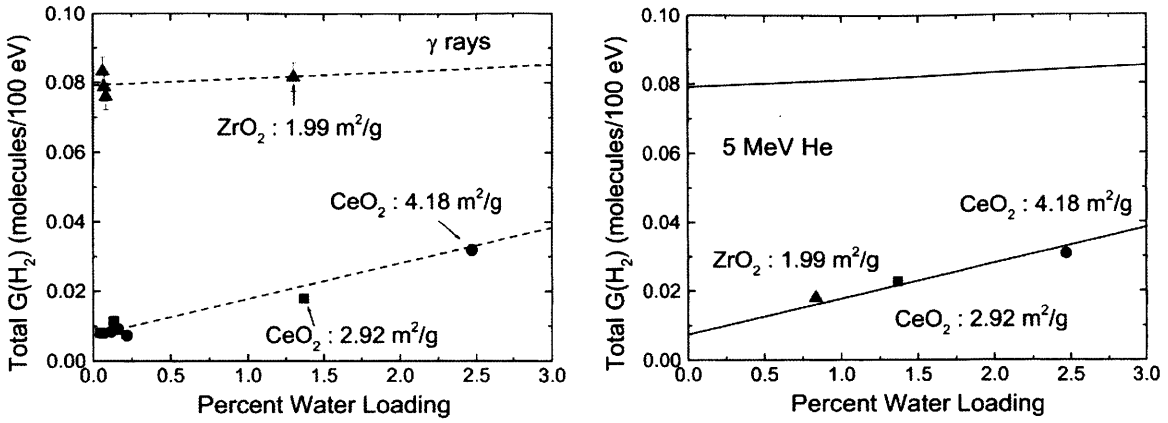

Figure 2-14. Production of molecular hydrogen relative to the total energy deposited by gamma (left) and 5 MeV alpha particles (right) to water absorbed on ZrO_2 and CeO_2 [68]

LaVerne performed an experiment to characterize H_2 formation from radiolysis of water on zirconia particles. [69] Samples included 107 nm monoclinic particles, 60 nm tetragonal particles, and 60 nm particles that were annealed to turn them monoclinic. Figure 2-15 below presents the measured H_2 yield as a function of weight percent ZrO_2. The H_2 yield was virtually the same for the 107 nm monoclinic particles, regardless of weight percent of ZrO_2. However, for the tetragonal particles, increasing the weight percent of ZrO_2 resulted in a dramatic increase in H_2 yield. The 60 nm monoclinic particles had a significantly smaller yield than the corresponding tetragonal particles. LaVerne proposed that the difference in crystalline structure between the monoclinic and tetragonal particles affect the number of excitons that reach the surface of the particle. Furthermore, the reactions that produce H_2 may be affected by surface structure. He proposed that possible reactions at the surface could involve exciton reactions with free OH groups, with bridged OH groups, or with bound/near surface water. He noted that

experiments have shown that monoclinic particles have more OH groups on the surface. [69]

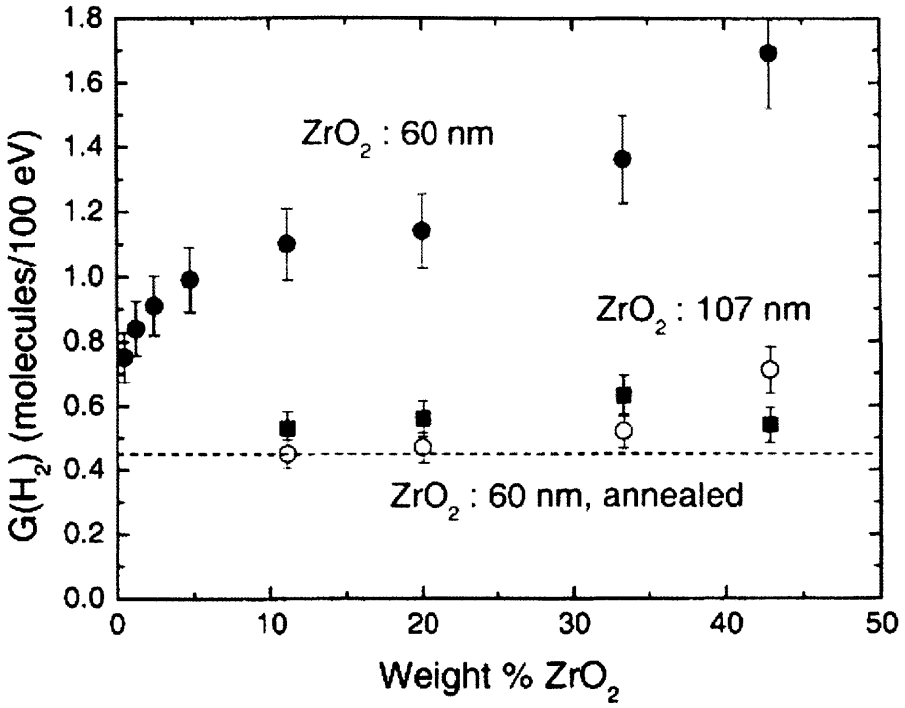

Figure 2-15. Molecular hydrogen yield as a function of ZrO_2 weight percent in γ-radiolysis of aqueous mixtures. (●) 60 nm diameter-tetragonal, (■) 107 nm diameter-monoclinic, (○) annealed 60 nm diameter-monoclinic.[69]

2.6.3 The connection to photocatalytic splitting of water

There are similarities between heterogeneous radiolysis at oxide surfaces and photocatalytic water splitting on oxides. Both processes occur via energy transport between the oxide surface and water molecules and depend on the electronic (band) structure of the oxide. Water splitting consists of two electrochemical reactions: the reduction of protons and H_2 formation, and the oxidation of oxygen ions and O_2 formation. In photocatalytic water splitting, the photocatalyst absorbs UV radiation,

which excites an electron in the valence band to the conduction band, thus producing an electron-hole pair. The excited electron and hole migrate to the surface of the catalyst. The energy required for the separation of water is 1.23 eV, which means that in theory, the photocatayst should have a band gap of at least 1.23 eV. In practice, band gaps need to be 1.6-2.4 eV. For electron transfer to occur, the conduction and valence band of the photocatalyst must be aligned with the hydrogen and oxygen potentials. The conduction band needs to be more positive on the energy scale than the H_2 potential, the and the valence band needs to more negative on the energy scale (or positive in the V SHE scale) than the O_2 potential. A second consideration for water splitting to occur requires that the hole and conduction electron must be able to migrate to the surface without recombination. [70]

2.6.4 Summary of Water Chemistry and Radiolysis

In this section, literature on radiolysis as it may affect the corrosion and hydrogen pickup has been reviewed. The most significant findings from the literature are:

- Local radiolysis effects at the oxide/coolant or crud/coolant interface may be quite important for cladding corrosion and hydrogen pickup. The main features to consider with local radiolysis are: (1) increased dose (2) chemical interactions between water / radiolysis products and the surface (3) energy transfer between the oxide and absorbed water
- Boron and alpha radiolysis are quite important for water chemistry. This will be quite important for CRUD with enriched boron.

- Radiolysis at oxide surfaces can be quite complicated: the yields depend on the oxide electronic structure.
- Photocatalytic water splitting has similarities to heterogeneous radiolysis at oxides. More importantly, one of the parts of water splitting is *hydrogen gas evolution*, which we have identified as a key factor in the hydrogen split.

2.7 Atomic level modeling of hydrogen entry

Glazoff et al. studied the thermodynamics of (Zr-O-H) systems with DFT. They could not explain the difference in hydrogen uptake of α-zirconium, Zircaloy-2, and Zircaloy-4 based on thermodynamics. They found that the suboxide Zr_3O may play an important role in slowing down hydrogen ingress. They suggest that oxygen and hydrogen "repell" each other in the α-zirconium matrix. As the solubility limit of oxygen is approached in α-zirconium, oxygen occupies nearly ¼ of the octahedral sites in the matrix, forming a checkerboard pattern that blocks the direct migration path of hydrogen. [71]

Youssef and Yildiz have performed multiple studies on defects in zirconia. As part of their research, they developed a method to predict equilibrium concentrations of charged defects in the non-interacting limit, in a material with a band gap. In their work on hydrogen defects in tetragonal zirconia, they found that interstitial hydrogen can exist as either a proton (H+) or hydride ion (H-) depending on the electron chemical potential. In oxygen poor conditions, the most stable defect complex is a single hydrogen in an oxygen vacancy, which has a binding energy of -2.2 eV. In oxygen rich conditions,

hydrogen can cluster in Zr vacancies, potentially leading to degradation of mechanical properties. [72] In his doctoral thesis, Youssef proposed that hydrogen in tetragonal zirconia reduces compressive stresses in the tetragonal zirconia, and may be responsible for the tetragonal to monoclinic transformation, which results in the cracking that is observed. Hydrogen would then be able to enter via the newly formed cracks. As a further investigation into hydrogen pickup effects, he studied the effect of 3d transition metals on hydrogen solubility in monoclinic ZrO_2. Results showed volcano-like behavior from Ti to Zn. The addition of chromium lowers hydrogen solubility, while iron and nickel increase solubility. The solubility effects were related to the electronic structure: metals that p-type dope the ZrO_2 increased solubility, while those that n-type doped the ZrO_2 decreased solubility. Youssef points out that lowering the electron chemical potential will raise the kinetic barrier for electron transfer from the oxide surface to an adsorbed proton. [73] On a note related to corrosion kinetics, they performed extensive studies on oxygen defects in tetragonal zirconia. Using DFT calculated energy barriers and equilibrium concentrations of oxygen defects, they predicted self-diffusivity of oxygen in zirconia as a function of temperature and oxygen chemical potential. The self-diffusivity can be used in physics based models of zirconium corrosion. However, it would require information on the oxygen chemical potential in the oxide. Our radiolysis calculations and calculated chemical potentials in the coolant, can be used to estimate the oxygen chemical potentials at the oxide/coolant.

Lindegran et al. studied hydrogen evolution in zirconium alloys using DFT. They proposed a mechanism in which water penetrates to nearly the metal/oxide interface, producing hydroxlyated grain boundaries. Recombination occurs via local hydride

formation, in which a proton "intercepts" two electrons, and forms a hydride at a metal site. A second proton, bonded to an oxygen ion combines with the hydride to produce molecular hydrogen which is confined within the grain boundary. The confinement limits the recombination step. They explored the role of 3d transition metals in aiding the hydrogen recombination reaction, and also found volcano-like behavior for the elements from titanium to zinc. Results showed that H_2 formation from a hydride is favored on chromium and iron but not nickel. Hydride formation was only energetically favorable on titanium, chromium, and vanadium. [18,74,75]

2.8 Summary and Discussion of Literature Review

Key observations from this literature review are:

1. The rate controlling step of oxide growth is believed to be either oxygen transport or electron transport.
2. Many factors, such as water chemistry, alloying elements, and burnup, affect corrosion and hydrogen pickup. However, it is not known why they affect corrosion and pickup rates. The mechanism of hydrogen entry into zirconium alloy is not known. The cathodic sites for the hydrogen evolution reaction are also not known.
3. Hydrogen pickup fractions have been observed to vary with time in a cyclical pattern that is related to oxide transitions.
4. The question of oxide porosity is difficult to address. Some researchers hypothesize that porosity provides fast ingress routes to the either the barrier

layer or to metal/oxide interface, and that radiolysis in pores affects the corrosion rate. Recent studies on porosity show that it extends into the oxide, as far as 0.7 μm from the metal/oxide interface, which leaves a significant layer of protective oxide. However, we cannot exclude the possibility of hydroxylated grain boundaries serving as transport routes.

5. The role of precipitates is also complicated. On the one hand, metallic precipitates likely serve as cathodic sites and could serve as fast ingress routes. However, the size of precipitates in cladding, typically less than 100-200 nm, are not large enough to bridge a barrier layer of 1 μm. It remains to be seen if metallic precipitates are exposed to the environment by interconnected porosity, and if so, whether such precipitates could serve as cathodic sites.
6. Oxide electrical resistance and the potential drop likely plays an important role in the hydrogen split. Low electrical resistance has been associated with lower pickup fractions.
7. From DFT studies, hydrogen likely exists in the oxide layer as a proton (H+) or hydride ion (H-). The charge of interstitial hydrogen depends on the electron chemical potential. It is also likely that recombination occurs via a proton-hydride mechanism

The literature review suggests that the oxide/coolant interface is a crucial part of the hydrogen split, as it is the location of the water dissociation reaction and therefore the source of protons. This interface is challenging to address because it is heterogeneous due to the presence of porosity, cracks, and second phase particles. In reactor, there are added

complications from local radiolysis effects which can change local coolant chemistry at the interface.

In both experiments and simulation, the potential or electron chemical potential in the oxide appear to have an important role in hydrogen pickup. It is important to recognize that the potential (V) scale and energy scale (eV) are opposite: a more positive ECP (in V) corresponds to a more negative electron chemical potential (eV). The *electron chemical potential gradient* across the oxide may affect electron and proton transport. The *electron chemical potential* at the oxide/coolant interface will affect the energetics of proton reduction.

A second consideration is the role of the second phase precipitates in hydrogen pickup. The effect could be from changing the transport properties of the oxide film, such as electron conductivity or providing an easy transport for hydrogen. A second possibility, which will be addressed in this thesis, is whether the precipitates affect the surface properties of the oxide/coolant interface by enhancing molecular hydrogen recombination or providing an easy entry point for hydrogen. In this thesis, we explore whether the *oxidized precipitates* have a likely effect on the hydrogen split.

Chapter 3: Modeling Water Chemistry and Electrochemical Corrosion Potential

This chapter contains an introduction to water chemistry and radiolysis modeling. We will briefly describe the RADICAL code, and the changes made to the code as a part of this thesis. RADICAL was originally developed for BWR chemistry modeling, and so modifications were made to address PWR water chemistry. In the second part of this chapter, water chemistry sets, g-values, and ECP models are tested against experimental data.

In the scope of the overall thesis, this chapter describes tasks that were performed in preparation for making a PWR radiolysis model. There is little data available to benchmark a PWR radiolysis model, and so we use data from BWR plants and the AECL (Atomic Energy of Canada Ltd.) to test different water reaction sets and g-values in RADICAL. Once we verified that we could correctly capture the effects of radiolysis on PWR type coolant chemistry (with a hydrogen overpressure), then we proceeded with developing the PWR model which is presented in the following two chapters.

3.1 RADICAL Description

The MIT Radiation Chemistry Analysis Loop (RADICAL) code determines the plant coolant loop chemistry in a radiation environment. It originated from Simonson's MITIRAD code (dating 1988), and was primarily developed by Chun and Grover. [76–78] It was originally developed for BWRs and thus can model effects from boiling. At the start of this thesis, it model the following processes: creation of species by gamma and

fast neutron radiolysis, transport via convection, mass transport between liquid and gas phases, and generation and annihilation of species by chemical reactions. A sensitivity model was included to determine the effect of various input parameters on the output concentrations. For two phase thermal hydraulic modeling, it has the Bankoff and Chexal-Lellouche correlations. An ECP model for BWRs by Lin was included. [79]

BWR input files had previously been created for a typical BWR-3, and BWR-4, and a BWR-1 (with no jet pumps). RADICAL has also previously been used to model the BWR Corrosion Chemistry Loop (BCCL) and Irradiation Assisted Stress Corrosion Cracking Loop (IASCC) at the MIT research reactor. [78]

As part of this thesis, the effects of alpha radiolysis was added. ECP models, based on the work of MacDonald et al. were implemented in the code. [80–83] Additionally, the rate constant input format was changed to allow for the implementation of the AECL water reaction set, which was published in 2009. [84] Figure 3-1 gives an overview of the input, output, and major subroutines of RADICAL.

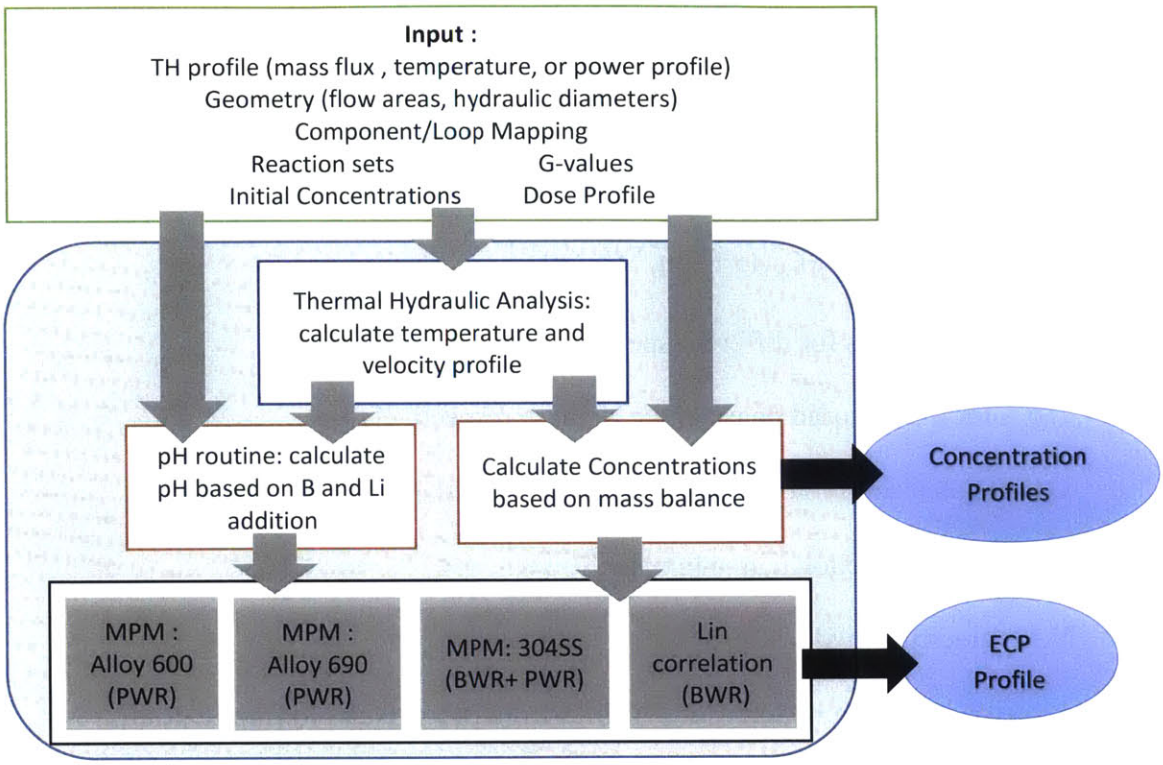

Figure 3-1. RADICAL Input and Output

At the center of RADICAL are partial differential equations for determining the concentration of species. A detailed derivation of these equations can be found in Appendix A.

The concentration equation for species in the liquid phase is:

$$\frac{dC_{li}}{dx} = \frac{1}{V_l(x)}\left\{k_{rad}G_i Q_i + \sum_{j=1}^{NRx} KOEFF_{ji}k_j \prod_{m=1}^{3} C_{l,mi} + \left[\mu_i^{g,l}C_{g,i}(x) - \mu_i^{l,g}C_{l,i}(x)\right]\frac{\alpha(x)}{1-\alpha(x)} + \frac{V_l(x)C_{li}(x)}{1-\alpha(x)}\frac{\partial\alpha}{\partial x} + \frac{V_l(x)C_{li}(x)}{A_T}\frac{\partial A_T}{\partial x} - C_{li}(x)\frac{\partial V_l}{\partial x}\right\} \quad (3\text{-}1)$$

The differential equation for species in the gas phase is:

$$\frac{dC_{gi}}{dx} = -\frac{1}{V_g(x)}\left\{\frac{C_{g,i}(x)V_g(x)}{\alpha(x)}\frac{\partial\alpha}{\partial x} + \frac{C_{g,i}(x)V_g(x)}{A_T}\frac{\partial A_T}{\partial x} + C_{gi}(x)\frac{\partial V_g}{\partial x} + \left[\mu_i^{g,l}C_{g,i}(x) - \mu_i^{l,g}C_{l,i}(x)\right]\right\} \tag{3-2}$$

i, j, m are indices for different species

l, g refer to the liquid phase and gas phase respectively

C is the concentration of the given species [mol/L]

A is the cross sectional area [cm^2]

V is velocity [cm/s]

k_{rad} is a conversion factor for g-values from [# / 100 eV] to [mol/L-Rad]

$\mathcal{G}$ is the g-value of the given species [# / 100 eV]

Q is the dose rate [Rad/s]

k is the rate constant for chemical reactions

$KOEFF_{ji}$ is a tally for the number of species i created or destroyed in a reaction

$\mu^{g,l}$ is the mass transfer coefficient from the gas to liquid

α is the void fraction

The concentration of each species at all points in a reactor coolant loop is determined by computationally traversing each node in the coolant flow path until a specified number of cycles are complete or convergence criteria are met. First, the thermal hydraulic profile is solved for the loop. Using the thermal hydraulic profile (temperature, velocities, and void fraction), at each interval along the coolant path the

concentration equations, (3-1) and (3-2) are solved. There are N simultaneous differential equations to solve, one for each chemical species being considered. To solve these equations the model uses a standardized non-linear differential equation solver, the Livermore Solver for Ordinary Differential Equations (DLSODE), which was developed by Hindmarsh at Lawrence Livermore National Laboratory. [85]

3.2 Modeling Electrochemical Corrosion Potential

After the concentration profiles have been calculated, the electrochemical corrosion potential (ECP) is calculated at each interval along the coolant path. Currently RADICAL has several ECP models:

1. An empirical BWR ECP model developed by Lin. [79] See Appendix A for the equations and implementation
2. Mixed Potential Models developed by MacDonald et al. for the following materials: [80–83]
    a. 304 SS BWRs
    b. 304 SS in PWRs
    c. Alloy 600
    d. Alloy 690

The Lin ECP model was implemented in RADICAL by Grover. [78] As part of this thesis, the mixed potential models were added, and the implementation was changed so that different ECP models can be used in the same RADICAL model for different parts of the system.

The following subsections present the mixed potential models as implemented in RADICAL for this thesis. MacDonald et al. have developed Mixed Potential Models for 304SS, Alloy 600, and Alloy 690. [80–83] The basis of Mixed Potential Models is the charge conservation equation:

$$\sum_{j=1}^{n} i_{R/O,j}(\mathbb{E}) + i_{corr}(\mathbb{E}) = 0 \tag{3-3}$$

Where

$i_{R/O,j}$ is the partial current due to the jth redox couple in the system

i_{corr} is the metal oxidation current

$\mathbb{E}$ is the potential

The corrosion potential is the point where the total oxidation and total reduction currents are equal in magnitude. Thus, solving Equation (3-3) for $\mathbb{E}$ will yield the electrochemical corrosion potential. The corrosion of primary coolant systems is due to the oxidation of the metal, coupled with the reduction of hydrogen peroxide and oxygen, and either the reduction or oxidation of hydrogen, depending on the coolant chemistry.

3.2.1 Redox Partial Currents

The redox reactions have the form:

$$O + ne^- = R \tag{3-4}$$

Where O is the oxidized specie, and R is the reduced specie. The redox couples are H^+/H_2 , O_2/H_2O, and H_2O_2/H_2O.

The corresponding reactions are:

$$2H^+ + 2e^- = H_2 \tag{3-5}$$

$$O_2 + 4H^+ + 4e^- = 2H_2O \tag{3-6}$$

$$H_2O_2 + 2H^+ + 2e^- = 2H_2O \tag{3-7}$$

The current density for a redox couple is given by a generalized Butler-Volmer equation: [81]

$$i_{R/O} = \frac{e^{\left(\frac{\mathbb{E}-\mathbb{E}^e_{R/O}}{b_a}\right)} - e^{-\left(\frac{\mathbb{E}-\mathbb{E}^e_{R/O}}{b_c}\right)}}{\frac{1}{i_{o,R/O}} + \frac{1}{i_{l,a}} e^{\left(\frac{\mathbb{E}-\mathbb{E}^e_{R/O}}{b_a}\right)} - \frac{1}{i_{l,c}} e^{-\left(\frac{\mathbb{E}-\mathbb{E}^e_{R/O}}{b_c}\right)}} \tag{3-8}$$

The equilibrium potential (in the bulk coolant) is given by the Nernst Equation:

$$\mathbb{E}^e_{R/O} = \mathbb{E}^o_{R/O} - \frac{2.303RT}{z\mathcal{F}} \log_{10}\left(\frac{\mathrm{a}_R}{\mathrm{a}_O}\right) \tag{3-9}$$

$\mathbb{E}^e_{R/O}$ is the equilibrium potential

$\mathbb{E}^o_{R/O}$ is the standard cell potential

R is the universal gas constant

T is the temperature in Kelvin

z is the number of electrons transferred in the reaction

$\mathcal{F}$ is Faraday's constant

$\mathrm{a}_R, \mathrm{a}_O$ is are the activities of species of the reduced and oxidized species

b_a, b_c are anodic and cathodic Tafel constants

The limiting currents are calculated from a correlation for turbulent pipe flow by Selman and Tobias: [14]

$$i_{l,R/O} = \pm 0.0165 z \mathcal{F} D \left[C^b_{O/R}\right] Re^{0.86} Sc^{0.33}/d \tag{3-10}$$

where

the sign is positive for the anodic reaction and negative for cathodic

$C^b_{O/R}$ is the bulk concentration for O or R [mol/cm^3]

D is the diffusivity of the species in water [cm^2/s]

$Re = Vd/\nu$ is the Reynolds number

$Sc = \nu/D$ is the Schmidt number

d is the hydraulic diameter [cm]

ν is the kinematic viscosity [cm^2 /s]

It should be noted that according to Selman and Tobias, this correlation is valid for 8000<Re<200,000 and 1000<Sc<6000. [86] In BWRs, the Reynold's number often exceeds this limit. Additionally, for the BWR and PWR radiolysis models, the Schmidt number is ~2-4.

Hydrogen Redox Couple

The hydrogen equilibrium potential, using Henry's law for the partial pressure of H_2 is:

$$\mathbb{E}^e_{H2/H+} = -\frac{2.303RT}{2\mathcal{F}}\left[\log_{10}\left(x_{H_2}\mathcal{K}_{H_2}\right) + 2pH\right] \tag{3-11}$$

Where x_{H_2} is the mole fraction of H_2 in the coolant, and $\mathcal{K}_{H_2}$ is the Henry's law constant for hydrogen.

The limiting currents, from Equation (3-10) are:

$$i_{l,a} = 0.0165(2)\mathcal{F}D_{H2}\left[C_{H2}^{b}\right]Re^{0.86}\left[\frac{\nu}{D_{H2}}\right]^{0.33}/d \tag{3-12}$$

$$i_{l,c} = -0.0165(2)\mathcal{F}D_{H+}\left[C_{H+}^{b}\right]Re^{0.86}\left[\frac{\nu}{D_{H+}}\right]^{0.33}/d \tag{3-13}$$

Oxygen Redox Couple

The oxygen equilibrium potential is:

$$\mathbb{E}_{O2}^{e} = \mathbb{E}_{O2}^{o} + \frac{2.303RT}{4\mathcal{F}}\left[\log_{10}\left(x_{O_2}\mathcal{K}_{O_2}\right) - 4pH\right] \tag{3-14}$$

Where x_{O_2} is the mole fraction of O_2 in the coolant, and $\mathcal{K}_{O_2}$ is the Henry's law constant for oxygen.

Because the concentration of H_2O is many orders of magnitude higher than the other species concentrations, $i_{l,a}$ will be significantly higher, and the second term in the denominator of Equation (3-8) will be negligible.

The limiting currents for the cathodic reaction, from Equation (3-10) is:

$$i_{l,c} = -0.0165(4)\mathcal{F}D_{O2}\left[C_{O2}^{b}\right]Re^{0.86}\left[\frac{\nu}{D_{O2}}\right]^{0.33}/d \tag{3-15}$$

Hydrogen Peroxide Redox Couple

The hydrogen peroxide equilibrium potential is:

$$\mathbb{E}_{H2O2}^{e} = \mathbb{E}_{H2O2}^{o} + \frac{2.303RT}{2\mathcal{F}}\left[\log_{10}\left(C_{H_2O_2}\right) - 2pH\right] \tag{3-16}$$

Where C_{H2O2} is the concentration of H_2O_2 [mol/L] in the coolant. Because the concentration of H_2O is many orders of magnitude higher than the other species

concentrations, $i_{l,a}$ will be significantly higher, and the second term in the denominator of Equation (3-8) will be negligible.

The limiting current for the cathodic reaction, from Equation (3-10) is:

$$i_{l,c} = -0.0165(4)\mathcal{F}D_{H2O2}\left[C^{b}_{H2O2}\right]Re^{0.86}\left[\frac{\nu}{D_{H2O2}}\right]^{0.33}/d \qquad (3\text{-}17)$$

Parameters for the Redox currents

Parameters used in this model are given in the table below. The majority of parameters ware consistent with those listed in [80,81].

Table 3-1. Parameters of H_2, O_2, and H_2O_2 redox currents.

Parameter	Value	Source
$\mathbb{E}^o_{H_2}$	$\mathbb{E}^o_{H_2} = 0\ V$ Reference state: 1 atm pressure	[87]
$\mathbb{E}^o_{O_2}$	$\mathbb{E}^o_{O_2} = 1.229\ V$ $\frac{dE^o}{dT} = -0.846\ mV/K$ Reference state: 1 atm pressure	[87]
$\mathbb{E}^o_{H_2O_2}$	$\mathbb{E}^o_{H_2O_2} = 1.763\ V$ $\frac{dE^o}{dT} = -0.643\ mV/K$ Reference state : 1 mol/kgH_2O	[87]
$\ln(\nu)$ $[cm^2/s]$	$-6.140832 - 1103.164/T + 457155.3/T^2$	[88] Table 3
D_{H_+} $[m^2/s]$	$10^{-9} \times 10\text{^} (2.672 - 9.847 \times 10^2/T + 3.306 \times 10^5/T^2 - 5.621 \times 10^7/T^3)$	[84]
b_{a,H_2}, b_{c,H_2}	$0.65\ V$	[81]
b_{a,O_2}, b_{c,O_2}	$0.71\ V$	[81]
b_{a,H_2O_2}, b_{c,H_2O_2}	b_{a,O_2}, b_{c,O_2}	[81]
$i^o_{H_2}$ 304SS $[A/cm^2]$	$0.0114841 \times [C_{H_2}]^{0.5} e^{\frac{-14244}{RT}}$ Concentration in [mol/cc H_2O]	[81]
$i^o_{O_2}$ 304SS $[A/cm^2]$	$0.0114841 \times [C_{O_2}]^{0.48633} e^{\frac{-14244}{RT}}$ Concentration in [mol/cc H_2O]	[81]
$i^o_{H_2O_2}$ 304SS $[A/cm^2]$	$0.0114841 \times [C_{H_2O_2}]^{0.48633} e^{\frac{-14244}{RT}}$ Concentration in [mol/cc H_2O]	[81]
$i^o_{H_2}$ Alloy 600 $[A/cm^2]$	$1.79 \times 10^{-10} \times [C_{H_2}]^{0.64} [C_{H^+}]^{-1.39} e^{\frac{-30562}{RT}}$ Concentration in [mol/kg H_2O]	[80]
$i^o_{H_2}$ Alloy 690 $[A/cm^2]$	$1.18 \times 10^{-10} \times [C_{H_2}]^{0.54} [C_{H^+}]^{-1.45} e^{\frac{-35619}{RT}}$ Concentration in [mol/kg H_2O]	[80]

The Henry's law constants for hydrogen and oxygen were updated for this work, and can be calculated from Prini's curve fit of experimental data: [89]

$$ln\mathcal{K}^{\infty} = \frac{B_o}{T}(T_{cl} - T)\ln\left(\frac{T_{cl} - T}{T_{cl}}\right) + \sum_{i=0}^{N} \frac{B_{i+1}}{T^i}(1000)^i \tag{3-18}$$

In this equation $\mathcal{K}$ is in GPa/mole fraction, $T_{cl} = 647.3\ K$ is the critical temperature, and B_o= -1. This equation is valid up to 635 K. The remainder of the fitting parameters are given in Table 3-2.

Table 3-2. Parameters for Prini's fit of Henry's law constants

Constants	H_2-H_2O	O_2-H_2O
B1	-38.4512	-13.3190
B2	53.4846	12.8557
B3	-27.4317	-3.4516
B4	6.3522	0.2592
B5	-0.5590	

The diffusion coefficients for oxygen and hydrogen in water were also updated for this work, and as before, the diffusion coefficient of hydrogen peroxide was assumed to be the same as that of oxygen. The diffusion coefficient is given by the following equation, which is fitted to data from MD simulations: [90]

$$D\rho = aT^{\alpha} + \rho\left(\frac{b_1}{T^2} + \frac{b_2}{T} + b_3 + b_4T\right) + \rho^2 ln\rho\left(\frac{c_1}{T^2} + \frac{c_2}{T} + c_3 + c_4T\right) + \rho^2\left(\frac{d_1}{T^2} + \frac{d_2}{T} + d_3 + d_4T\right) \tag{3-19}$$

D has units of $1x10^{-9}$ m^2/s, and ρ is in g/cm^3. The fitting parameters are listed in Table 3-3.

Table 3-3. Constants for the diffusion coefficient of O_2 and H_2 in water

Constants	H_2	O_2
a	116.211	1.82779
α	0.053892	0.422868
b_1	1	1
b_2	372312	-102443
b_3	-1794.21	334.021
b_4	1.42193	-0.11924
c_1	1	1
c_2	476427	-102959
c_3	-1880.99	334.195
c_4	1.62233	-0.11752
d_1	1	1
d_2	-377905	100433
d_3	1654.1	-347.059
d_4	-1.39764	0.125558

Finally, it should be noted that for BWRs, scaling factors were applied to the H_2 and O_2 exchange current densities for 304SS. These factors were determined by comparing measured ECP data in the recirculation at Dresden-2 and Duane Arnold. [81]

The scaling factors are as follows:

$SF(H_2) = 0.05$

$SF(O_2) = 0.44$

The Type 304 SS MPM was implemented as two separate models in RADICAL, one using the scaling factors for BWRs (called 'BSS304') and one without the scaling factors (called 'PWSS304').

3.2.2 Metal Oxidation Current

For Type 304 stainless steel, the oxidation current is given by an empirical model, based on data from Lee: [83]

$$i_{corr} = \frac{e^{(\mathbb{E}-\mathbb{E}_o)/b_f} - e^{-(\mathbb{E}-\mathbb{E}_o)/b_r}}{384.62 \times e^{4416/T} + X} \tag{3-20}$$

Where $b_f = b_r = 0.05\ V$ and X is given by:

$$X = \frac{e^{(\mathbb{E}-\mathbb{E}_o)/b_f}}{2.61 \times 10^{-3} \times e^{4416/[T+0.523(\mathbb{E}-\mathbb{E}_o)^{0.5}]}} \tag{3-21}$$

The standard potential is given by:

$$\mathbb{E}_o = 0.122 - 1.5286 \times 10^{-3} \times T \tag{3-22}$$

For Alloy 600 and Alloy 690, the oxidation current is given by: [80]

$$i_{corr} = \frac{e^{(\mathbb{E}-\mathbb{E}_o)/b_a} - e^{-(\mathbb{E}-\mathbb{E}_o)/b_c}}{\frac{1}{i_p} + \frac{e^{(\mathbb{E}-\mathbb{E}_o)/b_a}}{i_p e^{\alpha(\mathbb{E}-\mathbb{E}_o)^n}}} \tag{3-23}$$

The parameters in Equation (3-23) are given in Table 3-4.

Table 3-4. Parameters for Alloy 600 and 690 Oxidation Current [80]

Parameter	Value for Alloy 600	Value for Alloy 690
$\mathbb{E}_o$	$1.8 - 7.43 \times 10^{-3} \times T - \frac{9.13}{pH} + \frac{0.038}{pH}T$	$0.91 - 5.2 \times 10^{-3} \times T - \frac{4.9}{pH} + \frac{0.027}{pH}T$
b_a	0.035 V	0.55 V
b_c	0.095 V	0.95 V
i_p	$1.8 \times 10^{-2} \times e^{-5411.3/T}$	$3.13 \times 10^{-4} \times e^{-3572.7/T}$
α	7.18	6.14
n	0.44	0.43

3.2.3 Solving for the ECP

The charge conservation equation, Equation (3-3) is a nonlinear function of the potential. To solve this equation for the ECP, the Newton-Raphson Method is used. For an arbitrary function f(x), the value f(x+dx) can be calculated with a first order Taylor expansion:

$$f(x+dx) = f(x) + \left.\frac{df}{dx}\right|_x dx \tag{3-24}$$

Setting f(x+dx) = 0 and solving for dx:

$$dx = -\frac{f(x)}{\left.\frac{df}{dx}\right|_x} \tag{3-25}$$

For calculating the ECP, dx corresponds to E, and f(x) corresponds to the net current, which is given by the left hand side of Equation (3-3). The derivatives of the partial currents follow.

For the redox partial currents, given by Equation (3-8), noting that $b_a = b_c = b$, and that the limiting currents and exchange current density are not a function of potential:

$$\frac{d}{d\mathbb{E}}\left(i_{R/O}\right) = \frac{1}{b}\frac{\left[1-\frac{i_{R/O}}{i_{l,a}}\right]e^{\left(\frac{\mathbb{E}-\mathbb{E}^e_{R/O}}{b}\right)} + \left[1-\frac{i_{R/O}}{i_{l,c}}\right]e^{-\left(\frac{\mathbb{E}-\mathbb{E}^e_{R/O}}{b}\right)}}{\frac{1}{i_{o,R/O}} + \frac{1}{i_{l,a}}e^{\left(\frac{\mathbb{E}-\mathbb{E}^e_{R/O}}{b}\right)} - \frac{1}{i_{l,c}}e^{-\left(\frac{\mathbb{E}-\mathbb{E}^e_{R/O}}{b}\right)}} \tag{3-26}$$

For the corrosion partial current for 304SS, given by Equation (3-20):

$$\frac{d}{d\mathbb{E}}i_{corr} = \left[\frac{2}{b}\cosh\left(\frac{\mathbb{E}-\mathbb{E}_o}{b}\right) - i_{corr}\frac{dX}{d\mathbb{E}}\right]\frac{1}{384.62 \times e^{4416/T} + X} \tag{3-27}$$

$$\frac{dX}{d\mathbb{E}} = X\left[\frac{1}{b} - \frac{4416 \times 0.523}{2\sqrt{\mathbb{E}-\mathbb{E}_o} \times [T + 0.523(\mathbb{E}-\mathbb{E}_o)^2]}\right] \tag{3-28}$$

For the corrosion partial currents for Alloy 600 and 690, given by Equation (3-29):

$$\frac{d}{d\mathbb{E}} i_{corr} \tag{3-29}$$

$$= \frac{\frac{1}{b_a} e^{(\mathbb{E}-\mathbb{E}_o)/b_a} + \frac{1}{b_c} e^{-(\mathbb{E}-\mathbb{E}_o)/b_c} - i_{corr} \frac{e^{(\mathbb{E}-\mathbb{E}_o)/b_a}}{i_p e^{\alpha(\mathbb{E}-\mathbb{E}_o)^n}} \left[\frac{1}{b_a} - \alpha n(\mathbb{E}-\mathbb{E}_o)^{n-1}\right]}{\frac{1}{i_p} + \frac{e^{(\mathbb{E}-\mathbb{E}_o)/b_a}}{i_p e^{\alpha(\mathbb{E}-\mathbb{E}_o)^n}}}$$

3.2.4 pH Model

pH is required input for the equilibrium potentials for the redox reactions. To address this, three options were implemented in RADICAL for this thesis project:

1. pH calculated from Boron and Lithium equilibrium concentration
2. pH calculated from the H^+ concentration, as determined by the radiolysis model, according to pH=-log10([H^+])
3. pH can be entered as input into RADICAL

For the boron-lithium pH model, the following set of reactions was considered, according to [80]:

$$B(OH)_3 + OH^- = B(OH)_4^- \quad \text{(R1)}$$

$$2B(OH)_3 + OH^- = B_2(OH)_7^- \quad \text{(R2)}$$

$$3B(OH)_3 + OH^- = B_3(OH)_{10}^- \quad \text{(R3)}$$

$$Li^+ + OH^- = LiOH \quad \text{(R4)}$$

$$Li^+ + B(OH)_4^- = LiB(OH)_4 \quad \text{(R5)}$$

$$H_2O = H^+ + OH^- \quad \text{(R6)}$$

There are two other reactions, involving the formation of $B_4(OH)_{14}^{2-}$ and $B_5(OH)_{18}^{3-}$, however according to Kim, they are small enough to be neglected. Table 3-5 lists the equilibrium constants for Equations (R1)-(R6).

Table 3-5. Equilibrium Constants used in the boron-lithium pH subroutine [82]

Reaction	Reaction Constant (T is in Kelvin)	Original Source
R1	$\log_{10} K_1 = \frac{1573.21}{T} + 28.8397 + 0.011748\,T - 13.2258 \log_{10} T$	[91]
R2	$\log_{10} K_2 = \frac{2756.1}{T} - 18.966 + 5.835 \log_{10} T$	[91]
R3	$\log_{10} K_3 = \frac{3339.5}{T} - 8.084 + 1.497 \log_{10} T$	[91]
R4	$K_4 = 1.99$	[82]
R5	$K_5 = 2.12$	[82]
R6	$\log_{10} K_w = -4.098 - \frac{3245.2}{T} - \frac{2.2362 \times 10^5}{T^2} - \frac{3.9984 \times 10^7}{T^3} + \left(13.957 - \frac{1262.3}{T} + \frac{8.5641 \times 10^5}{T^2}\right) \log_{10} \rho_w$ K_w : units are molality ρ_w : [g/cm^3]	[92]

Thus for the case of water,

$$K_w = \frac{a_{H^+} a_{OH^-}}{a_{H_2O}} = m_{H^+} m_{OH^-} \gamma_{H^+} \gamma_{OH^-}$$

Where m_{H^+} and m_{OH^-} are the concentrations in (mol/kg H_2O)

Extended Debye-Huckel theory was used to calculate the activity coefficients, according to the relation: [82]

$$\log_{10} \gamma_i = \frac{-Az_i^2 \sqrt{I}}{1 + Ba_o \sqrt{I}} \tag{3-30}$$

Where the ionic strength is given by:

$$I = \sum_{i=1}^{n} m_i z_i^2 \tag{3-31}$$

z_i is the ionic charge and m_i is the molality (mol/kg H_2O)

T is in degree Celsius and $a_o = 4.65 \times 10^{-8}\ cm$

A and B are fitting parameters given by:

$$A = 0.4241 + 0.00321T - 2.0 \times 10^{-5} T^2 + 5.95143 \times 10^{-8} T^3 \tag{3-32}$$

$$B = 0.327 + 0.00019 - 2.12586 \times 10^{-7} T^2 + 1.4241 \times 10^{-9} T^3 \tag{3-33}$$

To calculate the concentration of hydrogen ions, there are the 6 equilibrium equations, as well as mass balances for lithium and boron, and charge neutrality. A

derivation of the solution can be found in Appendix A of Kim's thesis, [80] in which the set of nonlinear equations is reduced to 2 equations.

The solution scheme is to solve for the concentrations iteratively:

1. Initially guess the concentrations of H^+ and $B(OH)_3$, and the activity coefficent for the ionic species.
2. Calculate the remaining concentrations.
3. Calculate new activity coefficient (to be used for the next iteration)
4. Use the Newton-Raphson method to calculate new guesses for H^+ and $B(OH)_3$
5. Repeat steps 2-4 until the solution converges
6. Calculate the pH according to:

$$pH = -\log_{10}(\gamma m_{H^+}) \tag{3-34}$$

3.2.5 Summary of Changes to RADICAL

Table 3-6 summarizes the issues the changes made to the RADICAL code as part of this thesis.

Table 3-6. Summary of Changes made to RADICAL

Issue	Solution/Changes
Alpha radiolysis not included in RADICAL	Add implementation for alpha radiolysis: Alpha dose rates and g-values required as input
Reaction sets and g-values possibly not valid; previous values selected in 1993 for purpose of BWR water chemistry modeling	Implement newer sets and test: Christensen's water reaction set, AECL water reaction set, and G-values for both
AECL reaction set requires up to 5 coefficients for rate constant temperature dependence. It also requires acid/base dissociation constants for equilibrium rate constants	New rate constant implementation: allows for up to 5 coefficients. New rate constant types: allows different temperature treatments to be hard-wired into RADICAL.
ECP model used in RADICAL (Lin ECP model) likely not valid for PWRs	Implement Mixed Potential Models for ECP
Need pH for Mixed Potential Models	Add B /Li pH subroutine for PWRs Also allow pH to be directly input or use radiolysis chemistry results
Use of scaling factors in 304SS MPM : they were used to fit the mixed potential model results to experimental results. They may not be applicable to our radiolysis models	Implement model with and without scaling factors and test
Henry's law constants as implemented by MacDonald et al. not consistent with experimental data, particularly at high temperature.	Implement correlations valid for high temperature
Diffusion coefficients in Mixed Potential Model: uncertainty in coefficients and whether they are valid over a variety of temperatures	Add new correlations for diffusion coefficients

3.3 Benchmarking Water Reaction Sets and ECP Models

In the remainder of this chapter water reaction sets and g-values are tested against data from BWR plants and the AECL U2 loop. Additionally, the mixed potential models described in Section 3.2 are benchmarked against ECP measurements in BWRs. Several water reaction sets and g-value sets have been implemented for use in RADICAL. The original reaction set and g-values used in RADICAL were selected in 1992. Since then, new water reaction sets and g-values have been published, for example by Christensen [93] and the AECL. [84] Christensen's water reaction set was implemented in RADICAL, however, initial results indicated that the calculated pH was unphysically

high. Thus, the reaction set was not tested further. The g-value sets from Christensen were still tested in RADICAL. G-values and reaction sets are listed in Appendix B. Note that only Christensen's set includes g-values for alpha radiolysis. This does not affect the benchmarking results presented in this chapter, but would be significant for PWR radiolysis calculations.

3.4 BWR Benchmarking

BWR3 and BWR4 models had previously been developed and benchmarked for RADICAL. [78] These preexisting models were used to test the new reaction sets, g-values, and mixed potential models. All geometry, dose rates, and thermal hydraulic data and models were kept the same. Only the reaction sets, g-values, and ECP models were modified. Data from a 1993 EPRI report on Hydrogen Water Chemistry was used to benchmark the RADICAL results. [94]

3.4.1 Main Steam Line

Figure 3-2 and Figure 3-3 show the hydrogen and oxygen measured from the main steam line, compared to the RADICAL benchmarking simulations for a BWR3 and BWR4 respectively. The RADICAL and AECL water reaction sets were tested with their corresponding g-value sets and also with Christensen's g-value set.

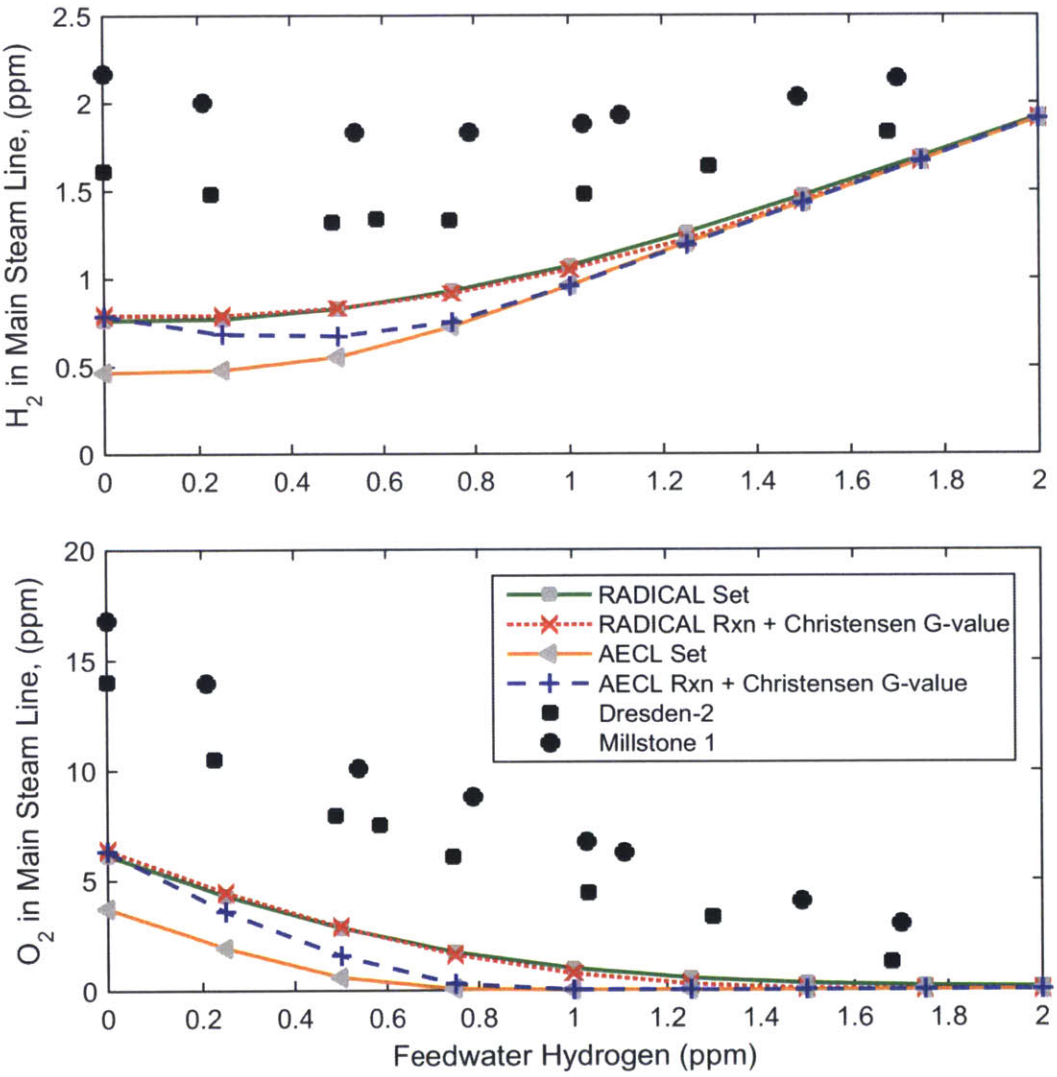

Figure 3-2. H_2 and O_2 Content in a BWR3 main steam line. Plant Data from [94]

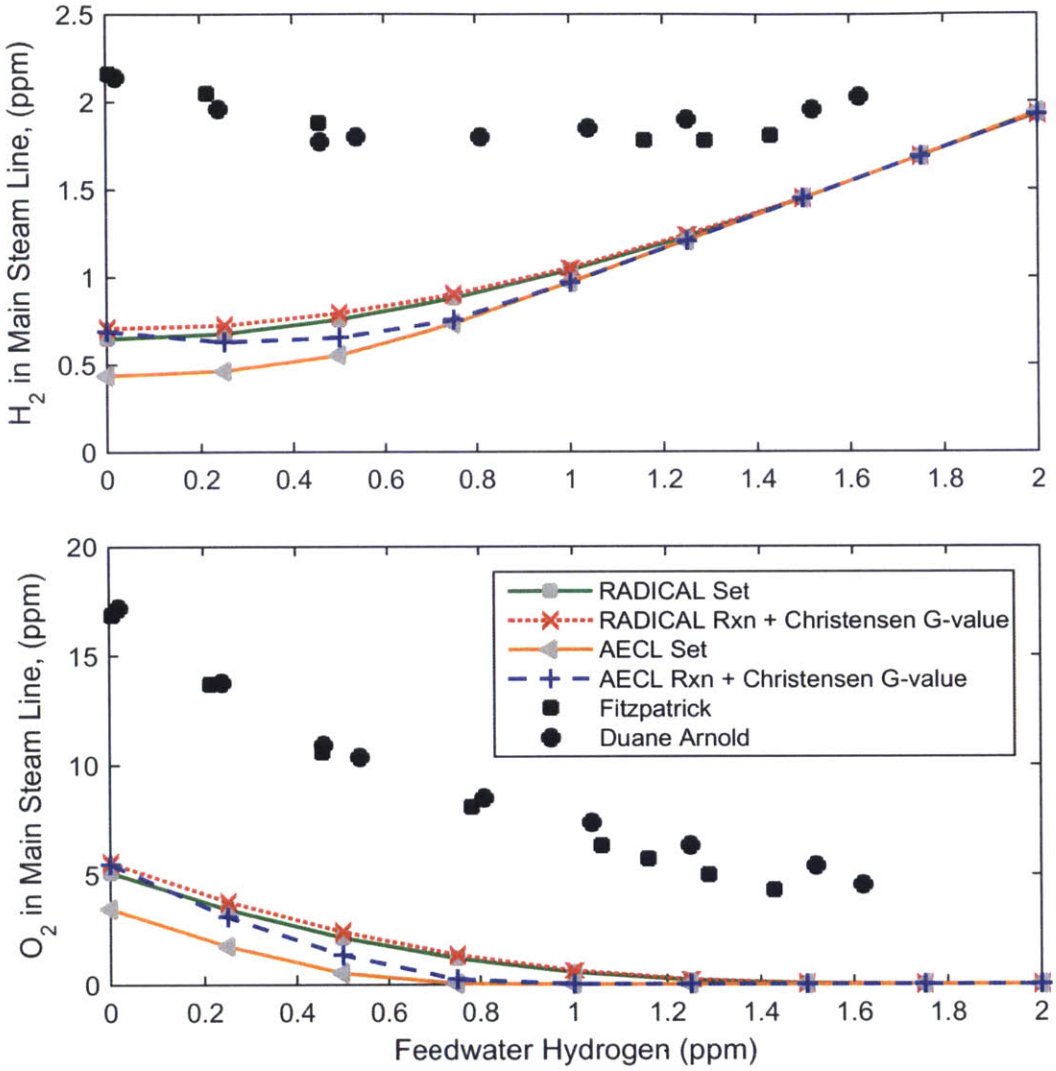

Figure 3-3. H_2 and O_2 Content in a BWR4 main steam line. Plant Data from [94]

For both the BWR3 and BWR4 models, the RADICAL reaction set yields nearly identical results with either the RADICAL g-values or Christensen's g-values. The AECL reaction set predicts slightly higher H_2 and O_2 concentrations with Christensen's g-values than with the AECL g-values. For both the BWR3 and BWR4, the RADICAL reaction set yields concentrations that are closer to the measured values. However, only

the AECL and Christensen combination properly predicts the shape of the steam H_2 content vs feedwater H_2 curve. All of the simulations predict lower oxygen and hydrogen content in the steam, which suggests that the coefficients for H_2 and O_2 mass transfer between the liquid and vapor phases (found in Table A-1 on page 305) may need calibration.

One noticeable difference is that the BWR3 plant data has more scatter than the BWR4 data. The Millstone concentrations are higher than the Dresden concentrations, by approximately 3-4 ppm for oxygen and 0.5 ppm for hydrogen. Slight differences in the two phase flow characteristics, for example the slip ratio or bubble diameter can change the partition between liquid and vapor phases and ultimately the water chemistry. For example, Figure 3-4, produced by Ibe et al., show the effect of bubble size on the oxygen and hydrogen concentration at the core exit. [95] For larger bubbles, a smaller quantity of oxygen and hydrogen are released into the coolant.

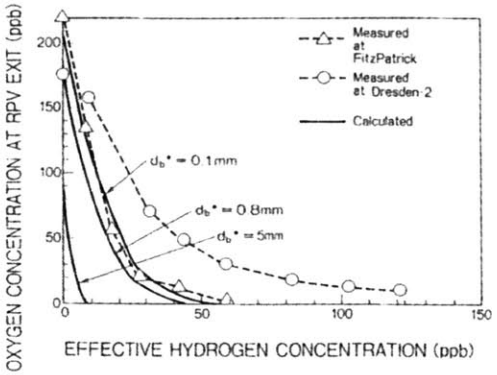

Figure 3-4. Effect of bubble size on oxygen content at the exit of a BWR 3. [95]

3.4.2 Recirculation Line Chemistry and ECP

Figure 3-5 and Figure 3-6 show the measured and modeled hydrogen, oxygen, and hydrogen peroxide concentrations in the recirculation line of a BWR3 and a BWR4, respectively.

As with the main steam line results, the BWR3 plant data exhibits scatter, especially in the oxygen concentrations. There is virtually no difference between using the RADICAL reaction set with either RADICAL g-values or Christensen's g-values.

All reaction sets and g-value combinations accurately predict the H_2 concentration. At zero feedwater hydrogen, both water reaction sets predict similar O_2 concentrations; however at concentrations of 0.25 ppm H_2 and higher, the RADICAL reaction set predicts O_2 concentrations that are two orders of magnitude greater than the AECL reaction set. While it would appear that the RADICAL set is closer to the plant data, plant equipment cannot measure concentrations below 1 ppb, so it is not possible to know which set is better. [94]

For hydrogen peroxide, the AECL reaction set predicts a higher concentration than the RADICAL reaction set. At zero feedwater hydrogen, there is a six order of magnitude difference. At higher feedwater hydrogen (greater than 1 ppm), the difference is two orders of magnitude.

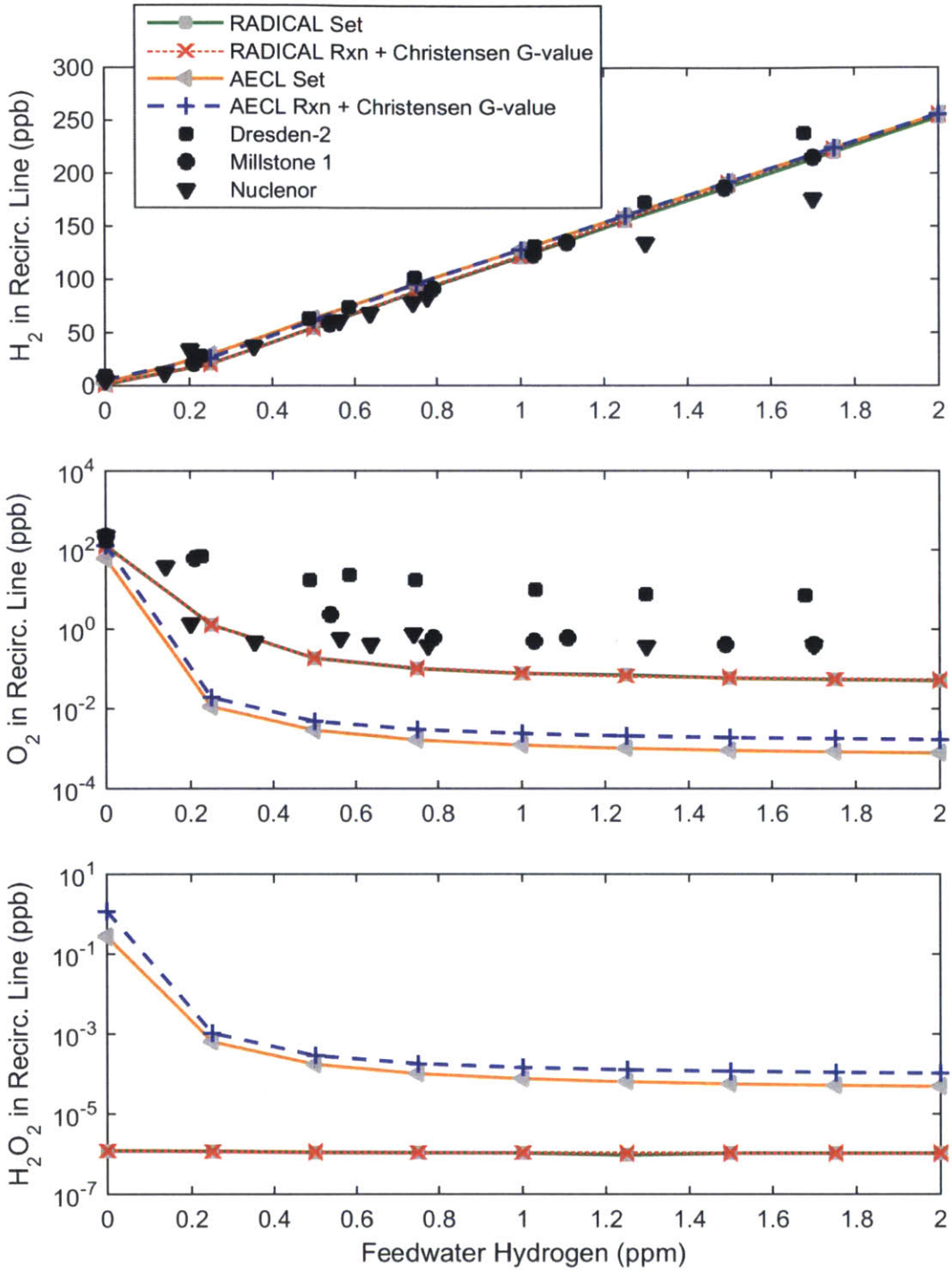

Figure 3-5. Dissolved hydrogen (top), oxygen (middle), and hydrogen peroxide (bottom) in a BWR3 recirculation line. Plant data from [94]

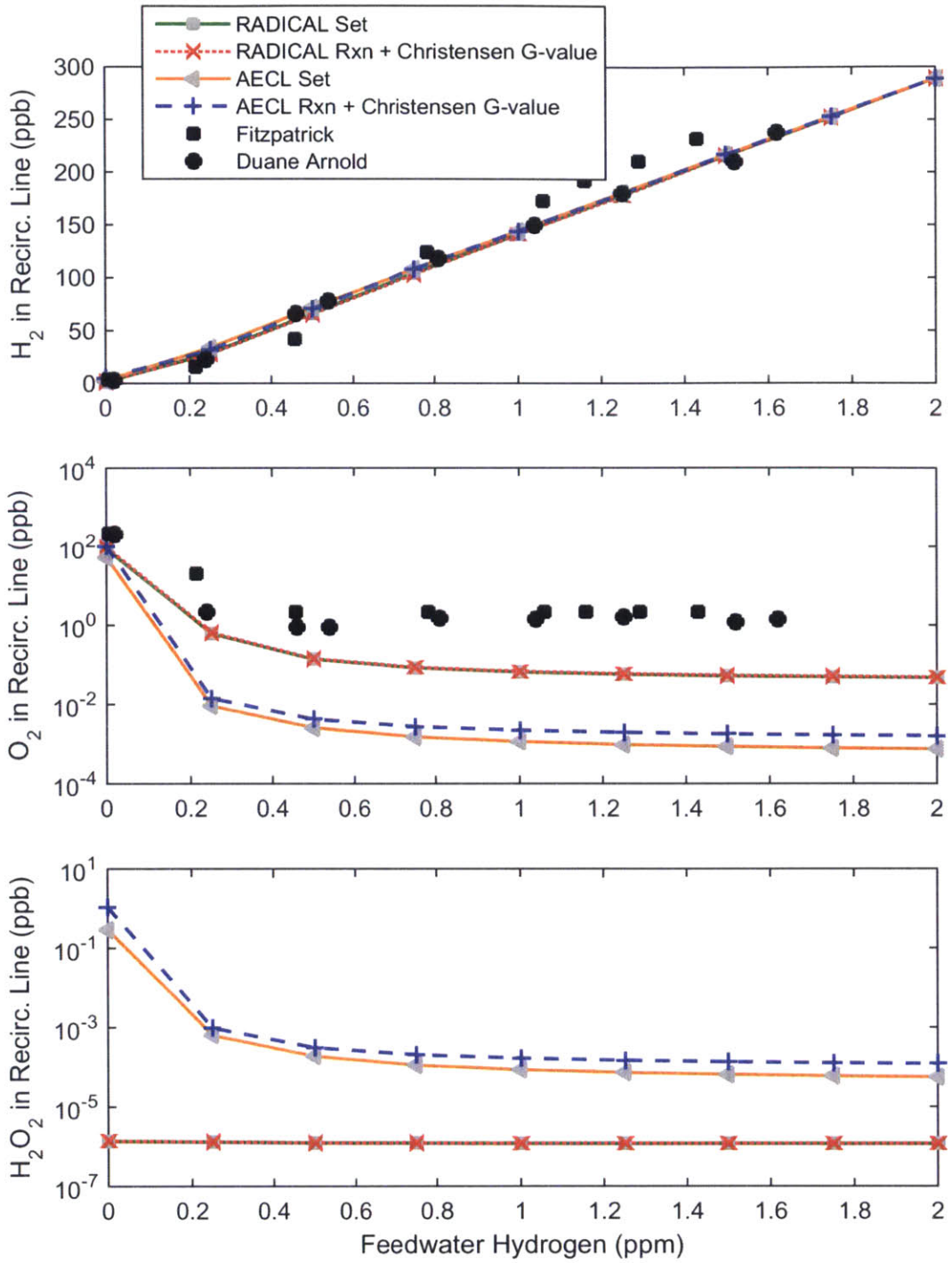

Figure 3-6. Dissolved hydrogen (top), oxygen (middle), and hydrogen peroxide (bottom) in a BWR4 recirculation line. Plant data from [94]

Figure 3-7 and Figure 3-8 show the calculated and measured corrosion potentials in the recirculation line. Based on the chemistry results in the previous section, the ECP was calculated using the RADICAL reaction and g-value set, and the combination of the AECL water reaction set with Christensen's g-values. The three ECP models for stainless steel were compared - the Lin model, the "PWR" mixed potential model for 304SS (by MacDonald et al., without scaling factors), [82] and the BWR mixed potential model for 304SS (by MacDonald et al.). [81]

As Figure 3-7 illustrates, the measured data has significant scatter, even for measurements taken at the same plant. Each ECP model yields nearly identical ECP, regardless of whether the RADICAL or AECL set was used. The Lin correlation yields results closest to measured data. At zero hydrogen addition, the BWR-MPM predicts a more positive ECP than the PWR-MPM, and at hydrogen overpressure, it predicts a more negative ECP. Recall that the exchange current densities of hydrogen and oxygen are reduced by a fitting factor in the BWR-MPM model. For the case with no hydrogen addition, the oxygen current is balanced by the corrosion and hydrogen currents. Thus, lowering the oxygen current shifts the ECP towards the oxygen equilibrium potential (more positive). At a hydrogen overpressure, the hydrogen current is balanced by the hydrogen peroxide current, so a reduction in the hydrogen current shifts the ECP toward the hydrogen equilibrium potential (more negative).

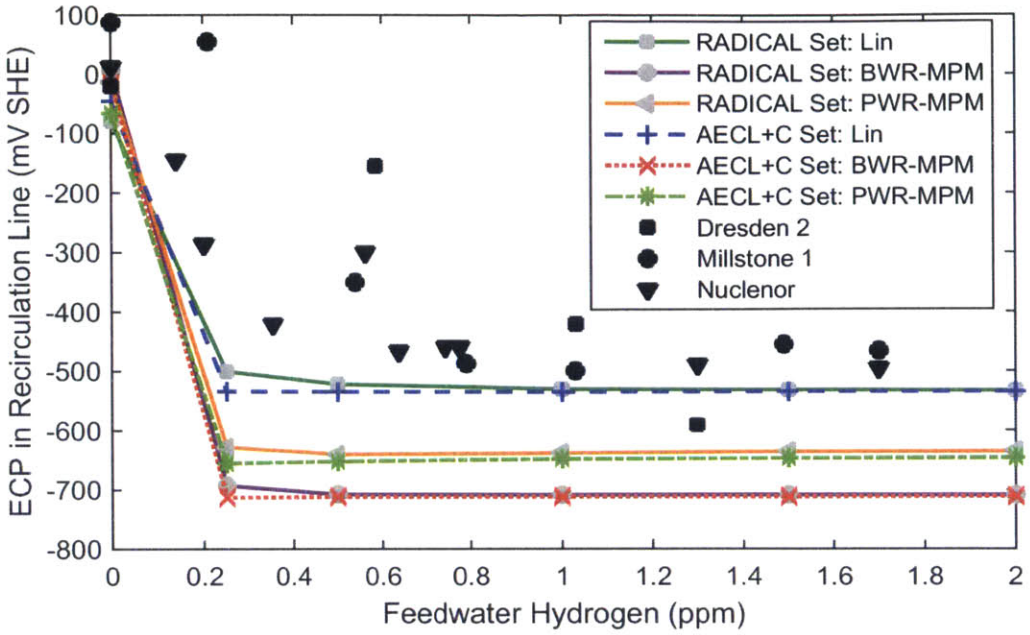

Figure 3-7. ECP in the Recirculation of a BWR3. Plant data from [94]

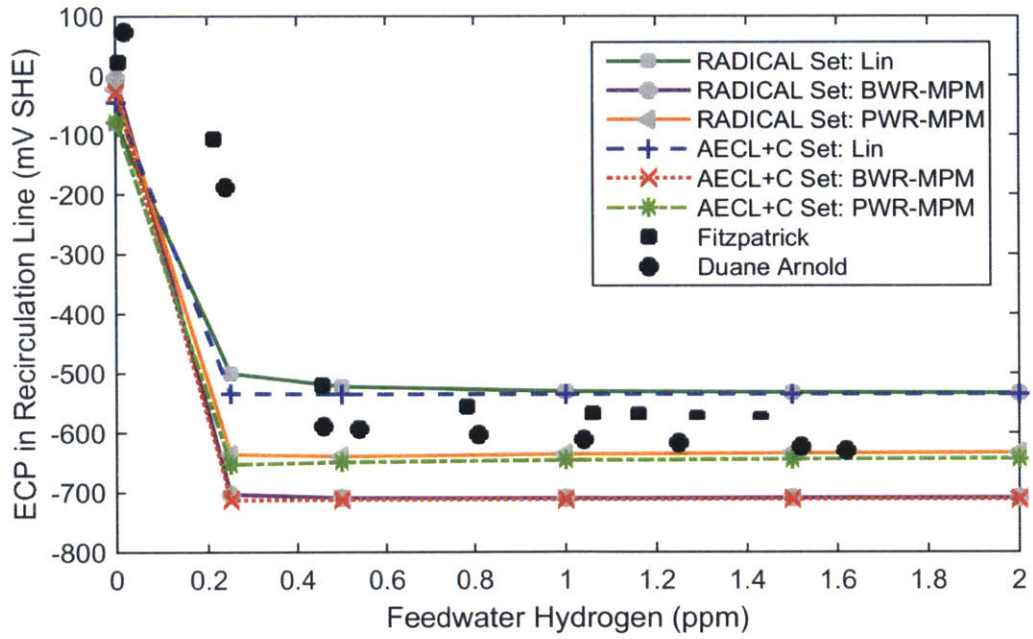

Figure 3-8. ECP in the Recirculation line of a BWR 4. Plant data from [94]

3.4.3 Core Bypass ECP

Lin et al, compared the results of their ECP model to in-core ECP measurements in the bypass of a BWR. [79] ECP measurements were taken near the top of the bypass, and near the bottom of the bypass. In this section, the results from the different water reaction sets and ECP models are compared to the measured data. The BWR3 RADICAL model was used for the comparison. The RADICAL reaction set and g-values were compared against the AECL reaction set with Christensen's g-values. The three ECP models for stainless steel were compared - the Lin model, the "PWR' mixed potential model for 304SS (by MacDonald et al., without scaling factors), [82] and the BWR mixed potential model for 304SS (by MacDonald et al. with scaling factors). [81]

Figure 3-9 shows the calculated and measured ECP at the bottom of the bypass (the entrance). The RADICAL reaction set appears to perform better than the AECL+ Christensen combination. At 0.5 ppm or less hydrogen, the RADICAL reaction set with either Lin's correlation or the BWR-MPM predict the ECP correctly. At 1 ppm and higher hydrogen injection, the PWR-MPM is the most accurate, while the BWR-MPM and Lin correlation overestimate the ECP.

For the AECL+ Christensen combination, the Lin correlation performs the best. At all feedwater hydrogen concentrations, the correlations underestimate the ECP. At less than 0.5 ppm H_2, the BWR-MPM performs better than the PWR-MPM, and at greater hydrogen concentrations the PWR-MPM performs better.

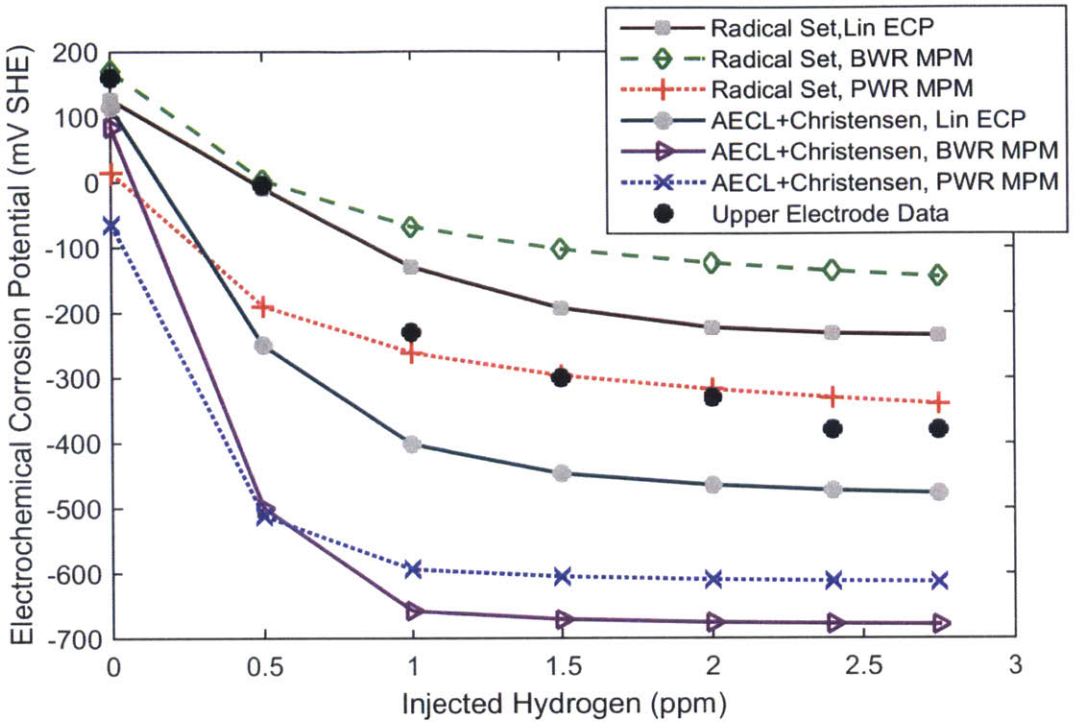

Figure 3-9. ECP at the bottom of the core bypass in a BWR3. Data from [79]

Figure 3-10 shows a comparison of the ECP at the top of the bypass. At the top of the bypass, the RADICAL reaction set performs better than the AECL+ Christensen's combination. The curves for Lin's correlation and the PWR-MPM correlation have similar shapes. However, the Lin correlation predicts a higher ECP. It appears that the BWR-MPM Correlation with RADICAL comes the closest at hydrogen less than 1.5 ppm. At hydrogen injection levels greater than 1.5 ppm, the Lin correlation comes the closest. For the AECL + Christensen set, the BWR-MPM calculates the greatest (most positive) ECP at hydrogen injection less than 1 ppm, and the smallest (most negative) ECP at hydrogen greater than 2 ppm.

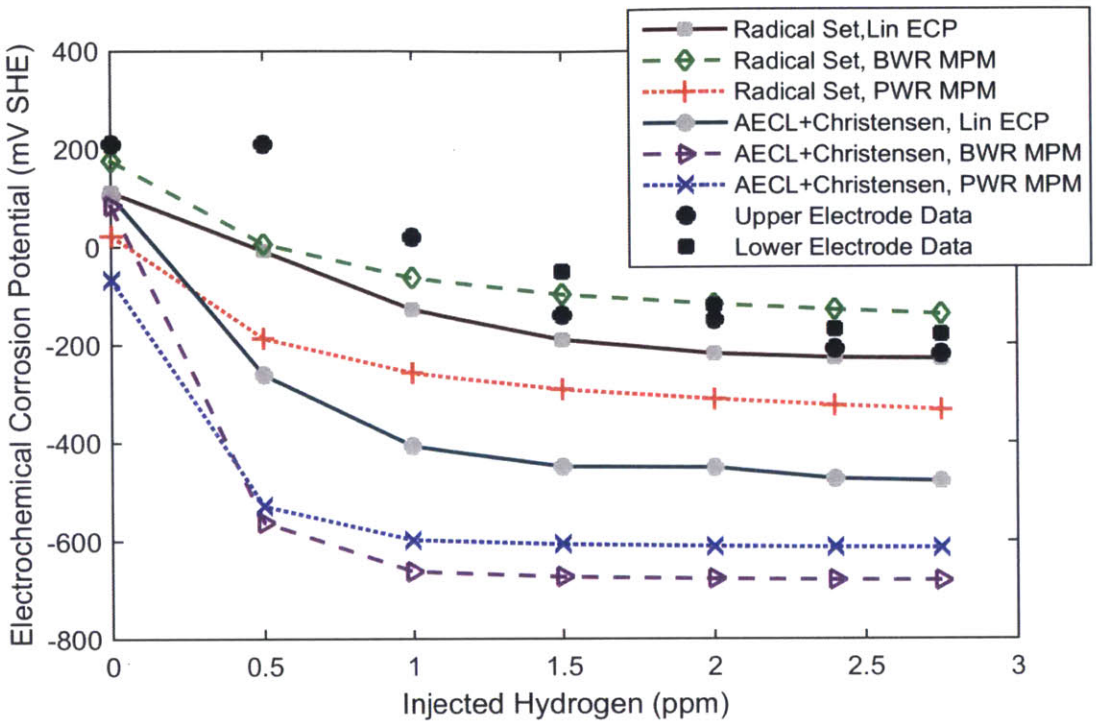

Figure 3-10. ECP at the top of the core bypass in a BWR3. Data from [79]

Comparing the bottom and top of the bypass region, the conditions at the top of the bypass should be more oxidizing because of radiolysis. None of the correlations predict a significant difference between the ECP at the top and bottom of the bypass. In the BWR3 model, the hydrogen peroxide and oxygen concentrations reach a maximum 0.7 m below the sample location for the top of the bypass, as shown in Figure 3-11. The difference in ECP between the most oxidizing position and the upper bypass sample point is less than 50 mV. One possible explanation for the large discrepancies at the top of the bypass is that the dose rates in the plant where measurements were taken are greater than those in the RADICAL BWR3 model.

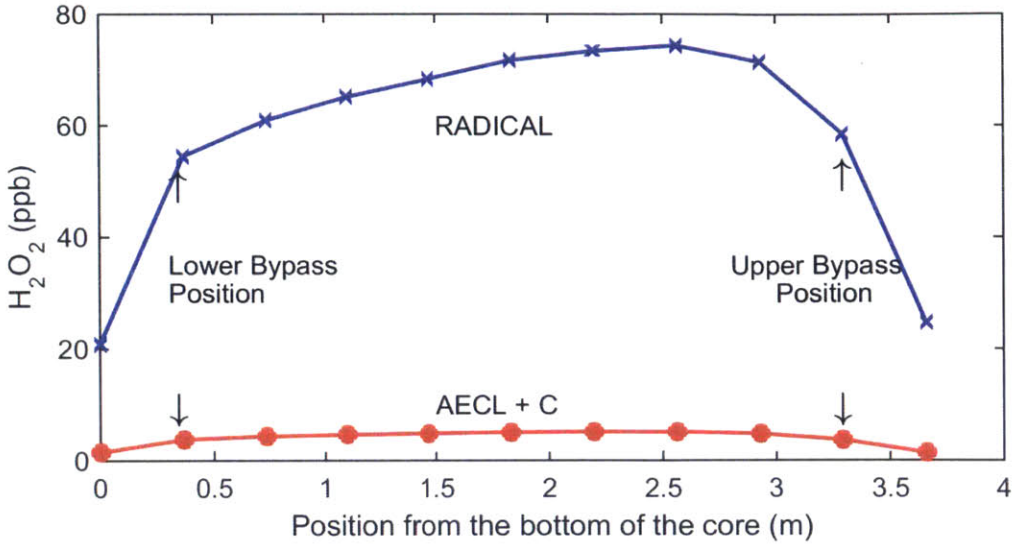

Figure 3-11. Hydrogen peroxide in a BWR3 bypass at 1.5 ppm H_2 injection

To better understand the difference between the two reaction sets, the polarization (Evans) diagrams can be compared. Polarization diagrams can be produced by plotting the partial currents of the mixed potential models as a function of potential. The coolant temperature in the bypass is 277°C. Using the AECL set, pH_T =5.7. Using the RADICAL reaction set, pH_T is 5.6. Figure 3-12 shows Polarization diagrams for zero and 1.5 ppm hydrogen injection, at the top of the bypass. These plots were produced using the BWR mixed potential model. The thick solid lines show the partial currents calculated using the AECL+Christensen results, and the dotted lines are used for the RADICAL results. The thin black line and dotted line show the ECP.

At zero hydrogen injection, the hydrogen partial current forms the majority of the oxidation current, while the hydrogen peroxide partial current dominates the reduction current. The hydrogen and oxygen redox potentials are nearly identical with both

reactions sets (within 0.04 V). The hydrogen peroxide redox potential is more positive for the RADICAL set, and the exchange current density is larger.

At 1.5 ppm H_2, the results are quite different between the two sets: for the RADICAL set, hydrogen is oxidized and for the AECL + Christensen set, hydrogen is reduced. The hydrogen peroxide limiting current with the RADICAL reaction set is ~16x the limiting current with the AECL + Christensen set.

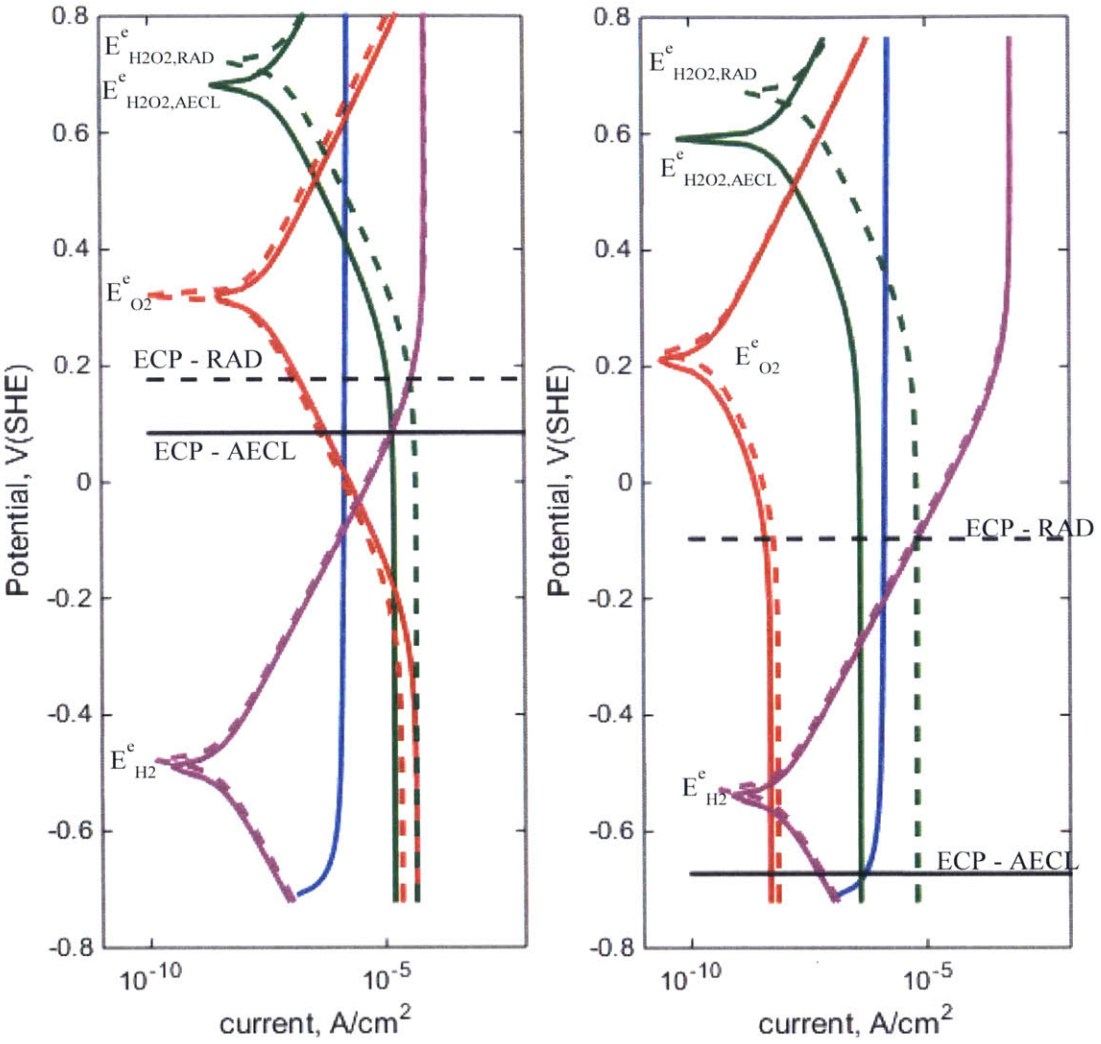

Figure 3-12. Evans diagram for ECP at the top of the core bypass in a BWR3, using the BWR-MPM ECP model, with no hydrogen (left) and 1.5 ppm hydrogen addition (right)

Potential-pH (Pourbaix) diagrams for iron and chromium at 300ºC are presented in Figure 3-13. [96,97] For all calculated ECP values, the stable phase of chromium is Cr_2O_3. At pH values of 5.7, the stable iron phase varies: at -0.82 to -0.47 V (SHE) it will

be Fe_3O_4, and at higher potentials, the stable phase will be Fe_2O_3. With the RADICAL reaction sets, the computed ECP in the bypass is always above -0.47 V(SHE), regardless of the ECP correlation. For the AECL + Christensen combination, the calculated ECP is below -0.47 V(SHE) at ≥0.5 ppm H_2 with both versions of the mixed potential model, meaning that Fe_3O_4 is likely the stable phase. The Lin correlation predicts the ECP will only be less than -0.47 at >2 ppm H_2, suggesting that Fe_2O_3 is likely the stable phase until this relatively high level of hydrogen injection.

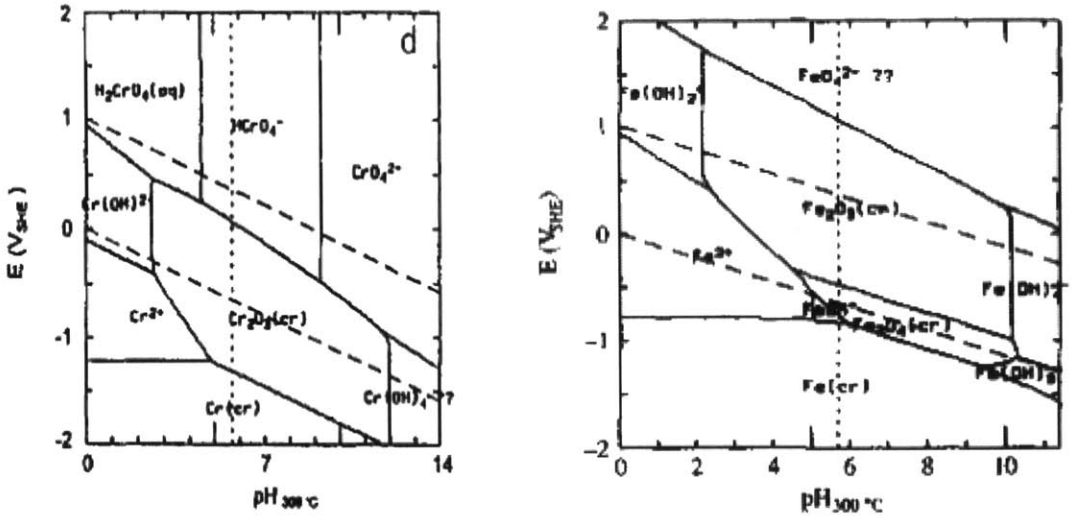

Figure 3-13. Pourbaix diagrams for Cr (left) and Fe (right) at $1x10^{-6}$ M at 300°C [96,97]

3.5 AECL Test Loop

Bartels et al. modeled a critical hydrogen concentration experiment in the U2 test loop in the Chalk River NRU reactor. [98] In their model they used the AECL water reaction set and g-values. Bartels et al. varied the concentration of hydrogen in the loop, and compared the hydrogen concentration to the excess reducing equivalent (ERE), which is calculated from the hydrogen, oxygen, and hydrogen peroxide concentrations:

$$ERE = [H_2] - 2[O_2] - [H_2O_2] \quad (3\text{-}35)$$

For this work, a RADICAL model of the U2 test loop was developed, so as to compare the results against those of Bartels et al. The dose profile shape is found in [99]. The geometry, flow rates, temperature, and peak dose rates of the loop can be found in [98]. Both the AECL reaction set and the RADICAL reaction set were used in the RADICAL U2 model.

Bartels et al. found that their model underpredicted the critical hydrogen concentration by a factor of 10. Additionally, the model also underpredicted the hydrogen concentration at which the ERE is zero; which was measured as 2.5 scc/kg. Figure 3-14 compares the Bartels et al. results against the RADICAL model results. The critical hydrogen concentration can be identified as a minimum in the ERE vs. H_2 plot.

The RADICAL U2 loop model likewise underpredicts the critical hydrogen concentration, and the hydrogen concentration at zero ERE. For the AECL reaction set and g-values, the critical hydrogen concentration is at an ERE of approximately -0.05 scc/kg H_2. However, the concentration of H_2 at 0 ERE is approximately the same as Bartels. Using the AECL reaction set with Christensen's g-values, the CHC occurs at 0.05 scc/kg H_2. The RADICAL reaction set fails to predict a critical hydrogen concentration.

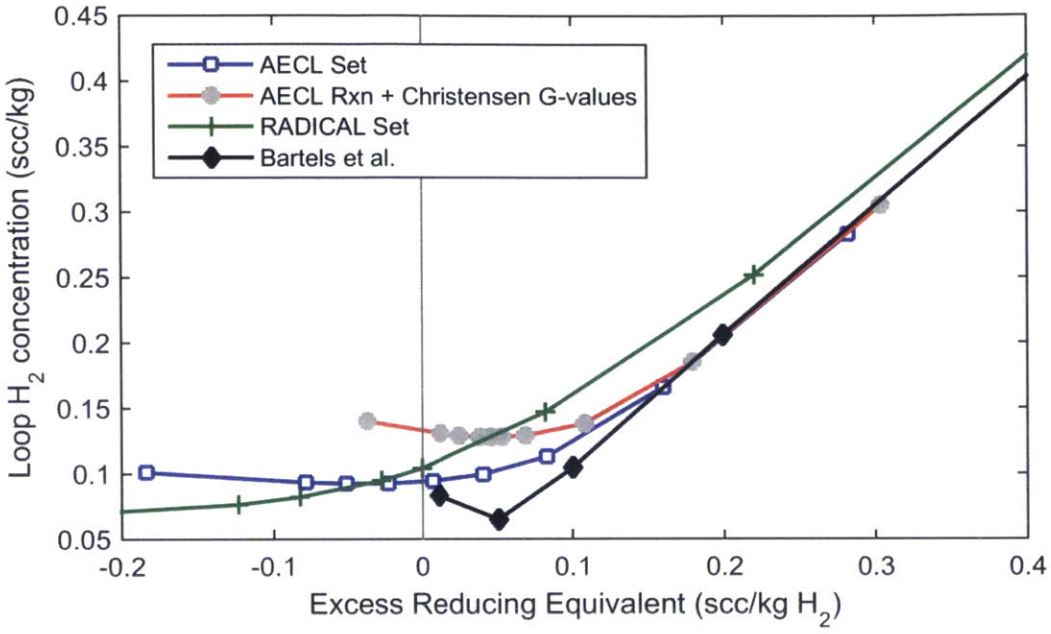

Figure 3-14. Hydrogen concentration vs. excess reducing equivalent in the U2 loop. Results compared to Bartels et al. [98]

3.6 Chapter Summary and Conclusions

In this chapter, Mixed Potential Models were implemented in RADICAL and compared to experimental data. A model to calculate the pH in PWRs based on boron and lithium additions was also added. Water reaction sets and g-values were tested using RADICAL models for BWR3, BWR4, and the AECL U2 loop. The AECL water reaction set with Christensen's g-values were best able to capture a critical hydrogen concentration in the AECL U2 loop and in BWR main steam lines. The RADICAL water reaction set was not able to predict a critical hydrogen concentration. A notable difference between the two reaction sets is that the RADICAL reaction set predicts

significantly higher hydrogen peroxide concentrations. However, without H_2O_2 experimental data, we cannot know definitively which is more accurate.

Our calculated ECP values in the recirculation line had good agreement with measured values, using either the Lin ECP model or MacDonald et al.'s 304 SS mixed potential model. However, ECP calculations in the core bypass showed differences of up to 0.25V between the two models. Additionally, there were substantial differences when comparing the two reaction sets. A comparison of the two implementations of the 304SS mixed potential model shows that at hydrogen overpressures, the version without scaling factors is better.

In light of all the benchmarking calculations, the AECL water reaction set with Christensen's g-values were selected for the PWR radiolysis model. The mixed potential model for 304 SS without scaling factors was selected as the ECP model. With the selection of a water reaction set, g-values, and ECP model complete, the development of the PWR radiolysis model can now proceed. The next steps in creating a radiolysis PWR model are determining the geometry, thermal hydraulics, and dose rates.

Chapter 4: Development of a PWR Radiolysis Model

In Chapter 3, changes were implemented to RADICAL to prepare for modeling radiolysis in a PWR. In this chapter, the development of the PWR radiolysis model is described, and water chemistry results are presented.

There are several differences between BWR and PWRs that affect the water chemistry. The coolant temperature and pressure are higher in PWR; in BWRs bulk boiling occurs, while in PWRs the coolant exits the core as a subcooled liquid. Subcooled nucleate boiling does occur in the PWR core but does not produce significant voiding. Thus, there is no stripping of oxygen and hydrogen into a vapor phase which can cause conditions to become more oxidizing. Furthermore, PWRs operate at a significant hydrogen overpressure, typically 25-50 scc H_2/kg H_2O or 2.23-4.46 ppm.

In PWRs, boron is added to the coolant for reactivity control. ^{10}B captures thermal neutrons, and decays into an alpha particle and lithium atom. This means that there is an additional source of radiation to account for in radiolysis models. Furthermore, the boron addition and thus the alpha dose changes throughout the cycle. The alpha dose will be especially important in CRUD-containing regions, where local boiling can concentrate boron and increase local dose. CRUD effects will be discussed in the following chapter.

Radiolysis modeling in PWRs has not been studied as extensively as in BWRs, because the hydrogen injection was believed to suppress oxygen and hydrogen peroxide production from radiolysis. Thus, in PWRs it is expected that the ECP is very low and controlled by the hydrogen overpressure.

4.1 PWR Model Development

The geometry and flow conditions of the model developed for this work are based on a 4-loop Westinghouse PWR that was modeled using RELAP (Reactor Excursion and Leak Analysis Program). The core power was taken from Seabrook. [100] There were no openly available dose rates in the literature, so dose profiles were calculated using the MCNP (Monte Carlo N-Particle) code.

4.1.1 Nodalization and Model Development

Table 4-1 lists the general parameters in the PWR Radiolysis Model developed for this work.

Table 4-1. General Plant Parameters used in the PWR radiolysis model

Coolant Pressure	15.5 MPa
Hot Leg Temperature	599 K
Cold Leg Temperature	569 K
Thermal Power	3587 MW
Number of Fuel Assemblies	193
Cycle Length	500 EFPD, 19.47 MWd/kgU
Fuel Assembly	17x17, 264 fuel rods

A schematic of the PWR RADICAL model is shown in Figure 4-1 and the nodalization, along with relevant geometry is listed in Table 4-2. In the core region, the hot pin and a twice-burned (two cycle) pin have been isolated from the rest of the core to study the effects of burnup and power on chemistry. The fraction of coolant diverted to these fuel rods is small enough to have no effect on the chemistry in the remainder of the model.

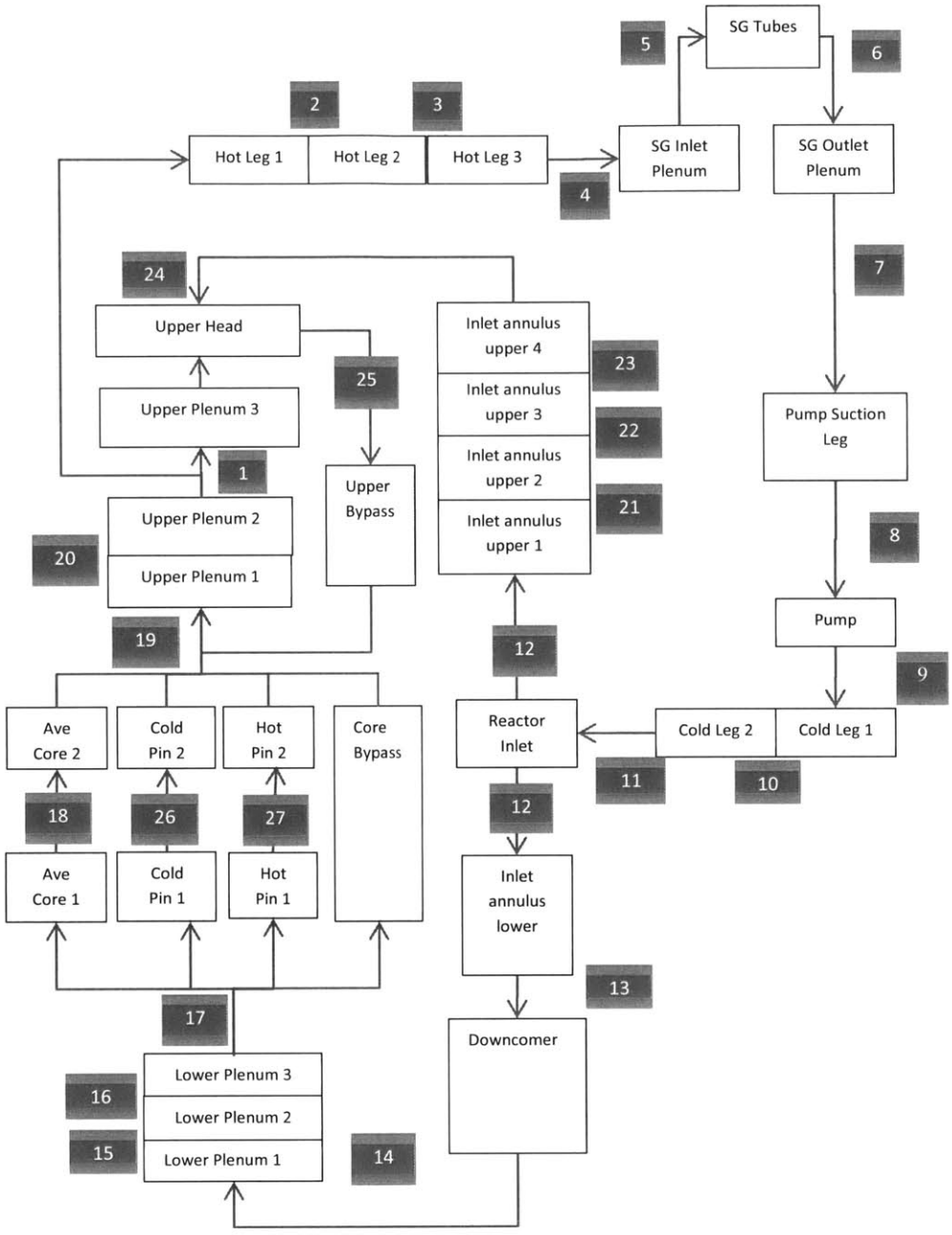

Figure 4-1. PWR RADICAL Model

Table 4-2. PWR RADICAL Model Nodalization

Component Name	Start Node	End Node	Mass Flow (g/s)	Area (cm^2)	Length (cm)	Hydraulic Diameter (cm)
HOT LEG 1	1	2	18691	19100	101.8	77.97
HOT LEG 2	2	3	18691	17044	478.6	73.67
HOT LEG 3	3	4	18691	18572	165.1	76.90
SG INLET PLENUM	4	5	18691	106080	159.5	183.80
SGTUBE	5	6	18691	41240	2130.4	1.97
SG OUTLET PLENUM	6	7	18691	106080	159.5	183.80
PUMP SUCTION LEG	7	8	18691	19476	830.1	78.73
PUMP	8	9	18691	19476	325.7	0.00
COLD LEG 1	9	10	18691	15328	688.7	69.86
COLD LEG 2	10	11	18691	18244	156.8	76.20
REACTOR INLET	11	12	18691	18388	63.5	41.95
INLET ANNULUS LOWER	12	13	18663	27268	68.6	32.54
INLET ANNULUS UPPER 1	13	21	27.85	18388	63.5	41.95
INLET ANNULUS UPPER 2	21	22	27.85	30324	74.9	46.99
INLET ANNULUS UPPER 3	22	23	27.85	14380	74.9	46.99
INLET ANNULUS UPPER 4	23	24	27.85	14020	45.7	21.59
DOWNCOMER	13	14	18663	24824	553.8	19.20
CORE BYPASS	17	19	883.7	17350	407.7	29.23
LOWER PLENUM 1	14	15	18663	120800	55.3	70.10
LOWER PLENUM 2	15	16	18663	84730	101.6	35.05
UPPER BYPASS	25	19	220.23	17060	381.9	22.56
LOWER PLENUM 3	16	17	18663	104400	44.5	97.54
AVERAGE CHANNEL 1	17	18	17687	49750	45.3	0.99
AVERAGE CHANNEL 2	18	19	17687	47870	362.4	0.95
HOT CHANNEL 1	17	26	92.1	258	45.3	0.99
HOT CHANNEL 2	26	19	92.1	248	362.4	0.95
UPPER PLENUM 1	19	20	18883	105000	68.6	50.90
UPPER PLENUM 2	20	1	18883	105000	63.5	50.90
UPPER PLENUM 3	1	24	192.38	105000	249.9	50.90
UPPER HEAD 1	24	25	220	65870	52.6	39.62
HOT ROD 1	17	27	0.35	0.98169	45.3	0.99
HOT ROD 2	27	19	0.35	0.94404	362.4	0.95

In PWR's the boron concentration changes as a function of time, as shown in Figure 4-2.

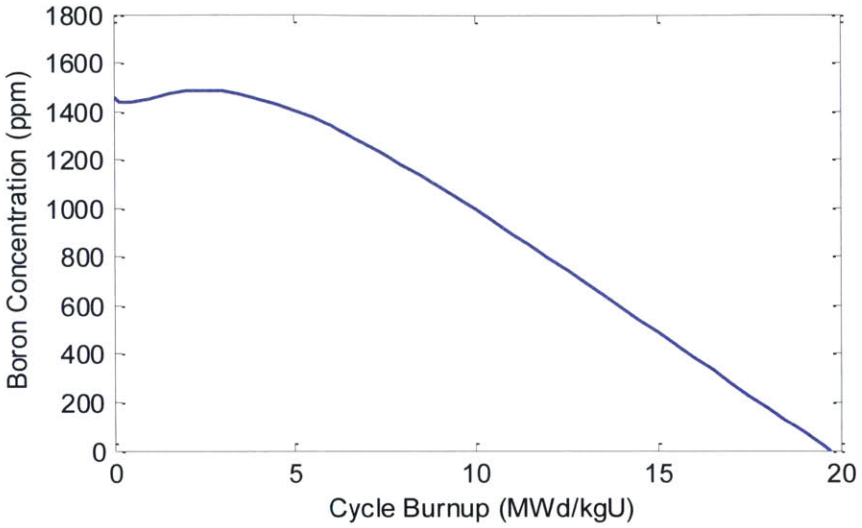

Figure 4-2. Typical boron letdown curve for a PWR Data from [10]

Four conditions were selected to model; Beginning of Cycle, Middle of Cycle, End of Cycle, and the time of maximum boron concentration. The core modeled contained 40% fresh fuel, 40% once burned fuel, and 20% twice burned fuel. The boron concentrations and lithium concentrations are shown in Table 4-3. The boron data is taken from Figure 4-2, and the lithium concentrations were calculated using the EPRI recommendations for a Modified Chemistry regime. [11] The fuel burnups and pin linear heat generation rate are listed in Table 4-4 and Table 4-5 respectively. The axial power shapes are shown in Figure 4-3.

Table 4-3. Boron and Lithium addition

	Cycle Burnup [MWd/kgU)	Boron [ppm]	Li [ppm]	pH @ 310°C
Beginning of Cycle	0.1	1440	2.4	6.9
Maximum Boron	2.5	1486	2.632	6.9
Middle of Cycle	10	1000	2.2	7.13
End of Cycle	19.47	0	0.54	7.4

Table 4-4. Fuel burnup in (MWd/kgU)

	Fresh Fuel	**Once Burned**	**Twice burned**	**Core Averaged burnup**
BOC	0.1	19.47	38.94	15.62
Max. Boron	2.5	21.97	41.44	18.076
MOC	10	29.47	48.94	25.576
EOC	19.47	38.94	58.41	25.046

Table 4-5. Average linear heat generation rate for a single fuel pin in (kW/m) [100]

	Average Core	**Peak Pin**	**High Burnup Pin**
BOC	19.03	25.97	18.75
Max. Boron	19.03	26.22	18.57
MOC	19.03	26.28	17.81
EOC	19.03	25.30	17.89

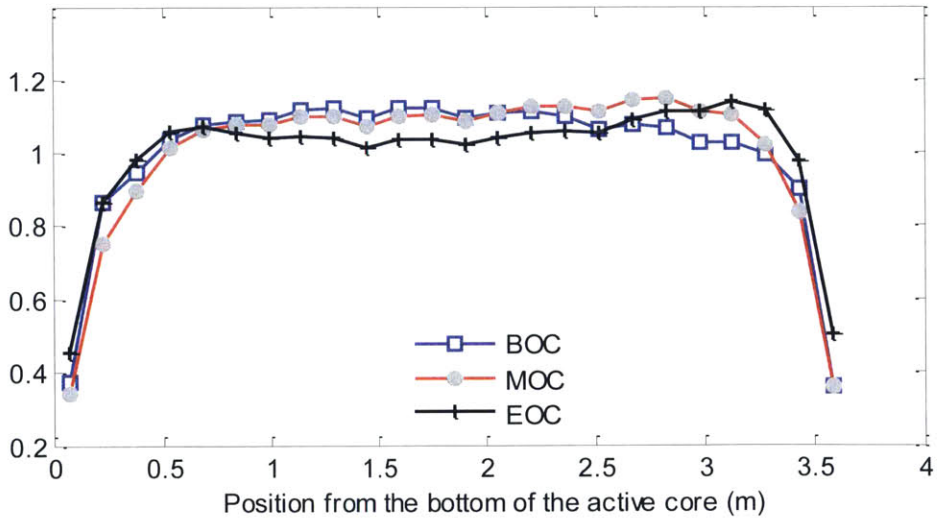

Figure 4-3. Axial Power Shapes at Beginning of Cycle, Middle of Cycle, and End of Cycle. [100]

4.1.2 PWR Dose Development

The following subsections describe the process of creating the dose profiles. The dose rates in the core were estimated using a criticality calculation for a single pin cell in MCNP. [101] Figure 4-4 shows the pin cell, and Table 4-6 lists the dimensions.

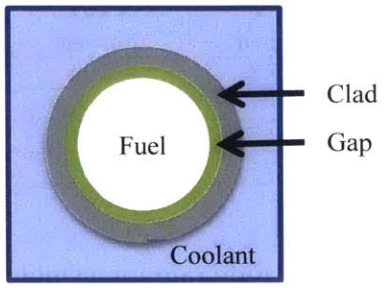

Figure 4-4. Pin cell for MCNP calculation

Table 4-6. Cell dimensions for MCNP dose calculations

Region	Outer radius (cm)	Material	Density [g/cc]
Fuel	0.39218	UO_2	10.4
Gap	0.40005	Vacuum	-
Clad	0.45720	Zircaloy-4	6.55
coolant	1.26 (rod pitch)	Water, boron	0.588-0.737

The following tallies were performed:

- total energy deposition in Fuel
- total energy deposition in Clad
- total energy deposition in coolant
- neutron flux <1 eV in coolant
- neutron dose in coolant
- neutron dose in coolant >0.5 MeV

Using the material densities, the cross sectional areas, and the computed dose, the heat generation in the fuel rod per length is:

$$\mathcal{E}'\left[\frac{MeV}{cm}\right] = \rho_{Cool}A_{Cool}\mathcal{E}_{Cool} + \rho_{Clad}A_{Clad}\mathcal{E}_{Clad} + \rho_{Fuel}A_{Fuel}\mathcal{E}_{Fuel} \quad (4\text{-}1)$$

ρ_i is the density of i [g/cm^3]

A_i is the cross sectional area of i [cm^2]

$\mathcal{E}_i$is the total energy deposition in i [MeV/g]

The alpha dose rate can be calculated from the thermal neutron flux as:

$$Dose_\alpha\left[\frac{MeV}{g\ coolant}\right] = \Phi\sigma_a E_{10B(\alpha,Li)}\frac{C_B N_A}{M_B} \times 10^6 \quad (4\text{-}2)$$

Φ is the thermal neutron flux from MCNP [n/cm^2]

$\sigma_a = 6.55 \times 10^{22} cm^2$ is the absorption cross section for natural boron [102]

$E_{10B(\alpha,Li)} = 2.33\ MeV$ the effective total energy of the α and ^7_3Li recoil nuclei [102]

C_B is the concentration of boron in the coolant [ppm]

N_A is Avagadro's number

M_B is the molar mass of boron

The dose to linear heat generation ratio is calculated using MCNP doses and Equation (4-1):

$$Dose\ Ratio\left[\frac{cm}{kg\ coolant}\right] = \frac{Dose\left[\frac{MeV}{g\ coolant}\right]}{\mathcal{E}'\left[\frac{MeV}{cm}\right]} \times \frac{1000\ g}{kg} \quad (4\text{-}3)$$

The dose rate can then be calculated from the dose ratio:

$$Q\ [Rad/s] = \frac{Rad}{0.01\ J/kg} \times \frac{m}{100\ cm} \times Dose\ Ratio\left[\frac{cm}{kg\ coolant}\right] \times q'[W/m] \qquad (4\text{-}4)$$

where q' is the linear heat generation rate for a single fuel rod.

A database for the dose ratios at different coolant densities, boron concentrations, and fuel burnups was created. Eleven coolant densities were used, ranging from 0.5888 g/cc to 0.737 g/cc. Three burnups were used, ranging from 0.1 to 40 MWd/kgU. The composition of the fuel was taken form CASMO depletions. [103] Three boron concentrations were used from 0-2000 ppm. In general, the dose increased with burnup and boron concentration. The gamma and fast neutron dose decrease as the coolant density increases, whereas the alpha dose increases as the coolant density increases. The dose ratios can be found in Figure C-1 to Figure C-3.

The dose rate profiles were created as follows:

1. Interpolate the dose ratios for boron concentrations. The resulting dose ratios are a function of coolant density and fuel burnup.
2. Determine the coolant density profile from the power profile and thermal hydraulic conditions
3. Interpolate the dose ratios for burnup and coolant density, and then use the linear heat generation rate to calculate the dose rate profile.

Bypass and Downcomer Dose Rates

The core bypass and downcomer dose rates were calculated similarly as for the pin cell calculations. A fixed source calculation was performed in MCNP. The core dimensions for the model were taken from BEAVRS. [104] To simplify the geometry, all of the regions were approximated as cylinders, and the cylindrical geometry was obtained by conserving the mass of each region. The core was treated as a homogenous mixture of fuel, clad, and water. There is assumed to be negligible change in coolant density in the downcomer and core bypass. The effect of burnup was also neglected, instead the core average was modeled at 40 MWd/kgU. Cases were run at 0 ppm B, 1000 ppm B and 2000 ppm B. The full core linear heat generation rate was used in these calculations to scale the dose rates.

The model and dimensions are given in Figure 4-5 and Table 4-7.

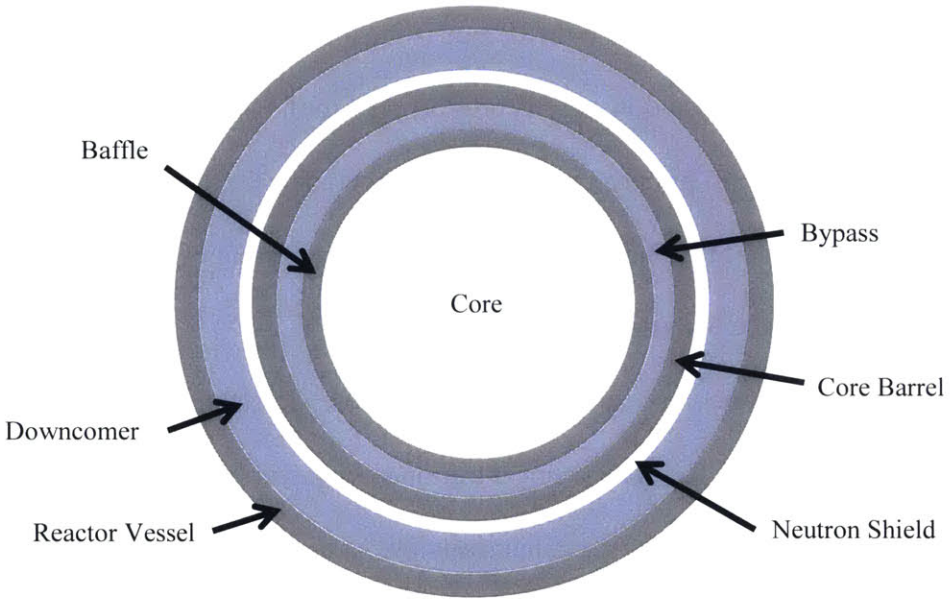

Figure 4-5. MCNP Model for Downcomer and Bypass Dose Calculations

Table 4-7. MCNP Model Parameters for Downcomer and Bypass Dose Calculations

Part	Outer Radius [cm]	Material	Density (g/cc)
Core	168.545	Mix of Fuel, water, clad	7.25
Baffle	170.767	Steel	8.03
Bypass	187.96	Water + boron	0.737
Barrel	193.675	Steel	8.03
Neutron Shield	194.16	Steel	8.03
Downcomer	230.00	Water + boron	0.737
Reactor Vessel	251.9	steel	8.03

Results of Dose Profile Calculations

The dose rates were calculated for each region: the average core, the hot pin, the high burnup pin, the bypass, and the downcomer. A few select plots highlighting trends in the dose rates are presented in this section.

Figure 4-6 shows the dose rates at beginning of cycle in each of the core sections modeled. In all three plots, the dose rates are greatest for the hot pin, because of the higher linear heat generation rate. The difference is most pronounced for the alpha dose, as would be expected, since the dose rate is proportional to the thermal neutron flux. The dose rates at the high burnup pin are greater than the average core, because the dose to linear heat generation rate ratio increases with burnup. The burnup effects outweigh the decrease in dose due to the lower power.

Figure 4-7 shows the dose rates in the average core, at each point in the cycle. The alpha dose rates decrease as the boron concentration is lowered. At peak boron, the alpha dose rate is the greatest. The gamma and neutron dose rates do not change significantly with time. The dose rate profile shifts to become top-heavy in as the cycle progresses, from the change in power shape. Additionally, it can be seen that the maximum dose rate increases slightly as the cycle progresses.

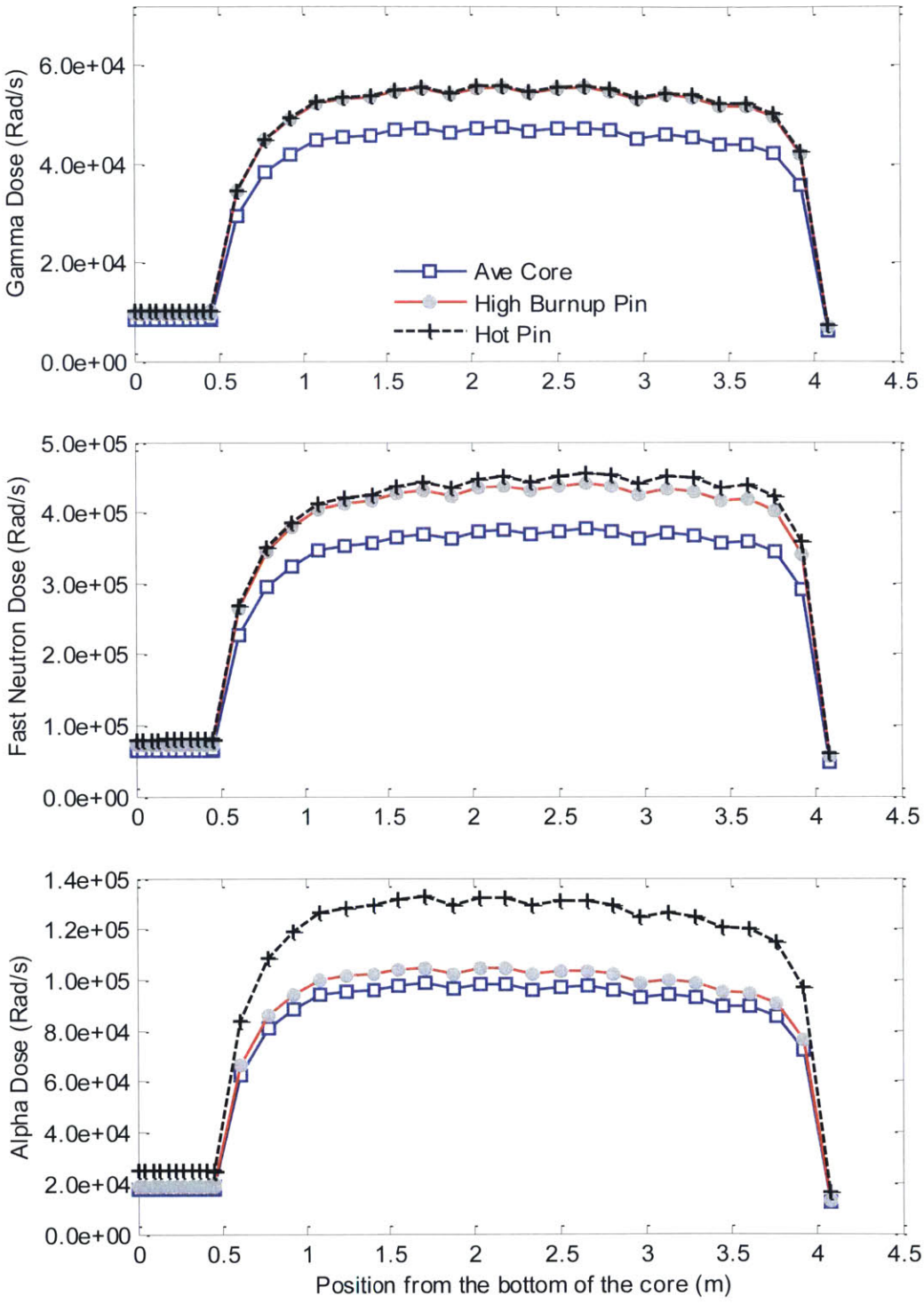

Figure 4-6. Dose rates in the core at the beginning of cycle

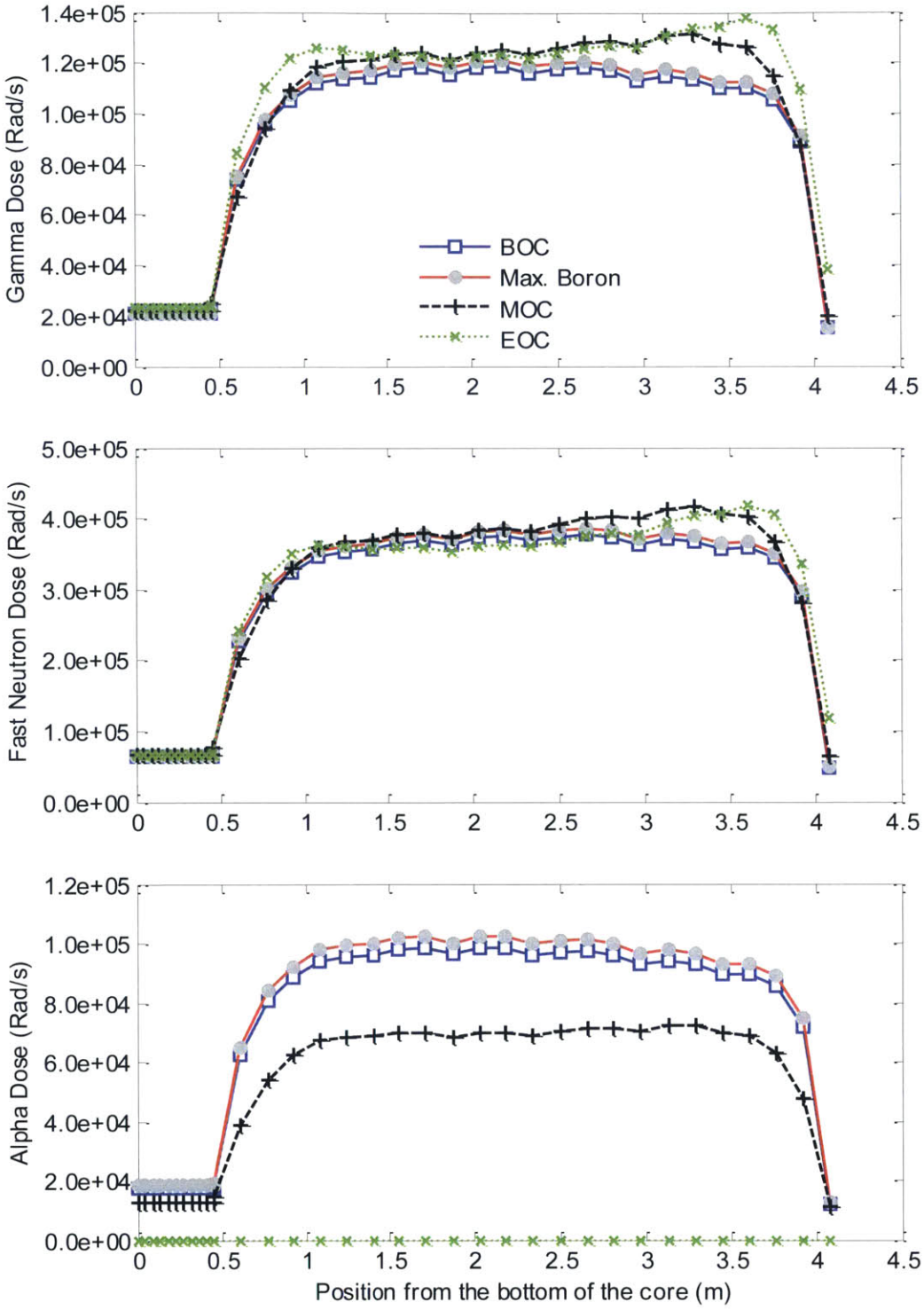

Figure 4-7. Dose rates in the "averaged" core

The average dose rates in the active core region, bypass, and downcomer are listed in Figure 4-7. The dose rates in the core bypass and downcomer are orders of magnitude smaller than dose rates in the core. The average gamma dose increases throughout the cycle. In the bypass and downcomer the alpha dose is higher than the fast neutron dose, while in the core (the fuel) the fast neutron dose is greater. The alpha dose decreases significantly between the peak boron addition and the middle of cycle.

Table 4-8. Axially-averaged dose rates in a PWR core

Cycle Point	Region	Gamma Dose Rate (Rad/s)	Fast Neutron Dose Rate (Rad/s)	Alpha Dose Rate (Rad/s)
BOC	Average	1.03E+05	3.26E+05	8.51E+04
	Hot Pin	1.21E+05	3.93E+05	1.14E+05
	Twice Burnt Pin	1.20E+05	3.80E+05	9.04E+04
	Core Bypass	6.19E+02	5.27E+02	1.03E+03
	Downcomer	3.54E+01	1.09E+01	1.64E+01
Max Boron	Average	1.05E+05	3.33E+05	8.85E+04
	Hot Pin	1.27E+05	4.10E+05	1.18E+05
	Twice Burnt Pin	1.16E+05	3.67E+05	8.93E+04
	Core Bypass	6.16E+02	5.27E+02	1.05E+03
	Downcomer	3.52E+01	1.09E+01	1.66E+01
MOC	Average	1.10E+05	3.42E+05	6.17E+04
	Hot Pin	1.30E+05	4.10E+05	7.75E+04
	Twice Burnt Pin	1.22E+05	3.76E+05	6.25E+04
	Core Bypass	6.46E+02	5.28E+02	8.98E+02
	Downcomer	3.72E+01	1.09E+01	1.43E+01
EOC	Average	1.16E+05	3.42E+05	0
	Hot Pin	1.45E+05	4.36E+05	0
	Twice Burnt Pin	1.31E+05	3.88E+05	0
	Core Bypass	8.67E+02	5.27E+02	0
	Downcomer	5.54E+01	1.09E+01	0

The computed dose values are compared to other values from the literature in Table 4-9. The MNCP results are slightly lower than the values from the literature, but overall there is good agreement.

Table 4-9. Core dose rates compared to values from the literature

Plant	Gamma Dose [Rad/s]	Fast Neutron Dose [Rad/s]	Boron Concentration [ppm]	Alpha Dose [Rad/s]
Ringhals [102]	1.45E+05	4.85E+05	800	3.13E+05
Tsuruga-2 [105]	1.50E+05	5.00E+05	-	-
Model: PWR-ECP [83]	2.86E+05	5.14E+05	840	3.17E+04
Calculated with MCNP (average dose in average core)	1.10E+05	3.42E+05	1000	6.17E+04

4.2 PWR Model Results

In this section, the results from the newly developed PWR radiolysis models are presented. Preliminary calculations indicated that the RADICAL g-values and reaction set overpredict the hydrogen peroxide concentration: calculated values were near 20-30 ppb, whereas EPRI reports peroxide concentrations in the range of 5 ppb. [11] Therefore only the AECL reaction set along with Christensen's g-values were used.

4.2.1 Burnup and Power Effects: The "Averaged" Core vs Single Channel Chemistry

Figure 4-8 shows the chemistry at the beginning of cycle with 25 scc H_2/kg H_2O addition. Figure 4-9 and Figure 4-10 show the corresponding temperature profile and

ECP. At the entrance to the core, the concentration of hydrogen peroxide increases by a factor of nearly 100, from 0.02 ppb to 2 ppb. The oxygen concentration increases from approximately $2x10^{-4}$ ppb to $1x10^{-3}$ ppb, while the hydrogen concentration is virtually unchanged. At the entrance to the active core region (0.45 m), the dose increases dramatically. Consequently, the concentrations of peroxide and oxygen both jump, and at higher elevations increase nearly linearly. Near the end of the core, these concentrations start to decrease, as the dose has decreased dramatically. Thus, the production rate of O_2 and H_2O_2 from radiolysis has decreased, and water recombination dominates over the decomposition.

The hot pin has the highest concentration of radiolysis products, as the dose rates are highest for the hot pin (see Figure 4-6). There may also be temperature effects: the higher temperature means that the rate constants for the water reactions will be different. The concentrations are nearly identical for the high burnup pin and the average core, with the high burnup pin having slightly higher concentrations of oxidizing species. The average and high burnup channel have essentially the same temperature, meaning there should be little difference in the reaction rates, so this particular difference can be attributed to the higher dose rates at the high burnup pin.

The ECP rapidly increases at the entrance to the core, from -737 mV SHE (which is slightly above the hydrogen line) to 610 mV SHE. This increase coincides with the increase of peroxide. The ECP reaches a maximum at 0.92 m, and subsequently decreases along the channel. The decrease in ECP is due to the rising temperature, which shifts the equilibrium potentials in a more negative direction.

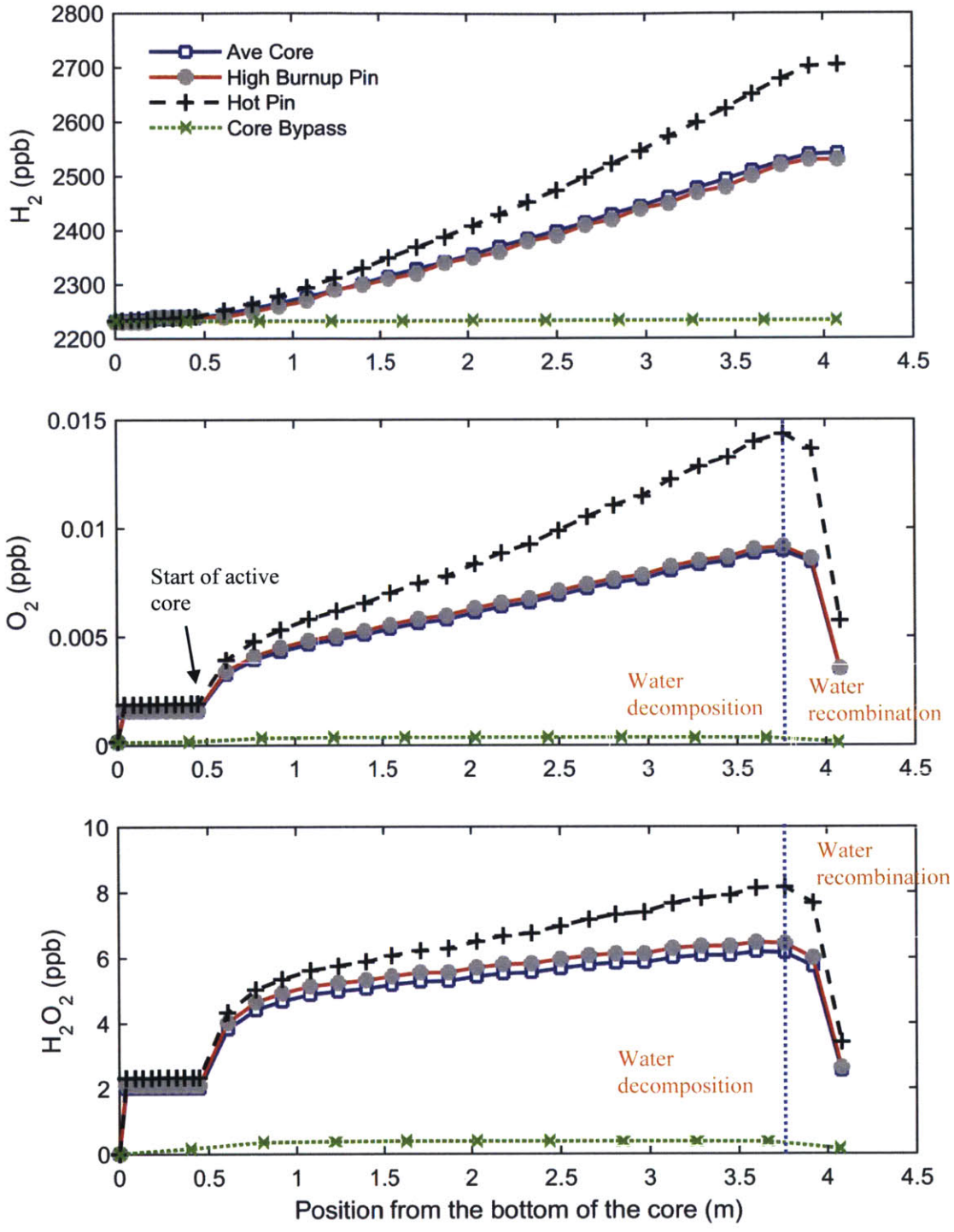

Figure 4-8. Calculated H_2 (top), O_2, and H_2O_2 concentrations in a PWR core at BOC

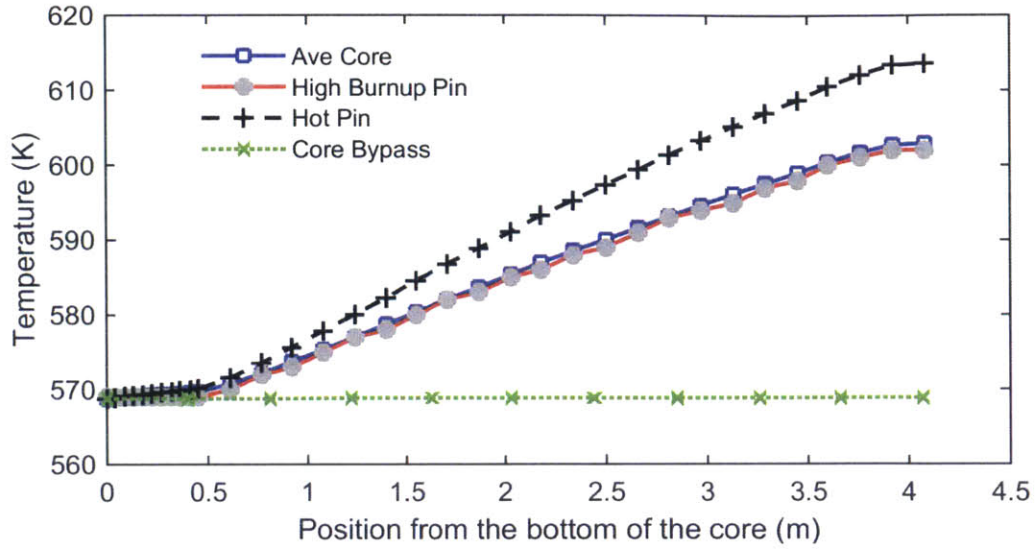

Figure 4-9. Coolant temperature in the core at BOC

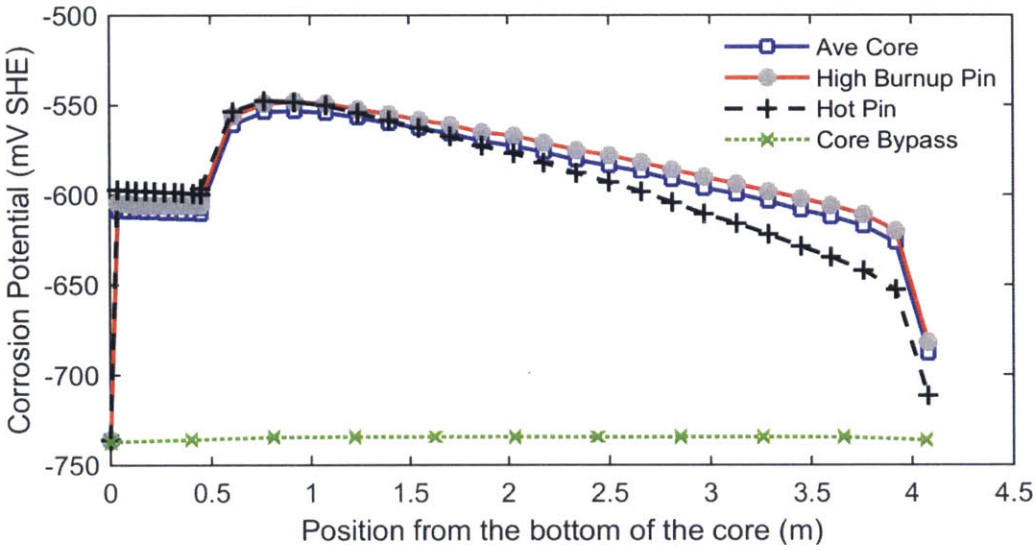

Figure 4-10. Corrosion potential in the core at BOC

Polarization (Evans) diagrams for the average channel at 0.92 m and at 3.45 m and the hot pin at 3.45m are shown in Figure 4-11 below. At higher temperature the equilibrium potentials become more negative. An increase in hydrogen peroxide and

oxygen concentrations will shift their respective potentials to a more positive voltage. However, in these cases the temperature effect dominates over the concentration effects. As the concentrations of species increase, the exchange current densities and limiting currents become larger. In all cases, the ECP occurs where the H_2O_2 and H_2 currents balance each other. The oxygen current is too small to affect the ECP.

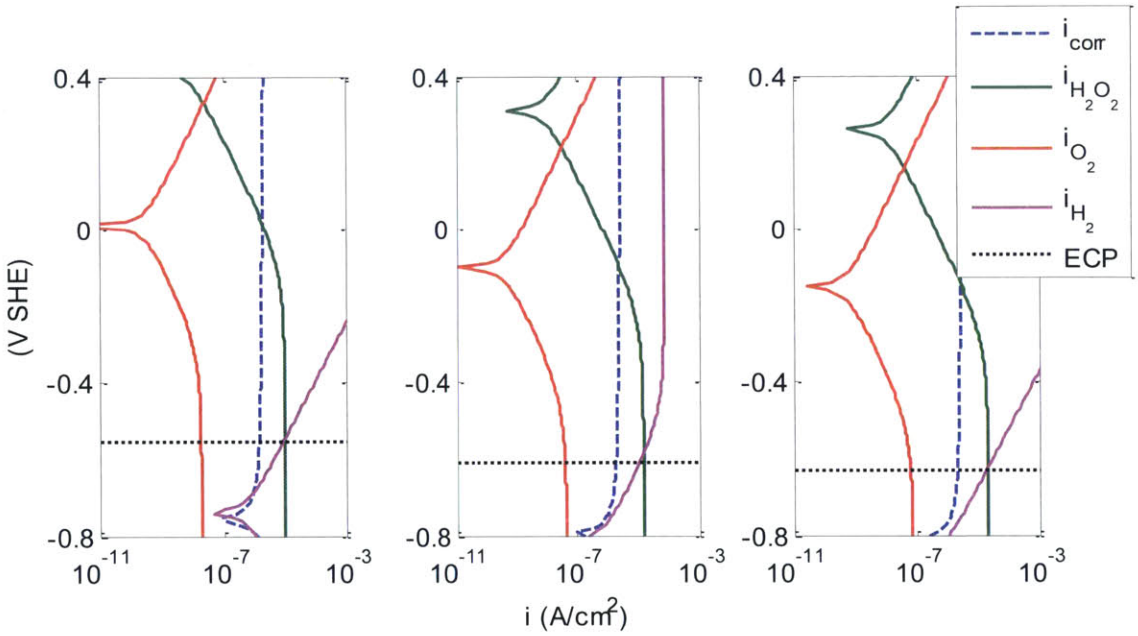

Figure 4-11. Evans diagrams for the average core at 0.92m (Left), the average core at 3.45m (Center), and the hot pin at 3.45 m (Right)

4.2.2 Cycle Effects: Boron Concentration

Figure 4-12 shows the water chemistry in the average core throughout the cycle. The concentrations of oxygen and hydrogen peroxide increase from the beginning of cycle to the time of peak boron concentration, and decrease until the end of cycle. As to be expected, these concentrations follow the alpha dose rate; however, the hydrogen concentration remains virtually unchanged. These changes in concentration of the oxidizing species cause the ECP to become more negative, as shown in Figure 4-13.

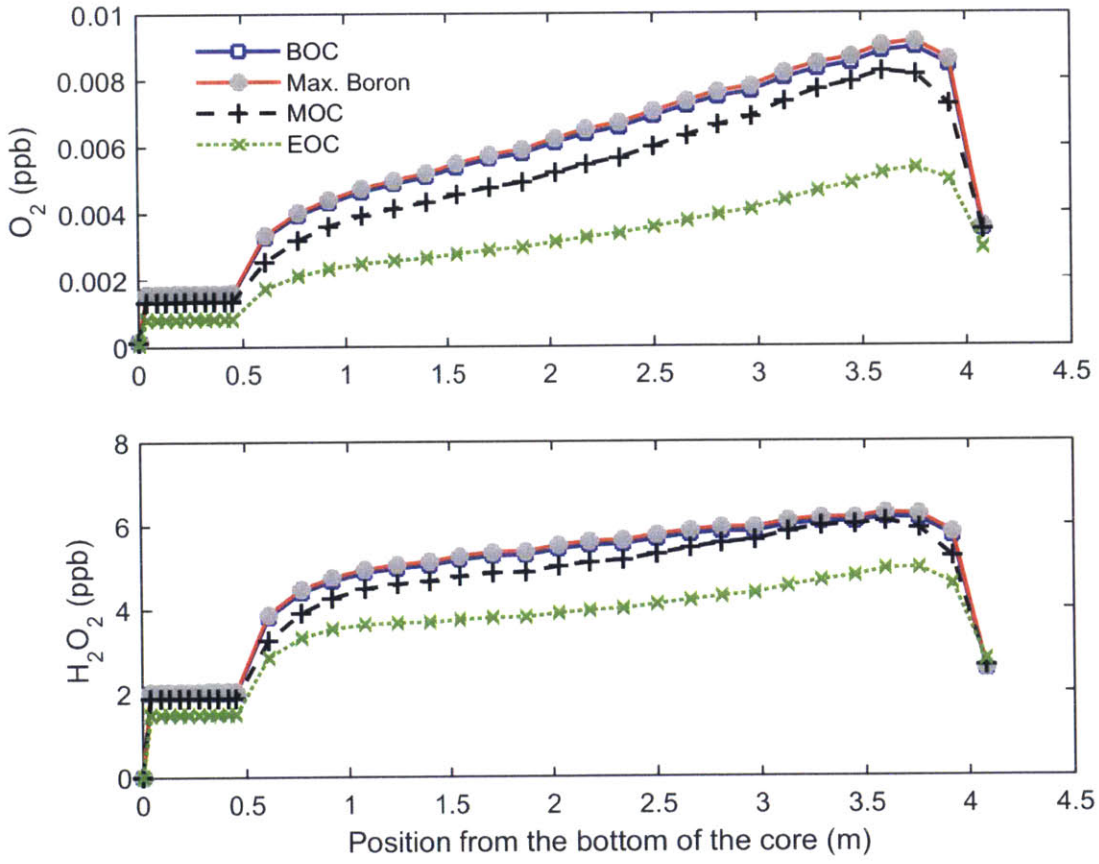

Figure 4-12. Calculated O_2 (middle) and H_2O_2 (bottom) concentrations in the "averaged" core of a PWR

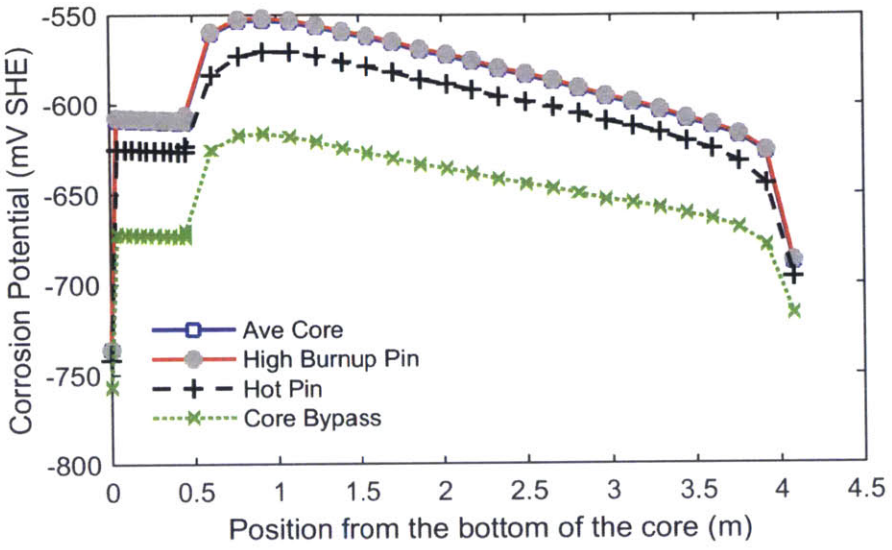

Figure 4-13. ECP in the "averaged" core of a PWR

The average (in the active core), and maximum O_2, H_2O_2 and ECP are given in Table 4-10. Both the average and maximum concentrations increase and decrease with boron concentration.

Table 4-10. Maximum and Average O_2, H_2O_2 and ECP in the average core

	Max O_2 (ppb)	**Average O_2 (ppb)**	**Max H_2O_2 (ppb)**	**Average H_2O_2 (ppb)**	**Max ECP (mV SHE)**
BOC	0.00896	0.00614	6.19	5.17	-553
Max. Boron	0.00914	0.00627	6.28	5.25	-552
MOC	0.00823	0.00540	6.09	4.86	-571
EOC	0.00534	0.00337	4.98	3.91	-616

4.3 Effects of H_2 addition and Fe and Ni impurities on Water Chemistry

The effect of increasing the hydrogen injection is to reduce the oxygen and hydrogen peroxide concentration, and drive down the ECP. Two cases at the time of maximum boron concentration with 37.5 and 50 cc STP H_2/kg H_2O were run. Table 4-11 compares oxygen and hydrogen peroxide concentrations for these different hydrogen injections.

Iron and nickel both interact with radiolysis products to slow the recombination of water molecules. According to the EPRI PWR Primary Water Chemistry Guidelines, [11] the solubility of iron in the at coolant temperatures in the core is between 4.6 and 6.4 ppb, depending on the local temperature and pH. The solubility of nickel is from 0.35 to 0.8 ppb. The Notre Dame Iron and Nickel reaction sets were used to incorporate iron and nickel into the radiolysis model. [77] The reaction set and rate constants are listed in Table B-6 on page 314. Two cases were run at the time of peak boron (2.5 MWd/kgU cycle burnup and 1486 ppm boron), with 25 scc H_2/kg H_2O. A summary of the results from the addition of impurities is in Table 4-11. The presence of Ni and Fe increase the concentration of hydrogen peroxide and the ECP slightly. However, at the concentrations of Fe and Ni that would be soluble in the coolant, the effect is very small, less than 1 mV SHE on the ECP.

Table 4-11. Water Chemistry in the Averaged Core at Peak boron addition, with variable H_2 addition and Fe, Ni impurities

H_2 addition (cc STP H_2/kg H_2O)	Fe, Ni	Max O_2 (ppb)	Ave. O_2 (ppb)	Max H_2O_2 (ppb)	Ave. H_2O_2 (ppb)	Max ECP (mV SHE)
25	None	0.00914	0.00627	6.28	5.25	-552
37.5	None	0.00584	0.00405	6.08	5.11	-576
50	None	0.00429	0.00299	5.97	5.05	-593
25	4.5 ppb Fe 0.03 Ni	0.00914	0.00627	6.29	5.25	-552
25	9 ppb Fe 0.1 Ni	0.00917	0.00628	6.35	5.30	-552

4.4 Chapter Summary

This chapter documents the development of a detailed radiolysis model of the primary loop in a PWR. MCNP was used to calculate coolant dose rates in the core for various boron concentrations, fuel burnups, and power. Dose rates tend to increase with fuel burnup and the linear heat generation of the fuel. Dose rates were also calculated for the downcomer and core bypass, and they were significantly smaller than core dose rates.

The radiolysis calculations showed that hydrogen peroxide and oxygen concentrations decrease with boron concentrations. Single channel analysis of the hot pin showed that the concentrations of oxidizing species are higher at the hot pin than in the average core, however the higher temperature lowered the ECP calculated with the mixed potential model. Single channel analysis of a twice burned pin showed there was minimal difference from the averaged core.

Chapter 5: Water Chemistry in a PWR with CRUD

This chapter describes the development of a PWR primary loop chemistry model with CRUD in the core. First, we determine the effects of CRUD on the dose rates to both the bulk coolant and the coolant that may be within deposits. These dose rates are then incorporate into a radiolysis model to study water chemistry in a PWR with CRUD. The crudded core model is an extension of the PWR radiolysis model presented in Chapter 4.

CRUD deposits in PWRs can have multiple effects on neutronics, thermal hydraulics and coolant chemistry. In general, the deposits raises the temperature at the cladding outer surface. The combined conditions of a CRUD layer with boiling and boron addition to the coolant, boron (as well as lithium) can become enriched in the deposit, which is often referred to as boron hideout. High concentrations of boron can suppress the neutron flux and power in the top of the reactor causing an Axial Offset Anomaly (AOA). Additionally, if the solubility of boron is exceeded in CRUD, then boron will precipitate out. The presence of a CRUD layer raises the surface the temperature at the outer surface of the cladding. With boron and lithium enrichment, boiling, and radiolysis, the local chemistry can become quite different from the bulk. Between altered local chemistry and higher temperatures, CRUD can accelerate corrosion of the cladding.

There has been recent interest in understanding the changes produced by CRUD: researchers have produced models to predict CRUD deposition rates and to understand the thermal hydraulics, and boron behavior, and chemistry within this layer. [13,106,107]

The models for chemistry within CRUD deposits require concentrations from the bulk coolant. To our knowledge, there have been no radiolysis and water chemistry models that consider the effects of CRUD. Thus, the model developed in this work can (1) provide more realistic information and boundary conditions (2) determine what conditions, such as deposit thickness, boron concentration, and axial offset are likely to cause significant changes to these chemistry boundary conditions.

5.1 Model Description

In general, maximum CRUD deposits occur on the top of the core, where subcooled boiling occurs. For this model, it is assumed that the core contains CRUD deposits on the top 1/3 of the active fuel and that 30% of the fuel pins are covered in CRUD. The geometry and flow rates are identical to the clean core model. The core is divided into: the hot pin, a once-burned pin, a twice burned pin, and the "averaged" core, as shown in Figure 5-1.

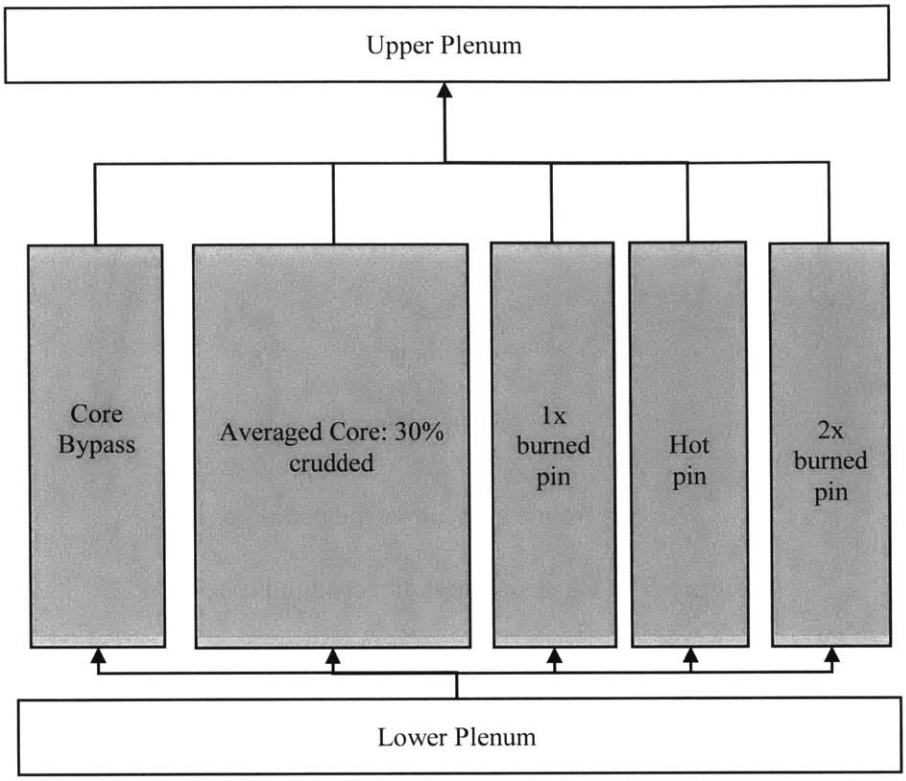

Figure 5-1. Core region for the crudded PWR radical model

For the crudded core model, the total core power is the same as the clean core model (3587 MWth). However, the axial power distribution is changed to reflect the presence of an AOA. Figure 5-2 shows the power shapes for the crudded core at the beginning of cycle (BOC), middle of cycle (MOC), and end of cycle (EOC). Comparing the three power shapes, the MOC axial power distribution is most heavily shifted to the bottom of the core, and the shape at EOC is the least offset. This likely occurs because at the end of cycle, there is very little, if any, boron injected into the coolant. [14]

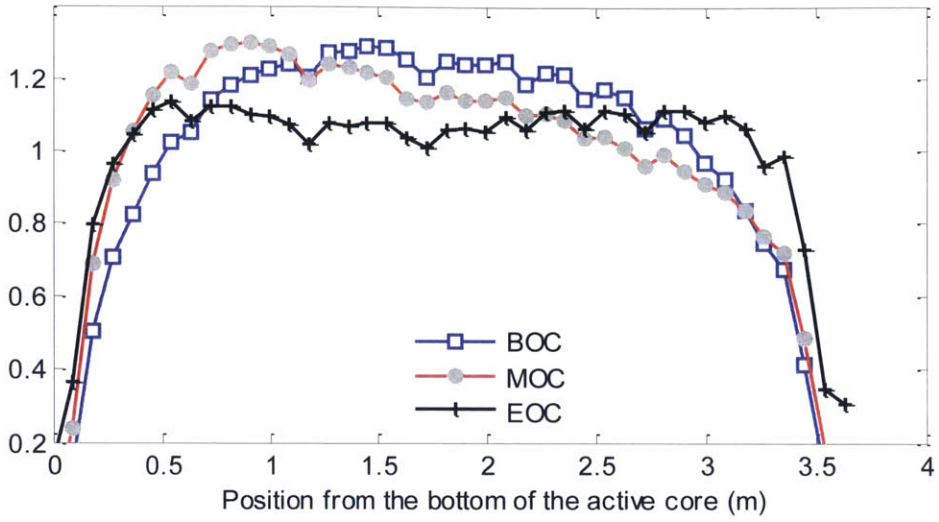

Figure 5-2. Power shapes for crudded core [14]

For this model, it is assumed that the crudded region is 50% coolant by volume. The assumed composition of the solid CRUD is listed in Table 5-1. [13] The confined coolant in the CRUD is assumed to have a void fraction of 0.05.

Table 5-1. Composition of Solid CRUD [13]

Species	Volume Fraction	Density (g/cc)
NiO	0.15	5.33
Fe_3O_4	0.1	8.9
$NiFe_2O_4$	0.75	5.17

The boron concentration in the CRUD was calculated by using the following equation for the concentration profile of boron as a function of crud thickness: [12]

$$C(x) = C_o \exp\left[\frac{q''(\delta - x)}{h_{fg}\rho_f \phi D_B}\right] \tag{5-1}$$

Where

C_o is the boron concentration in the bulk coolant

δ is the crud thickness (m)

$D_b = 0.0533 \times 10^{-6}\ m^2/s$ is the molecular diffusivity of boron in water

q'' is the heat flux (kW/m^2)

$h_{fg} = 966.2\ kJ/kg$ is the latent heat of evaporation

$\rho_f = 703\ kg/m^3$ is the density of the coolant

$\phi = 0.5$ is the porosity

For the MCNP calculations, the concentration of boron in the CRUD is assumed to be constant over each fuel pin. Therefore, the average linear heat generation rate was used. The average boron concentration is calculated as:

$$\bar{C} = C_o \frac{h_{fg}\rho_f \phi D_B}{q''\delta}\left\{\exp\left[\frac{q''(\delta - x)}{h_{fg}\rho_f \phi D_B}\right] - 1\right\} \tag{5-2}$$

The boron concentrations in CRUD are calculated using Equation (5-2). Table 5-2 lists the calculated boron concentrations at the beginning of cycle, for CRUD thickness of 12.5, 25, 50, and 75 μm. Table 5-3 lists the boron concentrations at the middle of cycle for a 75 μm CRUD layer. The boron concentration in CRUD at the end of cycle will be zero. Table 5-4 lists the burnup and the linear power at the end of cycle.

Table 5-2. Boron concentration in crudded fuel at the beginning of cycle. Boron concentration in the bulk coolant is 1440 ppm.

	Burnup (MWd/kgU)	Linear Power (kW/m)	Boron concentration (ppm)			
			12.5 μm	25 μm	50 μm	75 μm
Fresh pin	0.1	25.97	No crud			
1x burnt	19.47	24.75	1968	2767	5930	13913
2x burnt	38.94	18.75	1819	2337	4046	7422
Ave. core	15.62	19.03	1826	2355	4117	7636

Table 5-3. Boron concentration in crudded fuel (75 μm) in the middle of cycle. The bulk coolant has 1000 ppm boron.

	Burnup (MWd/kgU)	Linear Power (kW/m)	Boron Concentration (ppm)
Fresh pin	10	26.28	11411
1x burnt	29.47	21.12	6574
2x burnt	48.94	17.81	4689
Ave. core	25.58	19.03	5303

Table 5-4. Burnup and linear power for crudded fuel at the end of cycle.

	Burnup (MWd/kgU)	Linear Power (kW/m)
Fresh pin	19.47	25.30
1x burnt	38.94	20.78
2x burnt	58.41	17.89
Ave. core	35.05	19.03

5.2 Dose Calculations

The dose rates were calculated using MCNP. The procedure was the same as for the clean fuel core, which is discussed in Section 4.1.2. A schematic of the MCNP model for crudded fuel is given in Figure 5-3.

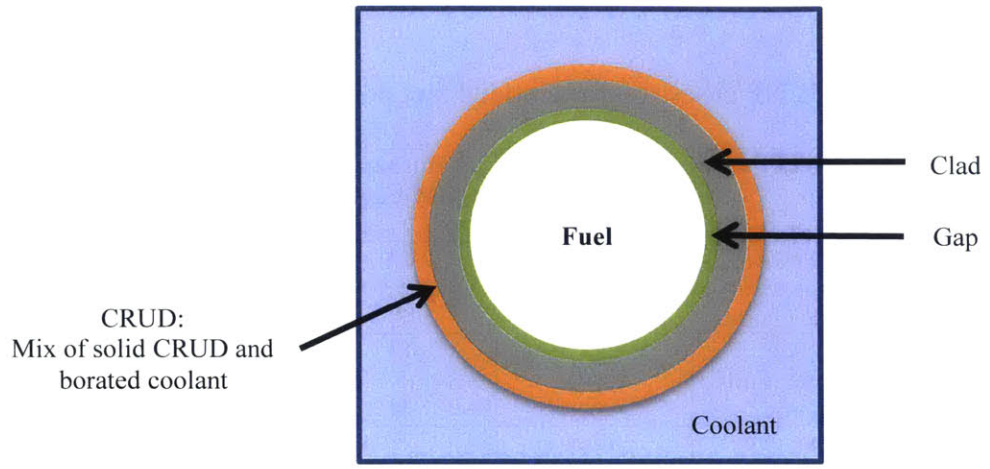

Figure 5-3. The crudded fuel rod unit cell used in MCNP calculations

For the crudded fuel, the bulk coolant density, the fuel composition, and the bulk coolant boron concentration all vary, just like for the clean fuel. In addition, the CRUD thickness and boron concentration in the confined coolant also vary. These additional variables greatly increased the required number of MCNP calculations. The bottom 2/3 of the fuel does not have CRUD, so the dose ratios for clean fuel can be used for part of the fuel. The number of MCNP calculations with CRUD can be reduced by determining the range of densities in the top 1/3 of the core for each different case (averaged core, hot pin, once burned pin and twice burned pin).

Full calculations were made for the beginning of cycle cases with 50 and 75 μm CRUD layers and the end of cycle case with a 75 μm CRUD layer. The bulk coolant

densities were varied by 0.0148 g/cc, as done for the clean fuel calculations. Additional cases were run at a fixed coolant density and burnup to better understand the effect of crud thickness and boron content in the bulk and confined coolant. A summary of all MCNP cases run is listed in Table 5-5.

Table 5-5. MCNP cases run for crudded fuel dose calculations.

	Fuel Pins	**Crud thickness (μm)**	**Burnup (MWd/kgU)**	**Coolant density (g/cc)**
Beginning of cycle	Average Once burnt Twice burnt	50 75	0.1 5 40	0.6036-0.6777
End of cycle	All (there is no boron)	75	0.1 5 40	0.6036-0.6925
Beginning of cycle	Average	12.5 25	5	0.6629
Middle of Cycle	Average Hot Once burnt Twice burnt	75	5	0.6629

To solve for the dose rate to the bulk coolant, the ratios of dose to linear heat generation were calculated from the MCNP output. The dose rate was then computed by interpolating for burnup and density, and multiplying by the linear power. The dose ratios from Chapter 4 were used for the bottom 2/3 of the core, and the CRUD dose ratios were used for the sections that have CRUD.

Determining the dose to the confined coolant in the CRUD is more complicated. MCNP can be used to determine the energy deposited to the homogenized CRUD region. However, this energy will be split between the solid CRUD and the confined coolant. There may be mechanisms of energy transfer between the solid and absorbed coolant that

are dependent on the structure of the solid and the solid/coolant interface and cannot be directly accounted for in the MCNP calculations.

The dose to the confined coolant can be calculated as:

$$Dose_{Cool\ in\ Crud}\left[\frac{MeV}{g\ H_2O}\right] = Dose_{Crud,MCNP} \times w_{cool} \times f_{cool} \tag{5-3}$$

Where

$Dose_{Crud,MCNP}$ is the calculated dose from MCNP

w_{cool} is the mass fraction of the coolant in the crud mixture, 0.088 in this work

f_{cool} is the fraction of the energy deposited in the CRUD that is absorbed by the coolant

The partitioning of the fast neutron dose and the gamma dose can estimated by using flux tallies for neutron and gamma heating in the CRUD volume.

$$Heating\left[\frac{MeV}{cc\ CRUD\ volume}\right] = N\int \Phi(E)\sigma_T(E)H(E)dE \tag{5-4}$$

Where

N is the atom density of the coolant or solid CRUD (atoms/cm-barn)

$\Phi(E)$ is the fluence (particles/cm^2)

$\sigma_T(E)$ is the total microscopic cross section (barns)

$H(E)$ is the heating (MeV/collision)

In Chapter 4, the alpha dose to the bulk coolant was calculated by using the thermal neutron flux to determine the reaction rate of the ^{10}B(n,α) reaction. The same procedure can be used to calculate the total alpha dose rate in the CRUD region,

assuming that the alpha particle range in the CRUD is small in comparison to the CRUD thickness. Figure 5-4 shows the liquid water, iron, and oxygen stopping powers for alpha particles. The stopping powers are the average energy loss per unit path length. Assuming that the stopping powers are additive, the energy partition can be estimated from the CRUD density and composition and the individual stopping powers.

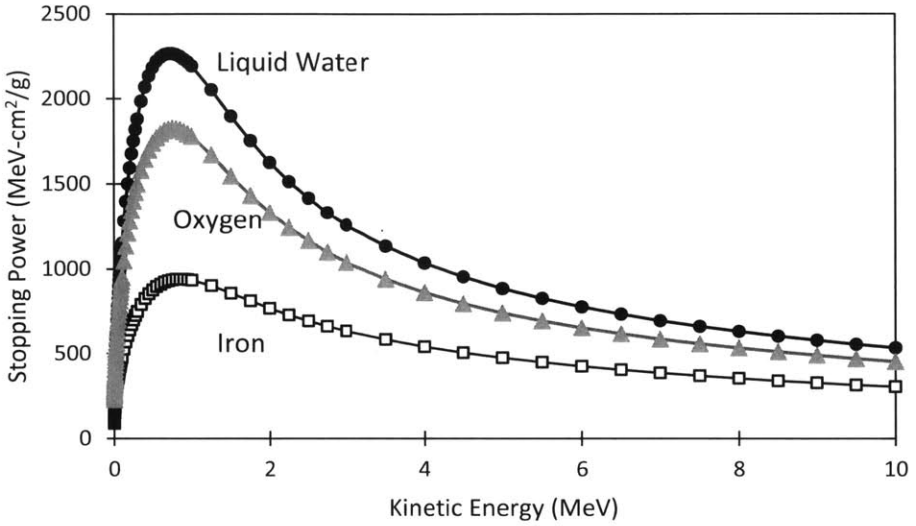

Figure 5-4. Liquid water, iron, and oxygen stopping powers of alpha particles [108]

5.2.1 Dose-to-Power Ratios for Crudded Fuel

In this section, we compare the dose ratios for both bulk and confined coolant can to the corresponding clean fuel dose ratios (same coolant density, bulk boron concentration, and burnup). For simplicity, we will look at the percent change in the dose ratios. The percent change was found to be independent of fuel burnup, and the bulk coolant density. Table 5-6 shows the percent increase in dose to the bulk coolant.

The change in dose (gamma, fast neutron, and alpha) to the *bulk coolant*, does not vary significantly with crud thickness, bulk coolant boron, and crud boron content. The increase in gamma dose to the bulk coolant is approximately 21%, the increase in fast neutron dose is 21-22%, and the increase in alpha dose is 21%. There is a slight variation in the increase of fast neutron dose with crud thickness, but it is within 2%. For the bulk, the change in dose is approximately the same for all three types of radiation, unlike the confined coolant.

Table 5-6. Percent increase of dose to the bulk coolant in a PWR core with CRUD relative to a clean core

Case	B_{bulk} (ppm)	t_{crud} (μm)	B_{crud}/B_{bulk}	% increase in dose		
				γ	n	α
BOC, Avg	1440	12.5	1.268	21.2	21.4	21.2
BOC, Avg	1440	25	1.636	21.1	21.5	21.0
BOC, Avg	1440	50	2.859	21.2	21.8	21.0
BOC, once burnt	1440	50	4.118	21.1	21.9	21.0
BOC, twice burnt	1440	50	2.810	20.9	21.8	21.0
BOC, Avg	1440	75	5.303	21.2	22.4	20.9
BOC, once burnt	1440	75	9.662	21.3	22.8	20.8
BOC, twice burnt	1440	75	5.154	21.1	22.5	20.8
MOC, Avg	1000	75	5.303	21.2	22.3	20.6
MOC, once burnt	1000	75	6.574	21.3	22.4	20.6
MOC, twice burnt	1000	75	4.689	21.2	22.3	20.7
MOC, hot	1000	75	11.411	21.1	22.6	20.6
EOC (all)	0	75	-	21.2	22.2	-
Min				20.9	21.4	20.6
Max				21.3	22.8	21.2

MCNP calculations were performed using flux tallies to estimate the fraction of dose deposited to the confined coolant in the CRUD volume. Cases were run with 75 μm

CRUD layer, corresponding to the average core at beginning of cycle and end of cycle. Two fuel burnups were used: 0.1 and 40 MWd/kgU. Table 5-7 shows the calculated fraction of the gamma and fast neutron dose deposited in the confined coolant. From these results, it appears that the fraction of gamma dose is relatively constant with respect to fuel burnup and boron concentration in the CRUD and coolant. The fraction of neutron dose is slightly higher with boron in the CRUD and coolant, and there is minimal difference between 0.1 and 40 MWd/kgU burnup. The fraction of gamma energy deposited is relatively small at 9.5%. The coolant makes up 8.8% of the CRUD layer by mass, so the gamma stopping power per unit mass of water is slightly higher than that of CRUD. The relatively high fraction of neutron dose absorbed can be explained by the fact that light nuclei, especially hydrogen, are best at moderating neutrons.

Table 5-7. Fraction of the total neutron and gamma dose in CRUD layer deposited to confined coolant

Case	Boron in bulk coolant (ppm)	Boron in CRUD (ppm)	Burnup (MWd/kgU)	f_n	f_γ
BOC	1440	13913	0.1	0.81	0.094
BOC	1440	13913	40	0.80	0.094
EOC	0	0	0.1	0.77	0.095
EOC	0	0	40	0.77	0.095

The partition of alpha dose was estimated using the stopping powers shown in Figure 5-4. The stopping power (in MeV-cm^2/g) for nickel is assumed to be the same as for iron. The CRUD composition and densities outlined in Section 5.1 are used to weigh the atomic stopping powers. The total stopping power in the CRUD region, along with the contributions from water and the solid CRUD, is shown in Figure 5-5. Based on this

calculation, water makes up 24-28% of the total stopping power. While water has a high stopping power per unit mass, the majority of the CRUD layer by mass consists of solid CRUD.

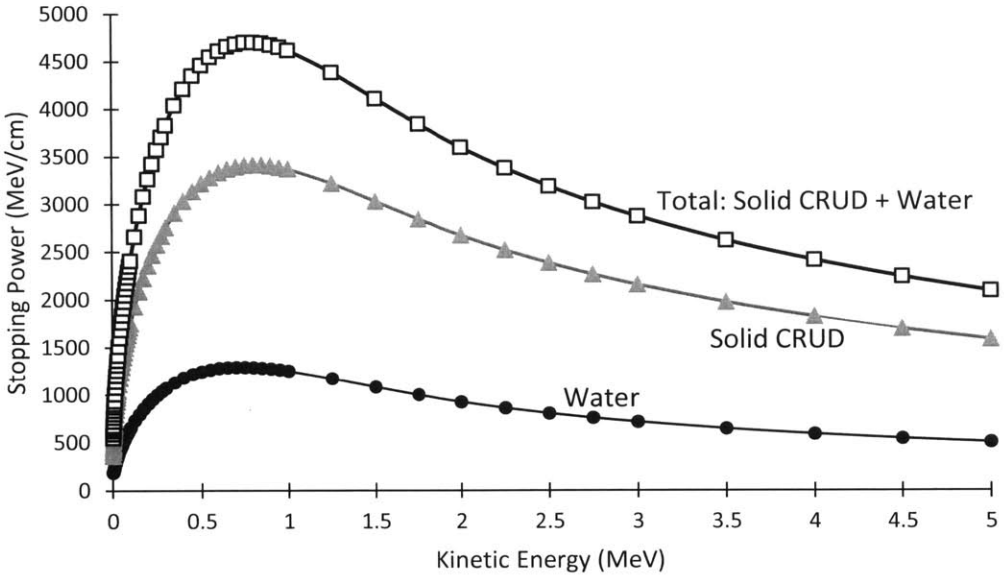

Figure 5-5. Estimated stopping power for alpha radiation in CRUD

Using the fractions calculated above: 0.095 for gamma, 0.8 for fast neutrons, and 0.25 for alphas, we compute the ratio of dose to linear heat generation rate ratio for the confined coolant. For simplicity, we compare results to the dose rates in a clean core, just as we did for the bulk coolant. The percent change in dose relative to the clean core doses are shown in Table 5-8. The change in gamma dose and neutron dose is independent of CRUD thickness and boron concentrations. Comparing these results to the bulk coolant dose at a fuel rod with CRUD (in Table 5-6), the gamma dose is the same in both cases. The neutron dose is slightly higher for the confined coolant, a 31-32% increase vs. 21-24%.

For alpha dose, the results vary with boron concentration in the CRUD. For the smallest boron concentrations in CRUD ($B_{crud}/B_{bulk} < 3$), the calculated dose to the confined coolant is smaller than that to the bulk coolant in the clean core case.

Table 5-8. Percent difference in dose to the confined coolant in a PWR core with CRUD compared to a clean core

Case	B_{bulk} (ppm)	t_{crud} (μm)	B_{crud}/B_{bulk}	% increase in dose		
				γ	n	α
BOC, Avg	1440	12.5	1.268	21.2	31.0	-63.2
BOC, Avg	1440	25	1.636	21.1	31.1	-52.6
BOC, Avg	1440	50	2.859	21.1	31.3	-17.3
BOC, once burnt	1440	50	4.118	21.0	31.2	19.1
BOC, twice burnt	1440	50	2.810	20.9	31.5	-19.0
BOC, Avg	1440	75	5.303	21.0	31.7	53.1
BOC, once burnt	1440	75	9.662	21.1	31.6	179
BOC, twice burnt	1440	75	5.154	21.0	32.0	48.5
MOC, Avg	1000	75	5.303	21.0	31.6	52.9
MOC, once burnt	1000	75	6.574	21.1	31.7	89.5
MOC, twice burnt	1000	75	4.689	21.1	31.8	35.3
MOC, hot	1000	75	11.411	21.1	31.6	229
EOC (all)	0	75		21.0	31.9	
Min				20.9	31.0	-63.2
Max				21.2	32.0	229.0

The increase in the alpha dose to the confined coolant increases linearly with the ratio of the CRUD boron concentration to the bulk coolant boron concentration, as shown in Figure 5-6. For comparison, alpha dose rates from differ different energy partitions have been included in Figure 5-6. For thick crud deposits with high boron

concentrations, 5-10% changes in the energy partition can have a non-negligible effect on the alpha dose.

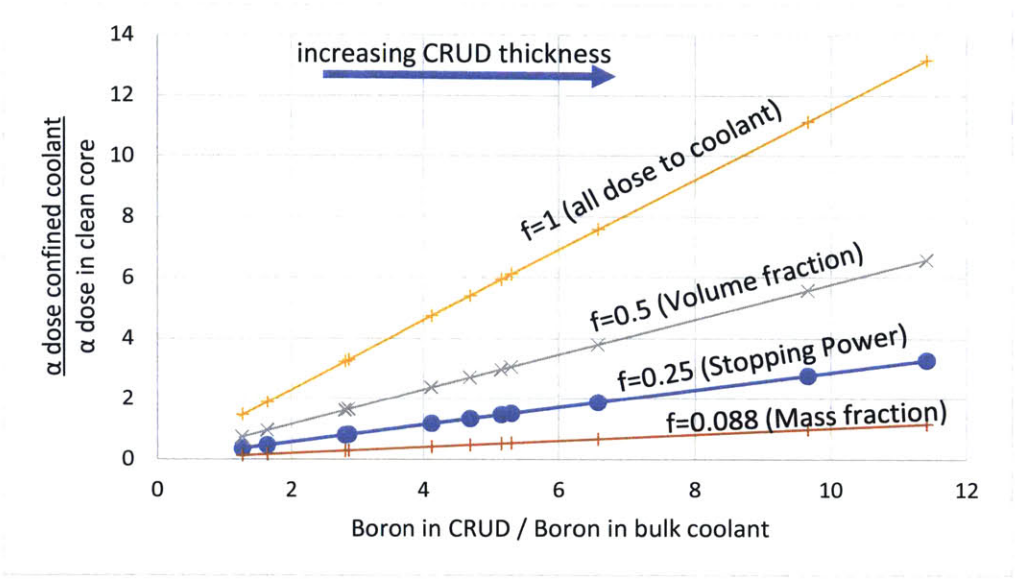

Figure 5-6. Ratio of alpha dose to confined coolant to dose for clean fuel. f is the fraction of the total alpha dose (energy) deposited to the CRUD region that is absorbed by the confined coolant.

The comparisons in this section show that it is possible to predict the dose rates to the bulk coolant and confined coolant for fuel with CRUD based on the clean fuel dose rates. This means that MCNP calculations for all permutations of boron concentrations in the CRUD and CRUD thickness are not necessary. The results presented in this section can be used to predict the dose rates, for cases with similar solid crud composition, porosity, and confined coolant density. For the dose rates to the confined coolant, there is some uncertainty in how the doses are distributed between the coolant and solid CRUD. MCNP was used to calculate the energy partition for gamma and neutron dose. For the

alpha dose, the stopping powers of the individual elements in CRUD were used to obtain a rough estimate of the energy partition. A more sophisticated model would be necessary to obtain a better estimate of alpha dose. This is important for predicting chemistry in CRUD deposits, as the radiolysis calculations in Chapter 4 have shown that hydrogen peroxide concentrations are sensitive to boron concentration and the alpha dose rate.

5.2.2 Dose Profiles

In the previous section, the dose rates to the bulk coolant were found to be independent of CRUD thickness, which means that only three RADICAL models will be necessary: one for BOC, MOC, and EOC. For simplicity, the bulk coolant dose rates calculated for a 75 μm CRUD layer will be shown. Figure 5-7 shows the dose rates at the beginning of cycle, Figure 5-8 shows the dose rates at the middle of cycle, and Figure 5-9 shows the dose rates at end of cycle. In all three models, the clean (or non-crudded) section of the fuel is from the bottom of the core to an elevation of 2.8 m. At the beginning of cycle, the dose rates are highest for the once-burned pin and at the middle and end of cycle, the dose rates are highest for the hot pin. Recall from Chapter 4, that dose rates increase with power and burnup. The burnup is consistently ~20 MWd/kgU greater for the once burned pin than the hot pin (see Table 5-2 to Table 5-4). At the beginning of cycle, there is a relatively small difference in the linear heat generation rate (LHGR) for the hot pin and once burnt pin (26 vs. 25 kW/m), whereas at MOC and EOC, the difference is substantial (25-26 vs. 21 kW/m).

In all plots, there is a marked increase in the dose rates at 2.8 m, which is where the CRUD layer starts. Note that at the beginning of cycle, the hot pin is clean, and the

dose rate profile lacks this sudden jump. The jump is more subtle for the average core, as 30% of the fuel has CRUD. In the previous section, we observed that the dose rate is approximately 21% greater for a fuel rod with CRUD compared to a clean fuel rod. Thus, for the average core, the increase in dose rate is approximately 6%.

Next, we can compare the effect of the different power shapes (shown in Figure 5-2) on the dose profiles. The axial offset is most negative at the middle of cycle, meaning that the power distribution is the most bottom heavy. Because dose rates are proportional to the linear heat generation rate and the AOA, there is less spread in dose rates for the fuel pins with CRUD at the top of the core compared to the bottom of the core at MOC. This is most noticeable in the alpha dose rates. For the end of cycle, the axial power distribution is flatter. The dose rates remains relatively level from 2.8 m to 3.5 m, and starts decaying at 3.5 m. In comparison, for BOC and MOC, the maximum dose is at the start of the CRUD layer, 2.8 m, and the dose decrease at higher elevations. The significance of dose profile shapes will become clearer when we examine the results from the radiolysis models.

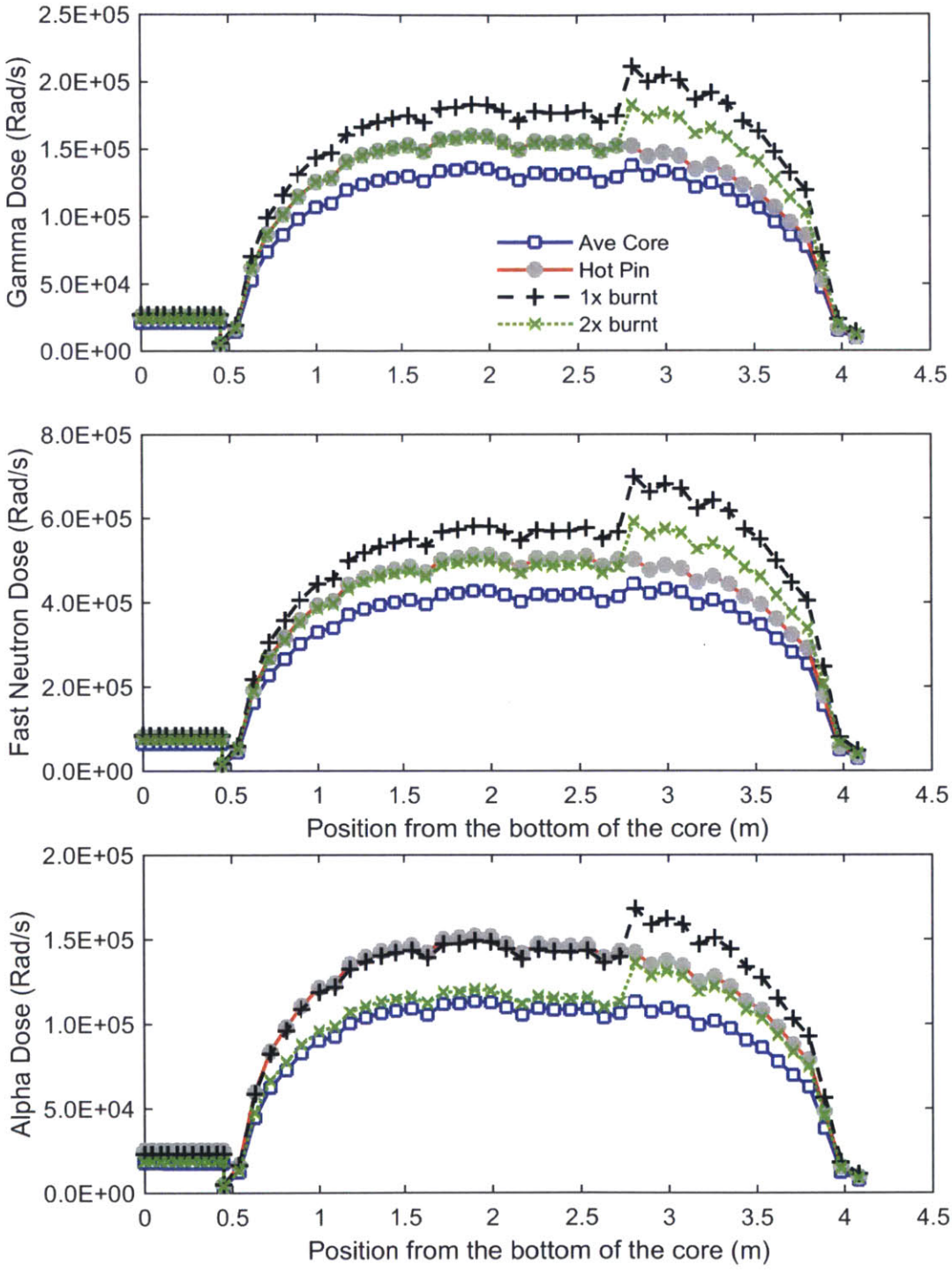

Figure 5-7. Dose rates to the bulk coolant in a PWR core with 75 μm CRUD at BOC

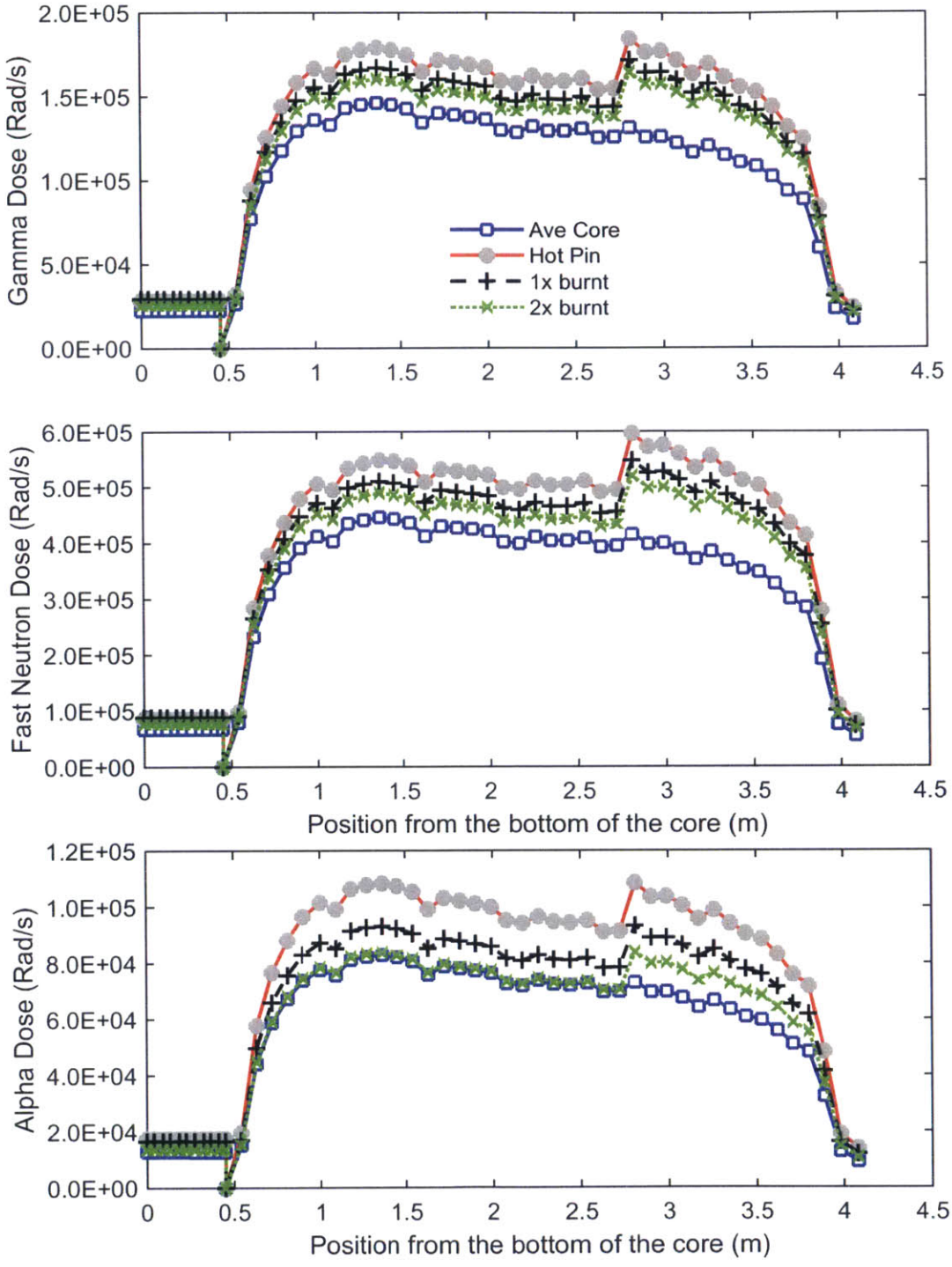

Figure 5-8. Dose rates to the bulk coolant in a PWR core with 75 μm CRUD at MOC

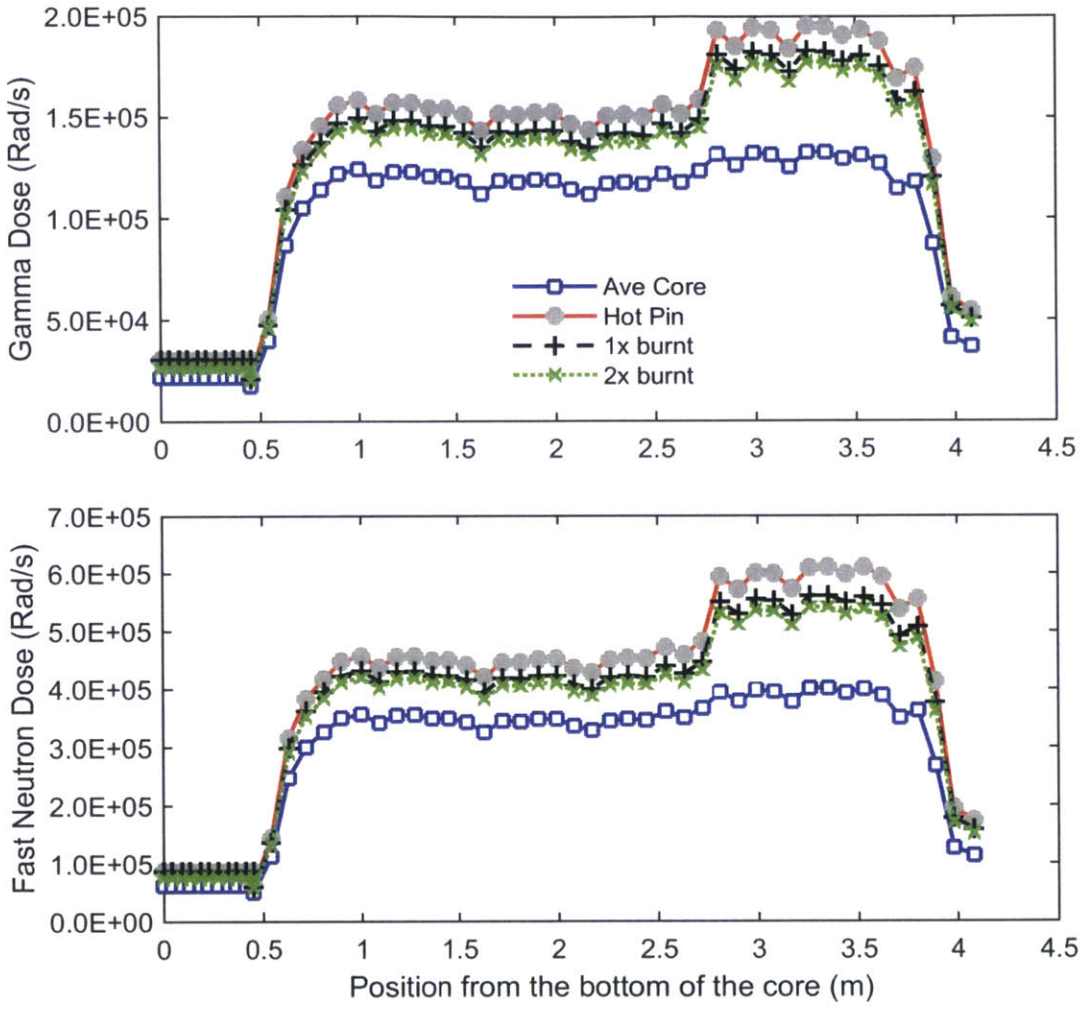

Figure 5-9. Dose rates to the bulk coolant in a PWR core with 75 μm CRUD at EOC

5.3 Water Chemistry in Crudded Core

The following subsections present the results from the RADICAL PWR crudded core models. For all simulations, the injected hydrogen was 25 scc H_2/kg H_2O (2.23 ppm), the same as the majority of simulations in Chapter 4. Typically values for

hydrogen concentrations are 25-50 scc H_2/kg H_2O. The effects of radiolysis, especially oxygen and hydrogen peroxide production are more pronounced with a lower hydrogen injection level. As in Chapter 4, the Type 304 SS ECP model without scaling factors (the "PWR" 304SS ECP model) was used to calculate the ECP.

Before examining the results from the radiolysis model, we must consider what exactly is calculated. RADICAL computes the chemistry averaged over a channel of interest. For the "averaged" core, the RADICAL results give the chemistry averaged over the flow area of the entire core. The individual fuel pin calculations give the calculated chemistry in the channel surrounding the fuel rod, as shown in Figure 5-3, assuming no mixing with the remainder of the coolant in core, and using the dose rates for a pin with CRUD. The results of these individual pin calculations will be a reasonable approximation for a fuel assembly where the pin powers are similar, and all the fuel is covered in CRUD. For the cases where only a few fuel rods in an assembly have CRUD, the coolant in a channel surrounding a pin with CRUD would likely fall between the pin-calculated chemistry and the averaged core chemistry.

It is important to recognize that the Mixed Potential Model, as implemented, does not calculate the ECP of fuel with CRUD. For crudded fuel, the chemistry at the CRUD/oxide interface is likely to be significantly different from the chemistry in the bulk coolant. Furthermore, the mass limited partial currents for the H_2, O_2, and H_2O_2 redox reactions in the Mixed Potential Model are for a case where mass transfer is limited by diffusion across a turbulent boundary layer. In fuel with CRUD, mass transfer will be limited by diffusion across the porous CRUD layer. Although the calculated ECP is thus

of limited value, it is useful for comparison to the ECP in a clean PWR core. Expected ECP behavior will be discussed later in this chapter.

5.3.1 Beginning of Cycle with 75 μm CRUD

Figure 5-10 shows the hydrogen, oxygen, and hydrogen peroxide in the bulk coolant for the BOC case with a 75 μm thick CRUD layer, and Figure 5-11 shows the corresponding ECP. The dotted lines on the graphs show the start of the CRUD layer. For the once and twice burned fuel pins, there is a pronounced increase in the oxygen and hydrogen peroxide production rates at the start of the CRUD layer. The spike is smaller for the average core, in which 30% of the fuel is crudded. The hot pin, which has no CRUD, does not show this spike in oxidizing species. The increase in oxygen and hydrogen peroxide production at the start of the CRUD region causes the ECP to increase briefly. After this spike, the ECP decreases, due to the increase in temperature, just as for the clean core radiolysis model.

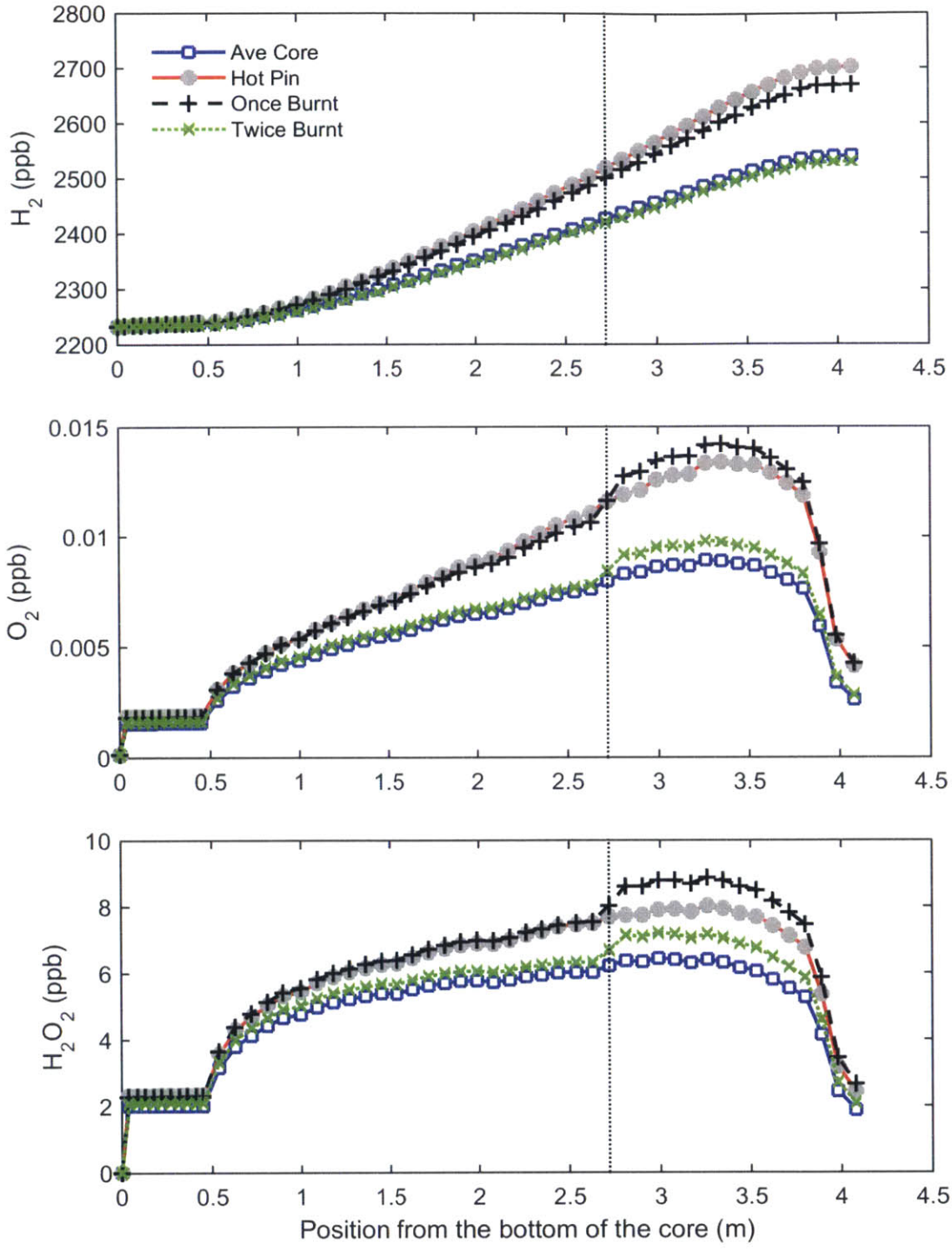

Figure 5-10. H_2, O_2, and H_2O_2 in a PWR core with 75 μm CRUD at beginning of cycle.

The dotted line shows the start of the CRUD region

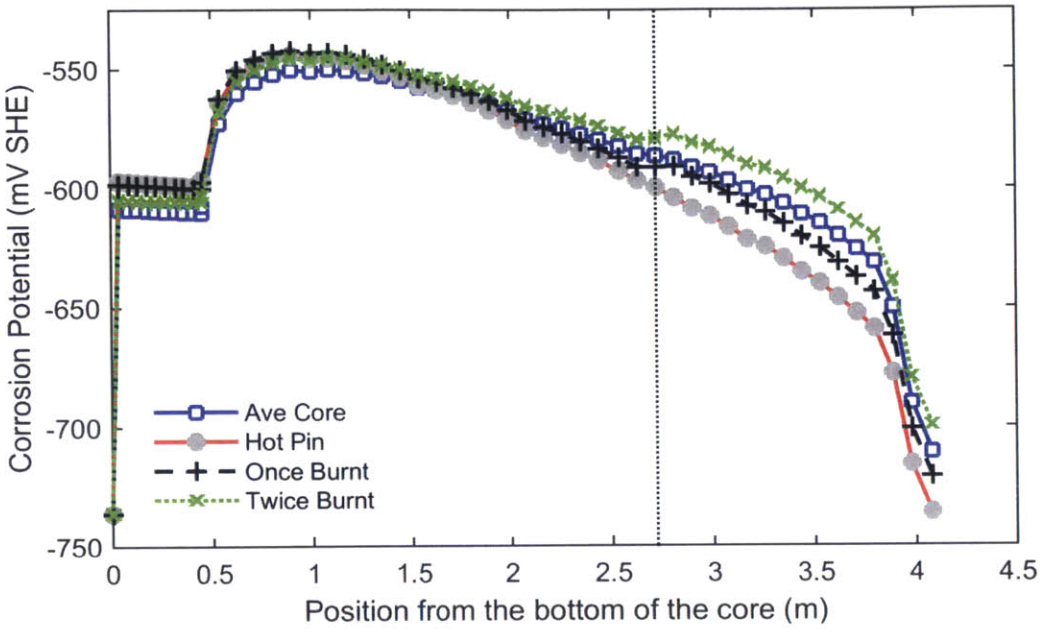

Figure 5-11. ECP in a PWR core with 75 μm CRUD at beginning of cycle. The dotted line shows the start of the CRUD region.

5.3.2 Middle of Cycle with 75 μm CRUD layer

Figure 5-12 shows the hydrogen, oxygen, and hydrogen peroxide in the bulk coolant for the MOC case with a 75 μm thick CRUD layer, and Figure 5-13 shows the corresponding ECP. The hot pin, which now has CRUD at MOC, has the highest concentrations of oxygen and hydrogen peroxide throughout the core. Compared to the beginning of cycle case, the concentration of oxygen and hydrogen peroxide are lower. This is consistent with the lower boron concentration in the bulk coolant and smaller alpha dose rate. The ECP is also more negative than the BOC case. At 2.8 m, where the CRUD layer starts, the oxygen and hydrogen peroxide clearly increase for the pins with CRUD. The increase is much smaller for the average core.

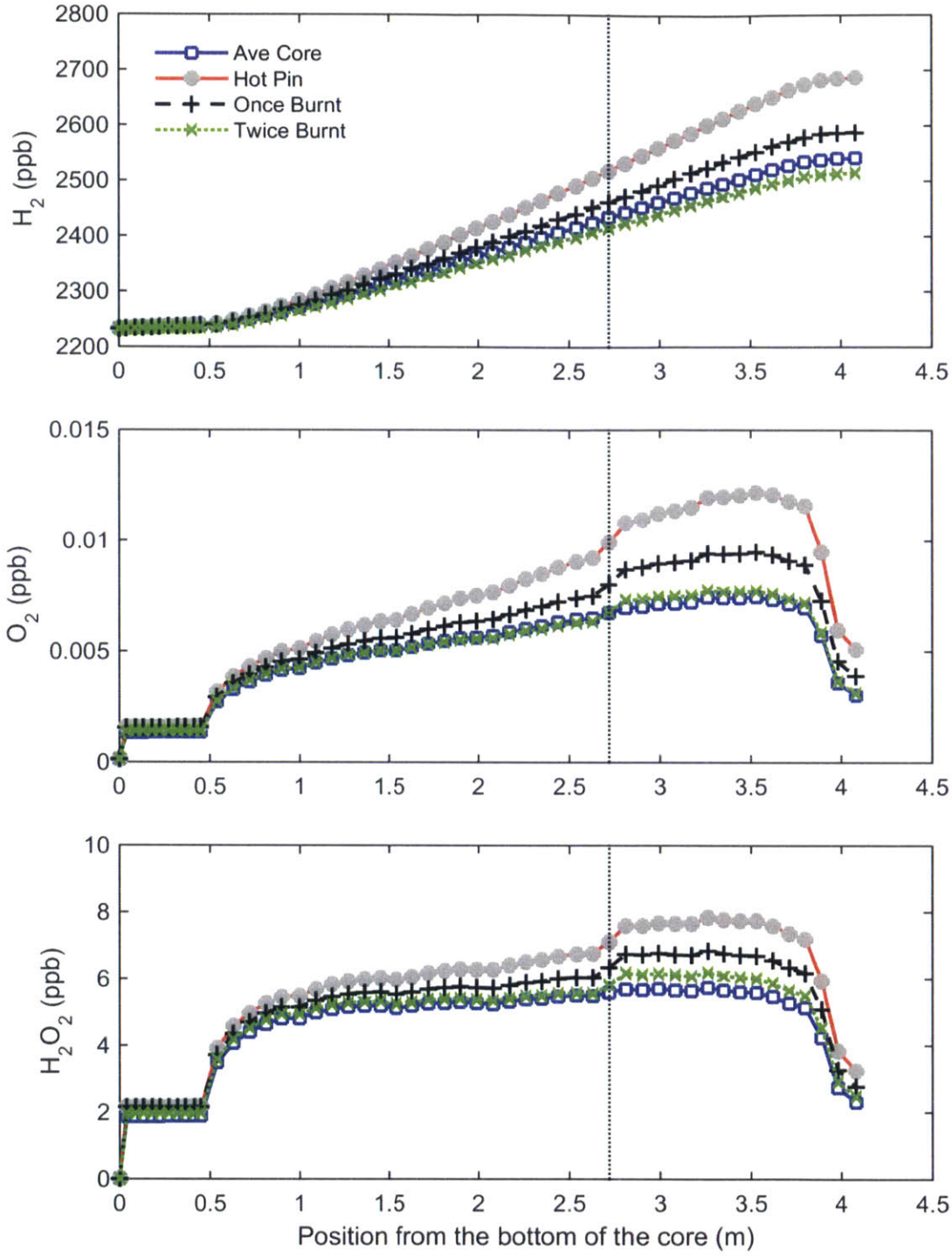

Figure 5-12. H_2, O_2, and H_2O_2 in a PWR core with 75 μm CRUD at middle of cycle. The dotted line shows the start of the CRUD region

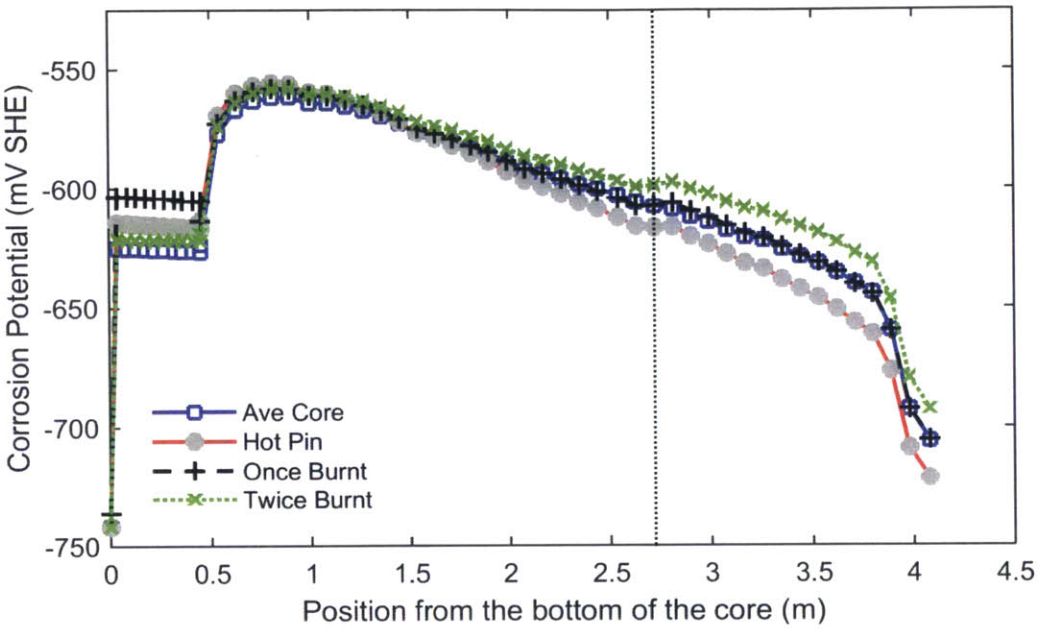

Figure 5-13. ECP in a PWR core with 75 μm CRUD at middle of cycle. The dotted line shows the start of the CRUD region

5.3.3 End of Cycle with 75 μm CRUD layer

Figure 5-14 shows the hydrogen, oxygen, and hydrogen peroxide in the bulk coolant for the EOC case with a 75 μm thick CRUD layer, and Figure 5-15 shows the corresponding ECP. At the start of the CRUD layer (2.8 m above the bottom of the core), there is an increase in the production of oxygen and hydrogen peroxide due to the higher dose rates. Compared to the beginning of cycle and middle of cycle chemistry, the jump at in oxidizing species at 2.8 m is not as pronounced, due to the lack of boron and alpha dose. The maximum oxygen and hydrogen peroxide occurs at ~3.8 m for the end of cycle case. For the beginning and middle of cycle, these peaks occur at ~3.5 m.

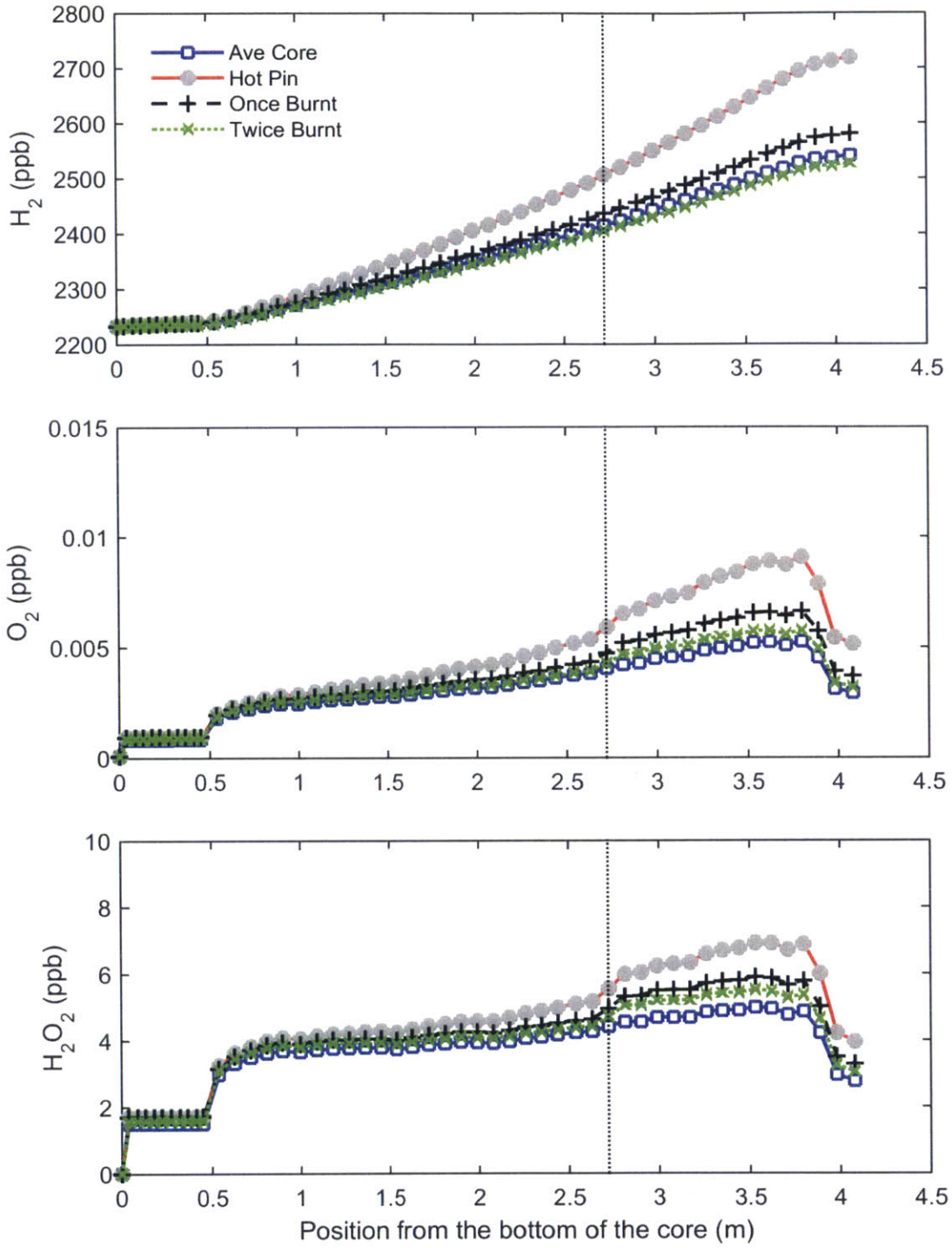

Figure 5-14. H_2, O_2, and H_2O_2 in a PWR core with 75μm CRUD at the end of cycle. The dotted line shows the start of the CRUD region.

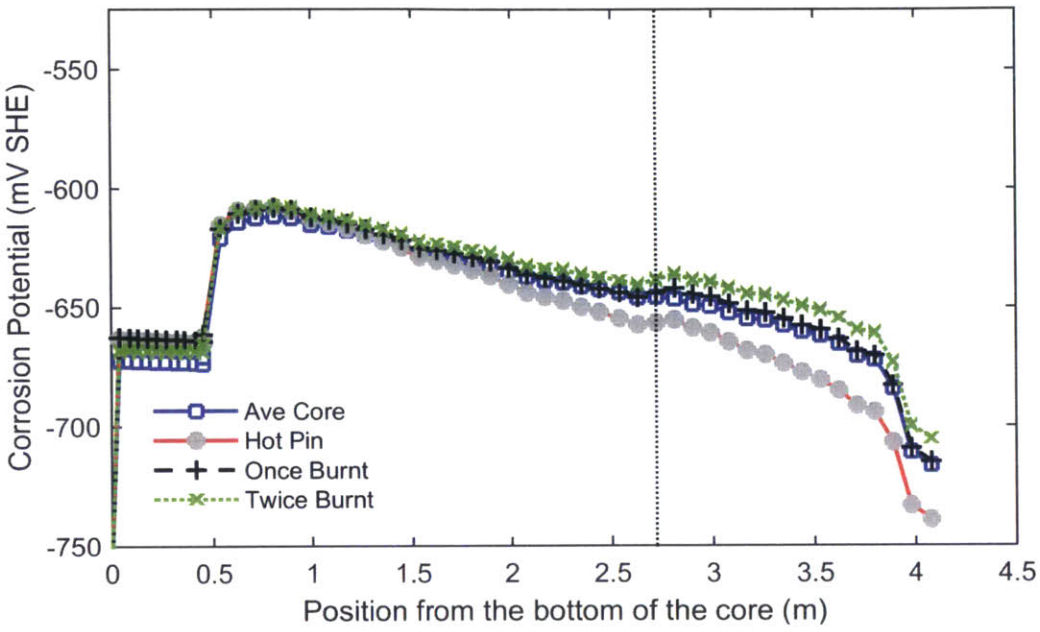

Figure 5-15. ECP in a PWR core with 75 μm CRUD at the end of cycle. The dotted line shows the start of the CRUD region

5.3.4 Comparison to Clean Core Water Chemistry

The hot pin at the beginning of cycle has no CRUD, so comparing the hot pin in the crudded core and the clean core at BOC will show the effects of changing only the axial power distribution. Figure 5-16 shows beginning of cycle gamma dose rate at the hot pin for the clean and crudded core. Figure 5-17 shows the corresponding oxygen and hydrogen peroxide concentrations at the clean and crudded hot pin.

The gamma dose rate profile for the crudded core has a higher peak dose rate. The dose rates for the crudded core are greater in the middle of the core for the CRUD case. At the top of the core, the dose rates are higher in the clean core. The difference in dose rates at the top of core will change the location where net recombination of water

begins. Throughout the core there are two competing effects: the production of oxidizing species by radiolysis and the recombination of water by chemical reactions, which consumes the oxidizing species. When the dose rates are sufficiently low, the consumption rate of oxidizing species exceeds the production rate, and net water recombination occurs.

In Figure 5-17, the oxygen and peroxide concentrations are higher for the crudded core until 3.25 m from the bottom of the core, which is where net water recombination begins. In the clean core, net water recombination begins at 3.75 m from the bottom of the core.

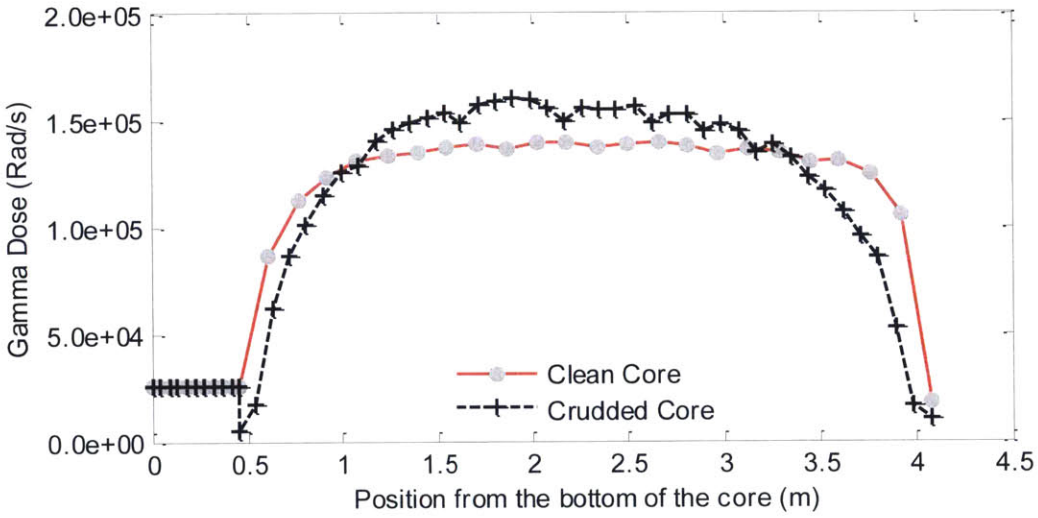

Figure 5-16. Dose at the hot pin in a clean and crudded core at BOC

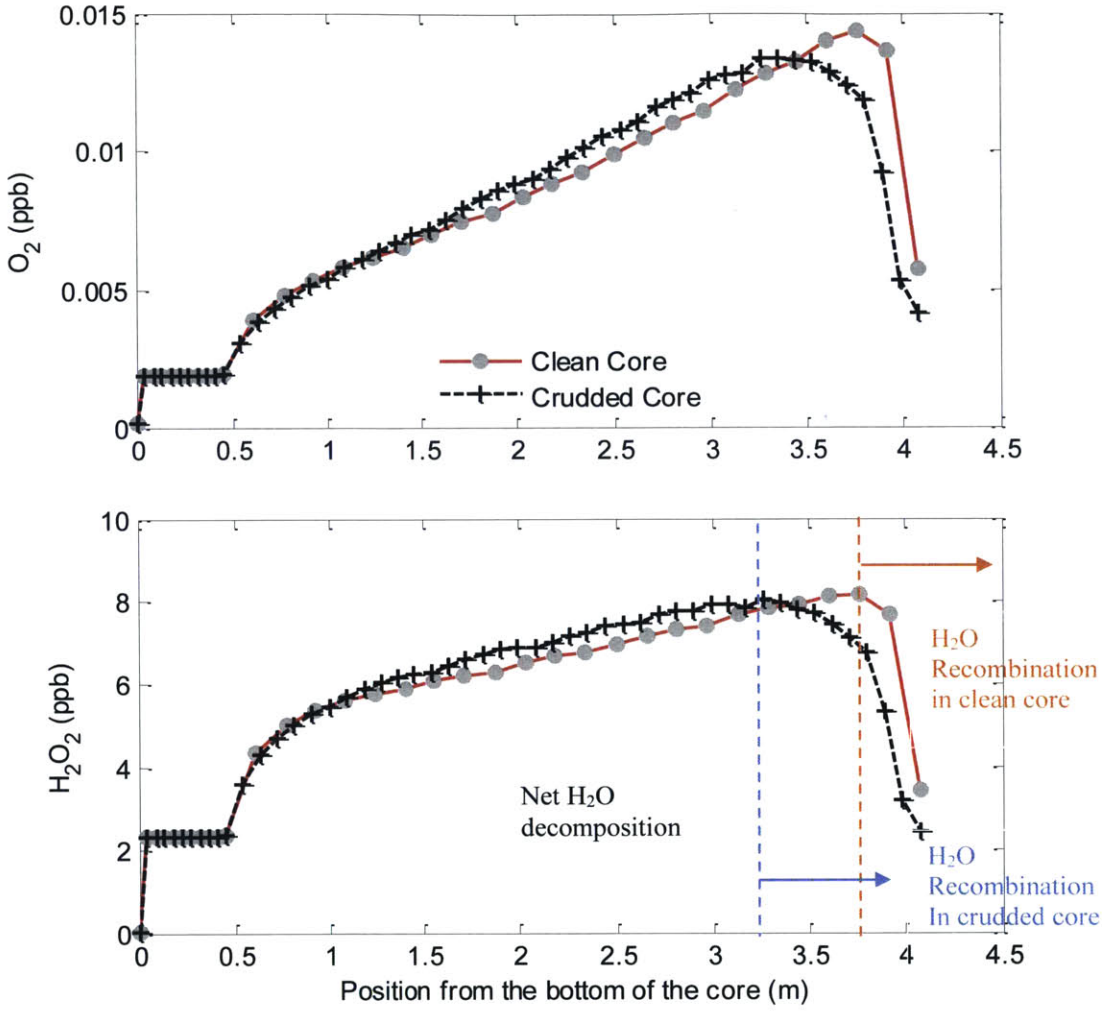

Figure 5-17. O_2 and H_2O_2 at the hot pin in a clean and crudded core at BOC

A comparison of the twice burned pin and the averaged core at beginning of cycle will show the combined effects of higher dose rates in the crudded region and the change in the axial power shapes. Recall that the average core doses reflect that 30% of the fuel is covered with CRUD, whereas the twice-burned pin is crudded. Figure 5-18 shows the hydrogen peroxide concentrations for the clean and crudded averaged core and twice burned pin. As with the hot pin, recombination begins at a lower elevation for fuel with

CRUD. For the hot pin, the H_2O_2 concentration in the core with CRUD dropped below the clean core case after recombination began at 3.25 m. The higher dose rates due to CRUD cause the H_2O_2 concentration to remain higher than the clean core case until ~3.5 m for the averaged core and approximately 3.7 m for the twice burned pin. For the twice burned pin, the greatest difference in H_2O_2 between the two models is approximately 1.2 ppb, at the start of the CRUD.

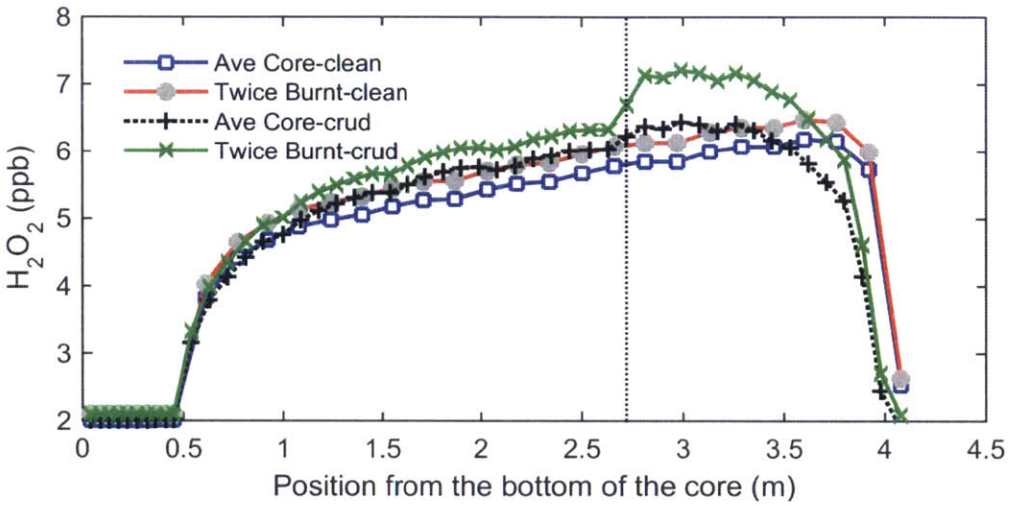

Figure 5-18. H_2O_2 a clean and crudded core at BOC

Figure 5-19 compares the concentrations of hydrogen peroxide for the clean and crudded cores at the middle of cycle and end of cycle. We can also compare these results with the results from the BOC calculation in Figure 5-18. For all calculations, the H_2O_2 concentrations are higher for fuel rods with CRUD at the beginning of the CRUD region (2.8 m) and lower at the top of the core. The switch occurs because the dose rates at the clean fuel exceed those at fuel with CRUD near the top of the core, due to the AOA. This switch does not necessarily coincide with net water recombination for the CRUD case, as

evident by the H_2O_2 concentrations for averaged core at MOC in Figure 5-19. The height where H_2O_2 concentrations are equal depends on the axial offset and the dose increase due to CRUD. For the twice-burned fuel pin, H_2O_2 is equal at 3.5m for MOC (when the axial offset is greatest) and 3.7m for BOC and EOC. The smaller dose enhancement at the average core means that the point of equal H_2O_2 occurs at a lower elevation for the averaged core than for the twice burned or hot pin.

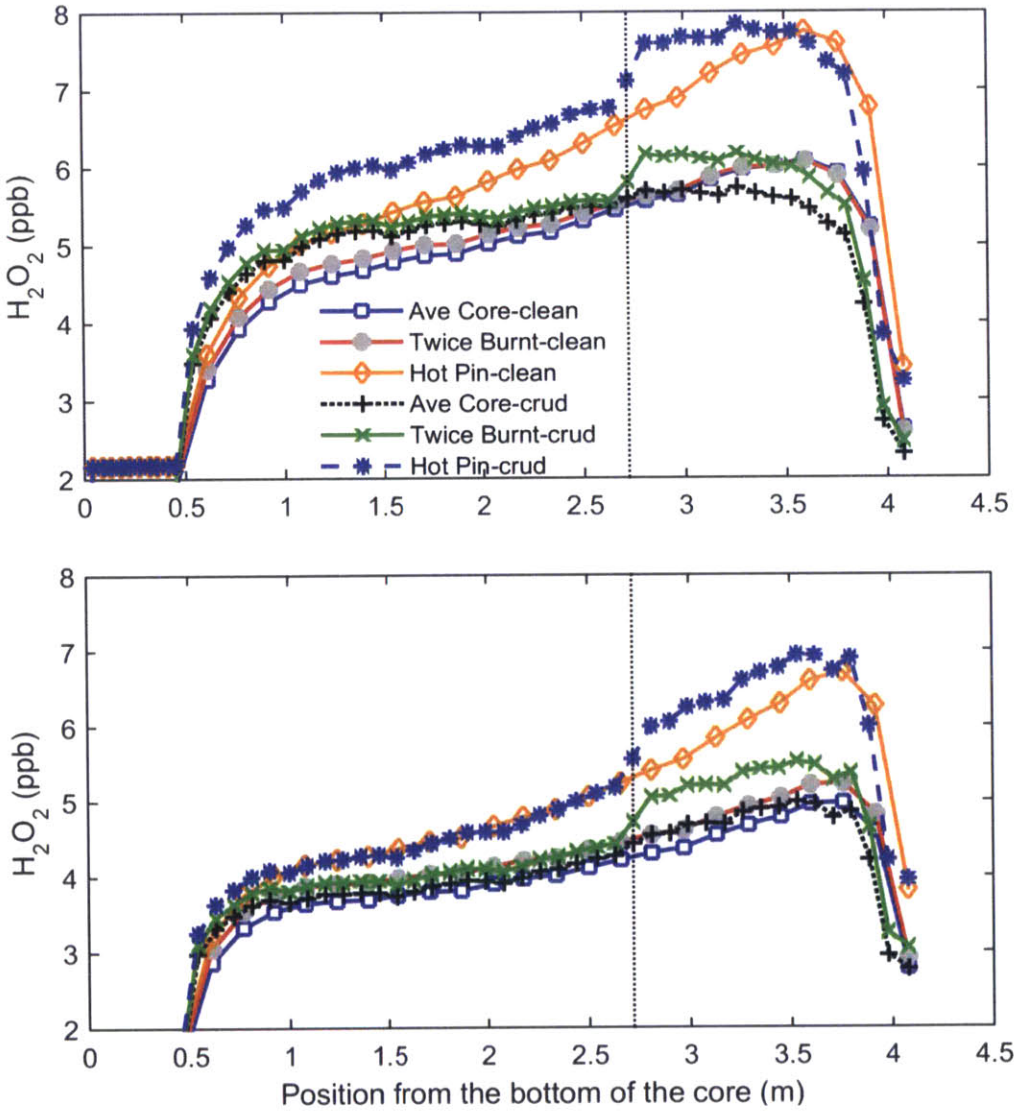

Figure 5-19. H_2O_2 a clean and crudded core at MOC (top) and EOC (bottom)

If we average the concentrations over the length of the core, the difference between a clean and crudded core is minimal. Table 5-9 has a comparison of the average oxygen and hydrogen peroxide concentrations and of the ECP in the active core of a clean and crudded PWR core. For all cases, the average concentrations of oxygen and hydrogen peroxide are greater for a crudded core than for a clean core. The difference in ECP is less than 3 mV. For the average core, the changes in oxygen and hydrogen peroxide are 2-3% at the three modeled points in the cycle. The largest change in chemistry occurs for the hot pin at the middle of cycle, it is a 9% increase in oxygen and 7.7% increase in hydrogen peroxide.

Table 5-9. Average oxygen, hydrogen peroxide, and ECP in a clean core and core with 75 μm thick CRUD layer

	Clean Core			**75 μm Crud**			**Change in value**		
	O_2 (ppb)	**H_2O_2 (ppb)**	**ECP (mV SHE)**	**O_2 (ppb)**	**H_2O_2 (ppb)**	**ECP (mV SHE)**	**O_2 (ppb)**	**H_2O_2 (ppb)**	**ECP (mV)**
BOC									
Average	6.14E-03	5.17	-587	6.27E-03	5.28	-586.4	2.1%	2.1%	0.6
Hot Pin	8.84E-03	6.36	-594.6	8.84E-03	6.39	-595.1	0.0%	0.5%	-0.5
2xburned	6.31E-03	5.42	-581.6	6.66E-03	5.68	-579.1	5.6%	4.8%	2.5
1xburned				8.99E-03	6.71	-587.6			
MOC									
Average	5.40E-03	4.86	-602.3	5.56E-03	4.99	-602.6	3.0%	2.7%	-0.3
Hot Pin	7.37E-03	5.80	-609.6	8.03E-03	6.24	-607.7	9.0%	7.7%	1.9
2xburned	5.29E-03	4.95	-596.5	5.64E-03	5.21	-595	6.6%	5.3%	1.5
1xburned				6.60E-03	5.63	-601.1			
EOC									
Average	3.37E-03	3.91	-645.6	3.47E-03	4.02	-643.5	2.9%	2.8%	2.1
Hot Pin	4.87E-03	4.83	-653.1	5.08E-03	5.00	-651.1	4.3%	3.5%	2
2xburned	3.53E-03	4.13	-639.1	3.70E-03	4.30	-636.6	4.8%	3.9%	2.5
1xburned				4.10E-03	4.50	-641			

Likewise, the difference in peak hydrogen peroxide and oxygen are not substantially different. Table 5-10 compares the maximum values of oxygen, hydrogen peroxide, and calculated ECP, as well as the change in location of these maximums. The difference in peak values oxygen and hydrogen peroxide concentrations are on the order of 10%, and the changes in calculated ECP are less than 12 mV. However, the location of the maximum oxygen and hydrogen peroxide is at a lower axial height, especially for the BOC and MOC cases.

Table 5-10. Peak values of oxygen, hydrogen peroxide, and ECP in cores with 75 μm CRUD.

	75 μm Crud			Change in value from clean core			change in axial height of peak value		
	O_2 (ppb)	H_2O_2 (ppb)	ECP (mV SHE)	O_2 (ppb)	H_2O_2 (ppb)	ECP (mV SHE)	O_2 (ppb)	H_2O_2 (ppb)	ECP (mV)
BOC									
Average	8.93E-03	6.44	-550.1	-0.3%	4.2%	3.2	-0.5	-0.61	0.17
Hot Pin	1.34E-02	8.02	-544.3	-6.7%	-1.7%	3.1	-0.41	-0.5	0.13
2xburned	9.82E-03	7.21	-545.1	7.3%	11.3%	2.9	-0.5	-0.61	0.17
1xburned	1.42E-02	8.87	-542.1						
MOC									
Average	7.46E-03	5.74	-561.7	-9.4%	-5.8%	8.9	-0.07	-0.34	-0.02
Hot Pin	1.22E-02	7.84	-555.7	-1.2%	1.1%	11.3	-0.23	-0.34	-0.11
2xburned	7.74E-03	6.19	-558.2	-0.9%	1.8%	8	-0.34	-0.34	-0.02
1xburned	9.48E-03	6.85	-558.1						
EOC									
Average	5.25E-03	5.00	-611.6	-1.6%	0.4%	4.8	0.04	-0.23	-0.11
Hot Pin	9.08E-03	6.93	-607.8	3.9%	3.3%	3.9	0.04	-0.23	0.04
2xburned	5.76E-03	5.52	-607.4	3.9%	5.5%	3.3	0.04	-0.23	-0.11
1xburned	6.64E-03	5.91	-608.2						

The significance of these results is that while changes to *core averaged* oxygen and hydrogen peroxide from CRUD are minimal, changes *locally* can be significant. In particular, the greatest difference between clean and crudded cores is near the start of the CRUD layer. The individual pin chemistry calculations show that "local" bulk water chemistry can be significantly more oxidizing than the averaged core. If there is a region within PWR core where most of the fuel has a CRUD layer, than the "averaged" core chemistry may underpredict hydrogen peroxide concentrations by up to 3 ppb, which is significant when the concentrations are typically 5-10 ppb.

5.5 Local Chemistry in CRUD and Implications on Corrosion

Determining the water chemistry within porous CRUD deposits will be significantly more complicated than modeling bulk water chemistry. The flow patterns can be complex and boiling occurs within chimneys in the CRUD. High concentrations of boron and lithium in the confined coolant will raise the saturation temperature of the coolant. [109] The coolant velocities in CRUD are on the order of 2 mm/s [13], which is significantly smaller than those of the bulk coolant in the core, which are on the order of 5 m/s. With the slow velocities in CRUD, mass transport by diffusion is likely to be significant.

Based on the modeling performed, a summary of the effects likely to be affecting chemistry within CRUD include the following:

1. Increase in oxidizing species due to radiolysis. The extent will depend the flow rates in the CRUD; namely the coolant flow rates in and out of the CRUD
2. The effect of boiling is to strip off dissolved H_2 and O_2 into the vapor phase, which will make conditions more even oxidizing. However, concentrated boron and lithium will also raise the saturation temperature of the coolant.
3. Higher temperatures in the CRUD will change the rate constants of the water reactions. As the reaction sets are complex, it is difficult to determine if this will have a significant effect on coolant chemistry
4. pH effects. Lithium and boron enrichment in the CRUD is likely to change the local pH. The pH in turn will affect the stability of oxides

5. Reactions between metal ions and radiolysis products (hydrolysis and radiolysis scavengers)
6. Possible reactions between hydrogen peroxide and the CRUD surface. Some oxides catalyze the dissociation of hydrogen peroxide, and the surface to volume ratios in porous CRUD will be high.

The calculations for dose at fuel rods with CRUD indicate that the gamma dose rates to the confined coolant will be approximately the same as in the coolant adjacent to the CRUD. The neutron dose will be slightly higher, about an 8% increase. The alpha dose rates will depend on the concentration of boron within CRUD, and for the thickest CRUD deposits, they could be 3x times higher than in the adjacent bulk coolant.

The radiolysis calculations for PWR cores with CRUD show that at the start of CRUD, there are brief increases in oxygen and hydrogen peroxide production rates, over a distance of 0.2 m. The observed increases corresponded to a 21-22% increase in dose. For the average core, which has a 6% increase in dose at the start of CRUD, the increases in production rate is scarcely noticeable. The temporary increase in net production rate occurs because the production rate due to radiolysis increases. The recombination rate also increases but there is a slight delay, which causes the observed spike.

As an order of magnitude estimate, the time required for a unit volume of fluid to transverse 75 μm at 2 mm/s, is 0.0375 s. This is the same time required for a unit volume of fluid to travel 0.1875 m at 5 m/s, which is the velocity in the PWR core. Thus, for CRUD with significant boron enrichment and a higher alpha dose to the confined coolant,

the net production rate of oxygen and hydrogen peroxide is likely to be higher than in the bulk coolant.

The Mixed Potential Model results for the clean PWR core showed that the ECP is determined by the balance of hydrogen peroxide and hydrogen. The concentrations of oxygen in the coolant are low enough that the oxygen redox reaction has little effect on the ECP. For a given temperature, an increase in hydrogen peroxide shifts the hydrogen peroxide redox potential in the positive direction and raises the mass transfer limited current. The result is an increase in the ECP. In PWRs, hydrogen concentrations are a few ppm, and the increase in hydrogen due to radiolysis is on the order of ppb. Consequently, changes to the hydrogen redox potential and mass transfer limited current have less of an effect on ECP.

Applying these observations to CRUD chemistry, the increase in hydrogen peroxide due to radiolysis will result in a more positive ECP. In reality, the comparison of ECP for clean and crudded fuel is more complex. The CRUD layer will change the mass-transfer limited partial currents from those for clean fuel. In the MPM model as implemented, these mass transfer limited partial currents are calculated for high Reynolds number flow (mass transport is limited by transport across a boundary layer). For CRUD, mass transport will be limited by diffusion/convection across the CRUD layer, and this will likely be much lower.

5.6 Chapter Summary

In this chapter a radiolysis model for primary water chemistry in a PWR with CRUD was developed. MCNP was used to estimate the dose to the bulk coolant as well as coolant confined in the CRUD. The results for the CRUD compositions studied in this chapter indicate that bulk coolant chemistry does not vary with either CRUD thickness or boron concentrations in the CRUD.

Gamma, neutron, and alpha dose rates to the *bulk coolant* are 21-22% higher for fuel with CRUD compared to fuel without CRUD. The gamma dose to confined coolant within porous CRUD deposits is estimated to be the same as dose rate to the adjacent channel. Neutron dose rates to confined coolant will be 8% higher than in the adjacent channel. Alpha dose rates vary with boron concentration in the CRUD, it is estimated that 25% of alpha dose deposited to CRUD volume will be to the coolant within the deposit.

The effect of AOA is to increase the concentrations of O_2 and H_2O_2 in the lower part of the core. It also moves the location of the peak O_2 and H_2O_2 concentrations towards the bottom of the core. The bulk coolant is expected to be more oxidizing near fuel with CRUD, because of the increase in dose.

The next step in understanding the effects of CRUD on local chemistry is to study radiolysis within porous deposits. Henshaw et al. developed a 1-D model for chemistry within PWR CRUD deposits, which included the effect of radiolysis, hydrolysis reactions, boron and lithium enrichment, and boiling. [109] In the past few years, more advanced models for thermal hydraulics and boron deposition in CRUD deposits have been developed. The information from these models, along with the new dose rate

information presented in this work, can be used to create a more advanced model for water chemistry in CRUD. The implementation of RADICAL makes it difficult to include diffusion, 2-D or 3-D flow, and variable saturation temperature. However, the output from the RADICAL PWR model with CRUD would need to be used as input for a CRUD chemistry model.

Chapter 6: From Bulk Water Chemistry to Interfacial Electrochemistry

The past three chapters have focused on modeling the bulk water chemistry in a PWR core including the effects of CRUD. In the next three chapters, we will investigate the role of precipitates in the hydrogen split. Returning to the coolant/oxide/clad system, in Figure 6-1, the overall waterside corrosion reaction contains multiple steps, including adsorption, diffusion, electron transfer, and desorption. The hydrogen split occurs at the oxide/coolant interface: the adsorbed protons will ether recombine and form molecular hydrogen or be incorporated into the oxide. The hydrogen pickup fraction of Zircaloy-4 in PWRs is approximately 15%, so the majority of the protons are reduced at the interface, and proton recombination is an important step in the hydrogen split.

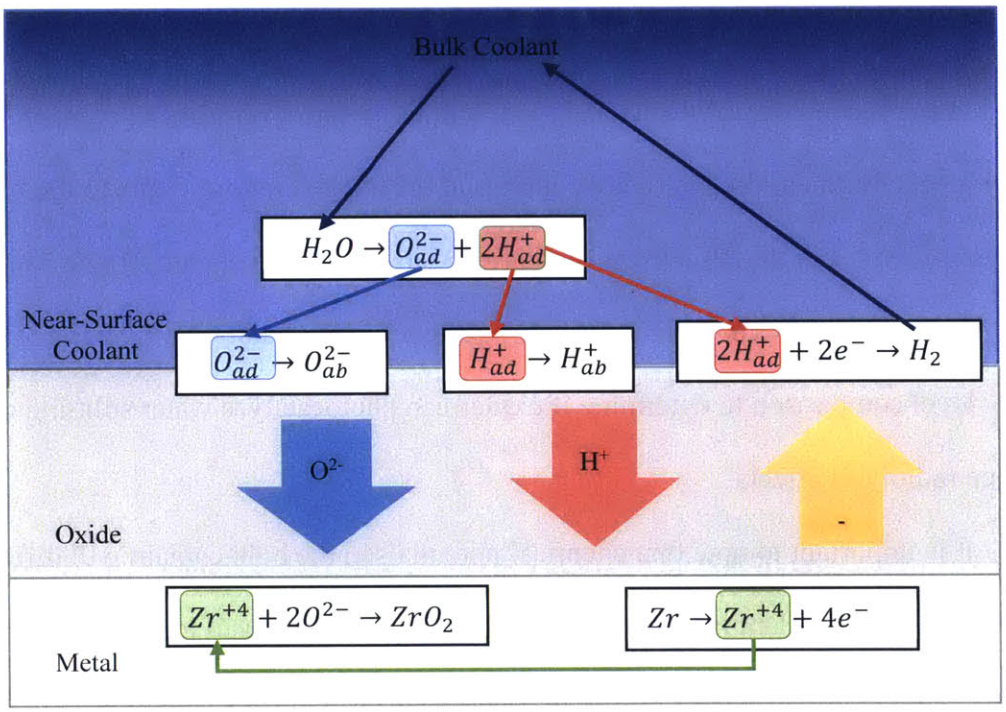

Figure 6-1. The coolant/oxide/clad system

The oxide layer consists primarily of zirconia. The outer layer is primarily monoclinic, and closer to the oxide/metal interface there is also tetragonal zirconia. Precipitates (second phase particles) are exposed to the surface, and there are also cracks and pores at the surface. However, it is not clear where surface reactions occur: on the zirconia surface, at a grain boundary, in a crack or pore, or at a precipitate.

In this chapter the link between the bulk water chemistry and the electrochemical processes occurring at the oxide/coolant interface is explored using thermodynamics. In first part of this chapter we will determine the chemical potentials of hydrogen and oxygen in the bulk coolant. These chemical potentials at the oxide/coolant interface will determine the thermodynamics of surface reactions, such as adsorption and desorption. The difference between the oxygen and hydrogen chemical potentials at the oxide/coolant interface and in the bulk zirconium is the driving force that determines oxygen and hydrogen transport across the oxide.

In the second part of this chapter, we will use electrochemistry to compare the energy levels for the hydrogen redox couple and the oxygen redox couple to the band structure of oxides in the Zircaloy-4 oxide film. This energy level comparison can show which oxides are likely candidates for hydrogen evolution. Additionally, we can used the energy level comparison to determine if oxides can photocatalyze water splitting or enhance radiolysis effects.

It is important to note that chemical potentials in the bulk coolant will differ from those at the oxide/coolant interface. The coolant will be hotter, and local concentrations may be different due to surface reactions, heterogeneous radiolysis, and transport to and from the interface. The complexity of the oxide/coolant interface makes it difficult to

quantify the changes in chemistry. However, as a first approximation, the bulk chemistry can be used to provide insight into corrosion and hydrogen pickup.

6.1 Chemical Potentials of O_2 and H_2 in the Coolant

The chemical potential of a gas is calculated as:

$$\mu(T,P) = \mu(T^o,P^o) + k_B T ln\left(\frac{P}{P^o}\right) \tag{6-1}$$

where:

$\mu(T,P)$ is the chemical potential at temperature T, P

$\mu(T^o,P^o)$ is the chemical potential at STP, at $T^o = 25°C$ and $P^o = 0.1\ MPa$

P is the partial pressure of the gas

For density functional theory calculations, we need the chemical potential relative to 0 K. For example, the chemical potential of oxygen is calculated : [110]

$$\mu_{O_2}(T,P) = E_{O_2,DFT} + \Delta\mu_{O_2}(T,P^o) + k_B T ln\left(\frac{P_{O_2}}{P^o}\right) \tag{6-2}$$

Where

$E_{O_2,DFT}$ is the DFT calculated energy for an isolated oxygen molecule

$\Delta\mu_O\ (T,P^o)$ is the difference between the oxygen chemical potential at (T,P^o) and (T=0 K, P^o=0.1 MPa)

P_{O_2} is the partial pressure of oxygen

The partial pressure can be calculated using Henry's Law. See Equation (3-18) and Table 3-2 in Section 3.2.1 for the Henry's Law constants which were used in the mixed potential models. The difference in chemical potentials due to temperature can be determined using data from thermodynamic tables. [111]

As an example, we show the chemical potentials from the radiolysis calculations in Section 4.2.1: a clean (no CRUD) PWR core, at the beginning of cycle, with 1440 ppm boron, and 25 scc H_2/kg H_2O.

The hydrogen chemical potential, relative to the chemical potential at 0 K and 0.1 MPa, is shown in Figure 6-2. Three parts of the core are compared: the "averaged" core, a fresh fuel pin with the highest heat generation rate (the "hot pin"), and a twice burned pin which has a lower heat generation rate (the "cold pin"). The hydrogen chemical potential is primarily dependent on the temperature, and decreases throughout the core as the temperature rises. Radiolysis causes the concentration and partial pressure of hydrogen to increase over the entire length of the core. However, the term $\left(\frac{P}{P^o}\right)$ in Equation (6-2) is always less than unity. The temperature effects outweigh the change due to partial pressure, causing the chemical potential to decrease. At the core entrance, the temperature and chemistry concentrations are the same for all three regions and so is μ_{H2}. The chemical potentials for the averaged core and the twice burned pin are essentially the same throughout the core. The hot pin has a more negative hydrogen chemical potential, due to the higher temperature, and at the core exit it is approximately 0.03 eV less than the hydrogen chemical potential of the averaged core.

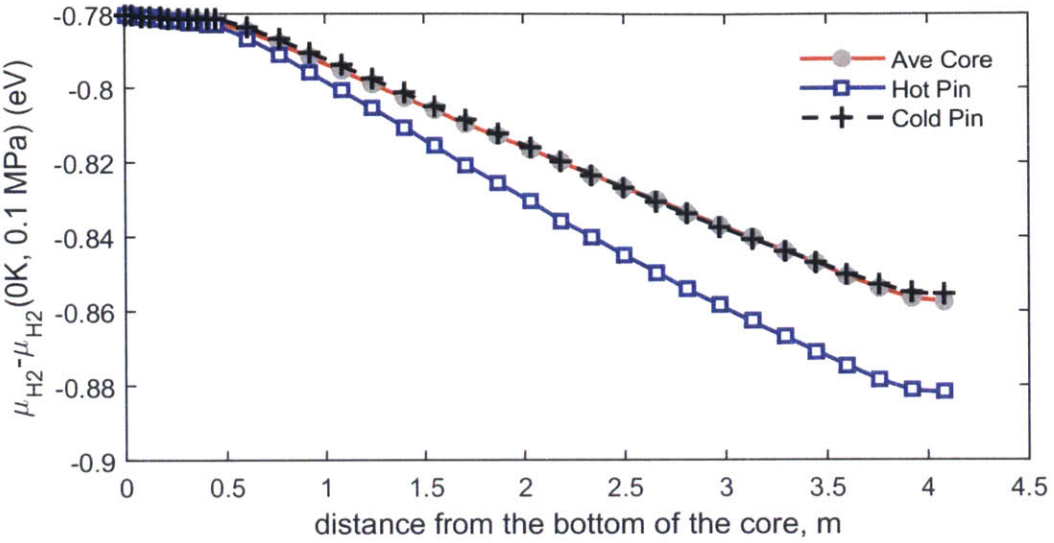

Figure 6-2. H_2 Chemical Potential in the clean core at BOC with 25 cc (STP) H_2/kg H_2O

The calculated hydrogen chemical potentials do not appear to be influenced by radiolysis behavior. Figure 6-3 shows the hydrogen chemical potential with variable hydrogen injection as a function of coolant temperature. The hydrogen chemical potentials are nearly a linear function of temperature. Figure 6-4 shows the hydrogen chemical potentials in PWR coolant with 25 scc H_2/kg H_2O for both the clean core and crudded core. All points in the cycle, BOC, peak boron, MOC, and EOC are included in this plot. All of the data points fall on a single line, implying that at this hydrogen injection level, μ_{H2} only depends on the coolant temperature and is not affected by fuel

burnup, boron injection, local power, or the presence of CRUD.

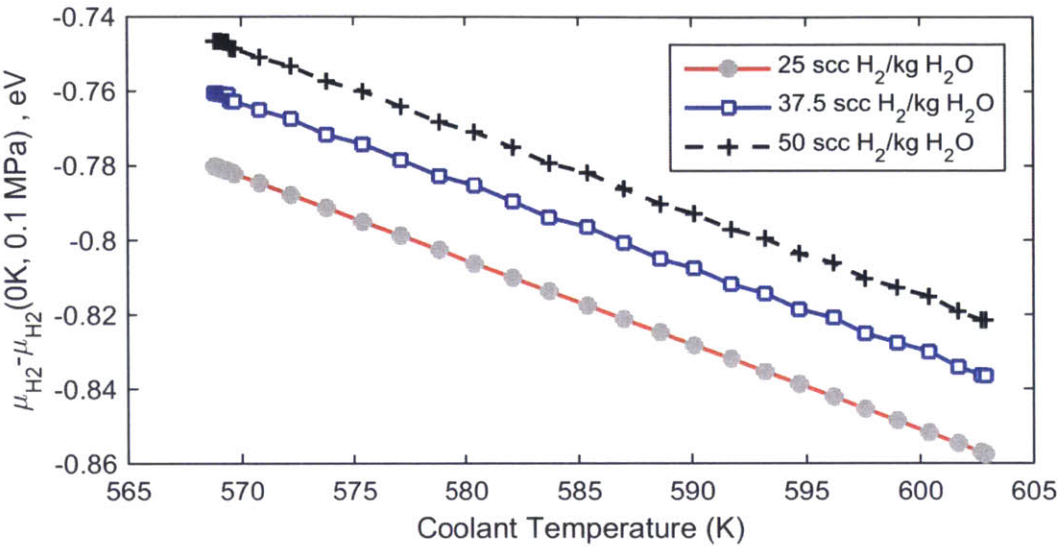

Figure 6-3. Hydrogen chemical potential in PWR core as a function of hydrogen injection

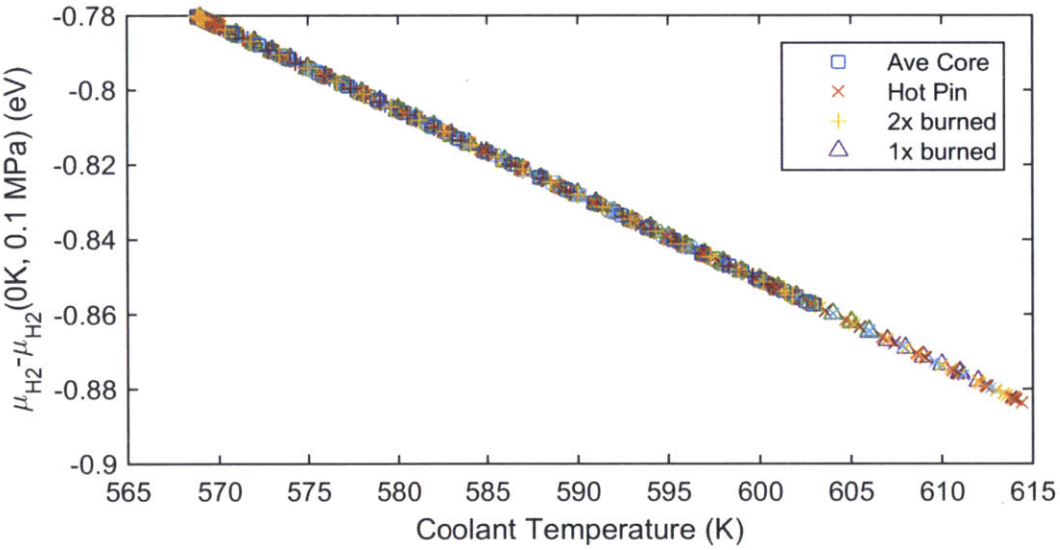

Figure 6-4. Hydrogen chemical potential in PWR coolant with 25 scc H_2/kg H_2O with and without CRUD

The oxygen chemical potential (once again relative to the chemical potential at 0 K and 0.1 MPa) is shown in Figure 6-5. For comparison, the oxygen concentration and alpha dose for the average core are shown in Figure 6-6. In Figure 6-5, there is a sudden increase in the oxygen chemical potential at the start of the active core, approximately 0.5 m from the bottom of the core. This increase is due to the increase in oxygen from radiolysis, which can be seen in Figure 6-6. However after this initial increase, the chemical potential decreases due to temperature effects. Although the chemical potential decreases, the concentration of oxygen actually increases up to a height of 3.9 m. At this axial height, the dose rates in the core decrease, and net water recombination occurs. The concentration of oxygen decreases, and correspondingly the oxygen chemical potential decreases. The differences between μ_{O2} of the average core, hot pin, and twice burned pin can be explained as follows: the temperature of the average core and twice burned pin are very close, but the oxygen concentration is slightly higher for the twice burned pin. The oxygen concentration of the hot pin is the highest, but the temperature increase is also the greatest. At low axial positions, with little temperature difference between the different fuel pins, μ_{O2} at the hot pin is closest to the high burnup pin. As the axial height increases, the temperature at the hot pin increases more than the rest of the core, and so the chemical potential decreases more rapidly.

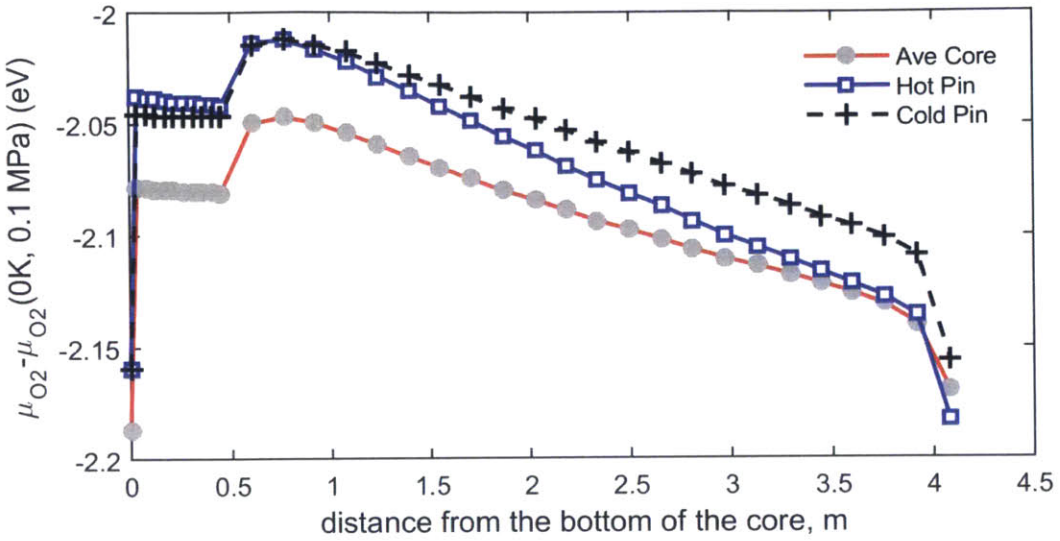

Figure 6-5. O_2 Chemical Potential in the clean core at BOC with 25 cc (STP) H_2/kg H_2O

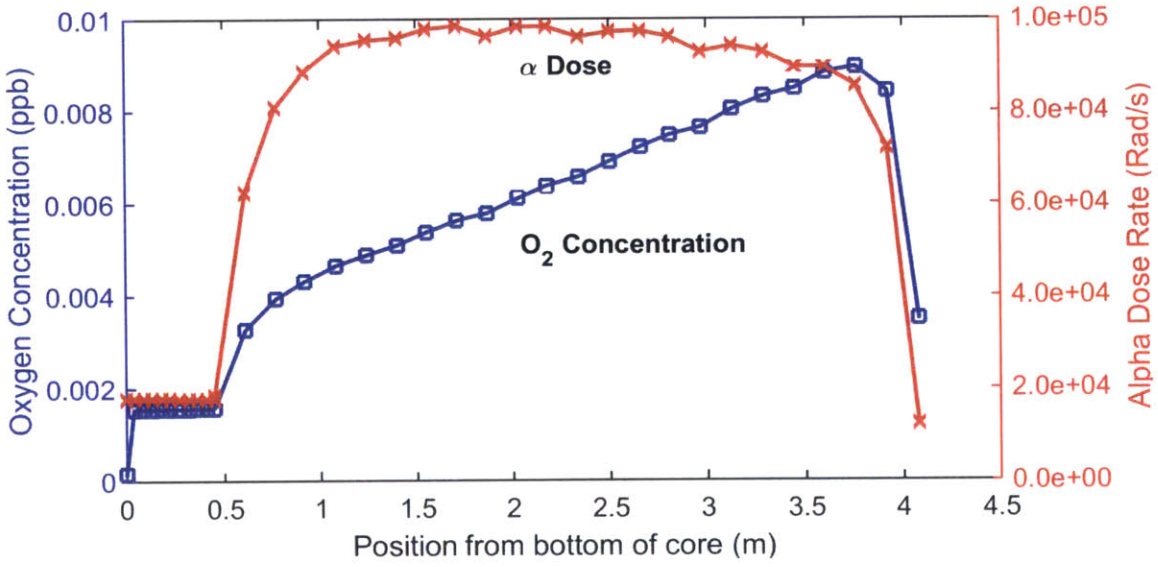

Figure 6-6. Oxygen concentration and alpha dose rate in the average core at BOC with 25 STP cc H_2/kg H_2O

Unlike the hydrogen chemical potential, the oxygen chemical potential depends on radiolysis effects. Figure 6-7 shows the oxygen chemical potential in the averaged core with 25-50 scc H_2/kg H_2O. As expected, the oxygen chemical potential is lower (more negative) for higher levels of hydrogen injection, as the oxygen concentration is lower. Figure 6-8 shows the calculated oxygen chemical potential for *all cases* with 25 scc H_2/kg H_2O: at various points in the cycle (BOC, MOC, EOC), with and without CRUD, averaged cores and single channel analyses. In the previous chapters, we observed that oxygen concentrations change significantly with alpha dose rates. Thus, the oxygen chemical potentials depend on both oxygen partial pressure (determined by dose rates) and the coolant temperature (determined by power).

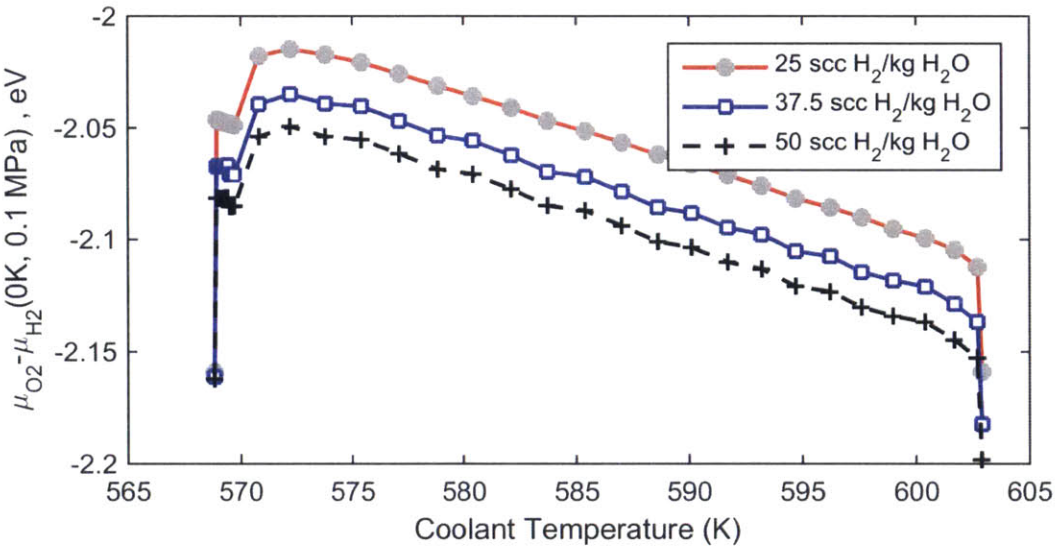

Figure 6-7. Oxygen chemical potential in PWR core as a function of hydrogen injection. Results are shown for the averaged core without CRUD without 1486 ppm boron addition.

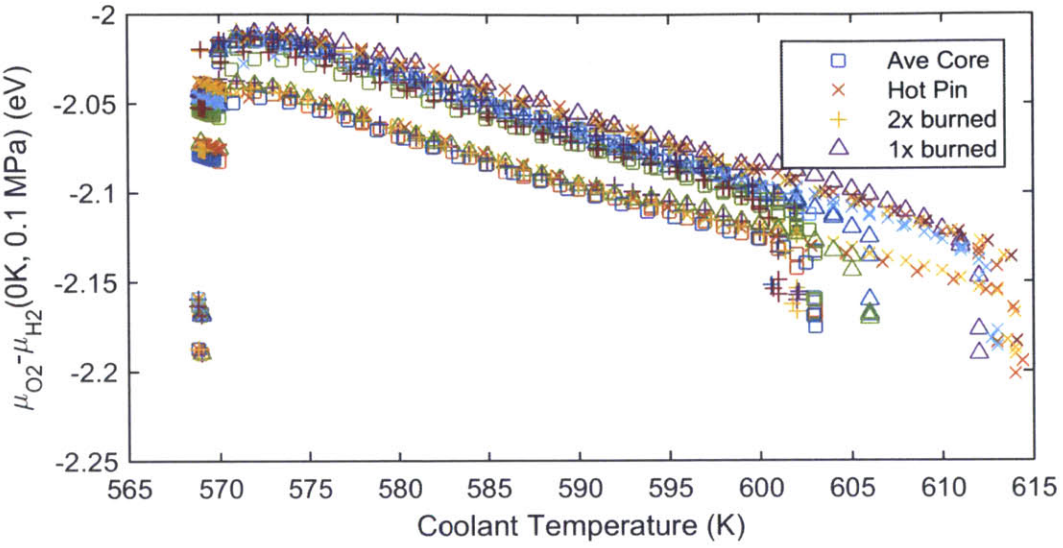

Figure 6-8. Oxygen chemical potential in PWR coolant with 25 scc H_2/kg H_2O with and without CRUD. Results are shown for 1440, 1486, 1000, and 0 ppm B

6.2 Theory of Electron Transfer Processes at Semiconductors

For semiconductors and insulators, electron transfer can only occur when the electron energy levels in the electrode and in the solution are approximately equal. [112] For metals, electrons are transferred at the Fermi energy. For semiconductors and insulators, the Fermi energy is in the band gap. Electron transfer can occur at either the conduction band or valence band energies.

6.2.1 Density of States and the Band Gap

Figure 6-9 shows a schematic of the energy levels of a material with a band gap. On the y-axis is g(E), the *density of states* as a function of electron energy, E. For semiconductors and insulators, there is a forbidden region, the *band gap,* in which there are no allowed energies. Normally the states in the *valence band* are occupied, and the

states in the conduction *band* are unoccupied. The top of the valence band is at energy E_v and the bottom of the conduction band is at energy E_C. *Holes* are unoccupied levels in the valence band, and *conduction electrons* are occupied levels in the conduction band. The Fermi level, E_f, is the chemical potential of electrons in a material. For non-degenerate semiconductors, the Fermi energy is located in the band gap.

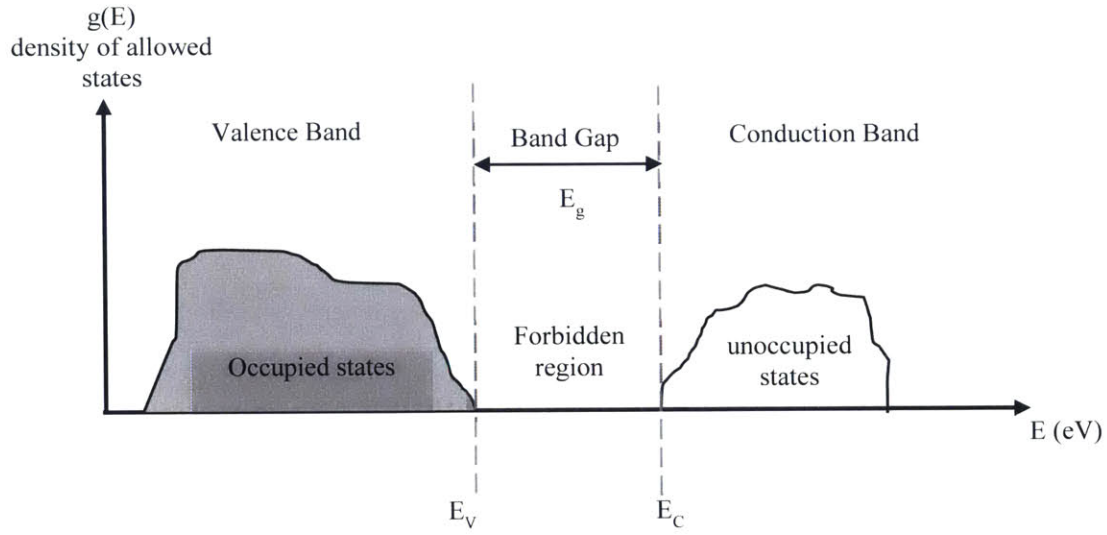

Figure 6-9. Band model of a semiconductor

In semiconductors, charge can be transferred by either holes or conduction electrons. In an *n-type* semiconductor the majority carriers are electrons, and in a *p-type* semiconductor, the majority carriers are holes. The density of electrons in the conduction band, n, and the density of holes in the valence band, p, are given by: [112,113]

$$n(E_c) = \frac{N_c}{1 + \frac{\exp(E_c - E_F)}{k_B T}} \tag{6-3}$$

$$p(E_v) = \frac{N_V}{1 + \frac{\exp(E_F - E_v)}{k_B T}} \tag{6-4}$$

where N_c and N_V are given by:

$$N_c = \int_{E_v}^{\infty} \frac{g_c(E)}{1 + \frac{\exp(E_F - E)}{k_B T}} dE \tag{6-5}$$

$$N_V = \int_{-\infty}^{E_v} \frac{g_v(E)}{1 + \frac{\exp(E - E_F)}{k_B T}} dE \tag{6-6}$$

And $g_c(E)$ and $g_v(E)$ are the density of states in the conduction band and valence band respectively

6.2.2 Energy Levels of Redox Species in Solution

The acceptor and donor energy levels of hydrated redox species are not at the equilibrium energy level, E^o_{redox}, but separated by a reorganization energy. This separation of energy levels results from the difference in charge of the particles and the polarization of water; the water molecules surrounding the redox particles rearrange to form a hydrated structure. The reorganization energies for the oxidized and reduced energies, λ_{ox} and λ_{red}, are often approximated as being identical: $\lambda = \lambda_{red} = \lambda_{ox}$. The energy levels of the oxidized species fluctuate in the range of λ. Figure 6-10 shows the distribution of energy levels in solution.

The distribution of energy levels in the solution, normalized to one, are: [112,114]

$$W_{ox}(E) = \frac{1}{\sqrt{4k_B T \lambda}} \exp\left[-\frac{\left(E - E^o_{F,redox} - \lambda\right)^2}{4k_B T \lambda}\right] \tag{6-7}$$

$$W_{red}(E) = \frac{1}{\sqrt{4k_B T\lambda}} \exp\left[-\frac{\left(E - E^{o}_{F,redox} + \lambda\right)^2}{4k_B T\lambda}\right] \tag{6-8}$$

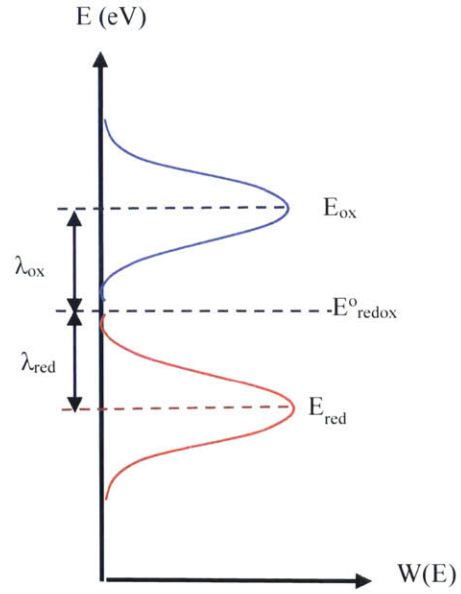

Figure 6-10. Electron energy levels of oxidized and reduced redox species in solution

6.2.3 The Gerischer Model of Electron Transfer

As previously mentioned, electron transfer at semiconductors can only happen when the electron energy levels in the electrode and in the solution are approximately equal. Electron transfer can occur at either the conduction band or valence band energies. Figure 6-11 shows electron transfer from the conduction band to an unoccupied (acceptor) energy level in solution.

Electron transfer can be far more complex than the simple example shown in Figure 6-11. There may be surface states in the band gap which can participate in electron

transfer reactions. [112,115] A high number of surface states can "pin" the Fermi level at the surface, and cause band bending. The left side of Figure 6-12 shows electron transfer thorough a surface state. The right side is an example of band bending; for an n-type semiconductor, this upward band bending will give rise to a depletion layer of the majority n-charge carriers.

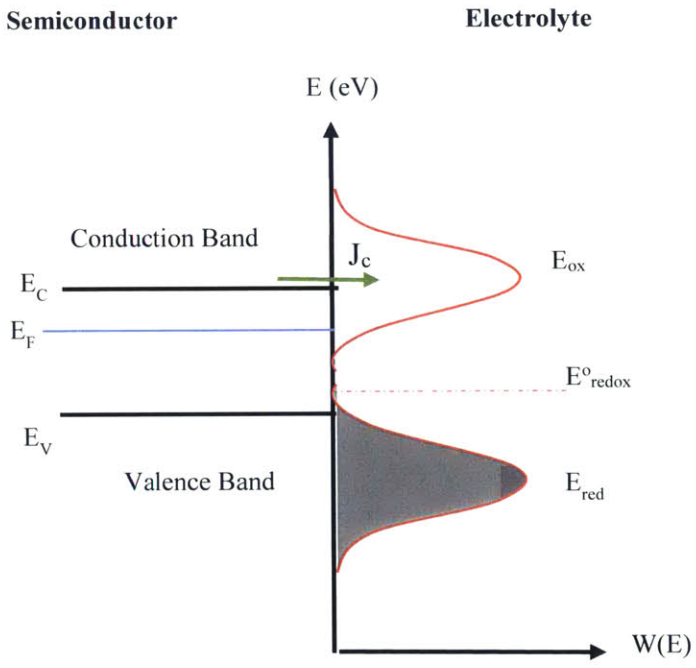

Figure 6-11. Electron transfer from the conduction band to the oxidized specie in solution

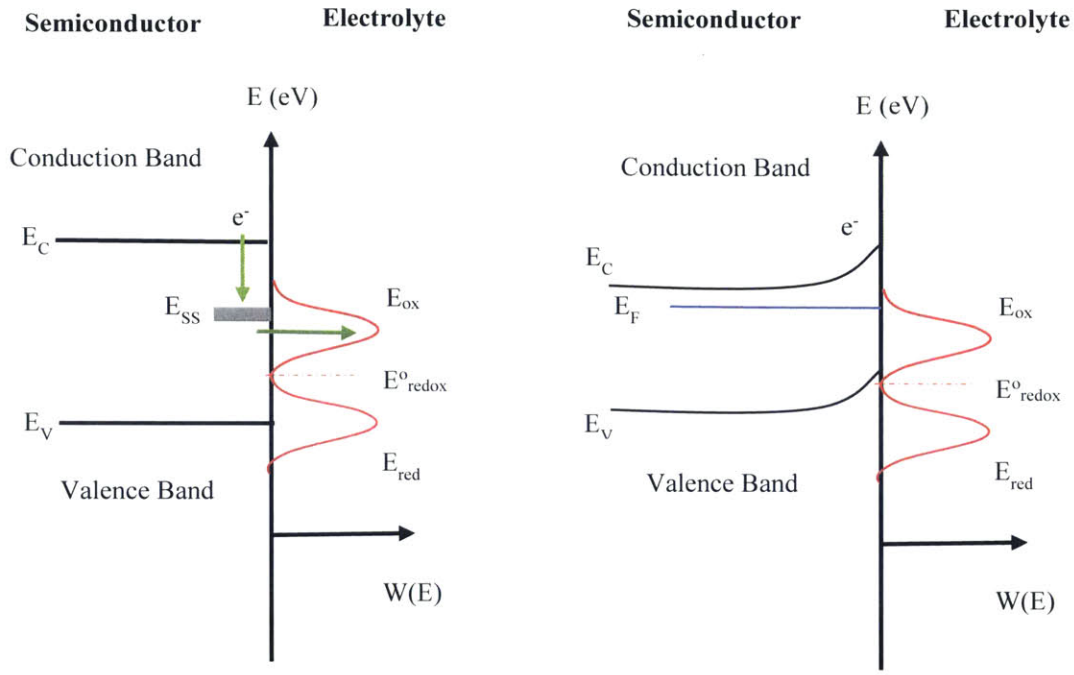

Figure 6-12. Left: Electron transfer through a surface state. Right: Upward band bending due to Fermi Level pinning

Using the Gerischer [53] model for electron transfer, the total current is given by:

$$J = z\int_{-\infty}^{\infty} \nu^{-}(E)n(E)g_{ox}(E)dE - z\int_{-\infty}^{\infty} \nu^{+}(E)n(E)g_{red}(E)dE \tag{6-9}$$

where :

z is the charge transferred

$g_{ox} = c_{ox}\, W_{ox}(E)$

c_{ox} is the concentration of oxidized species

W_{ox} is the distribution of the oxidized species given by Equation (6-7)

n(E) is the electron density at the surface, given by $N(E)g(E)$, where N is the total density of levels per unit energy

The cathodic current is given by:

$$J_c = z\int_{E_{cs}}^{\infty} \nu(E)\, n(E) \frac{c_{ox}}{\sqrt{(4\pi\lambda k_b T)}} \exp\left(-\frac{(E-E_{ox})^2}{4\lambda k_b T}\right) dE \tag{6-10}$$

Where E_{cs} is the conduction band energy at the surface.

If electron transport occurs within $1k_bT$ of the conduction band, then the cathodic current density is approximately:

$$J_c \approx z\nu(E_c)n(E_C)\, c_{ox}\sqrt{\frac{k_bT}{4\pi\lambda}} \exp\left(-\frac{[E_c-(E^o_{redox}+\lambda)]^{\,2}}{4\lambda k_bT}\right) \tag{6-11}$$

A comparison of the band positions for the different oxides, Fe_2O_3, ZrO_2, Cr_2O_3, SnO_2 to the electron energy levels in the coolant will show if the oxides may be able to support the hydrogen evolution reaction. It is important to note that although the energy levels may align properly for electron transport, if there are insufficient electrons in the conduction band at the oxide surface, then the charge transfer rate will be extremely small and/or negligible.

6.3 Constructing the Energy Level Diagram

For the purpose of creating the energy level diagram, we consider the average core at the beginning of cycle (BOC), at an elevation of 3.29 m above the bottom of core. The hydrogen injection is 25 scc H_2 /kg H_2O. The local conditions are listed in Table 6-1.

Table 6-1. Coolant conditions used for constructing the energy level diagram

Temperature	598K/325°C
pH	7.17
ECP	-0.604 V (SHE)
E^O_{H2}	-0.808 V (SHE)
E^O_{O2}	-0.093 V SHE)

6.3.1 Energy levels of the Proton and Neutral Hydrogen Atom in Solution

The equilibrium redox potentials of hydrogen and oxygen, are extracted from the mixed potential model results. From the clean core calculations, the H_2 redox potential ranges from -0.726 to -0.917 V (SHE) and the O_2 redox potential ranges from 0.021 to -0.239 V (SHE) over the various cases modeled. The equilibrium potentials for the clean average core, at BOC with 25 scc H_2/kg H_2O addition are shown in Figure 6-2 below. The axial position used for the energy level diagram is marked with a dotted line.

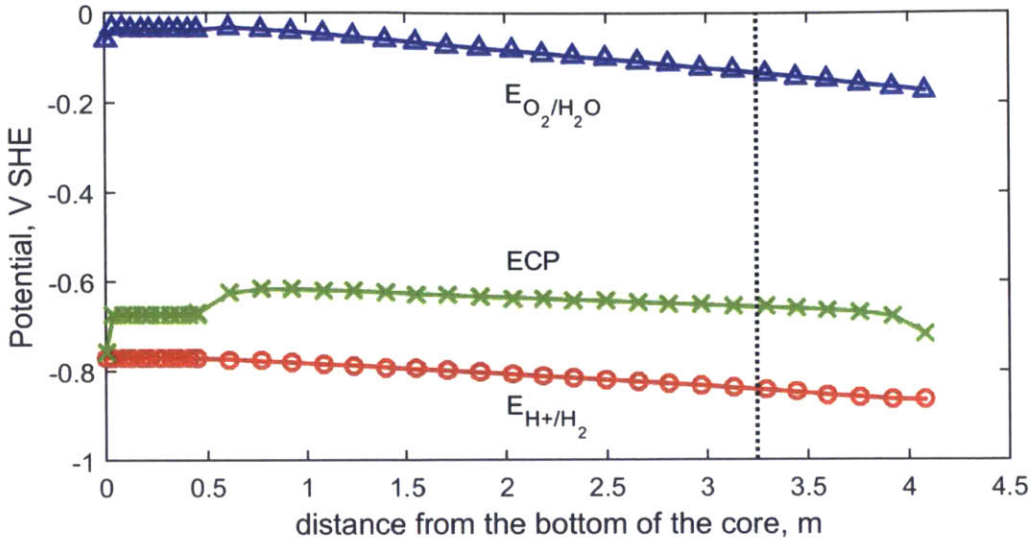

Figure 6-13. Equilibrium potentials of hydrogen and oxygen redox reactions in the average core at BOC with 25 cc STP H_2/kg H_2O

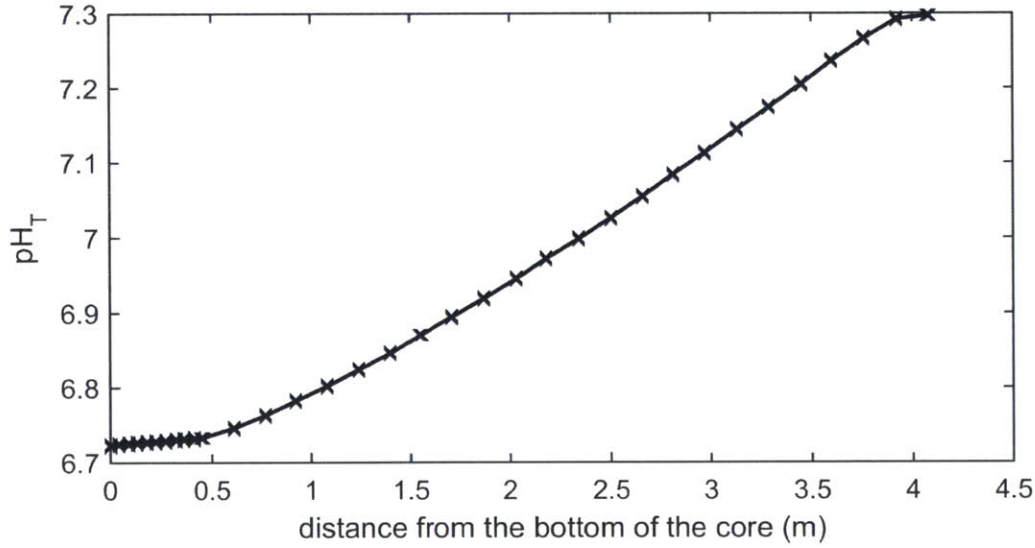

Figure 6-14. pH_T in average core at BOC. 1440 ppm B, and 3.5 ppm Li

The reorganization energy has an inner and outer component:

$$\lambda = \lambda_{in} + \lambda_{out} \tag{6-12}$$

Typical values of the reorganization energy are on the order of 0.1 to 3 eV. [112,114,115]

The reorganization energy at a semiconductor interface is calculated as: [114]

$$\lambda_{out} = \frac{(z)^2}{8\pi\epsilon_o r_{ion}}\left[\frac{1}{\epsilon_{opt,1}} - \frac{1}{\epsilon_{s,1}}\right] - \frac{(z)^2}{8\pi\epsilon_o \mathcal{R}}\left[\frac{1-\frac{\epsilon_{opt,1}}{\epsilon_{opt,2}}}{1+\frac{\epsilon_{opt,1}}{\epsilon_{opt,2}}}\cdot\frac{1}{\epsilon_{opt,1}} - \frac{1-\frac{\epsilon_{s,1}}{\epsilon_{s,2}}}{1+\frac{\epsilon_{s,1}}{\epsilon_{s,2}}}\cdot\frac{1}{\epsilon_{s,1}}\right] \quad (6\text{-}13)$$

where:

Δe is the change in charge

ϵ_o is the perimittivity of vacuum

r_{ion} is the radius of the ion

$\mathcal{R}$ is the distance to the mirror image of the ion

$\epsilon_{opt,1}$ and $\epsilon_{s,1}$ are the optical and static dielectric constant for water

$\epsilon_{opt,2}$ and $\epsilon_{s,2}$ are the optical and static dielectric constant for the semiconductor

This equation can also be applied to a metal; however, the dielectric constants of metal are much greater those that of water, so the equation reduces to:

$$\lambda_{out,metal} = \frac{(\Delta e)^2}{8\pi\epsilon_o r_{ion}}\left[\frac{1}{\epsilon_{opt,1}} - \frac{1}{\epsilon_{s,1}}\right]\left[\frac{1}{r_{ion}} - \frac{1}{\mathcal{R}}\right] \quad (6\text{-}14)$$

There is very little information available about the radius of the first solvation shell of a proton, so a value of r_{ion} =3 A was used, which corresponds to the approximate thickness of a Helmholtz layer. [112] The static dielectric constant of water is

approximately 20 at T = 573 K and 17 at T = 598 K. [116] The optical dielectric constant can be estimated from the refractive index: $\epsilon_{opt} \approx n^2 = 1.7$ for water. Table 6-2 lists values of dielectric constants for the oxides.

Table 6-2. Dielectric constants for oxides

Material	ϵ_s	ϵ_{opt}	Reference
Cr_2O_3	11	6	[117]
Fe_2O_3	24	7	[118]
SnO_2	15	4	[119]
Monoclinic ZrO_2	25	5	[120]

Using Equation (6-13), and the dielectric constants in Table 6-2, the calculated reorganization energies are 1.18-1.46 eV at 598 K. At 573 K, the reorganization energies are approximately 0.07 eV greater. Using Equation (6-14), for a metal, the reorganization energy is approximately 0.6 eV.

It should be noted that in Equation (6-13) and (6-14), the outer shell reorganization energy is proportionate to 1/r, so in order to get a good estimate of the reorganization energy, we would need a more accurate value for the radius of the first solvation shell. In addition, the calculated reorganization energy is sensitive to the relative dielectric constant of water. As the temperature of water increases, the dielectric constant decreases, and the reorganization energy approaches zero. If the coolant is in the vapor phase, the reorganization energy may be negligible. Furthermore, the dielectric constant of water is likely smaller close to a surface. Morrison suggests that using $\epsilon_s = 5$ is a good estimate. [112] Santos and Schmickler estimate the reorganization energy of a proton at a metal electrode as 3 eV. [121] They estimate that the reorganization energy should be ¼ of the hydration energy; attributing half of the hydration energy to

interactions with the particles, and noting that the proton loses half of its solvation shell when adsorbed. [121]

The energy levels of the redox couples on the absolute vacuum scale can be calculated from the redox potentials relative to the standard hydrogen electrode. [112]

$$E(eV\ AVS) = -1 \times [\mathbb{E}(V_{SHE}) - 4.5\ V] \quad (6\text{-}15)$$

The Fermi level of the $H_2/H+$ pair is calculated to be -3.69 eV (AVS) and the Fermi level of the O_2/H_2O pair is at -4.71 eV (SHE). The distribution of electron energy levels in the solution can then be calculated using Equation (6-16) and (6-17).

6.3.2 Band Structure in the Semiconductors

Xu and Schoonen calculated the band positions of many semiconductors on the absolute vacuum energy scale. The conduction band positions were calculated using the absolute electronegativity according to:

$$E_C = -\chi + 0.5\ E_g \quad (6\text{-}16)$$

Where

χ is the absolute electronegativity

E_g is the band gap

Note that absolute electronegativity is a measure of the Fermi energy of an intrinsic semiconductor without acceptor and donor states. Data on the relevant oxides is listed in Table 6-3.

Table 6-3. Band positions of oxides on the absolute vacuum scale [122]

	Abs. electronegativity, χ (eV)	**Bandgap, E_g (eV)**	**E_c (eV)**	**Flat band potential E_{fb}, at pH_{zpc} (eV)**	**pH_{zpc} at 298K**
Cr_2O_3	5.68	3.5	-3.93	-4.22 *	8.1
Fe_2O_3	5.88	2.2	-4.78	-4.69	8.6
Fe_3O_4	5.78	0.1	-5.73		6.5
SnO_2	6.25	3.5	-4.5	-4.55	4.3
ZrO_2	5.91	5	-3.41	-3.08	6.7

* taken from Carmezim et al.'s measured flat band potential of -0.5 SCE at pH 8.4 and 298K [123]

Band energies at the semiconductor/electrolyte interface change with pH, according to the equation below: [112,122]

$$E_{Cs}(eV\ AVS) = -\chi + 0.5\,E_g - 2.303k_BT(pH_{zpc} - pH) \quad (6\text{-}17)$$

The pH_{zpc} is observed to change with temperature; it has been observed to decrease by 1-2 pH units as the temperature rises from 25°C to 200-300°C, and increases after 200-300°C. [122] There is minimal information on the pH_{zpc} of these oxides at reactor temperatures, and there can be significant spread in the measured values.

An alternate approach is to estimate the band positions from the flat band potential. The flat band potential is the *measured potential* in the absence of a space charge film. For n-type semiconductors, the flat band potential is near the conduction band, and for p-type semiconductors, it is near the valence band. The flat band potential changes with pH as in Equation (6-17). [112]

Using the data from Table 6-3 and the coolant conditions listed in Table 6-1 (pH_T=7.17, T= 598 K), we estimate conduction band positions for the energy level

diagram. In Table 6-4, the left column is the conduction band estimated according to (6-17), and the right column is the conduction band estimated from the flat band potential. For these calculations, pH_{zpc}(598 K) is assumed to be 2 pH units smaller than the pH_{zpc} at 298K. Note that if $pH_{zpc}(598K) \approx pH_{zpc}(298K)$, the conduction bands would be -0.243 eV lower than the values presented here. For Fe_2O_3, SnO_2, and ZrO_2, the flat band estimate is slightly higher than the electronegativity estimate. For Cr_2O_3, the flatband estimate is lower, however Cr_2O_3 can be either p or n-type.

Table 6-4. Estimated conduction band energies on the absolute vacuum energy scale, from electronegativity and flat band potentials.

	E_c (electronegativity)	**$E_c = E_{fb}$**
Cr_2O_3	-3.80	-4.10
Fe_2O_3	-4.71	-4.62
Fe_3O_4	-5.41	
SnO_2	-3.92	-3.97
ZrO_2	-3.12	-2.79

The difficultly with using the pH_{zpc} to estimate the conduction band position at the oxide/coolant interface, is that the pH_{zpc} depends on the nature of the interface. This means that it depends on acceptor and donor states at the surface, the surface orientation, etc. We would expect the oxide layer of zirconium alloys to have defects: vacancies, impurities, etc. Thus, this approach may not be very useful for corrosion of zirconium alloys, especially under irradiation.

6.3.3 Assembling the Energy Level Diagram

In this section, we compare the calculated conduction band energies to the energy level distribution of the hydrogen redox reaction, calculated using Equations (6-7) and (6-8). Based on the calculation in Section 6.2.2, we consider two values of the reorganization energy: 1.5 eV for oxides, and 0.6 eV for metals. For one of these oxides to serve as a cathodic site it should be n-type, meaning conduction band electrons are the dominate charge carrier. ZrO_2, SnO_2, Fe_2O_3 are normally n-type, and Cr_2O_3 can be either n or p-type.

Figure 6-15 compares the conduction band energies from absolute electronegativities (listed in Table 6-4) to the energy levels of the proton/neutral hydrogen pair for a reorientation energies of 0.6 eV and 1.5 eV. Only the conduction band of ZrO_2 is above (higher in energy) than the Fermi energy of the H^+/H_2 pair, E^o_{H2}. Based on these calculated band positions, only ZrO_2 would be a likely site for proton reduction. Cr_2O_3 and SnO_2 might be able to transfer electrons to protons, but only if the reorganization energy is negligible. If the reorientation energy is large, then the conduction band for an "ideal" recombination site would be at a more positive energy than what we predicted for ZrO_2.

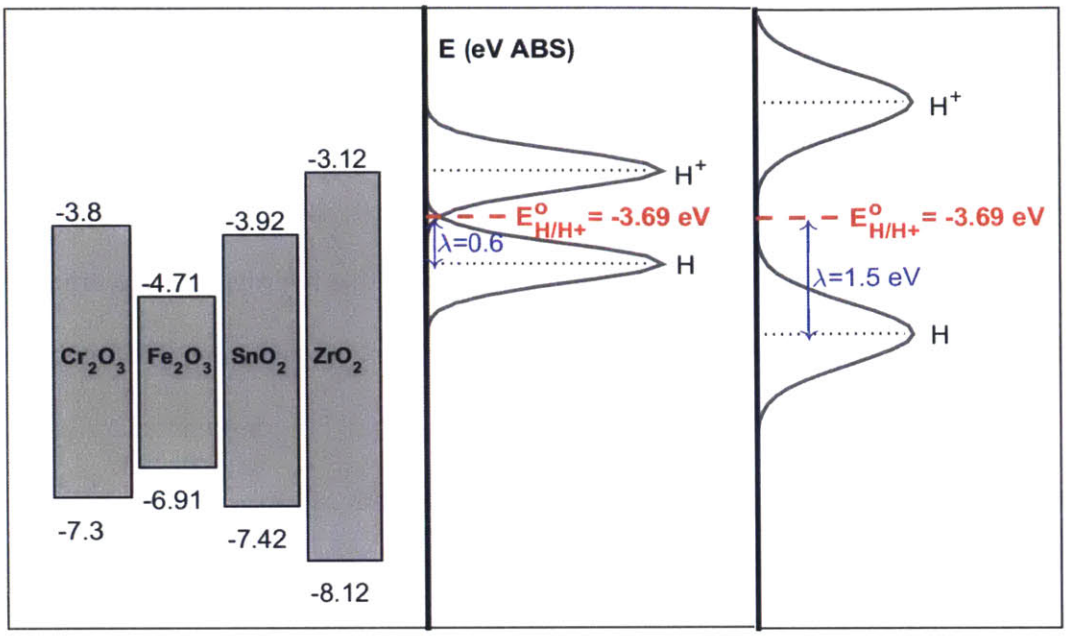

Figure 6-15. Electron energy level diagrams comparing conduction band energies at the oxide coolant interface to the energies of the $H+/H_2$ redox couple. All energies are on the absolute vacuum scale. Conduction band energies determined from absolute electronegativity and pH_{zpc}

In the water chemistry calculations, we calculated the ECP, or corrosion potential, which is a measure of the Fermi level in the metal. For PWR type conditions with a hydrogen overpressure, the measured ECP are reported to be close to the hydrogen potential. For the coolant conditions shown in the energy diagram, the calculated ECP was -0.604 V (SHE), corresponding to -3.9 eV (AVS). The calculated ECP is close to the hydrogen potential, as expected. However, the mixed potential model is for type 304 stainless steel and not Zircaloy-4. The difference in ECP of the two materials should be relatively small at least for thin oxide films, based Kim et al.'s measured values of ECP

in 300°C water. [51] A brief summary of their findings follows. In reducing conditions, 150 ppb H_2, ECP measurements were similar for Zircaloy-2 and 304 SS. The ECP of Zircaloy-2 was more negative than that of 304 SS, but the difference was less than 0.1 V. ECP measurements taken in more oxidizing conditions, with oxygen added to the water, showed greater differences between the two alloys. We note that hydrogen concentration is significantly higher in a PWR reactor than these experiments (a minimum 2000 ppb H_2), so it stands to reason that the ECP of Zircaloy-4 should not be significantly different from that of 304SS in PWR conditions, at least at for thin oxide layers.

For electron transport to occur from the metal to the oxide, the Fermi level in the oxide layer must be lower than the Fermi level in the metal. This allows us to place an *upper bound* on the Fermi level in the oxide. Figure 6-16 shows the conduction and valence bands from Xu and Schoonen. The significant finding from this comparison is that the ECP/Fermi energy of -3.9 eV is outside of the band gap for all oxides except for ZrO_2. This behavior is expected: from potential-pH diagrams, we know that at a fixed pH, there is a threshold potential below which oxides are not stable. Experiments show that precipitates are metallic near the oxide/metal interface, and oxidized farther from the the metal. Given that the Fermi level in the oxide decreases from the metal/oxide interface to the oxide/coolant interface, the band energies and ECP appear to be consistent, and the mixed potential model ECP appears to be an upper bound for the potential in the oxide.

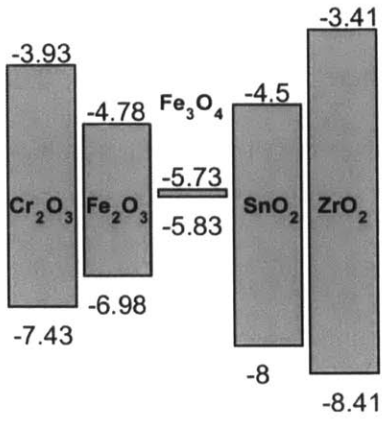

Figure 6-16. Band positions of oxides, from absolute electronegativities, on the absolute vacuum scale [122]

However, in experiments, the measured ECP (open-circuit potential) changes as the oxide grows. Measured open circuit potentials consist of the changes in potential across the metal-oxide interface, the oxide layer, and the electrolyte. From experiments, the potential at the oxide surface becomes more positive as the oxide layer grows. This corresponds to a drop in Fermi energy. In order for the oxides to exist at the surface without becoming degenerate, the Fermi energy must be within the band gap. A degenerate oxide would be metallic-like in its ability to conduct electrons. For example, if Fe_3O_4 was degenerate at the surface, the Fermi level, which would be less than -3.9 eV AVS would still be lower than $E_{H/H+}$. Electron transport to the unoccupied H+ states in the coolant would be unlikely, as there would be a significant number of states in the oxide at a lower energy.

If we assume that the conduction band and valence band in the bulk to be fixed, we can estimate the maximum possible conduction band energy at the interface, provided

that the oxide does not become degenerate. For an n-type conductor, if the Fermi level is near the conduction band and there is a depletion layer, then the valence band at the electrolyte interface must be lower than the conduction band in the bulk, as shown in the left side of

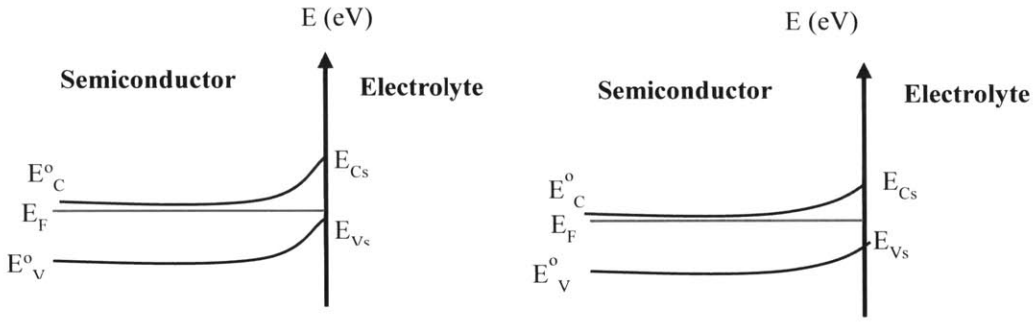

Figure 6-17. With such extreme band bending, conduction electrons would be extremely depleted at the surface, so as a more reasonable limit, we can consider the case where the band energies are $1/2E_g$ greater than the bulk values, as shown on the right side of

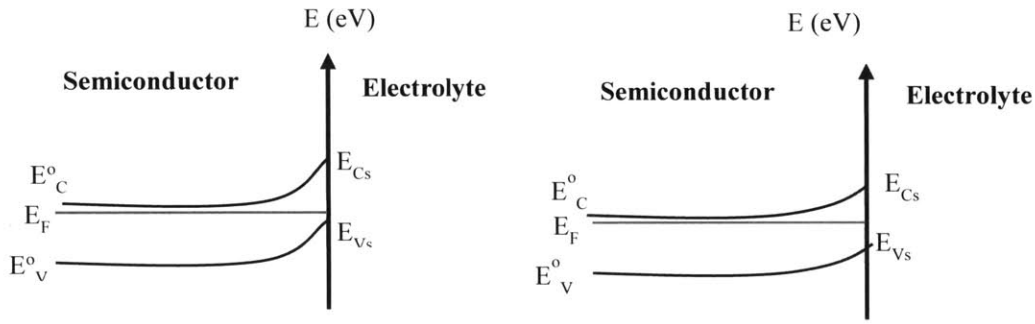

Figure 6-17.

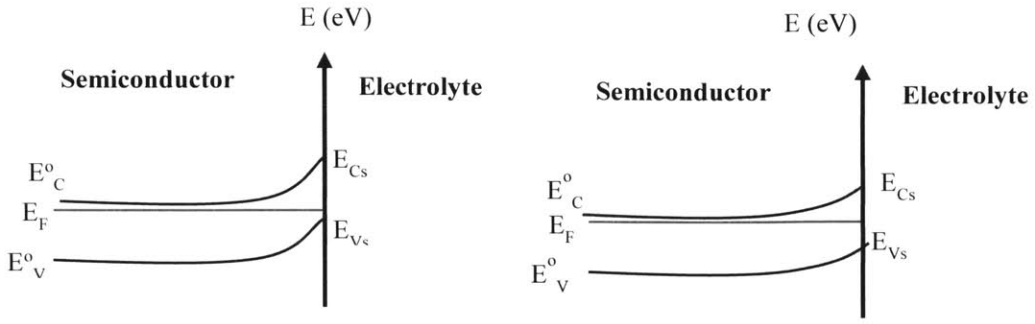

Figure 6-17. Band bending for a depletion layer at an n-type semiconductor

Assuming upward band bending of $1/2E_g$, we calculate the bands at the surface, as shown in Figure 6-18, and compare to the energy levels of the proton and neutral hydrogen in solution. The conduction band minimum of Fe_2O_3 is at the same energy as $E^o_{H/H+}$. If reorientation energies are non-negligible, then it does not seem a likely site for the proton reduction reaction. The conduction bands of Cr_2O_3, SnO_2, and ZrO_2 are positioned such that electron transfer could occur from the conduction band to the acceptor energy level. However, we must note that band bending will deplete the number of conduction electrons at the oxide surface. If significant band bending occurs, the conduction band energies may be positioned favorably for electron transport, but fewer conduction electrons will be available.

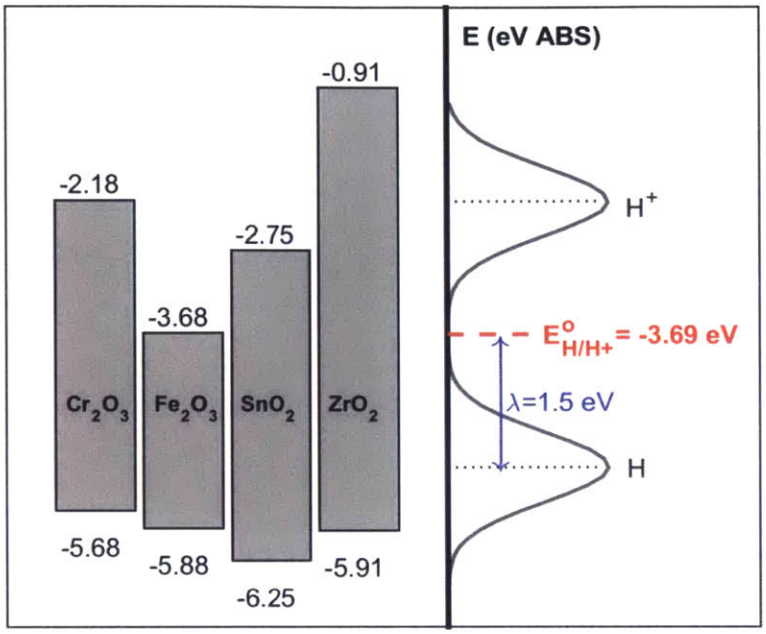

Figure 6-18. Energy level diagrams comparing conduction band energies of oxide with upward band bending to the energies of the H/H+ redox couple. Bands edges are assumed to shift ½ E_g up from E_c and E_v in the bulk

6.3.4 Conclusions from the energy level comparisons

It is difficult to draw conclusions from this energy level approach. Although we can calculate the equilibrium energy of the H/H+ redox pair in the coolant, $E^o_{H+/H}$, we cannot determine the energy levels for the reduction reaction in the coolant without a reorientation energy. Nonetheless, this electron energy level comparison shows that if the reorganization energy is large, then ZrO_2 will be the most likely site for proton reduction.

A second difficulty with the energy level approach is that we need to determine the band edges at the oxide/coolant interface. This is particularly challenging, as the band

edges depend on properties of the interface - meaning the orientation of the exposed surface, pH, surface states, and any defects.

A third challenge is that this energy level approach is typically used for equilibrium conditions, meaning that the Fermi energy would be constant throughout the oxide. For zirconium alloys undergoing corrosion, this is not the case. There must be a drop in Fermi energy for electrons to migrate from the metal to the cathodic sites. While we can apply the mixed potential model to estimate the Fermi level in the metal. However, we cannot quantify the Fermi energy change across the oxide; we can only predict an upper bound.

Ramasubramanian et al. had previously applied this energy level approach to hydrogen evolution. [8] In their results, they concluded that the conduction band energy of ZrO_2 is too high for proton reduction and that the valence band of SnO_2 would align with the energy distribution for proton reduction. In this thesis, we find that the energy for proton reduction is relatively high, either near or above the conduction band energy of SnO_2.

6.4 Implications for Radiolysis and Photocatalytic Water Splitting

For the coolant conditions, the energy difference between the HER and OER is relatively small, ~0.7eV, while at standard conditions it is 1.2 eV. For photocatalytic water splitting, the conduction band energy should be above the energy of the hydrogen evolution reaction ($E^{o}_{H/H+}$), and the valence band energy should be below the energy

oxygen evolution. For now, we do not consider the role of reorientation energy. Based on the estimated band positons, the valence bands of the oxide are likely to be below the OER. The primary concern is whether the conduction bands are at a high enough energy for proton reduction. Based on the energy level comparison, only ZrO_2 has a conduction band energy that is high enough. For the other oxides, significant band bending would be required.

6.5 Chapter Summary

In this chapter, the molecular oxygen and molecular hydrogen chemical potentials in the bulk coolant of a PWR core are calculated. The energy levels for the hydrogen redox reaction have also been studied, and compared against estimates of conduction band energies of oxides that could be present in the Zircaloy-4 oxide layer.

The chemical potential calculations showed that in PWR conditions (25-50 scc H_2/kgH_2O), the hydrogen chemical potentials are independent of radiolysis effects. Consequently, only temperature and the concentration of hydrogen added to the coolant are needed to estimate the hydrogen chemical potential. The effects of radiolysis should be considered in oxygen chemical potential calculations.

There are numerous uncertainties in the energy level comparisons, namely the reorganization energy for the redox couples and the band energies at the oxide/coolant interface. The energy level comparison can be used to rule out Fe_3O_4 as a likely site for the hydrogen evolution reaction. Unfortunately, it can do little else: Cr_2O_3, Fe_2O_3, SnO_2, and ZrO_2 should not be ruled out. The results indicate that if reorientation energies for

hydrogen reduction are substantial, then ZrO_2 is most likely better than the other oxides- as its conduction band is positioned at a higher energy, and the large band gap allows for more band bending at the surface. It should also be noted that Fe_2O_3 is less likely to be a site for proton reduction than Cr_2O_3 and SnO_2, because the conduction band is at a lower energy. Surface states and doping effects from alloying elements in Zircaloy-4 are likely to play an important role in electron transport.

Regardless of uncertainty in the reorganization energy, the energy analysis shows that a small potential drop across the oxide would be advantageous for proton reduction. Similarly, cracks and large pores would be ideal sites for the cathodic reaction, because the Fermi level at these sites would be higher. However, the chemistry within the cracks and pores is difficult to determine. For small cracks and pores, coolant/surface interactions are likely to be very important. The Helmholtz layer is typically thought to be ~3 A, and if pore diameters are 1-3 nanometers, then a typical electrode/electrolyte model would not be applicable. In such a situation, molecular dynamics could be used to better understand this oxide/coolant interface.

A more important question is whether this energy level analysis is useful for understanding proton reduction at an oxide surface. Protons can adsorbed to oxide surfaces at very close distances, as we will see in Chapter 8. If proton reduction involves chemisorption, it is an inner shell electron transfer process. While Marcus theory may still be applicable, the outer shell reorganization energy, as calculated in this chapter may not. In such a case, it would be better to explicitly model protons and water molecules at the oxide surface.

The next step in understanding the hydrogen split is to understand the nature of hydrogen-oxide interactions. This brings us to the next two chapters, where we will study Fe_2O_3, Cr_2O_3, and their interactions with hydrogen.

Chapter 7: Bulk and Surface Properties of Cr_2O_3 and Fe_2O_3

In this chapter, the bulk and surface structure of α-Cr_2O_3 and α-Fe_2O_3 will be explored using density functional theory (DFT). From the literature review, the oxidized $Zr(Cr,Fe)_2$ precipitates can contain: ZrO_2, Cr_2O_3, Fe_2O_3, Fe_3O_4, $(Fe_x,Cr_{1-x})_2O_3$, as well as metallic Cr and Fe. For fully oxidized precipitates, such as those found at the outer oxide surface, it is unlikely that chromium and iron remain in a metallic form. Oxidized precipitates have been reported to be depleted in iron, with Fe/Cr ratios less than one. Thus, for these cases it is likely that Cr_2O_3 makes up a substantial part of the oxidized precipitate surface. Fe_2O_3 and Cr_2O_3 have the same crystallographic structure which make them ideal to compare for DFT calculations. Furthermore, studying the two oxides separately may help us predict the behavior of mixed $(Fe_x,Cr_{1-x})_2O_3$.

To put the DFT studies in this thesis into context, we present a brief overview of the literature. There have been several comprehensive studies on using DFT+U to model the electronic, magnetic, and tensile properties of bulk Fe_2O_3 and Cr_2O_3, the most notable are those by Rohrbach et al. and Mosey and Carter. [124–128] Researchers have also studied the structure of the (0001) surfaces. [124,129–134] There are several studies of water interactions with the (0001) surface of Fe_2O_3, [129,133–136] and a few with the (0001) surface of Cr_2O_3. [131,137] However, there have been relatively few studies on hydrogen interactions with either of these materials. A list of DFT studies of hydrogen interactions with Fe_2O_3 or Cr_2O_3 follows:

- Nigussa et al. studied atomic adsorption of hydrogen, chlorine, and sulfur on (0001) Cr_2O_3. [130]
- Chen et al. studied hydrogen diffusion in bulk Cr_2O_3 [138]
- Malki et al. studied defects in bulk Cr_2O_3, including hydrogen defects [139]
- Souvi et al. studied the stability of the (0001) Fe_2O_3 surface under exposure to water, hydrogen, and oxygen [129]

The calculations presented in this chapter are not "unique" in that similar calculations have already been performed by other researchers. However, they are a necessary step in studying hydrogen interactions with the Fe_2O_3 and Cr_2O_3 oxide surfaces. The first steps to studying these interactions is to model the bulk crystal and compare it against experimental data, such as lattice parameters, magnetic moments, bulk moduli, and the band gap. If the bulk model is satisfactory, then it can be used to create a surface model. If experimental data is available, it can be used to verify the surface model. A satisfactory surface model can then be used to study adsorption.

7.1 Crystallographic Structure

Cr_2O_3 (eskolaite) and Fe_2O_3 (hematite) both have the corundum structure (space group $R\bar{3}c$, group 167). The primitive cell is rhombohedral and has 10 atoms, and this structure is equivalent to a 30 atom cell on a hexagonal lattice.

Table 7-1 and Table 7-2 list the coordinates of the atoms in the rhombohedral cell and hexagonal cell respectively. Note that there are two internal lattice parameters, x and z, which determine the position of oxygen and the metal ions, respectively. Figure 7-1 shows the two cells and how they align.

Table 7-1. Wyckoff Positions for corundum structure in rhombohedral axes [140–142]

Atom	Wyckoff Position	Atomic Positions
O	6e	(x, 0.5-x, 0.25) (0.25, x, 0.5-x) (0.5-x, 0.25, x) (-x, x+0.5, 0.75) (0.75, -x, x+0.5) (x+0.5, 0.75, -x)
Cr	4c	(z, z, z) (0.5-z, 0.5-z, 0.5-z) (-z, -z, -z) (z+0.5, z+0.5, z+0.5)

Table 7-2. Wyckoff Positions for corundum structure in hexagonal axes [140–142]

Atom	Wyckoff Position	Atomic Positions (0,0,0)+ , (2/3,1/3,1/3) +, (1/3,2/3,2/3) +
O	18e	(x, 0, 0.25) (0, x, 0.25) (-x , -x, 0.25) (-x, 0, 0.75) (0, -x, 0.75) (x, x, 0.75)
Cr	12c	(0, 0, z) (0, 0, 0.5-z) (0, 0, -z) (0, 0, z+1/2)

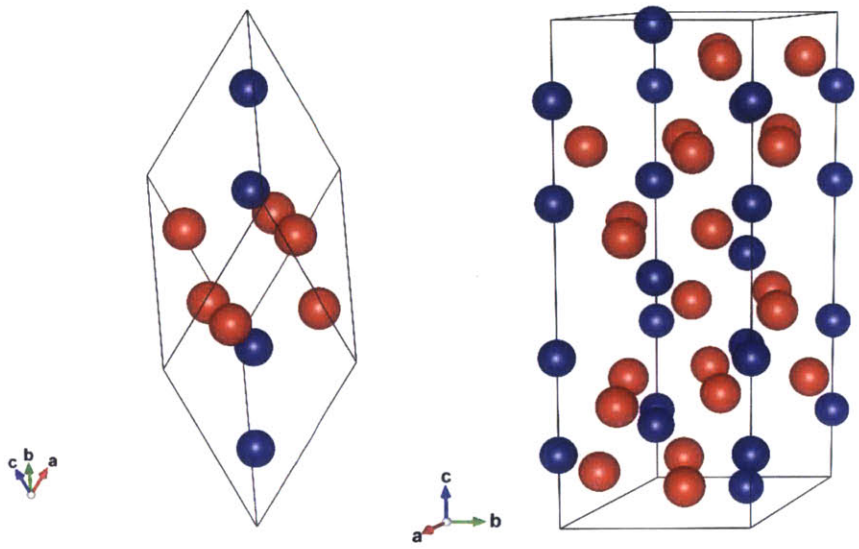

Figure 7-1. The rhombohedral cell (left) and hexagonal cell (right) of Cr_2O_3. Oxygen atoms are shown in red, and Cr in blue. The (1,1,1) direction in the rhombohedral cell aligns with the (0001) direction in the hexagonal cell.

7.2 Calculation Details

Density functional theory calculations were performed using the Vienna Ab-initio Simulation Package (VASP) [143–146] with the Projector-Augmented Wave (PAW) method. [95, 96] The exchange-correlation was treated with the generalized gradient approximation (GGA) of Perdew-Burke-Ernzerhof. [149,150] On-site coulomb interactions were treated with the simplified rotationally invariant DFT+U method of Duderev et al. [151]. A value of U-J=4 was used for both Fe and Cr, as recommend by Rohrbach et al. and Mosey and Carter for Cr_2O_3, and Rollmann et al. for Fe_2O_3. [124–126]

A plane wave cutoff energy of 520 eV was used. The valence electrons modeled were $3p^6 4s^1 3d^5$ for Cr, $4s^1 3d^7$ for Fe, and $2s^2 2p^4$ for O. For relaxations, ions were relaxed until the total force on each atom was less than 0.01 eV/A.

Bulk calculations were performed with the 10 atom rhombohedral unit cell, using the tetrahedral method with Blochl corrections. [152]A 3x3x3 gamma centered k-point grid was used. A 10x10x10 k-point grid was used for density of state calculations.

Surface calculations were performed with the hexagonal cell, using a 3x3x1 gamma centered k-point grid. Gaussian smearing with σ=0.05 eV was used for surface relaxations.

Bader charge analysis was performed using the code by the Henkelman group. [153–155] VESTA was used for visualization. [156,157]

The bulk modulus was determined by using the Birch-Murnaghan equation of state: [110]

$$E_{tot}(a) = E_o + \frac{9\mathbb{V}_o B_o}{16}\left\{\left[\left(\frac{a_o}{a}\right)^2 - 1\right]^3 B_o' + \left[\left(\frac{a_o}{a}\right)^2 - 1\right]^2 \left[6 - 4\left(\frac{a_o}{a}\right)^2\right]\right\} \quad (7\text{-}1)$$

where

a_o is the equilibrium lattice constant

$\mathbb{V}_o$ is the equilibrium volume per atom

B_o is the bulk modulus at zero pressure

$B_o' = \frac{\partial B_o}{(\partial P)_T}$

E_o is the DFT calculate energy at the equilibrium volume

To solve for the bulk modulus, the parameters a_o, B_o, B_o', E_o are treated as parameters. After optimizing the rhombohedral unit cell, we vary the lattice parameter slightly and perform DFT calculations to obtain the total energy as a function of lattice parameter. The data was then fit to a 3rd order polynomial using a least squares fit as follows:

$$E_{tot}(a) = c_3\left(\frac{1}{a}\right)^6 + c_2\left(\frac{1}{a}\right)^4 + c_1\left(\frac{1}{a}\right)^2 + c_o \tag{7-2}$$

a_o, B_o, and B_o' can be calculated from the following equations:

$$c_1 a_o^4 + 2c_2 a_o^2 + 3c_3 = 0 \tag{7-3}$$

$$B_o' = \frac{14c_3 + 4a_o^2 c_2}{a_o^2 c_2 + 3c_3} \tag{7-4}$$

$$B_o = \frac{16c_1}{9V_o a_o^2(3B_o' - 16)} \tag{7-5}$$

7.3 Cr_2O_3 Bulk Properties

We begin the DFT calculations by studying bulk Cr_2O_3. In this section, we compare the use of the local density approximation (LDA) and generalized gradient approximation (GGA) for the exchange correlation energy. We will also compare results with and without U corrections. The DFT calculations are compared against experimentally measured bulk properties to select a method for the remaining DFT calculations in this thesis.

7.3.1 Magnetic Configuration

The Cr atoms are aligned along the [111] axis in the rhombohedral cell with two different distances between neighboring atoms, as shown in Figure 7-2. Four different magnetic configurations of the Cr atoms, one ferromagnetic and three antiferromagnetic were compared.

Experiments have shown that Cr_2O_3 is antiferromagnetic. The DFT calculations confirmed that the antiferromagnetic +-+- spin alignment, in which neighboring Cr atoms have opposite spin, is the lowest energy configuration. This configuration was found to have the lowest energy, with both LDA and GGA and with and without U corrections. A summary of the calculations results is shown below in Table 7-3.

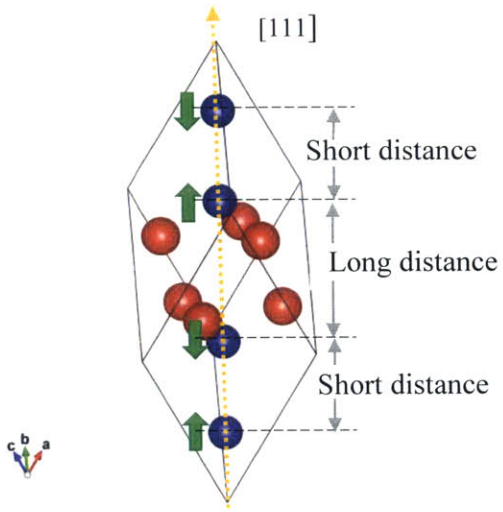

Figure 7-2. Magnetic configuration of Cr_2O_3. The spin moments of the chromium are aligned +-+- along the [1,1,1] direction.

Table 7-3. DFT energies for bulk Cr_2O_3 with different magnetic configurations. Ionic loop convergence set to $1x10^{-3}$ eV

	Magnetic State	Total energy of cell (eV)	Mag. Mom. of Cr	Mag. mom. of O
LDA	Ferromagnetic	-95.3099	2.831	0.011
	Antiferromagnetic. +-+-	**-96.3786**	2.193	0
	Antiferromagnetic, ++--	-96.0759	2.262	0.008
	Antiferromagnetic, +--+	Did not converge to this magnetic state		
GGA	Ferromagnetic	-87.3205	2.888	0.018
	Antiferromagnetic. +-+-	**-87.7955**	**2.635**	**0**
	Antiferromagnetic, ++--	-87.5918	2.641	0.009
	Antiferromagnetic, +--+	-87.3532	2.621	
LDA+U	Ferromagnetic	-85.8291	2.968	-0.047
	Antiferromagnetic. +-+-	**-85.9317**	2.862	0
	Antiferromagnetic, ++--	-85.8332	2.861	0.011
	Antiferromagnetic, +--+	Did not converge to this magnetic state		
GGA+U	Ferromagnetic	-78.5629	3.005	0.064
	Antiferromagnetic. +-+-	**-78.6332**	2.932	0
	Antiferromagnetic, ++--	-78.545	2.926	0.009
	Antiferromagnetic, +--+	78.4514	2.911	0

7.3.2 Bulk Properties

Additional calculations were performed for the (+-+-) ordering, to determine the band gap and the bulk modulus. Additionally, the internal lattice parameters, the hexagonal lattice parameters, and the magnetic moment of the chromium atoms were determined. These results are presented in Table 7-4, along with Cr_2O_3 calculations from the literature. [124,126,131,158,159] All of the information from the literature is for the antiferromagnetic (+-+-) ordering. The results are grouped into LDA, GGA, LDA+U, and GGA+U. The results from the present study have good agreement with the results found in literature.

Table 7-4. Comparison of bulk Cr_2O_3 calculated properties to results from literature

	Plane wave cutoff energy (eV)	k points	a (Å)	c (Å)	x (O)	z (Cr)	B_o (GPa)	E_g (eV)	Mag. Moment of Cr (μ_b)	Ref.
LDA	550	3x3x1	4.73	13.8	0.322	0.341	215	0.9	2.2	[126]
LDA	520	3x3x3 (rhomb.)	4.71	13.84	0.323	0.341	213	0.808	2.19	This work
GGA (PW91)	350	4x4x1 8x8x1 for DOS	4.94	13.83			204	1.2	2.68	[124]
GGA (PBE)	550	3x3x1	4.95	13.83	0.311	0.345	205	1.5	2.61	[126]
GGA (PBE)	520	3x3x3 (rhomb.)	4.94	13.82	0.311	0.345	207	1.44	2.64	This work
LDA+U U=4.5, J=1*	500	11x11x11 (rhomb.)	4.94	13.55	0.305	0.348		3.36		[158]
LDA+U U-J=3.42	520	4x4x4 (rhomb.)						3.07	2.86	[159]
LDA+U U-J=4	550	3x3x1,	4.94	13.55	0.305	0.347	240	3.2	2.9	[126]
LDA+U U-J=4	520	3x3x3, (rhomb.)	4.95	13.57	0.305	0.348	238	3.01	2.86	This work
GGA +U (PW91)	520	3x3x1	5.07	13.84				2.8	2.91	[131]
GGA +U (PW91) U-J=4	350	4x4x1 8x8x1 for DOS	5.07	13.84			230	2.6	3.01	[124]
GGA+U (PBE) U-J=4	550	3x3x1	5.07	13.87	0.304	0.348	200	3.1	2.97	[126]
GGA+U (PBE) U-J=4	520	3x3x3 (rhomb.)	5.07	13.86	0.304	0.348	199	3.19	2.93	This work

*Uses Leichtenstein method for U corrections. The remaining calculations use Dudarev's method.

Table 7-5 below compares the calculated results to experimental values. As to be expected, GGA slightly over predicts the volume, and LDA under predicts it. GGA+U over predicts the volume by 7%, while LDA+U is very close to the experimental values (within 1%). The c/a ratio is approximately 2% larger than experimental values for GGA, and 7% for LDA. However, for GGA+U and LDA+U, the c/a ratios are less than 1% off from experiment. For the internal lattice parameters, x(O) and z(Cr), LDA+U and GGA+U are in nearly perfect agreement with experimental values, while GGA and LDA over predict x(O) and under predict z(Cr).

For the band gap, LDA and GGA grossly under predict the band gap. With the U corrections, the calculated band gaps approach the experimental value. LDA+U underestimates the band gap by 11%, and GGA+U underestimates the band gap by 6%.

All of the calculated bulk moduli are less than the experimental values. LDA+U, which performs the best, predicts the bulk modulus within 5% of experiment. GGA+U performs the worst, underpredicting the modulus by 13-14%.

Based on the above comparisons, the remaining calculations in this thesis were performed with GGA+U.

Table 7-5. Comparison of DFT calculated bulk properties of Cr_2O_3 to experimental values

	E_{coh} (eV/ atom)	Vol. per unit formula (Å^3)	a (Å)	c/a	x (O)	z (Cr)	Mag. Mom. of Cr (μ_b)	E_g (eV)	B (GPa)
GGA	5.46	48.78	4.94	2.796	0.311	0.345	2.64	1.44	207
LDA	6.65	44.39	4.71	2.937	0.323	0.341	2.19	0.81	213
GGA+U	4.95	51.46	5.07	2.734	0.304	0.348	2.93	3.19	199
LDA+U	6.02	47.93	4.95	2.744	0.305	0.348	2.86	3.02	238
Exp. [160]									231
Exp. [161]		47.9967	4.951	2.7340	0.3051	0.34766			228
Exp. [162]		48.3028	4.9607	2.7414	0.306	0.3475			
Exp. [163]								3.4	
Exp. [164]							2.48		
Exp. [165]							2.76		

Bader charge analysis was performed, and the charges were calculated as +1.8 for chromium and -1.2 for oxygen. The electronic density of states is shown in Figure 7-3. In this plot, the Fermi energy is set to zero eV, and the spin up and spin down density of states are shown separately. The valence and conduction band edges are clearly visible at 0 and 3.2 eV; there is no gradual transition in g(E) near the band edges. In the calculations that follow, we will use atom *projected densities of states* to compare local electronic structure to the bulk structure.

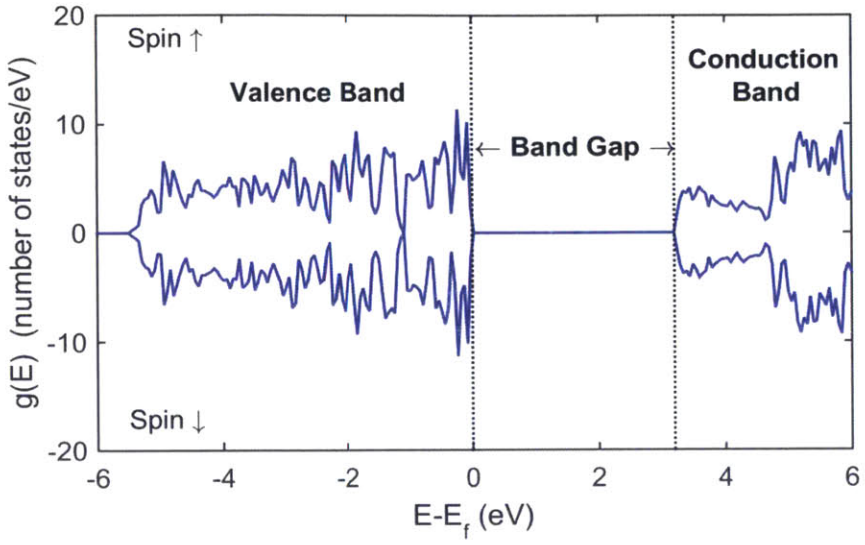

Figure 7-3. Density of States for bulk Cr_2O_3

7.4 Fe_2O_3 Bulk Calculations

For hematite, calculations were only performed using GGA+U. The magnetic ordering was confirmed to be +--+ along the [111] direction, as shown in Figure 7-4. The iron atoms with the shorter distances between them have opposite spin, whereas those with the longer distance between them have the same magnetic moments.

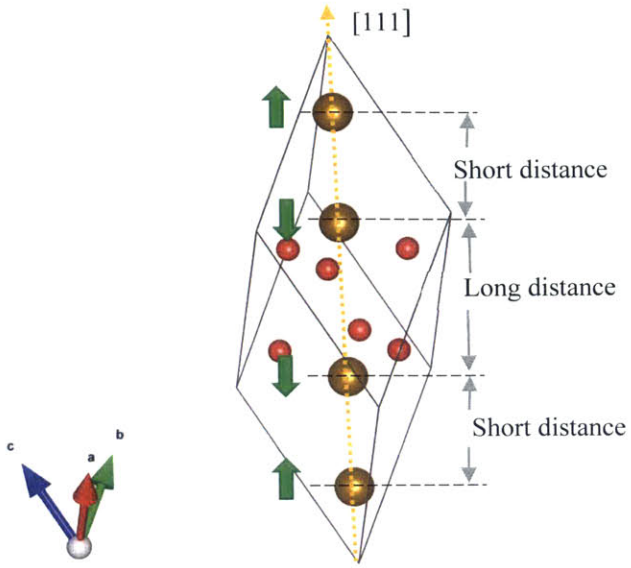

Figure 7-4. Magnetic Alignment of Fe_2O_3. The spin moments of the chromium are aligned +--+ along the [1,1,1] direction

The DFT calculated lattice parameters in the hexagonal cell, the magnetic moment, band gap, and bulk modulus are listed in Table 7-6 along with experimentally determined values. PBE+U overpredicts the cell volume. The internal lattice parameters have very good agreement with experiment, however the c/a ratio is 0.4% higher than experiment. The magnitude of the magnetic moment for Fe is smaller than experiment. The band gap is reasonable, falling between the two reported values. The calculated bulk modulus is smaller than reported, similar to the PBE+U calculations for Cr_2O_3.

Table 7-6. Bulk properties of Fe_2O_3 compared to experimental values

	Vol. per unit formula (Å^3)	a (Å)	c/a	x (O)	z (Fe)	Mag. Moment of Fe (μ_b)	E_g (eV)	B (GPa)
PBE+U (This work)	51.44	5.066	2.741	0.306	0.354	4.16	2.14	192
[160]								231
[90]	50.29	5.0347	2.7305	0.3056	0.35534			225
[162]	50.30	5.0345	2.7310	0.3	0.355			
[163]							2	
[166]						4.9		
[167]							2.2	

Bader charges were calculated, and were +1.73 for iron, and -1.15 for oxygen. The density of states for bulk Fe_2O_3 is shown in Figure 7-5. The Fe_2O_3 band gap is smaller than that of Cr_2O_3. There is a slight decrease in the density of states just below the start of the band gap.

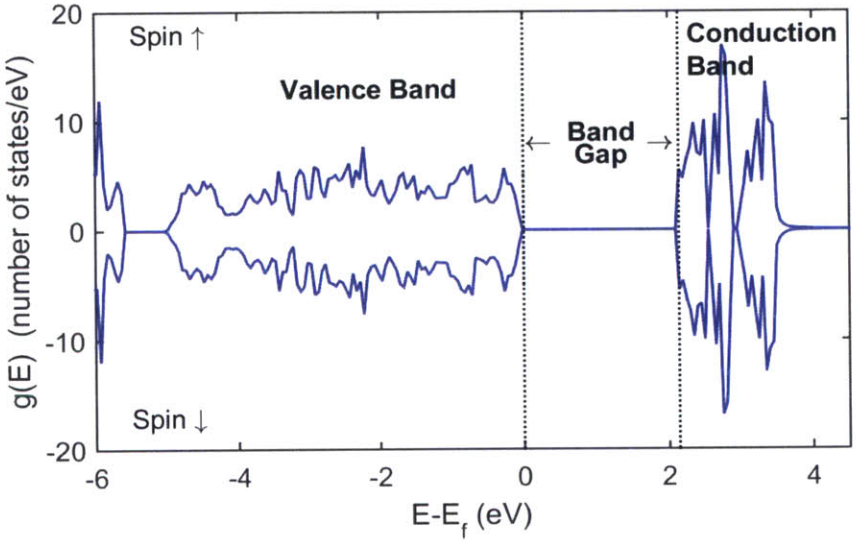

Figure 7-5. Density of states for bulk Fe_2O_3

7.5 Surface Energy Calculations

In the previous two sections of this chapter, we concluded that PBE+U can adequately model Cr_2O_3 and Fe_2O_3. The calculated bulk properties in good agreement with experimentally measured values. With the bulk models complete, we can now begin surface calculations. In this thesis, we study the energy of the (0001) surfaces, which have high symmetry and are the most widely studied surface of Cr_2O_3 and Fe_2O_3. For these calculations, we switch to the 30-atom hexagonal unit cell.

Surface energy calculations were performed with a slab model such as the one shown in Figure 7-6. The atoms from the bulk crystal lattice have been "cut" along the (0001) plane and a vacuum layer has been added, which creates two exposed surfaces. The dimensions of the supercell size were fixed throughout the calculation.

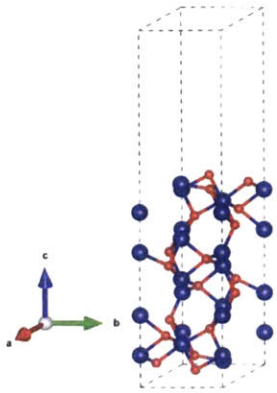

Figure 7-6. Sample supercell for a slab calculation

In the hexagonal unit cell, the atoms form repeating layers in the c-direction, according to: M-M-O_3-M-M-O_3 … In one unit cell, there are 6 oxygen planes and 12 metal ion planes. Because of this layered structure, there are multiple terminations

of (0001) α-M_2O_3 oxides. We consider the stoichiometric M-terminated surface, the nonstoichiometric O_3–terminated surface, and the nonstoichiometric M_2-terminated surface. Symmetric slabs were used to avoid dipole interactions. A (1x1) supercell with six stoichiometric units was used for the surface calculations. For the O_3-termination and M_2-termination, extra atoms were added to produce a symmetric slab. The center 3-4 atom layers were fixed, and the remainder of the cell was allowed to relax.

The surface free energy can be calculated using the Gibbs free energy of the system:

$$G_{slab} = G_{bulk} + \gamma A_{surf} \tag{7-6}$$

Following the approach of Rohrbach et al, and Scheffler et al., the Gibbs free energy of condensed phases can be approximated by the DFT energy. With this approximation, the surface energy is given by: [124]

$$\gamma = \frac{1}{2A}\left[E_{slab} - \frac{1}{2}\mathcal{N}_M E_{bulk} - \frac{1}{2}\left(\mathcal{N}_O - \frac{3}{2}\mathcal{N}_m\right)\mu_{O_2}\right] \tag{7-7}$$

where

E_{bulk} is the DFT energy of one stoichiometric unit of the metal oxide M_2O_3

A is the surface area of one side of the slab

7.5.1 Cr_2O_3 surface energy calculations

Three surfaces were studied: the (0001) Cr, Cr_2, and O_3 terminated surfaces. Equation (7-7) was used to calculate the surface energy as a function of oxygen chemical

potential. Figure 7-7 shows the surface phase diagram at 0 K without zero point energy corrections. The space between the dotted lines shows the range of oxygen chemical potentials at which Cr_2O_3 is stable: at lower chemical potentials, it is reduced to metallic chromium, and at higher chemical potentials, it is oxidized to CrO_2.

According to these calculations, the Cr_2-terminated surface would not be expected to be stable. At low oxygen chemical potentials within the range of Cr_2O_3 stability, the stoichiometric chromium terminated surface is preferred. At higher oxygen chemical potentials, the oxygen terminated surface is preferred. In Chapter 6, we found that the oxygen chemical potential in the bulk coolant of a PWR core is on the order of -2.2 eV relative to the chemical potential at (T=0K, P^o= 0.1 MPa). From Figure 7-7, we would expect the Cr-terminated surface to be stable at this oxygen chemical potential. Recall that the calculated surface energies do not include zero point energy corrections or entropy. In drawing a conclusion about the surface termination based on the oxygen chemical potential, we are assuming that the *net change in free energy* between the bulk and surface due to vibrational free energy, electronic entropy, and volume changes is small.

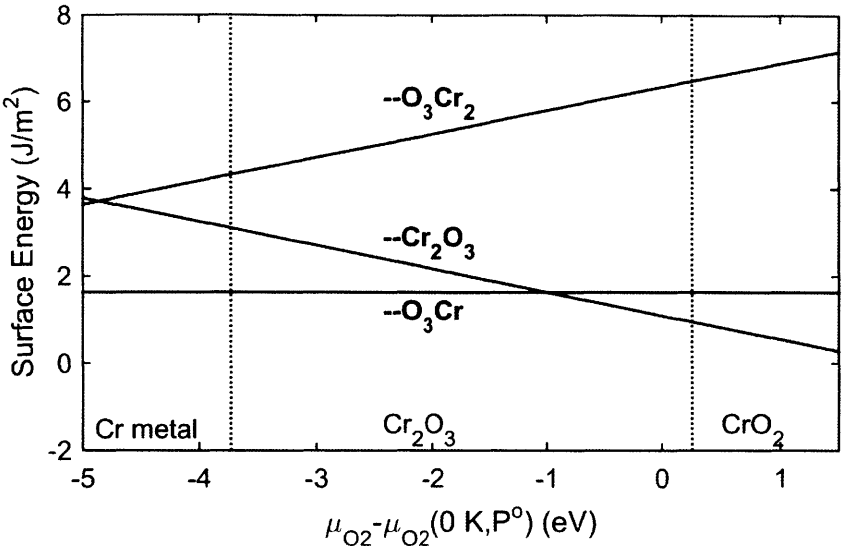

Figure 7-7. Surface phase diagram for different (0001) terminations of Cr_2O_3 at 0 K as a function of the O_2 chemical potential. The dotted lines show the allowed range of O_2 chemical potential, limited by reduction to Cr metal and oxidation to CrO_2

Figure 7-8 shows the relaxed Cr and O_3 terminated surfaces. Table 7-7 shows the changes in the interlayer spacing in the Cr-terminated surface. The spacing between the Cr^s and O^s planes is reduced by 60%. The distance between O^s and Cr^{s-1} planes increases slightly from the bulk spacing. The spacing decreases between Cr^{s-1} and Cr^{s-2} decreases by 43%. The overall result is an inward relaxation of the surface layers. Table 7-8 lists the changes in the interlayer spacing at the O_3-terminated surfaces. The O^s - Cr^s distance decreases by 33%, and the Cr^s - Cr^{s-1} distance decreases. Overall, the relaxation distances calculated in this work has good agreement with results from the literature.

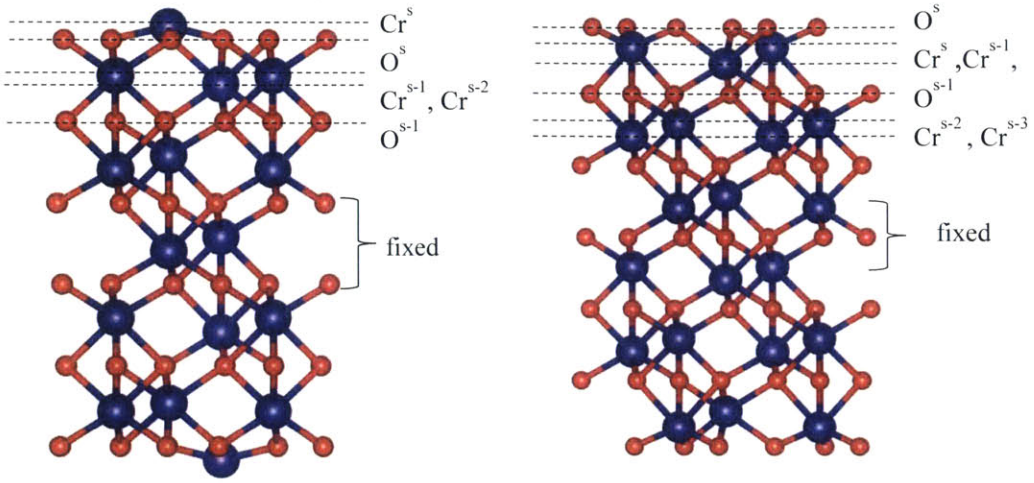

Figure 7-8. Cr-terminated (left) and O_3-terminated (right) (0001) Cr_2O_3 slabs

Table 7-7. Relaxation of Cr-terminated (0001) Cr_2O_3. Percent change from bulk interlayer spacing

	This work	**Rohrbach et al.** [124]	**Nigussa et al.** [130]	**Costa et al.** [131]
Cr^{s}-O^{s}	-60.1%	-60.0%	-58.2%	60.0%
O^{s}-Cr^{s-1}	7.6%	12.0%	7.1%	8.0%
Cr^{s-1}- Cr^{s-2}	-42.6%	-44.0%	-43.8%	
Cr^{s-2}-O^{s-1}	11.8%	9.2%		
Functional	PBE+U	PW91+U	PW91	PW91+U

Table 7-8. Relaxation of O_3-terminated (0001) Cr_2O_3. Percent change from bulk interlayer spacing

	This work	**Rohrbach et al.** [124]	**Cline et al.** [168]
O^s-Cr^s	-33.2%	-32.0%	-33.0%
Cr^s- Cr^{s-1}	27.1%	29.0%	2.6%
Cr^{s-1}-O^{s-1}	4.3%	3.3%	11.7%
Functional	PBE+U	PW91+U	LDA

The projected density of states (PDOS) for the surface atoms of the Cr-terminated (0001) surface along with the PDOS from the bulk crystal are shown in Figure 7-9. In the bulk crystal, the conduction band is formed primarily by the 3d orbital of chromium, and the valence band is formed by both 2p oxygen states and 3d chromium states. At the surface, the band gap is reduced to 2.2 eV. There are peaks in the Cr PDOS at both the valence and conduction band edges. The PDOS for oxygen at the surface also has a peak at the valence band edge, and g(E) is no longer identical for spin up and spin down states.

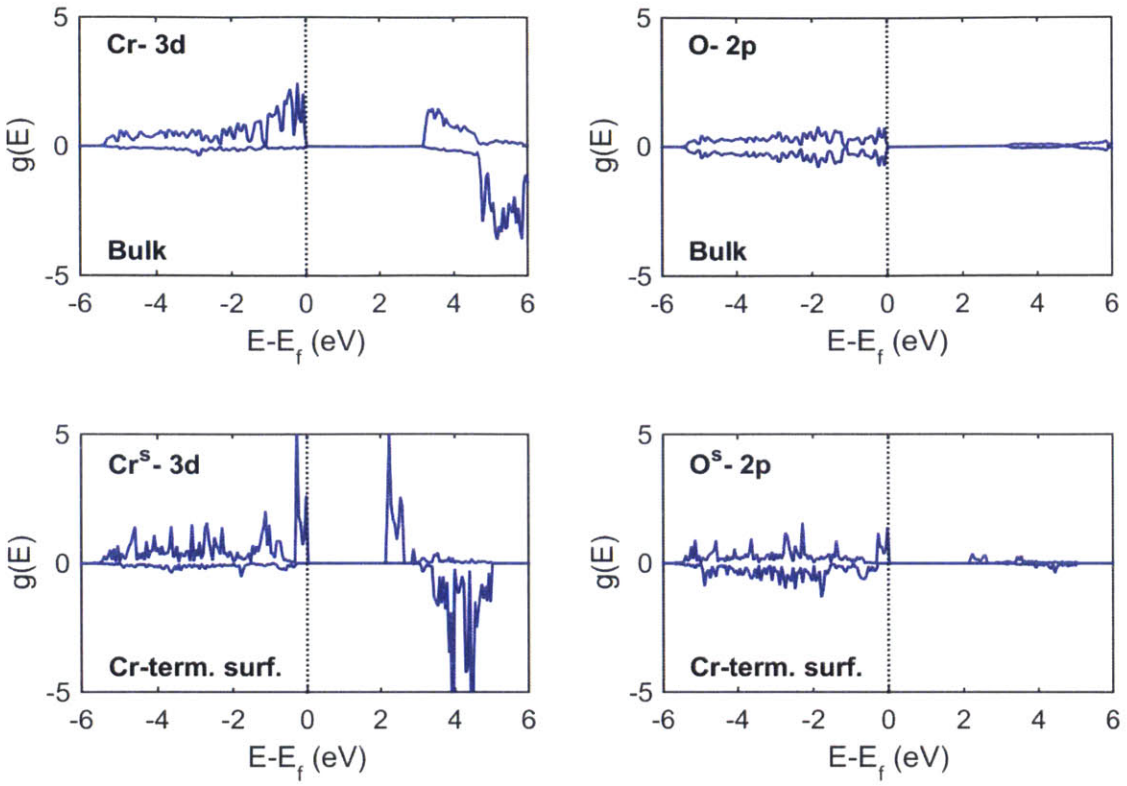

Figure 7-9. Projected density of states for the surface atoms of Cr-terminated (0001) Cr_2O_3

7.5.2 Fe_2O_3 Surface calculations

The surface phase diagram for the (0001) Fe_2O_3 surface is shown in Figure 7-10. Similar to Cr_2O_3, at low oxygen chemical potentials, the preferred termination is the stoichiometric single metal ion terminated surface. The O_3-terminated surface is expected to be stable at higher oxygen chemical potentials, and the Fe_2 termination is not expected to be stable.

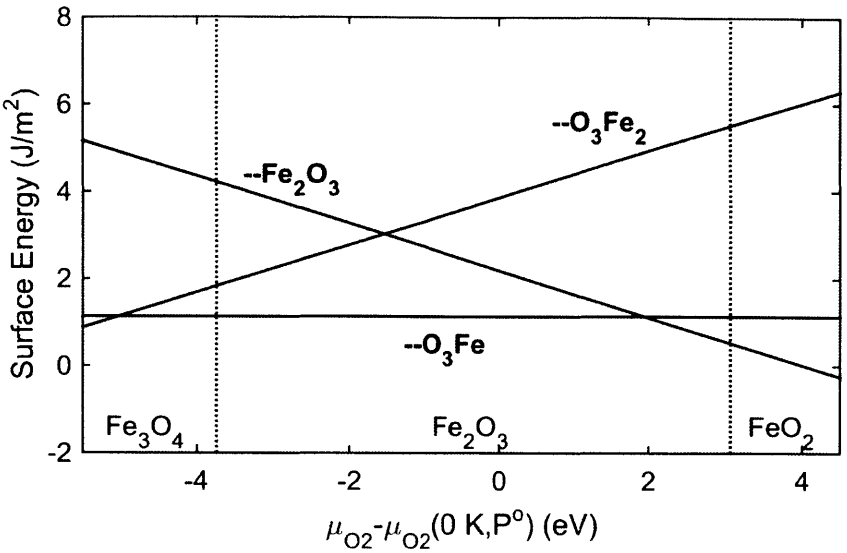

Figure 7-10. Surface phase diagram for (0001) terminated Fe_2O_3. The dotted lines show the limits of the chemical potential

Table 7-9 lists the change in interlayer spacing at the Fe-terminated surface compared to other DFT+U calculations and experiments. The Fe^s-O^s distance decreases significantly by 68%, and there is a slight increase in the O^s-Fe^{s-1} distance of 7%. The Fe^{s-1}-Fe^{s-2} distance decreases by 37%. Overall, these changes are quite similar to those for Cr-terminated Cr_2O_3. Our results are in good agreement with the other DFT+U calculated values. However, the reported changes in spacing from experiments are significantly smaller; the change in Fe^s-O^s distance is less than half of what we calculate, and the change in the O^s-Fe^{s-1} distance is 3% smaller than we calculate.

Table 7-9. Relaxation of Fe-terminated (0001) Fe_2O_3 surface. Percent change from bulk interlayer spacing

	This Work (PBE+U)	**Rohrbach et al.** [124] **PW91+U**	**Kiejna and Pabisiak** [132] **PW91+U**	**Lübbe and Moritz** [169] **experiment**
Fe^{s} - O^{s}	-68	-57	-66.6	-27.4
O^{s} - Fe^{s-1}	7.0	9.6	7.2	3.6
Fe^{s-1} - Fe^{s-2}	-37	-40	-38	-8.3
Fe^{s-2}- O^{s-1}	16	17	16.3	7.1
O^{s-1} - Fe^{s-3}	3.6	3.5	3.7	

Table 7-10 lists the change in interlayer spacing at the O_3-terminated surface compared to other DFT+U calculations and experiment. Our results have good agreement with the other calculations. We calculate a small decrease in the O^{s}-Fe^{s} distance of 4.3% compared to the experimentally determined decrease of 67%. The Fe^{s}-Fe^{s-1} calculated decrease of 60% is in good agreement with the experimental value of 56%. The surface relaxations for O_3-terminated Fe_2O_3 differ from those of the O_3-terminated Cr_2O_3: O^{s}-Cr^{s} decreased by 33%, and the Cr^{s}-Cr^{s-1} distance increased.

Table 7-10. Relaxation of O_3-terminated (0001) Fe_2O_3 surface. Percent change from bulk interlayer spacing

	This work	**Rohrbach et al.** [124] **PW91+U**	**Kiejna and Pabisiak** [132] **PW91+U**	**Barbier et al.** [170] **experiment**
O^{s} - Fe^{s}	-4.3	-7.4	-5.5	-67
Fe^{s} - Fe^{s-1}	-60	-53	-56.1	-56
Fe^{s-1} - O^{s-1}	27	37	25.4	5
O^{s-1} - Fe^{s-2}	-5.0	-6	-5.4	-22
Fe^{s-2} - Fe^{s-3}	14	16	13.2	22

The projected density of states for surface atoms of the Fe terminated (0001) Fe_2O_3 terminated surface are shown in Figure 7-11. In the bulk, Fe-3d states make up the conduction band, and the valence band consists of oxygen-2p and Fe-3d states. At the surface, there are fewer states near the valence band edge for both Fe and O. The band gap at the surface decreases from the bulk value of 2.14 eV to 1.8 eV. The surface oxygen atom has a small peak near the bottom of the conduction band.

Comparing the two oxides, the band gap of Cr_2O_3, the band gap was reduced more that the surface than that of Fe_2O_3. There were also a number of states near the valence band edge at the surface, unlike in Fe_2O_3.

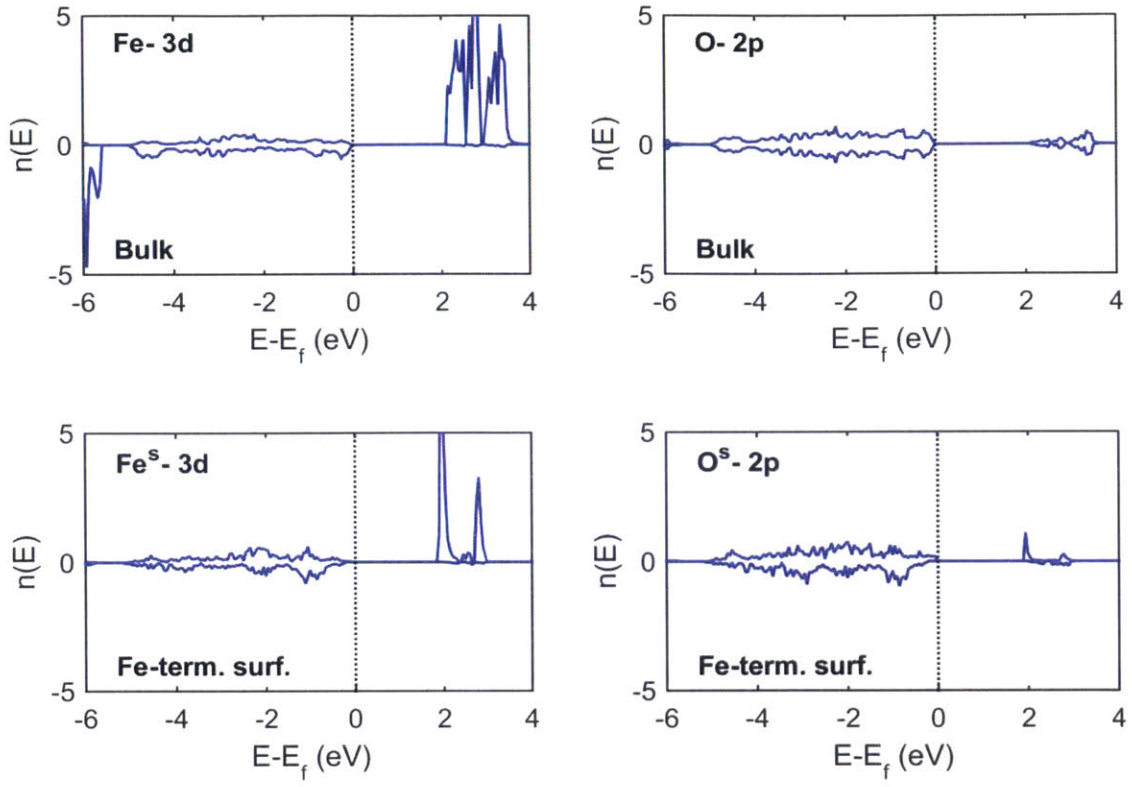

Figure 7-11. Projected density of states for the surface atoms of (0001) Fe-terminated Fe_2O_3 (bottom) compared to those of the bulk (top)

7.6 Chapter Summary

In this chapter, density functional theory was used to model bulk α-Fe_2O_3 and Cr_2O_3. The results were benchmarked against experimental data. On site Coloumb interactions (the U-correction) were needed to reproduce the proper c/a ratio for Cr_2O_3. GGA (PBE) parametrization proved best at determining the band gap for Cr_2O_3, although the lattice spacing is larger than experimental values. Based on these results, we selected to proceed with PBE+U for the remaining calculations.

Surface calculations of the (0001) surfaces were performed, comparing the O_3, M, and M_2 terminations. At oxygen chemical potentials expected in a PWR, the preferred surface termination is the stoichiometric Fe or Cr-terminated surface. Atom projected densities of states, showed that localized states form at the surface, and the effect is to narrow the band gap at the surface. In the case of Cr_2O_3, the band gap narrows from 3.19 eV in the bulk to 2.19 eV at the surface. For Fe_2O_3, it narrows from 2.14 eV in the bulk to 1.8 eV at the surface.

In the previous chapter, we determined that from an energy level perspective the conduction band minimum should be relatively high. If these surface states reduce the conduction band energy at the surface, they will likely hinder the ability of Cr_2O_3 and Fe_2O_3 to serve as cathodic sites in Zircaloy-4 PWR fuel cladding.

As a final note, the calculations presented in this chapter are not unique. Overall, the bulk and surface models have good agreement with experimentally measured properties (when available), and with other DFT+U calculations in the literature. Thus, it is possible to proceed to studying hydrogen interactions with the surfaces.

Chapter 8: Hydrogen Adsorption and Absorption

In this chapter, hydrogen interactions with the (0001) surfaces Fe_2O_3 and Cr_2O_3 will be analyzed. We begin by model atomic hydrogen adsorption at variable coverage. Next, we model molecular adsorption and hydrogen recombination. Finally, we examine hydrogen below the surface, and the energy barrier for hydrogen to migrate from the surface to subsurface. At the end of the chapter, we discuss these results and the implications on hydrogen recombination.

8.1 Hydrogen Adsorption on Cr_2O_3 and Fe_2O_3

For these calculations a (1x1) asymmetric slab with 30 atoms was used to model the surface. The vacuum spacing was set to 15 A, and the bottom 10 atoms were fixed. A 3x3x1 gamma centered k-point grid was used. Gaussian smearing with sigma = 0.05 eV was used to accelerate convergence. Dipole corrections were applied. For all calculations, the cell was allowed to relax until all forces on the ions were less than 0.01 eV/A.

Figure 8-1 shows the top layers of the pristine Cr-terminated (0001) Cr_2O_3 surface. There are three equivalent surface oxygen atoms, denoted as O_a^s, O_b^s, and O_c^s. Each of the oxygen atoms is bonded to the top three chromium atoms, Cr^s, Cr^{s-1}, and Cr^{s-2}. For this work, one monolayer (ML) coverage will be defined as one adsorbed species per (1x1) cell.

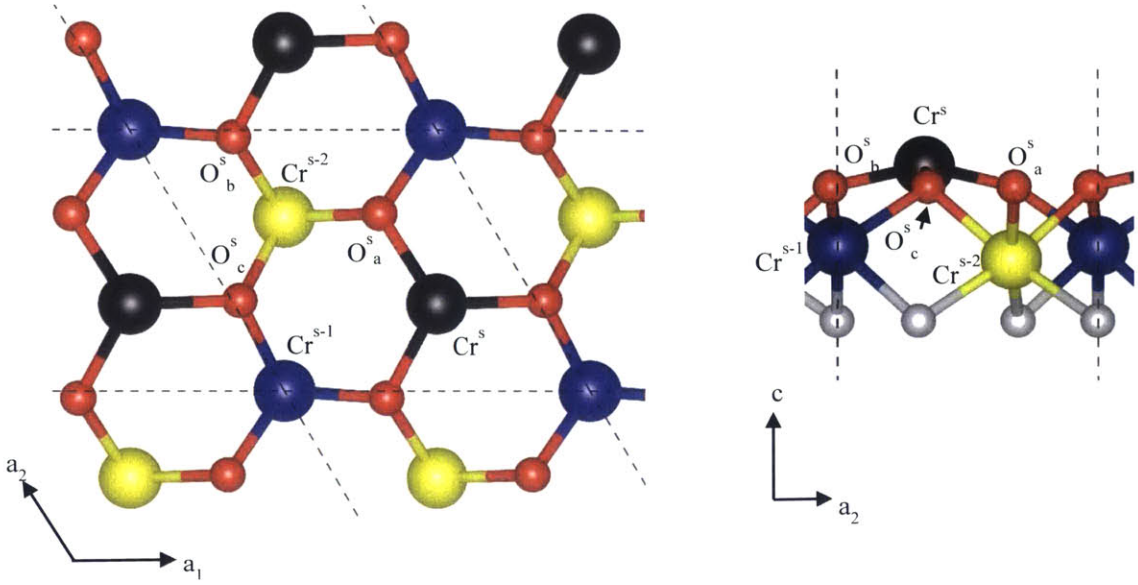

Figure 8-1. Cr terminated (0001) Cr_2O_3 surface. The dashed lines show the hexagonal cell boundaries. O = small atoms, Cr = large atoms

Throughout this chapter, we will consider the interactions in terms of the adsorption temperature at 0 K, neglecting zero point energy corrections. The adsorption energy is calculated as:

$$E_{ads} = E_{slab+\ adsorbed\ H\ atoms} - E_{clean\ slab} - \frac{\mathcal{N}_H}{2} E_{H_2} \tag{8-1}$$

To find adsorption sites, an energy scan was performed. A single hydrogen atom was added to the supercell at various locations, and the energy of the cell was calculated without relaxations. The coordinates of the hydrogen atom in the (0001) plane were selected by forming a grid over the surface, for example, a 6x6 grid. The hydrogen position in the [0001] direction were placed at a fixed height, for example 1 A above the

surface. The results from the energy scan were then used to identify possible local minima. Relaxations were then performed on these configurations. From the relaxations, hydrogen atoms were found to adsorb to oxygen sites or metal ion sites. It should be noted that bond lengths were different for the two sites: the O-H bonds were typically ~1 A and M-H bonds were ~1.8 A. To model the adsorption of two hydrogen atoms in a unit cell, we used the lowest energy configuration with one hydrogen atom as a starting configuration. A second hydrogen atom was added to this cell, at different locations to test adsorption sites at oxygen and metal ions.

8.1.1 Hydrogen adsorption on Fe_2O_3

Preliminary calculations revealed that at low coverage, hydrogen prefers to adsorb to one of the surface oxygen atoms, and adsorption to an iron atom is significantly weaker, with a 2 eV difference in adsorption energy. The lowest energy configurations for atomic hydrogen adsorption at coverages of 1-3 ML are shown in Figure 8-2.

The first hydrogen atom added to the (1x1) surface model adsorbs to one of the surface oxygen atoms, oriented away from the topmost Fe atom with an O-H bond length of 1 A. The resulting configuration in Figure 8-2 shows hydrogen adsorbed to O_c^s. Bader charge analysis shows the that hydrogen atom loses the majority of its charge; its electron is distributed among Fe^s and the O^s atoms. Thus hydrogen is adsorbed as a proton, forming a hydroxide ion at the surface.

For Fe_2O_3, the adsorption of a second hydrogen atom in the supercell (now at 2 ML coverage) causes a reconstruction of the surface. In Figure 8-2 the second hydrogen adsorbs at O_a^s. This surface oxygen atom is displaced out of the surface, and the bond

between this atom and the Fe^{s-2} atom (shown in yellow) is broken, increasing the Fe^{s-2}-O_a^s distance to 3.1 A, compared to the clean surface value of 2.05 A. These changes are marked by the solid blue oval in Figure 8-2. In addition, O_b^s, the surface oxygen without an adsorbed hydrogen, is displaced in the (0001) plane, as marked by the green dotted rectangle in Figure 8-2. The adsorbed hydrogen atoms both have bader charges of +0.59. The bader charges of O_a^s and Fe^{s-1} decrease by -0.12 and -0.35 from hydrogen adsorption at 1 ML.

The addition of a third hydrogen creates further rearrangement of the surface atoms. The third hydrogen atom adsorbs to O_a^s. This oxygen atom is displaced out from the surface, and the bond between this atom and the Fe^{s-2} atom (shown in yellow) is also significantly stretched. The Fe^{s-2}- O_b^s distance is 3.05 A, and the Fe^{s-2}- O_a^s distance is 3.06 A. Fe^s moves inward and is now located below the O^s atoms. The bader charges of the adsorbed hydrogens are +0.58 to +0.62, and the majority of the electron charge from the adsorbates is distributed among the top 3 iron and oxygen atoms.

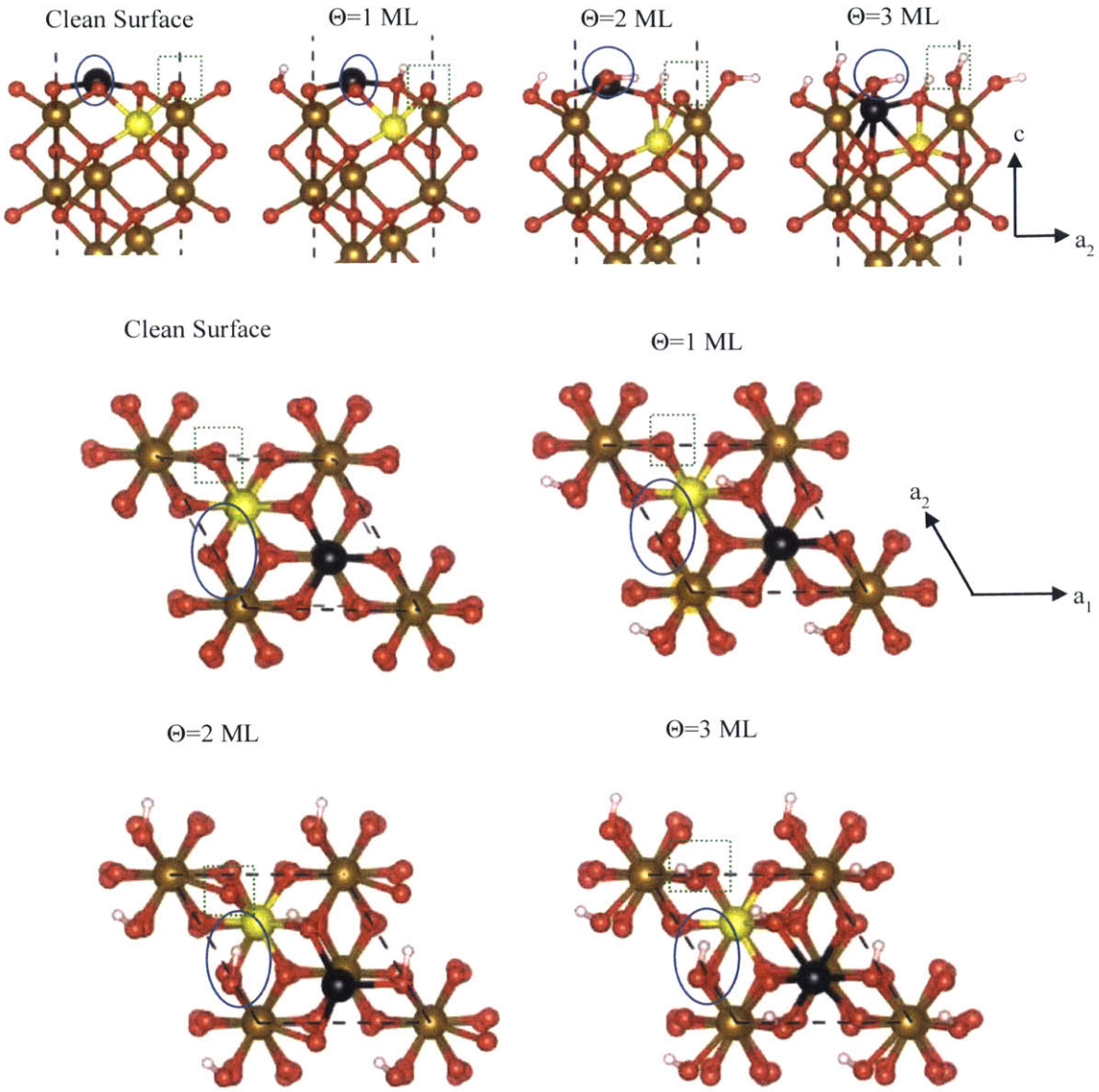

Figure 8-2. Adsorption of hydrogen on Fe terminated (0001) Fe_2O_3

Table 8-1. Bader Charges on Surface Atoms on Fe terminated (0001) Fe_2O_3 with atomic hydrogen adsorption

	Clean Surface	**Θ =1 ML**	**Θ=2 ML**	**Θ =3 ML**
Fe^S	1.58	1.25	1.25	1.31
Fe^{S-1}	1.70	1.70	1.35	1.34
Fe^{S-2}	1.74	1.72	1.66	1.31
O^S_a	-1.08	-1.13	-1.25	-1.25
O^S_b	-1.09	-1.15	-1.20	-1.24
O^S_c	-1.08	-1.24	-1.22	-1.27
H_a			0.59	0.59
H_b				0.58
H_c		0.62	0.59	0.62
Bulk Fe	1.73			
Bulk O	-1.15			

Adsorption energies relative to the hydrogen molecule and O-H bond distances are listed in Table 8-2. With each subsequent atom adsorption, the average adsorption energy decreases.

Table 8-2. Hydrogen adsorption energy on Fe terminated (0001) Fe_2O_3 as a function of surface coverage

Coverage (ML)	**Adsorption energy (eV per atom)**	**H-O bond length (A)**
1	-0.927	0.978
2	-0.698	0.975, 0.988
3	-0.607	0.979, 0.981, 0.974

Figure 8-3 shows the projected densities of states of the top three iron atoms for the different hydrogen coverages. As more hydrogen atoms are added to the supercell, the additional electrons fill the unoccupied 3d-orbitals of the Fe atoms. At 1 ML coverage, few unoccupied states remain at Fe^{s}. At 2 ML coverage, there are few unoccupied states at Fe^{s} and Fe^{s-1}. At 3 ML coverage, there are a small number of states near 2 eV in Fe^{s}, and there are small peaks in the PDOS of Fe^{s-1} and Fe^{s-2} at 3 eV. A smaller density of states at the surface will correspond to fewer conduction electrons at the surface.

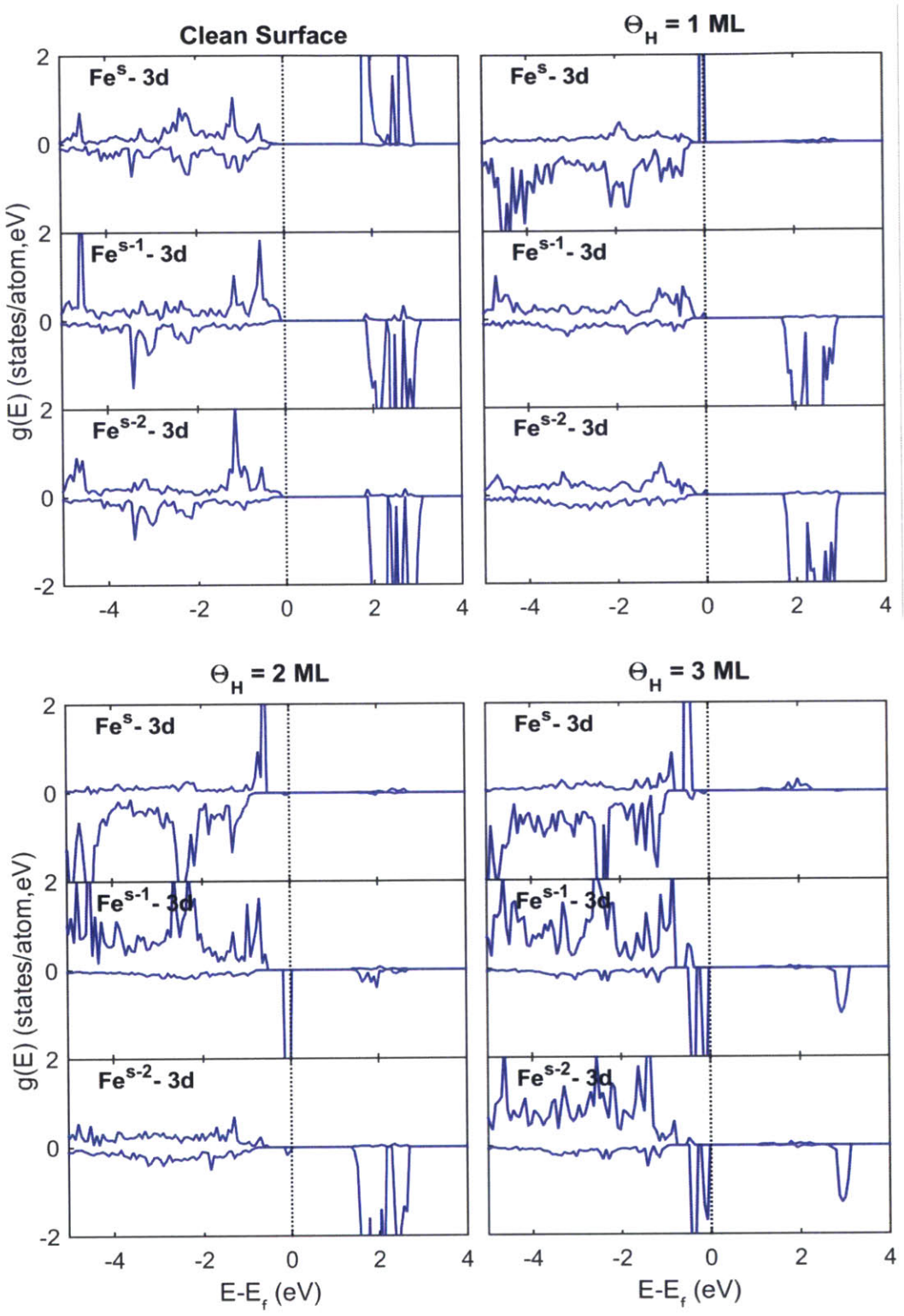

Figure 8-3. Projected densities of state of Fe atoms at the (0001) Fe_2O_3 surface with varying hydrogen coverage

8.1.2 Adsorption on Cr_2O_3

Hydrogen adsorption on Cr_2O_3 is slightly more complicated, because multiple configurations exist with similar energies. At 1 ML coverage, hydrogen preferentially absorbs to one of the surface oxygen atoms. Figure 8-4 shows hydrogen adsorbing to the O_a^s site. Bader charge analysis show that most of the hydrogen's electronic charge is redistributed to Cr^s and O^s.

At 2 ML coverage, the lowest energy configuration has one hydrogen adsorbed to a surface oxygen atom and one adsorbed to the surface chromium ion, shown as O_a^s and Cr^s in Figure 8-4. There is a higher energy configuration with both hydrogen atoms adsorbed to surface oxygen atoms, as there is for Fe_2O_3. In Figure 8-4, hydrogen is shown adsorbed to O_a^s and O_c^s. The distance between Cr^{s-2} and O_a^s has stretched to 2.78 A from the clean surface value of 2.03 A. However, when the second hydrogen adsorbs to Cr^s, then all three O^s-Cr^{s-2} bonds remain intact and relatively unchanged, with values of 1.99, 2.0 and 2.12 A. The bader charge of H adsorbed to Cr^s is -0.44, indicating that it is a hydride ion (H-). Bader charges for the protons adsorbed to O^s are +0.60-0.61.

At 3 ML coverage, the preferred configuration has two hydrogen atoms adsorbed to surface oxygen atoms, and the other adsorbed to Cr^s. For this case, all three Cr^{s-2} bonds remain intact, with lengths of 1.95, 2.08, and 2.14 A. Bader charges for the protons are -0.57, and for the hydride ion it is -0.55.

Table 8-3. Hydrogen adsorption energy on Cr terminated (0001) Cr_2O_3 as a function of surface coverage.

Coverage (ML)	Adsorption site	Adsorption energy (eV/atom)
1/3	O^s	-0.219
1/3	Cr^s	0.735
2/3	O^s, O^s	0.137
2/3	O^s, Cr^s	0.038
1	O^s, O^s, Cr^s	-0.017

Table 8-4. Bader Charges on Surface Atoms on Cr terminated (0001) Cr_2O_3 with hydrogen adsorption

	Clean Surface	Θ =1 ML	Θ=2 ML O^s+O^s	Θ=2 ML, O^s+Cr^s	Θ =3 ML
Cr^S	1.66	1.37	1.36	1.60	1.31
Cr^{S-1}	1.76	1.75	1.74	1.77	1.76
Cr^{S-2}	1.81	1.78	1.46	1.81	1.80
O^S_a	-1.14	-1.27	-1.30	-1.27	-1.26
O^S_b	-1.14	-1.19	-1.26	-1.13	-1.19
O^S_c	-1.14	-1.20	-1.27	-1.14	-1.22
H_a		0.62	0.60	0.60	0.57
H_c			0.61		0.57
H_M				-0.44	-0.55
Bulk Cr	+1.8				
Bulk O	-1.2				

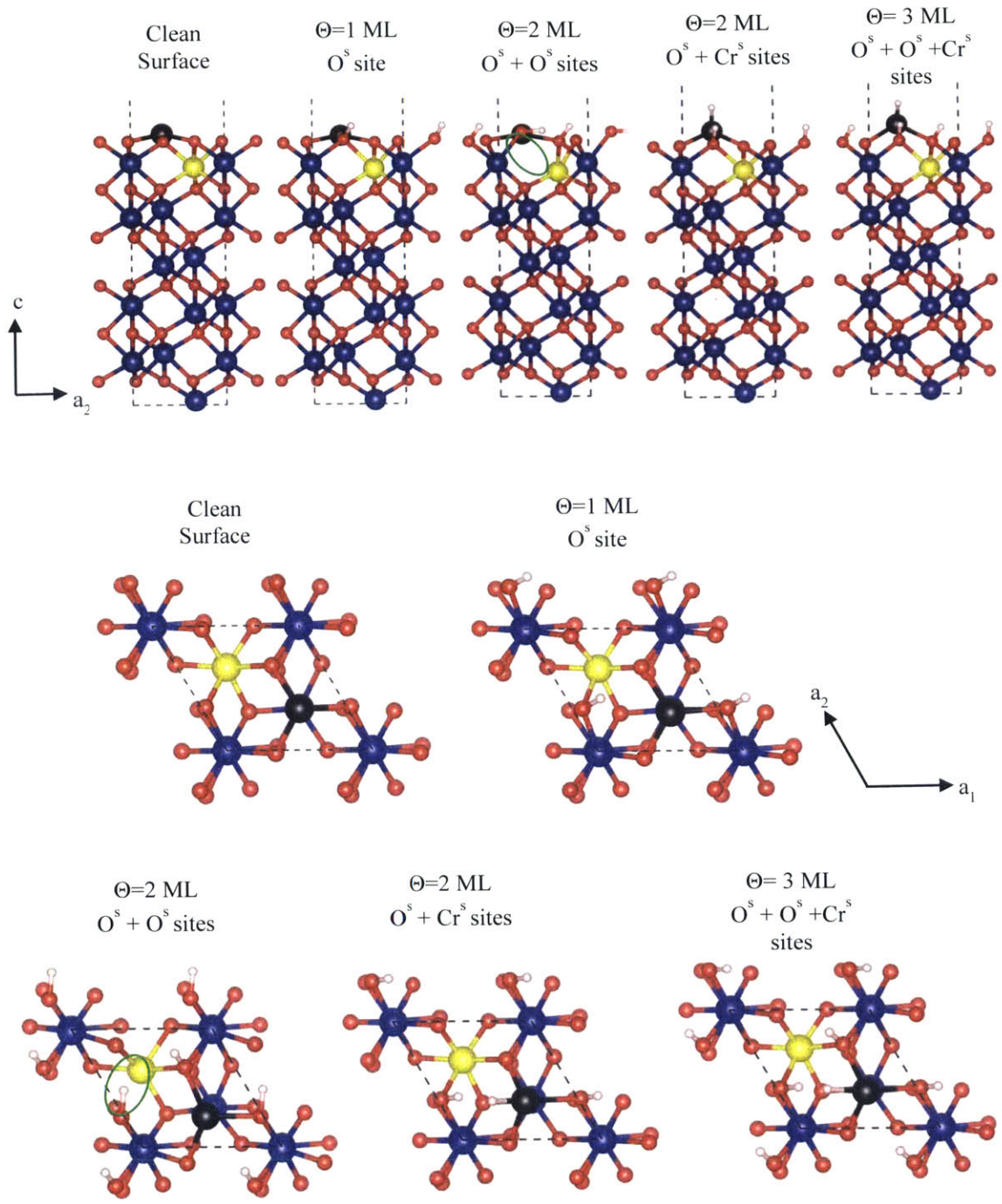

Figure 8-4. Hydrogen adsorption onto the (0001) Cr-terminated surface

Projected densities of states are shown in Figure 8-5 and Figure 8-6. The adsorption of one hydrogen atom causes a reduction in the unoccupied states in the surface chromium atoms. At 2 ML coverage, adsorption to two surface oxygen atoms causes significant changes to the electronic structure at the surface. The band gap is reduced at the surface; at Cr^{s}, the conduction band starts at 0.8 eV above the Fermi energy. At 2 ML coverage, if the second hydrogen atom adsorbs at Cr^{s}, then the band gap remains ~2.2 eV at the surface.

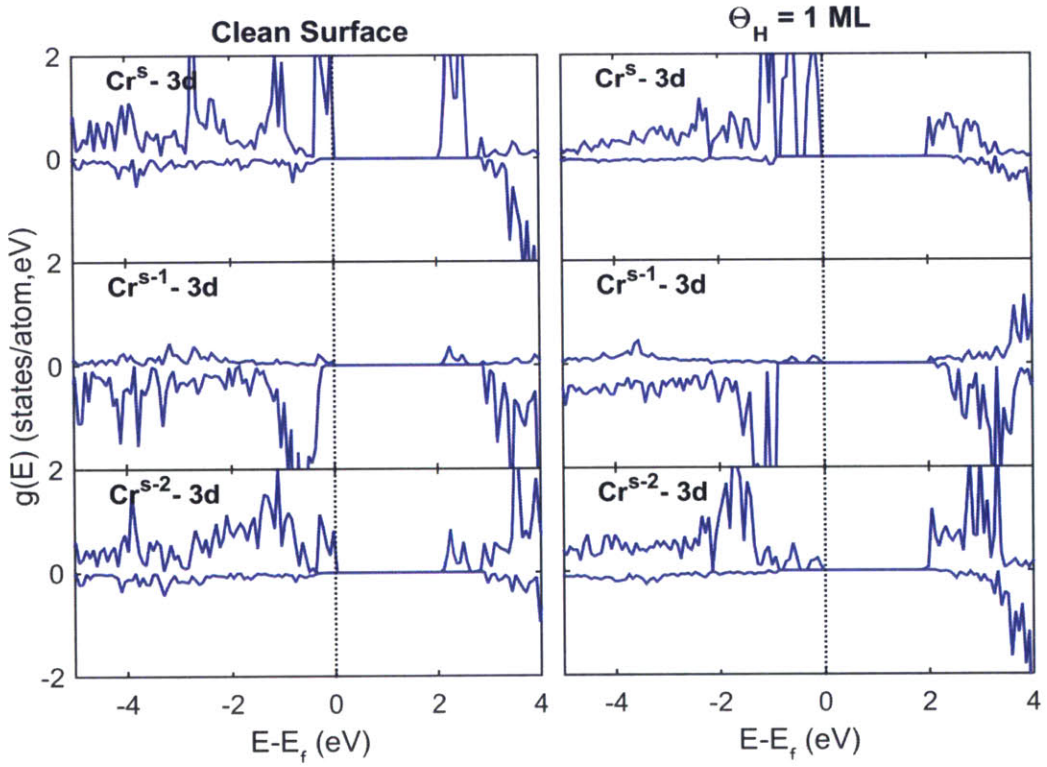

Figure 8-5. Projected Densities of states of surface Cr atoms of (0001) Cr_2O_3, at 0 and 1 ML H coverage.

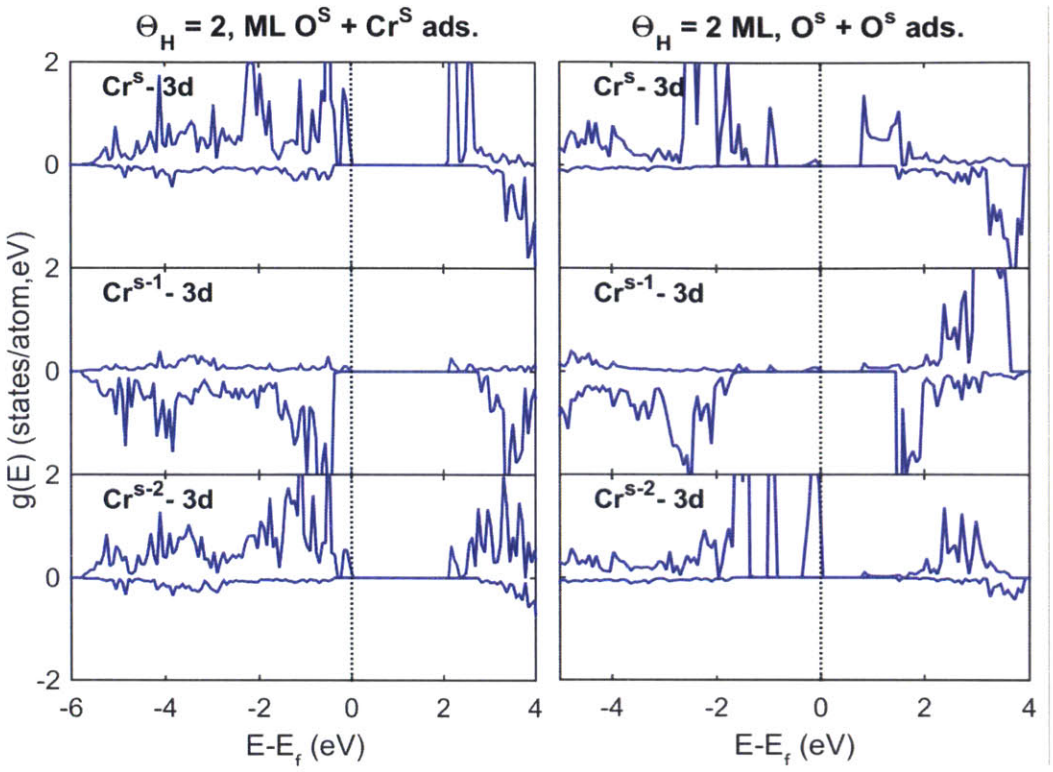

Figure 8-6, Projected Densities of states of surface Cr atoms of (0001) Cr_2O_3, at 2 ML H coverage, with hydrogen adsorbed to: O^s and Cr^s (left) and O^s and O^s (right)

8.1.3 Comparing adsorption energies to literature results

There have been very few studies on the adsorption of hydrogen on Fe_2O_3 or Cr_2O_3. Souvi et al. studied interactions of hydrogen, oxygen, and water on the (0001) Fe_2O_3 surface using PBE+U. For hydrogen adsorbed to the Fe terminated surface, they determined adsorption energies to be: -0.79 eV for 1 ML coverage, -0.69 eV/atom for 2 ML coverage, and -0.41 eV/atom for 3 ML coverage, which is in good agreement with our results. They also observed the same outward movement of the surface oxygen ions and the inward movement of Fe^s at high coverage. [129]

Nigussa et al. studied adsorption of hydrogen on the (0001) Cr_2O_3 surface with the PW91 functional without U-corrections. On the Cr terminated surface, they found an adsorption site on the Cr ion and one on an oxygen ion. They computed adsorption energies relative to the isolated H atom. Their calculated energies were -3.36 eV for the Cr site and -2.34 eV for the oxygen site. [130] The adsorption energies in the work relative to the isolated H atom are -1.64 eV for adsorption on the Cr atom and -2.63 eV for adsorption on the oxygen atom. However, it is important to note that adsorption energies calculated with DFT+U may not be comparable to those with pure DFT. Costa et al. note that they observed a reduction in the adsorption energy of dissociated water molecules with PW91+U compared to PW91 DFT calculations. [131] Rohrbach et al. observed that U corrections modify the "frontier orbitals" (the highest occupied states) at the surface of Fe_2O_3 and Cr_2O_3, which would affect the surface reactivity. [124]

For hydrogen interactions with ZrO_2, Syzgantseva et al. studied hydrogen adsorption on the $(\bar{1}11)$ and $(\bar{1}01)$ surfaces of monoclinic zirconia. On the $(\bar{1}11)$ the adsorption energies (relative to the energy of H_2) for dissociative adsorption were all positive. On the $(\bar{1}01)$ surface, the most favorable energy configuration had an adsorption energy of -0.08 eV (for two atoms). Hofmann et al. studied hydrogen interactions with the (101) surface of tetragonal zirconia. For dissociative adsorption, they found the lowest energy configuration was hydrogen atoms adsorbed on Zr and O, with an adsorption energy of -0.184 eV/molecule. [171]

Comparing only adsorption energies from this work to those for ZrO_2, adsorption is likely most favorable on Fe_2O_3, even at the high coverage used in this study. Adsorption on Cr_2O_3 would be favored over adsorption on ZrO_2, but only at low

coverage. From this simple comparison of adsorption energies, it is quite possible that the protons from dissociated water molecules will interact with Fe_2O_3 or Cr_2O_3 surfaces on exposed second phase particles.

8.2 Molecular Adsorption of H_2 and Hydrogen Recombination

Adsorption of molecular hydrogen was studied using the same surface models for atomic adsorption. With molecular adsorption of H_2, there are additional variables that must be considered. There are coordinates of the adsorbed molecule, as well as the orientation of the two atoms (are they positioned vertically, horizontally, or at an angle?). Multiple sites and orientations were tested to identify the lowest energy configurations. Once the lowest energy site for H_2 adsorption was identified, climbing image nudged elastic band calculations were performed to determine the energy barrier for recombination. The starting configuration used were the lowest energy configurations for atomic adsorption at 2 ML, found in the previous section.

On Fe_2O_3, the preferred adsorption site is at Fe^s, with the hydrogen atoms parallel to the surface. The adsorption energy relative to the energy of the hydrogen molecule was -0.13 eV. On Cr_2O_3, the adsorption energy is smaller and multiple configurations exist with small differences in energy. The lowest energy configuration was adsorption between an O^S and Cr^s atom, with the hydrogen atoms stacked vertically. Adsorption to the Cr^s atom with the hydrogen atoms parallel to the surface was only slightly less favorable: the adsorption energies were -0.038 eV and -0.033 eV.

CI-NEB calculations were used to estimate the energy barrier for recombination, with two hydrogen atoms per cell. For Fe_2O_3, the starting configuration is with two hydrogens adsorbed to surface oxygen, and the final configuration is the hydrogen molecule adsorbed to the Fe^s site. Figure 8-7 shows the results from the CI-NEB calculations. Recombination occurs in two stages. In the first step, a hydrogen migrates from O_a^s to Fe^s, and charge is transferred from the oxide surface to this hydrogen, which becomes a hydride (H-). This first step has an energy barrier of 2.21 eV and an energy change of +1.16 eV. In the second step, the proton adsorbed on oxygen and the hydride adsorbed on iron recombine to form a hydrogen molecule. The second step has an energy barrier of 0.72 eV and an energy change of +0.62 eV.

The energy of the H+ and H- pair adsorbed is lower than the energy of the two adsorbed separately: in the 1 ML calculations, hydrogen adsorption on Fe was 2 eV greater than on O. In addition, the H+ H- pair is lower in energy than physisorbed hydrogen.

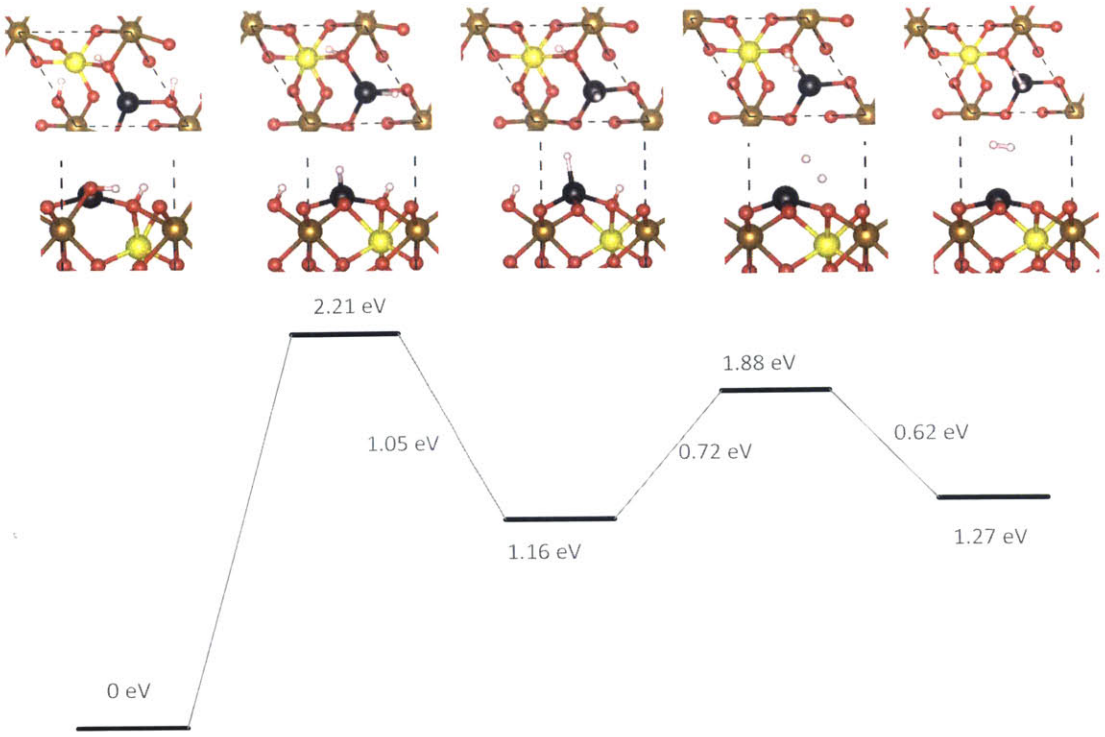

Figure 8-7. Hydrogen recombination on Fe_2O_3 at 2 ML coverage.

Bader charge analysis, the results of which are listed in in Table 8-5, shows that the first step involves the transfer of –0.94*e* charge from the surface to the migrating hydrogen atom. The majority of the charge transferred (-0.86*e*) comes from the top three iron and oxygen atoms. In the second step, an additional -0.25*e* is transferred from the surface to the two hydrogen atoms, mostly from Fe^s and O^s.

Table 8-5. Bader charges of surface atoms in the stages of hydrogen recombination on (0001) Fe_2O_3

	Initial State: Ads. $O^s + O^s$	**Intermediate State: Ads. $Fe^s + O^s$**	**Final State: H_2 Ads.**	**Δ(Initial to Intermediate)**	**Δ(Intermediate to final)**
Fe^S	1.25	1.45	1.57	+0.21	+0.12
Fe^{S-1}	1.35	1.70	1.70	+0.36	-0.01
Fe^{S-2}	1.66	1.72	1.74	+0.06	+0.01
O^S_a	-1.25	-1.10	-1.09	+0.15	+0.01
O^S_b	-1.20	-1.10	-1.09	+0.10	+0.01
O^S_c	-1.22	-1.23	-1.09	-0.01	+0.14
H^1	0.59	-0.35	0.00	-0.94	+0.35
H^2	0.59	0.62	0.02	+0.03	-0.61

In the previous section, the lowest energy configuration for hydrogen adsorption at 2 ML coverage on Cr_2O_3 was H^+ adsorbed to a surface oxygen, and H^- adsorbed to the surface chromium. Thus, this was used for the starting configuration for the CI-NEB calculations. The final configuration was the hydrogen molecule adsorbed between Cr^s and O^s as shown in Figure 8-8. This process occurs in one step, with a relatively small energy barrier of 0.28 eV. Note that recombination is exothermic: the final energy of adsorbed H_2 is -0.11 eV lower than the adsorbed H+ and H- pair.

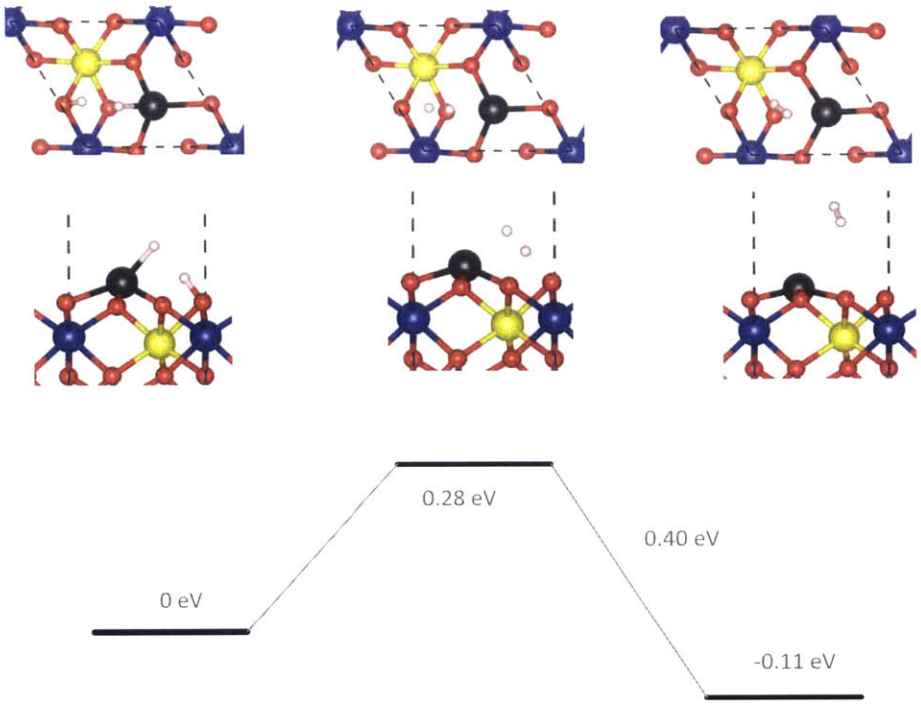

Figure 8-8. Hydrogen recombination on Cr_2O_3 at 2 ML coverage

These two recombination calculations suggest that recombination occurs via a proton-hydride (H+ H-) mechanism. For Fe_2O_3, the most important step is electron transfer to adsorbed H+ thereby forming adsorbed H^-. For Cr_2O_3, hydrogen adsorption at 2 ML is unfavorable compare to adsorption at 1 ML or 3 ML coverage. This means that we would need to consider either the formation of the H+ H- pair from proton adsorption at lower coverage, or start with the H+ H+ H- configuration at 3 ML coverage. Nonetheless, we have identified a likely mechanism for the hydrogen recombination reaction on Fe_2O_3 and Cr_2O_3.

8.3 Subsurface Hydrogen Atoms: Hydrogen Entry

The corundum structure consists of oxygen atoms arranged in an hcp lattice. Two thirds of the octahedral sites are occupied by metal ions, and the tetragonal sites are unoccupied. A preliminary study on interstitial hydrogen was performed using the bulk hexagonal cell. Multiple sites in the tetragonal and unoccupied octahedral were tested: by adding a hydrogen atom and relaxing the ionic positions. These calculations showed that the preferred location for interstitial hydrogen is in the unoccupied octahedral and bonded to an oxygen, forming a substitutional hydroxide.

Subsurface hydrogen was studied by placing a hydrogen atom between the top two layers of oxygen atoms of the clean surface. For these simulations, we are interested in hydrogen that is closer to the O^{s} plane than the O^{s-1} plane. For both Fe_2O_3 and Cr_2O_3, the preferred site for hydrogen is in the unoccupied octahedral site. The hydrogen bonds to one of the surface oxygen atoms. Figure 8-9 shows the octahedral sites in the top layer of the (0001) Cr_2O_3 surface.

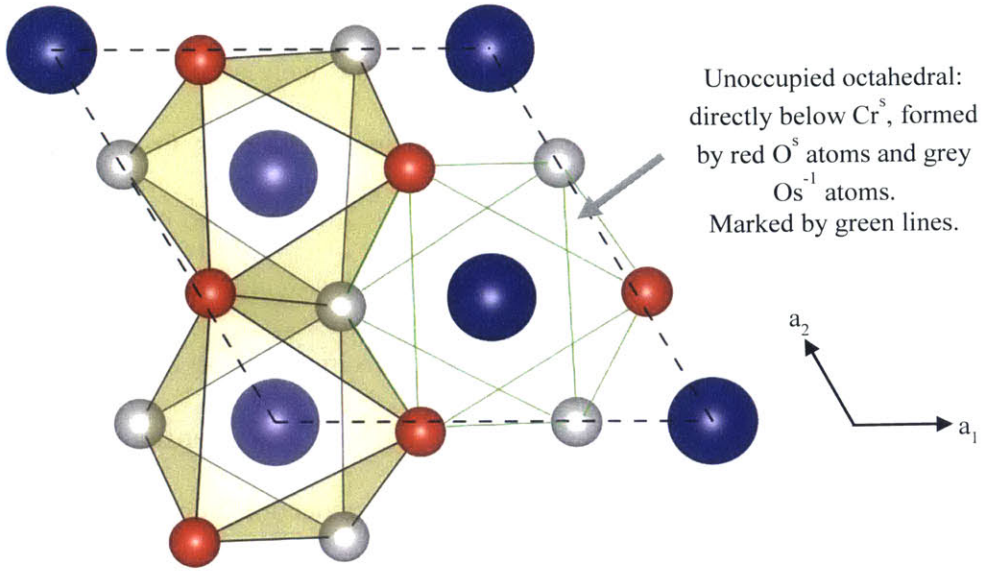

Figure 8-9. Octahedral Sites in Cr_2O_3

The calculated absorption energies for the subsurface sites are listed in Table 8-6. The energy change for hydrogen migration from a surface site to the first subsurface site is also listed. The subsurface energy for Fe_2O_3 is more negative than that of Cr_2O_3, Subsurface hydrogen in Fe_2O_3 is stable with respect to the energy of the hydrogen molecule. The energy change for a hydrogen atom to move from a surface to subsurface site is slightly more positive (less energetically favored) for Fe_2O_3 vs. Cr_2O_3.

Table 8-6. Energy for subsurface hydrogen at 1 ML coverage: adsorption energy relative to H_2 and the energy change for surface to subsurface migration.

	E_{sub} (eV)	**Bond length (A)**	**$\Delta E=E_{sub}-E_{ads}$ (eV)**
Cr_2O_3	0.545	0.995	0.764
Fe_2O_3	-0.138	1.007	0.789

Climbing Nudged Elastic Band (CI-NEB) calculations were used to find the transitions state of the surface to subsurface migration using five images. For Fe_2O_3, the energy barrier is 1.05 eV. From the initial to transition state, the adsorbed hydrogen rotates in the (0001) plane, toward the Fe^s atom, and moves below the surface. The Fe^s atom shifts slightly out of the surface, and it moves away from the adsorbed hydrogen in the (0001) plane. Between the transition state and the final subsurface configuration, the hydrogen atom moves slightly into the surface and into the unoccupied octahedral. In the (0001) plane, Fe^s moves back towards the starting position, but remains slightly displaced.

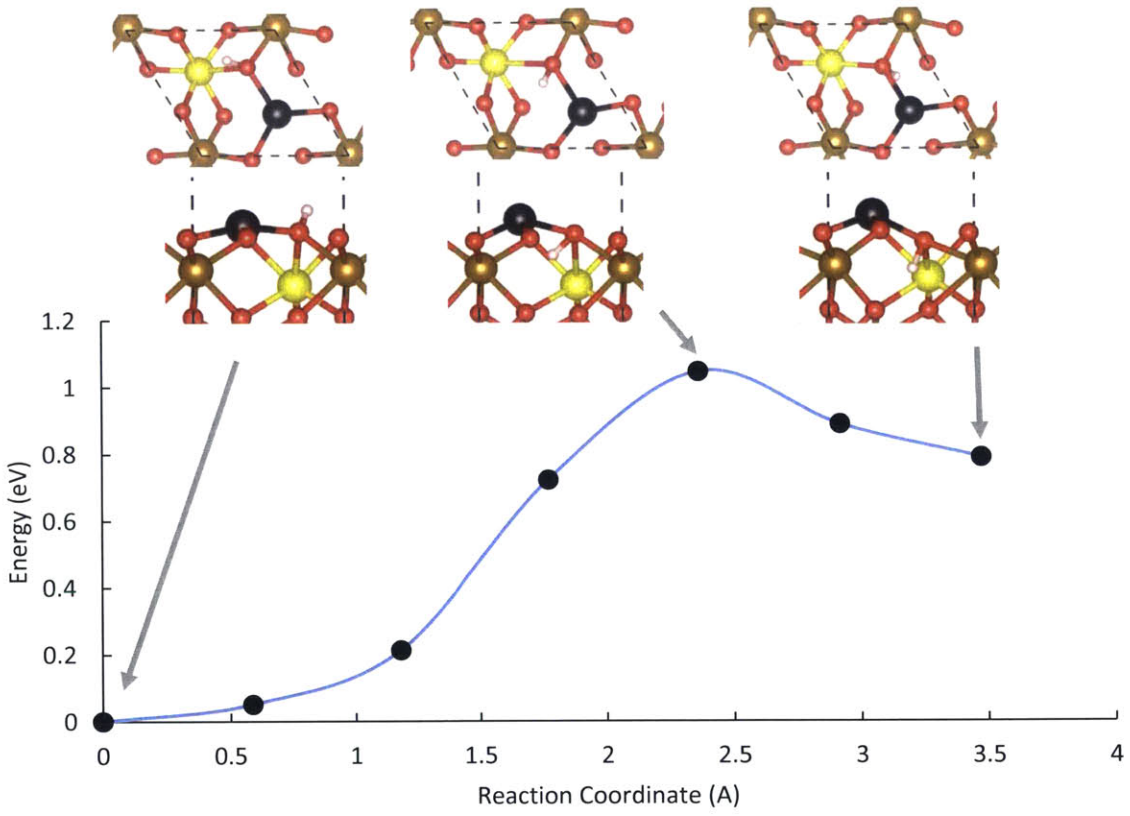

Figure 8-10. Minimum energy pathway for hydrogen migration from the surface to subsurface on (0001) Fe_2O_3 at 1 ML coverage

For Cr_2O_3, the calculated energy barrier is 0.93 eV. The minimum energy path for surface to subsurface migration is longer for Cr_2O_3 than Fe_2O_3, and there appears to be a slight local minimum between the transition state and final state, as seen in Figure 8-11. Between the initial and transition states, the adsorbed hydrogen rotates in the (0001) plane toward the unoccupied octahedral. There is little change in its height above the surface. The Cr^s atom moves out of the surface and in the (0001) plane it shifts away from the adsorbed hydrogen. At the transition state, the Cr^s-O_c^s bond has stretched to 2.84 A from an initial length of 2 A. Between the transition state and the final subsurface state, the adsorbed hydrogen moves into the surface and rotates in the (0001) plane. The Cr^s atom moves back towards its initial position, but remains displaced.

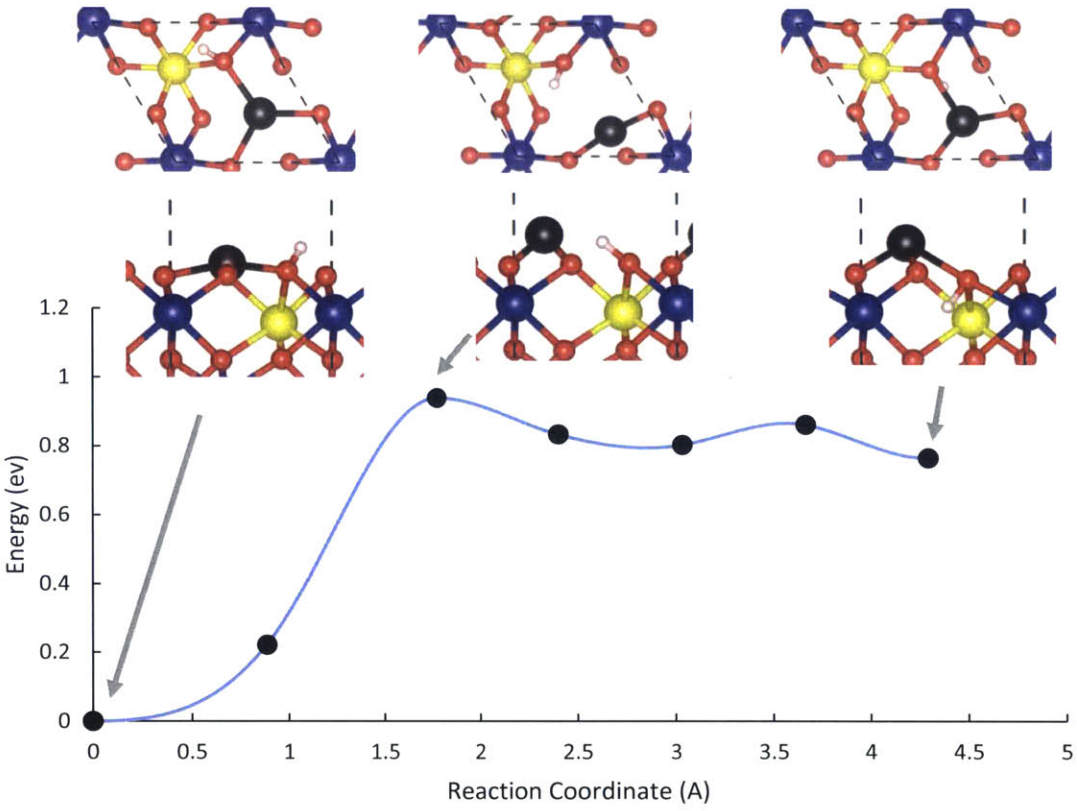

Figure 8-11. Minimum energy pathway for hydrogen migration from the surface to subsurface on (0001) Cr_2O_3 at 1 ML coverage

For the surface to sub-surface migration, the positions of atoms in the intial state are nearly identical for Fe_2O_3 and Cr_2O_3. The minimum energy pathway differs in that the Cr^s is displaced more than the Fe^s in order to accommodate the subsurface hydrogen. The transition state for Cr_2O_3 involves significant lengthening of the Cr^s-O_c^s distance and little displacement of H in the c-direction. For Fe_2O_3, the hydrogen rotation in the (0001) plane is the same, but it has already moved below the surface at transition state. The Fe^s has moved less in both the (0001) plane and c-direction, and the change in the Fe^s-O_c^s bond length is much smaller.

8.4 Recombination vs. Absorption

From a thermodynamic perspective, hydrogen is more stable chemisorbed or physisorbed on the perfect (0001) surfaces than below surface. Thus, both oxide surfaces should protect against hydrogen ingress to some degree. However, the calculations here are of a finite size, and do not include the effects of defects at the surface. With a larger simulation cell the energy for adsorption to a subsurface location is likely to be smaller. Defects, such as vacancies at the surface will also change the adsorption energy. Regardless it is important to keep in mind that adsorption energies only tell the relative stability of hydrogen and not the relative rates of absorption and desorption of pre-existing adsorbed hydrogen.

The energy barrier for Fe_2O_3 migration below the surface is significantly smaller than the barrier for recombination (1.03 vs. 2.21 eV). It is important to note that the 2.21 eV reported for the recombination barrier is for the electron transfer step. This energy barrier will change with the Fermi energy of the oxide. The barrier for H_2 formation is 0.72 eV. For Cr_2O_3, the energy barrier for recombination is lower than that for migration below the surface. However, as previously mentioned, the recombination energy barrier was determined from the most stable state at 2 ML coverage, which has higher adsorption energies than 1 ML and 3 ML coverage. This does not take into account the energy barrier for proton reduction.

Two other studies of hydrogen incorporation and recombination at oxide surfaces have been identified. Aschauer and Selloni investigated hydrogen interactions with the (101) anatase TiO_2 surface with PBE and PBE+U. Their results suggested that desorption

was favored by thermodynamics, but the kinetic barrier for incorporation was smaller than that for recombination. [172] Zhang et al. studied hydrogen interactions on α-Al_2O_3, which shares the same structure as Cr_2O_3 and Fe_2O_3. On the Al-terminated (0001) surface, they found a stable adsorption site on a surface oxygen atom. For one atom on a (2x2) cell, equivalent to 1/4 ML coverage in this present study, the adsorption energy was -2.35 eV, and the bond length was 0.98 A. For two atoms, the lowest energy configuration was an oxygen site and a surface Al site. The energy barrier for diffusion into the subsurface was 1.40 eV, and the barrier for recombination from the O-H and Al-H configuration was 0.93 eV. [173]

The main difference between Fe_2O_3 and Cr_2O_3 can be attributed to the electronic structure and cell size effects. Because the cell size is finite, the addition of each adsorbed hydrogen changes the work function, which is the energy to bring an electron from a vacuum to the oxide slab. Table 8-7 lists the work function of the slab models with adsorbed hydrogen atoms. When a hydrogen atom adsorbs in the form of a proton, its electronic charge is transferred to the oxide, and the work function decreases (the Fermi energy increases). When a hydrogen atoms adsorbs as a hydride ion, electronic charge is transferred from the oxide to hydrogen, and the work function increases (the Fermi energy decreases).

Table 8-7. Work function of Cr_2O_3 and Fe_2O_3 with adsorbed hydrogen

Case	Cr_2O_3	Fe_2O_3
Clean surface	5.42	5.32
1 ML	4.33	4.86
2 ML: $O^s + O^s$	3.29	4.85
2ML: $M^s + O^s$	5.84	6.62
3ML: $O^s + O^s + O^s$		4.85
3ML : $M^s + O^s + O^s$	5.15	

If the Fermi level in the oxide is sufficiently high, than hydride adsorption is favored over proton adsorption. Figure 8-12 illustrates this point using an electronic energy level diagram, similar to those in Chapter 6. Note that DFT calculates the ground state energy, and so in this figures, the Fermi level is shown at the valence band. The key variables to understanding proton vs. hydride adsorption are the relative positions with respect to the band structure and the work function in the oxide. The situation is more complicated than shown in Figure 8-12, because adsorption can change the position of surface ions, thus changing the local density of states.

For Cr_2O_3, the addition of a second hydrogen to an oxygen site lowers the work function to 3.29 eV, meaning that the DFT-calculated Fermi energy is 2.1 eV greater than that of the clean surface. Recall from Chapter 7 that the band gap at the surface was ~2.2 eV. For Fe_2O_3, the addition of the second hydrogen to an oxygen site causes minimal change to the work function. If the second hydrogen adsorbs to the Fe atom instead, then the work function increases to 6.62 eV, which is 1.3 eV greater than the work function of the clean surface. For Cr_2O_3, if the second hydrogen adsorbs to the Cr atom, then the work function increases to 5.84 eV, which is 0.4 eV higher than the clean surface work function. The differences between the two oxides reveals an important point: in order for

the surface to transfer charge to an adsorbed proton, the Fermi level in the oxide must be sufficiently high. Likewise, for a neutral hydrogen atom to transfer charge to an oxide, the Fermi level must be sufficiently low.

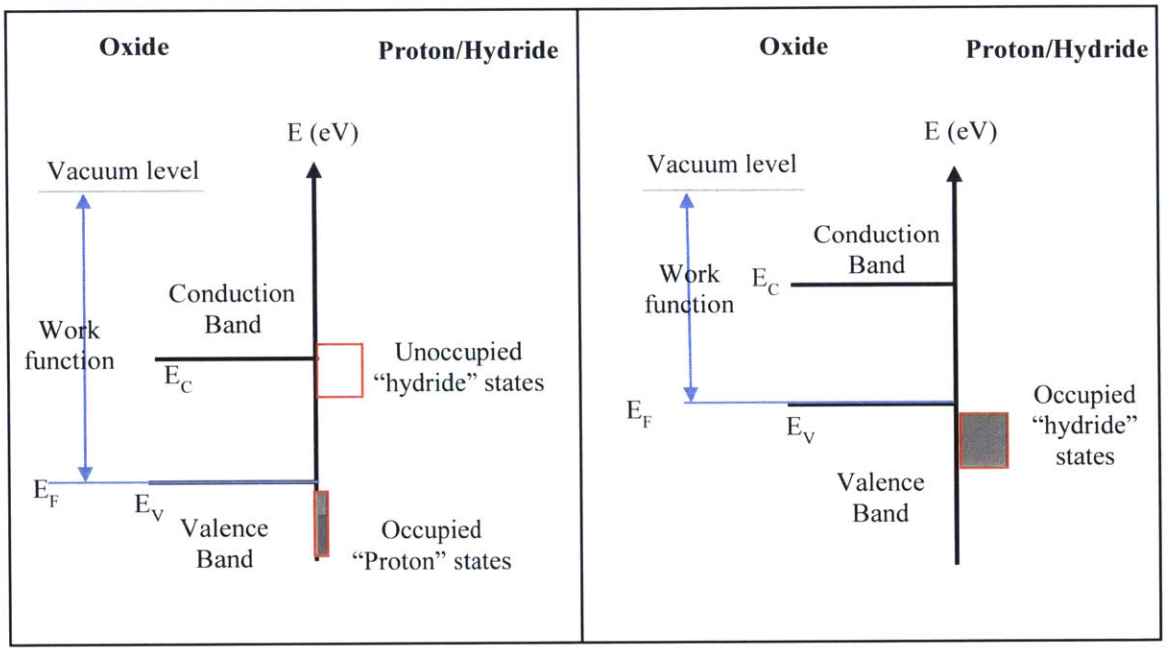

Figure 8-12. Energy levels of hydride (H-) and proton (H+) adsorption to Fe_2O_3 and Cr_2O_3 in DFT calculations

8.5 Chapter Summary and Future Work

In this chapter, DFT was used to study the interactions of hydrogen with the (0001) surfaces of Fe_2O_3 and Cr_2O_3. Atomic adsorption, Molecular adsorption, and subsurface adsorption energies were calculated. Additionally, CI-NEB calculations were performed to determine the energy barriers to hydrogen recombination and incorporation

into the oxide. The calculation presented in this chapter are an important step in understanding hydrogen interactions with these surfaces.

Hydrogen adsorbs in a charged state, either forming hydroxides with surface oxygen or adsorbing as a proton on a surface metal atom. Thus, when atomic hydrogen adsorption is modeled, there is some degree of electron transfer between the oxide and adsorbed atoms. Thus calculated adsorption energies include the effects of charge transfer: for example, the proton adsorption energy and the effect of injecting an additional electron into the oxide.

One key result is that proton incorporation into the oxide is an endothermic process. The energy change and barrier for hydrogen to migrate from the surface to a subsurface position is 0.76 eV and 0.93 eV for Cr_2O_3 and 0.79 eV and 1.05 eV for Fe_2O_3.

Concerning recombination, we have identified a mechanism for hydrogen recombination on the (0001) surfaces for hydrogen evolution. It involves the formation of a hydride ion (H-) adsorbed to the top most metal ion. The second step is recombination with a proton (H+) adsorbed to an adjacent surface oxygen ion. It is likely that electron transfer from the oxide surface to turn an adsorbed proton into an adsorbed hydride ion is the crucial step in the recombination process. This second step has a modest energy barrier, calculated at 0.72 eV and 0.28 eV for Fe_2O_3 and Cr_2O_3 respectively.

The work presented in this chapter is useful for understanding the mechanism of hydrogen recombination and incorporation into the oxide surface. These results can help identify areas for further investigation. There are four areas where further exploration could be fruitful: (1) surface coverage effects on energies and surface reconstructions (2) temperature effects to adsorption energies and energy barriers (3) changes in work

function with electron transfer to and from hydrogen and the oxides (4) the effect of water on charge transfer reactions.

Larger simulation cells would be necessary to calculate adsorption energies at lower surface coverage and determine if the energy barriers to hydrogen recombination and incorporation change at lower coverage. In this work, thick surface models were required to calculate the energy of hydrogen in subsurface positions and of hydrogen adsorption at high coverage with reconstructions to the oxide surface. Increasing the size of the surface supercell to (1x2) or (2x2) will be computationally expensive because of the number of atoms in the cell, the spin dependence, and on site coulomb repulsion. However, the hydrogen adsorption sites and bond lengths reported in this work will be useful for determining initial positions in large-cell relaxations.

One important question to consider is whether reconstructions occur with two adjacent O^S-H at low coverage, and how the energy of this pair compares to the O^s-H M-H pair. A sample calculation was run for Cr_2O_3, using a (2x2) supercell with (2x2x1) k-point mesh sampling and running to a force convergence of 0.05 eV/A, the adsorption energy for adjacent O^S-H is estimated to be -0.35 eV per atom, which is slightly more favored than adsorption at 1 ML coverage. With the larger slab model, the surface does not rearrange to the same degree found in the (1x1) supercell. It is likely that the proton to hydride transformation will be endothermic. Changes to the energies of the O^S-H O^S-H and O^s-H M-H configurations will likely affect the energy barriers for hydrogen evolution.

To include temperature effects to adsorption energies, we are interested in the change in Gibbs free energy, which is made up of the following contributions:

$$\Delta G_{ads} = \Delta E_{DFT} + \Delta E_{ZPE} + \Delta F_{vib} - T\Delta S_{config} + P\Delta V - \frac{\mathcal{N}_H}{2}\mu_{H_2} \quad (8\text{-}2)$$

If we neglect the volume term and configurational entropy terms, then the only difference between the adsorption free energy and the adsorption free energy defined in Equation (8-1) is the change in vibration free energy and change in zero point energy. A simple approach to treating the vibrational free energy is to use the harmonic quantum oscillator approximation and only consider the modes from absorbed atoms. Such a treatment assumes that the vibrational modes from the surface are separate from those of the adsorbed atoms and do not change with adsorption. The adsorbed atoms have three degrees of freedom, and thus the change in vibrational free energy is:

$$\Delta F_{vib} \approx -k_B T \sum_{i}^{3\times\mathcal{N}_H} ln\left(\frac{e^{-\frac{\hbar\omega_i}{2k_BT}}}{1-e^{-\frac{\hbar\omega_i}{k_BT}}}\right) \quad (8\text{-}3)$$

$$\Delta E_{ZPE} \approx \sum_{i}^{3\times\mathcal{N}_H} \frac{\hbar\omega_i}{2} \quad (8\text{-}4)$$

Table 8-8 shows the frequency modes for hydrogen adsorbed on Cr_2O_3 at 2ML coverage, and the corresponding ZPE correction and vibrational free energy at 600K, calculated according to Equations (8-3) and (8-4). From these results, the effect of vibrational energy is to destabilize adsorption. For reference, in Chapter 6 we calculated the chemical potential for molecular hydrogen in a PWR core to be ~ -0.9 eV relative to the chemical potential at 0K. In either configuration, dissociative hydrogen adsorption would not be favored, as the adsorption energies relative to the 0 K H_2 energy were slightly positive. However, in most of the adsorption calculations, there was noticeable

rearrangement of atoms in the top layers of the oxide. In those cases, the simple approach here may not be applicable, and the phonon calculations may be more involved.

Table 8-8. Modes for adsorbed hydrogen on Cr_2O_3 at 2 ML coverage

	O^s-H O^s-H	**O^s-H Cr^s-H**
Frequencies	3547 cm^{-1}	3017 cm^{-1}
	3051 cm^{-1}	1534 cm^{-1}
	1076 cm^{-1}	1051 cm^{-1}
	884 cm^{-1}	855 cm^{-1}
	817 cm^{-1}	655 cm^{-1}
	506 cm^{-1}	572 cm^{-1}
ZPE	0.61 eV	0.48 eV
ΔF_{vib}(600K)	0.58 eV	0.44 eV

The changing work function with hydrogen adsorption is an important factor to consider. In real world situations, oxides would be much larger than DFT model used in these calculations, and the work function would not be expected to change with adsorption. For adsorption, recombination, and incorporation, the quantity of interest is the change in energy (or energy barrier) when the change in work function is negligible. One way to determine these energies involves varying the size of the surface model. Skúlason et al. developed a method for addressing the change in work function for hydrogen evolution in order to estimate energy changes when the change in work function is zero. [174] Although their work was for platinum, the same methodology could be addressed to the oxide electrodes.

The effects of water can be quite complex. First, water molecules can adsorb and dissociate on the oxide surfaces. There have been several DFT studies on the interactions of water with the Fe-terminated (0001) hematite surface. With respect to the energy of

the water molecule, both molecular and dissociative adsorption are favorable. [129,134,135] Consequently, water adsorption will compete with proton adsorption, and the oxide surfaces may be hydroxlated. The second effect of water comes from space charge effects- ie. from the Helmholtz layer, which will affect reactions energies and energy barriers for charge transfer.

Chapter 9: Conclusions, Key Findings, Implications, and Future Work

In this thesis, we set out to better understand the process of hydrogen entry in zirconium alloy fuel cladding. We used two different approaches:

1. Understanding the coolant chemistry in a PWR. This sets the boundary conditions for corrosion and hydrogen pickup, including surface reactions. It also effects the properties of the oxide layer, including defect concentrations.
2. Directly studying hydrogen interactions with Fe_2O_3 and Cr_2O_3, two compounds found in the oxidized second phase particles (SPPs)

9.1 Summary of Findings

Water Chemistry in a PWR:

- We have identified the combination of the AECL water reaction set and Christensen's g-values to be the best at reproducing the effects of hydrogen addition on water chemistry under irradiation, in particular in predicting a critical hydrogen concentration.
- We have confirmed that dose rates to coolant in a PWR increase with the linear heat generation rate, as well as fuel burnup. In order to evaluate the effects of radiolysis on coolant chemistry in the core especially including local effects on fuel rods with higher burnup or high power, it is important to have accurate neutronic data- meaning individual fuel rod pin powers and burnup

- Boron addition (more specifically ^{10}B, which is responsible for the alpha dose) has the greatest effect on the concentration of oxidizing species in the coolant
- The effect of the radical scavengers Fe and Ni on coolant chemistry is likely relatively small in a PWR. Both species have very low solubility at PWR temperatures which limits the effects on bulk water chemistry
- Dose rate calculations for a PWR with CRUD indicate that dose rates to the bulk coolant are higher by ~21% than dose rates in a core without CRUD. This enhancement applies to alpha, gamma, and neutron dose.
- Gamma dose rates to the confined coolant within CRUD deposit will be the same as those to the adjacent coolant channel. Fast neutron dose rates to confined coolant will be slightly higher, approximately 8%, than in the adjacent channel.
- Alpha dose rates to confined coolant can be significantly higher than dose rates to the bulk coolant. Using stopping power, we estimate that 25% of the alpha dose deposited in the porous CRUD volume will go to the confined coolant. However, small changes in this energy partition will have a substantial effect on the dose rates to the confined coolant, in particular for CRUD deposits with significant boron enrichment.
- Axial Offset Anomaly (AOA) increases the concentration of oxidizing species in the lower part of the core, and moves the location of the peak O_2 and H_2O_2 concentrations, which corresponds to the point where net water recombination begins, toward the bottom of the core.

- An increase in dose rates to the coolant from CRUD will raise the concentrations of oxidizing species adjacent to CRUD deposits. The extent will depend on how much CRUD is present in the core. For the power profiles that were used, this increase outweighs the decrease due to AOA, at least at the axial heights where the CRUD region starts.
- For PWR type water chemistry, with hydrogen injection of 25-50 scc H_2/kgH_2O, the chemical potential of hydrogen in the core can be estimated from the hydrogen injection and coolant temperature. Radiolysis has little effect on the chemical potential. For the oxygen chemical potential, the effects of radiolysis should be included.

The energy level comparison for hydrogen evolution at oxidized Zircaloy-4 fuel cladding:

- Using water chemistry from radiolysis simulations in a PWR, we can estimate the ECP (corrosion potential), and the H_2/H^+ redox potential. If we use the ECP as an estimate of the Fermi level in the metal and thus an upper limit to the Fermi energy in the oxide layer, and the H_2/H^+ redox potential to estimate the energy of the individual redox reactions ($H^+ + e^- \rightarrow H$ and $H \rightarrow H^+ + e^-$), we find that the energy at which $H^+ + e^- \rightarrow H$ can occur is higher than the Fermi *energy* in the oxide.
- A small potential drop across the oxide is advantageous for proton evolution.
- The estimated Fermi level of the H_2/H^+ pair is relatively high compared to estimates of the conduction band minimum and valence band maximum of

ZrO_2, Fe_2O_3, Cr_2O_3, and SnO_2. Consequently, electron transfer will likely take place at the conduction band.

- Using the energy level comparison is difficult because there are numerous materials coupled (the metal, ZrO_2, SnO_2, Fe_2O_3, Cr_2O_3, mixed oxide $(Fe,Cr)_2O_3$, and the coolant) and the system is not in equilibrium. This approach can only be used to rule out possible sites for the cathodic reaction in the case that the conduction band *energy* is too low. To determine transfer rates, more information including the separation between the acceptor and donor s at the oxide interface, the concentration of conduction electrons, and degree of band bending would be required.

Density Functional Theory Calculations of Fe_2O_3 and Cr_2O_3

- Sites for hydrogen adsorption on (0001) Fe_2O_3 and Cr_2O_3 have been identified. At low Fermi energies, hydrogen most likely adsorbs as a proton (H+) on a surface oxygen ion, forming a hydroxide ion (OH^-) At high Fermi energies, hydrogen most likely adsorbs as a hydride (H-) on a surface metal ion.
- At high coverage, greater than 1 ML, hydrogen adsorption to either surface cause noticeable rearrangement of the surface ions.
- A mechanism for hydrogen recombination on the oxide surfaces has been identified. An adsorbed proton and an adsorbed hydride recombine to form a hydrogen molecule, i.e. $H^+_{ads} + H^-_{ads} \rightarrow (H_2)_{ads}$ The limiting step for

hydrogen recombination is likely the electron transfer step required to turn an adsorbed proton into a hydride. $H^+_{ads} + e^- \rightarrow H^-_{ads}$

- The energy for subsurface adsorption to Fe_2O_3 and Cr_2O_3 has been calculated. For both materials, hydrogen likely adsorbs to the unoccupied octahedral below the topmost surface metal ion, in the form of a hydroxide. In the absence of temperature effects, hydrogen is more stable adsorbed on surface than below the surface. The energy barriers for subsurface migration at 1 ML coverage are 1.05 eV for Fe_2O_3 and 0.93 eV for Cr_2O_3.

9.2 Implications for Hydrogen Pickup of Zirconium Alloy Fuel Cladding in PWR

The goal of this thesis was to better *understand* the mechanisms of hydrogen pickup and the hydrogen split. The more practical application of this thesis is: how can we reduce hydrogen pickup?

To reduce hydrogen pickup, we would need to shift the hydrogen split so as to encourage recombination and discourage hydrogen adsorption. Recall that the hydrogen split must be determined by kinetic factors. One approach is to limit the hydrogen entrance and diffusion rate in the oxide. Limiting ingress through the oxide layer may prove challenging, especially if porosity and/or grain boundaries provide fast transport paths. The second approach to reducing hydrogen pickup is to increase the recombination rate. Our results indicate that the electron transfer reaction may be the limiting step in hydrogen recombination. Possibilities for increasing the recombination rate include:

1. Providing a metal cathode, through some form of metallic deposition. A metallic cathode would likely be more efficient at conducting electrons and reducing protons. However, certain metals (such as metallic SPPs) can also provide fast ingress paths.
2. Increasing the conductivity of the oxide through doping. This could have deleterious effects if the rate limiting step to oxide growth is electron transport. If electron transport to the oxide surface is the limiting step to hydrogen recombination, this would increase the recombination rate.
3. Providing an oxide cathode with an "ideal" conduction band: Given the difficult in determining the electron energy distribution at which proton reduction occurs, this would be extremely difficult.

9.3 Major Contributions

1. The PWR radiolysis model: An advanced model has been developed that includes realistic geometry, core power profiles, dose rates, and boron /lithium addition. This is the first time that a detailed non-proprietary model has been developed. This model is useful for understanding chemistry within the core and it can also be used to study water chemistry in other parts of the primary loop, such as the steam generator. This model is already set up to perform single channel radiolysis chemistry calculations, so it can be used to further study local chemistry conditions in core.

2. Dose rates for a PWR: a detailed set of dose rates for a PWR core have been developed. The dose to power ratios presented in this work can be used to calculate dose rates for PWRs under other conditions, with different boron concentrations, axial power profiles, burnup, and power. Again, this is the first detailed, non-proprietary data set.
3. PWR water chemistry with CRUD: to the best of our knowledge, this work represents the first effort to study the effects of CRUD on radiolysis and water chemistry within a core. The results from these calculations can be used as in input to chemistry models within CRUD.
4. Chemical potentials of oxygen and hydrogen in PWR coolant: This is information required for mechanistic models for corrosion and hydrogen pickup. These chemical potentials are also required for the study of defect stability in ZrO_2.
5. DFT calculations for hydrogen adsorption on Fe_2O_3 and Cr_2O_3: The adsorption sites and energies at high coverage have been calculated and compared. To the best of our knowledge, this is the first study of hydrogen interactions with Cr_2O_3 using DFT+U.
6. Hydrogen adsorption to the subsurface in Cr_2O_3 and Fe_2O_3: the sites and adsorption energies at 1 ML coverage have been identified. Previous studies in on hydrogen defects, including interstitial hydrogen and hydrogen in vacancies, within bulk Cr_2O_3 and Fe_2O_3 have been performed, but not for hydrogen entry into the surface [138,139,175]
7. Mechanism for hydrogen evolution on Cr_2O_3 and Fe_2O_3: A path for hydrogen recombination on Cr_2O_3 and Fe_2O_3 has bene identified, which involves electron

transfer to an adsorbed proton, and molecular hydrogen formation from adjacent adsorbed proton and hydride ion (H^+ and H^-). This information can be useful for studying photocatalytic water splitting, as well as waterside corrosion of stainless steels and other Fe-Cr containing alloys.

9.4 Future Work

1. One crucial area to investigate is the partition of alpha dose within CRUD: how much of the dose is deposited in the solid CRUD and confined coolant. The mean free path of alpha particles is on the order of 1-10 μm. It is possible that geometry will have some effect on the dose deposited to the coolant. The boron concentration varies across the CRUD layer, and given the range of an alpha particle, it may be important to characterize.
2. Another area to investigate is the effects of radiolysis on chemistry within CRUD. In this work, we have determined the effects of CRUD on bulk water chemistry. The next step is to study the effect of radiolysis within CRUD deposits. This sort of study would be a natural continuation of thermal hydraulic models and boron deposition models within CRUD. The chemistry within CRUD will be important in understanding the effects of CRUD on corrosion and hydrogen pickup.
3. Interactions of hydrogen with Fe_2O_3 and Cr_2O_3 should be investigated further. In particular, low coverage adsorption should be investigated. Doing so will require a larger simulation cell, so it is important to determine if a thinner

surface model can be used before performing simulations. The adsorbed H^+ H^- pair at lower coverage should be studied to get an estimate of the energy barrier for electron transfer to an adsorbed proton at the surface. Large cell sizes will also be required to address the changes in work function with adsorption and desorption.

4. Hydrogen interactions on ZrO_2 surfaces should be studied. The energy level analysis suggests that ZrO2 may be a site for the cathodic reaction. More importantly, we would need to know how the energetics of these reactions compare to Fe_2O_3 and Cr_2O_3 to better understand the role of oxidized precipitates in the hydrogen split. The effects of iron defects in ZrO_2 would also be important to study, because iron enrichment is found in the vicinity of Fe-containing intermetallics. It is possible that these defects may alter the ability of ZrO_2 to reduce protons and could be associated with high hydrogen pickup fractions observed in Zr-Fe binary alloys.

References

[1] Waterside Corrosion of Zirconium Alloys in Nuclear Power Plants, IAEA, 1998.
[2] L.O. Jernkvist, A.R. Massih, Models for Fuel Rod Behavior at High Burnup, Swedish Nuclear Power Inspectorate, Sweden, 2004.
[3] F. Garzarolli, B. Cox, P. Rudling, J. ASTM Int. 7 (2010).
[4] B. Cox, P. Rudling, Hydriding Mechanisms and Impact on Fuel Performance, Advanced Nuclear Technology, Sweden, 2000.
[5] P. Rudling, G. Wikmark, J. Nucl. Mater. 265 (1999) 44.
[6] G. Lelievre, C. Tessier, X. Iltis, B. Berthier, F. Lefebvre, J. Alloys Compd. 268 (1998) 308.
[7] I. Takagi, K. Une, S. Miyamura, T. Kobayashi, J. Nucl. Mater. (n.d.).
[8] N. Ramasubramanian, P. Billot, S. Yagnik, in:, G.D. Moan, P. Rudling (Eds.), Zircon. Nucl. Ind. Thirteen. Int. Symp., ASTM International, West Conshohocken, PA, 2002, pp. 222–244.
[9] B. Cox, J. Nucl. Mater. 264 (1999) 283.
[10] B. Cox, Y.-M. Wong, J. Nucl. Mater. 270 (1999) 134.
[11] PWR Primary Water Chemistry Guidelines. Volume 1, Revision 4, EPRI, Palo Alto, CA, 1999.
[12] Rootcause Investigation of Axial Power Offset Anomaly, EPRI, Palo Alto, CA, 1997.
[13] M. Short, D. Hussey, B.K. Kendrick, D. Gaston, C. Permann, T. Besmann, J. Li, S. Yip, 3D Modeling of Real CRUD Scrapes Using MAMBA-BDM v2.0 (MPO Advanced Model for Boron Analysis - Boron Deposition Model), CASL, 2012.
[14] PWR Axial Offset Anomaly (AOA) Guidelines, Revision 1, Palo Alto, CA, 2004.
[15] M. Steinbrück, M. Böttcher, J. Nucl. Mater. 414 (2011) 276.
[16] M. Preuss, P. Frankel, S. Lozano-Perez, D. Hudson, E. Polatidis, N. Ni, J. Wei, C. English, S. Storer, K.B. Chong, M. Fitzpatrick, P. Wang, J. Smith, C. Grovenor, G. Smith, J. Sykes, B. Cottis, S. Lyon, L. Hallstadius, R.J. Comstock, A. Ambard, M. Blat-Yrieix, J ASTM Intl 8 (2011).
[17] M. Oskarsson, Study on the Mechanisms for Corrosion and Hydriding of Zircaloy, Royal Institute of Technology, KTH, 2000.
[18] M. Lindgren, G. Sundell, I. Panas, L. Hallstadius, M. Thuvander, H.-O. Andrén, in:, Zircon. Nucl. Ind. 17th Vol., ASTM International, 2014, pp. 1–25.
[19] C. Anghel, Modified Oxygen and Hydrogen Transport in Zr-Based Oxides, Royal Institute of Technology, KTH, 2006.
[20] N. Ni, S. Lozano-Perez, M.L. Jenkins, C. English, G.D.W. Smith, J.M. Sykes, C.R.M. Grovenor, Scr. Mater. 62 (2010) 564.
[21] R. Benaboud, P. Bouvier, J.-P. Petit, Y. Wouters, A. Galerie, J. Nucl. Mater. 360 (2007) 151.
[22] Y. Dali, M. Tupin, P. Bossis, M. Pijolat, Y. Wouters, F. Jomard, J. Nucl. Mater. 426 (2012) 148.

[23] K. Sakamoto, K. Une, M. Aomi, K. Hashizume, Nucl. Mater. Sel. Artic. E-MRS 2011 Spring Meet. 57 (2012) 101.
[24] J. Hyuk Baek, Y. Hwan Jeong, J. Nucl. Mater. 304 (2002) 107.
[25] Y. HATANO, M. SUGISAKI, J. Nucl. Sci. Technol. 34 (1997) 264.
[26] X. Iltis, F. Lefebvre, C. Lemaignan, J. Nucl. Mater. 224 (1995) 121.
[27] B.V. Cockeram, K.J. Leonard, L.L. Snead, M.K. Miller, J. Nucl. Mater. 433 (2013) 460.
[28] B. Cox, J. Nucl. Mater. 336 (2005) 331.
[29] E. Hillner, D.G. Franklin, J.D. Smee, J. Nucl. Mater. 278 (2000) 334.
[30] P. Bossis, G. Lelie\`vre, P. Barberis, X. Iltis, F. Lefebvre, in:, Zircon. Nucl. Ind. Twelfth Int. Symp., ASTM International, 2000, pp. 918–918–27.
[31] K. Une, I. Takagi, K. Sawada, H. Watanabe, K. Sakamoto, M. Aomi, J. Nucl. Mater. 420 (2012) 445.
[32] B. Cox, Mechanisms of Hydrogen Absorption by Zirconium Alloys, Atomic Energy of Canada Limited, Chalk River, Ontario, 1985.
[33] Assessment of the Effect of Elevated Reactor Coolant Hydrogen on the Performance of PWR Zr-Based Alloys, EPRI, Palo Alto, CA, 2006.
[34] B. Cox, J. Alloys Compd. 256 (1997) 244.
[35] K. Takeda, H. Anada, in:, Zircon. Nucl. Ind. Twelfth Int. Symp., ASTM International, 2000, pp. 592–608.
[36] Y. Broy, F. Garzarolli, A. Seibold, L.V. Swam, in:, Zircon. Nucl. Ind. Twelfth Int. Symp., ASTM International, 2000, pp. 609–609–14.
[37] B.H. Lim, H.S. Hong, K.S. Lee, J. Nucl. Mater. 312 (2003) 134.
[38] T. Murai, T. Isobe, Y. Mae, J. Nucl. Mater. 226 (1995) 327.
[39] T. Murai, T. Isobe, Y. Mae, J. Nucl. Mater. 230 (1996) 178.
[40] T. Murai, T. Isobe, Y. Takizawa, Y. Mae, in:, Zircon. Nucl. Ind. Twelfth Int. Symp., ASTM International, 2000, pp. 623–623–18.
[41] M.Y. Yao, J.H. Wang, J.C. Peng, B.X. Zhou, Q. Li, J. ASTM Int. 8 (2011).
[42] A. Couet, A.T. Motta, R.J. Comstock, J. Nucl. Mater. 451 (2014) 1.
[43] A. Couet, A.T. Motta, R.J. Comstock, Zircon. Nucl. Ind. 17th Vol. (2014) 1.
[44] C. Anghel, G. Hultquist, M. Limbäck, J. Nucl. Mater. 340 (2005) 271.
[45] C. Anghel, G. Hultquist, M. Limbäch, P. Szakalos, in:, Zircon. Nucl. Ind. 15th Int. Symp., ASTM International, 2009, pp. 285–285–18.
[46] W.G. Luscher, E.R. Gilbert, S.G. Pitman, E.F. Love, J. Nucl. Mater. (n.d.).
[47] K. Baur, F. Garzarolli, H. Ruhmann, H.-J. Sell, in:, Zircon. Nucl. Ind. Twelfth Int. Symp., ASTM International, 2000, pp. 836–836–17.
[48] K. Kakiuchi, N. Itagaki, T. Furuya, A. Miyazaki, Y. Ishii, S. Suzuki, T. Terai, M. Yamawaki, in:, Zircon. Nucl. Ind. Fourteenth Int. Symp., ASTM International, 2005, pp. 349–349–18s.
[49] K. Kakiuchi, N. Itagaki, T. Furuya, A. Miyazaki, Y. Ishii, S. Suzuki, T. Terai, M. Yamawaki, Proc. 11th Int. Conf. High Temp. Mater. Chem. HTMC-XI 66 (2005) 308.
[50] P.J. Shirvington, J. Nucl. Mater. 37 (1970) 177.
[51] Y.-J. Kim, R. Rebak, Y.-P. Lin, D. Lutz, D.C. Crawford, A. Kucuk, B. Cheng, in:, Zircon. Nucl. Ind. 16th Int. Symp., ASTM International, 2010, pp. 91–117.

[52] N. Ramasubramanian, P.V. Balakrishnan, in:, A.M. Garde, E.R. Bradley (Eds.), Zircon. Nucl. Ind. Tenth Int. Symp., ASTM International, Philadelphia, 1994, pp. 378–399.
[53] N. Ramasubramanian, V. Perovic, M. Leger, in:, Zircon. Nucl. Ind. Twelfth Int. Symp., ASTM International, 2000, pp. 853–853–24.
[54] M. Kiran Kumar, S. Aggarwal, V. Kain, T. Saario, M. Bojinov, Nucl. Eng. Des. 240 (2010) 985.
[55] D. Pecheur, J. Godleweski, J. Peybernes, L. Fayette, M. Noe, A. Frichet, O. Kerrec, in:, Zircon. Nucl. Ind. Twelfth Int. Symp., ASTM International, West Conshohocken, PA, 2000, pp. 793–809.
[56] P. Bossis, D. Pe^cheur, K. Hanifi, J. Thomazet, M. Blat, in:, Zircon. Nucl. Ind. Fourteenth Int. Symp., ASTM International, 2005, pp. 494–525.
[57] P. Bossis, B. Verhaeghe, S. Doriot, D. Gilbon, V. Chabretou, A. Dalmais, J.-P. Mardon, M. Blat, A. Miquet, in:, Zircon. Nucl. Ind. 15th Int. Symp., ASTM International, 2009, pp. 430–456.
[58] C.C. Lin, Radiochemistry in Nuclear Power Reactors, National Academy Press, Washington, D.C., 1996.
[59] S. Le Caër, Water 3 (2011) 235.
[60] G.V. Buxton, in:, Farhataziz, M.A.J. Rodgers (Eds.), Radiat. Chem. Princ. Appl., VCH Publishers, New York, New York, 1987, pp. 321–349.
[61] B. Pastina, J. Isabey, B. Hickel, in:, Water Chem. Nucl. React. Syst. 7, BNES, Bournemouth, 1996, pp. 153–155.
[62] B. Pastina, J. Isabey, B. Hickel, J. Chim. Phys. Phys.-Chim. Biol. 94 (1997) 226.
[63] B. Pastina, J. Isabey, B. Hickel, J. Nucl. Mater. 264 (1999) 309.
[64] C. Lemaignan, J. Nucl. Mater. 187 (1992) 122.
[65] C. Lemaignan, R. Salot, in:, IAEA-TECHDOC-927, 1997, pp. 131–142.
[66] M. Jonsson, in:, J.F. Wishart, B.S.M. Rao (Eds.), Recent Trends Radiat. Chem., World Scientific Publishing Co. Pte. Ltd, Singapore, 2010, pp. 301–323.
[67] N.G. Petrik, A.B. Alexandrov, A.I. Vall, J. Phys. Chem. B 105 (2001) 5935.
[68] J.A. LaVerne, L. Tandon, J Phys Chem B 106 (2001) 380.
[69] J.A. LaVerne, J. Phys. Chem. B 109 (2005) 5395.
[70] X. Chen, S. Shen, L. Guo, S.S. Mao, Chem. Rev. 110 (2010) 6503.
[71] M.V. Glazoff, A. Tokuhiro, S.N. Rashkeev, P. Sabharwall, J. Nucl. Mater. 444 (2014) 65.
[72] M. Youssef, B. Yildiz, Phys Chem Chem Phys 16 (2014) 1354.
[73] M. Youssef, Predicting the Equilibria of Point Defects in Zirconium Oxide: A Route to Understand the Corrosion and Hydrogen Pickup of Zirconium Alloys, Massachusetts Institute of Technology, 2014.
[74] M. Lindgren, I. Panas, RSC Adv 4 (2014) 11050.
[75] M. Lindgren, I. Panas, RSC Adv 3 (2013) 21613.
[76] S.A. Simonson, Modeling of Radiation Effects of Nuclear Waste Package Materials, PhD Thesis, Department of Nuclear Engineering, Massachusetts Institute of Technology, 1988.
[77] J.H. Chun, Modeling of BWR Water Chemistry, Massachusetts Institute of Technology, 1990.

[78] D.J. Grover, Modeling Water Chemistry and Electrochemical Corrosion Potential in Boiling Water Reactors, Massachusetts Institute of Technology, 1996.
[79] C.C. Lin, Y.J. Kim, L.W. Niedrach, K.S. Ramp, Corrosion 52 (1996) 618.
[80] H.S. Kim, A Study for Modeling Electrochemistry in Light Water Reactors, The Pennsylvania State University, 2007.
[81] D.D. Macdonald, Corrosion 48 (1992) 194.
[82] D.D. Macdonald, M. Urquidi-Macdonald, J.M. Mahaffy, A. Jain, H.S. Kim, V. Gupta, J. Pitt, Electrochemistry of Water-Cooled Nuclear Reactors, Pennyslvania State University, 2006.
[83] M. Urquidi-Macdonald, J. Pitt, D.D. Macdonald, J. Nucl. Mater. 362 (2007) 1.
[84] The Reaction Set, Rate Constants and G-Values for the Simulation of the Radiolysis of Light Water over the Range 20° to 350°C Based on Information Available in 2008, Atomic Energy of Canada Limited, Ontario, Canada, 2009.
[85] A.C. Hindmarsh, IMACS Trans. Sci. Comput. 1 (1983) 55.
[86] J.R. Selman, C.W. Tobias, in:, G.R.C. Thomas B. Drew (Ed.), Adv. Chem. Eng., Academic Press, 1978, pp. 211–318.
[87] A.J. Bard, R. Parsons, J. Jordan, Standard Potentials in Aqueous Solution, Taylor & Francis, 1985.
[88] D.D. Macdonald, J. Mankowski, M. Karaminezhaad-Ranjbar, Y.-H. Hu, Corrosion 44 (1988) 186.
[89] R.F. Prini, R. Crovetto, J. Phys. Chem. Ref. Data 18 (1989) 1231.
[90] D.T. Kallikragas, A.Y. Plugatyr, I.M. Svishchev, J. Chem. Eng. Data 59 (2014) 1964.
[91] R.E. Mesmer, C.F. Baes, F.H. Sweeton, Inorg. Chem. 11 (1972) 537.
[92] W.L. Marshall, E.U. Franck, J. Phys. Chem. Ref. Data 10 (1981) 295.
[93] H. Christensen, Fundamental Aspects of Water Coolant Radiolysis, Swedish Nuclear Power Inspectorate, Sweden, 2006.
[94] C.C. Lin, Prediction of Electrochemical Potenials in BWR Primary Systems: Volume 1: Evaluation of Water Chemistry and ECP Measurements Under Hydrogen Water Chemistry, EPRI, Palo Alto, CA, 1993.
[95] E. Ibe, H. Karasawa, M. Nagase, H. Tagawa, M. Endo, in:, Water Chem. Nucl. React. Syst. 5, BNES, Bournemouth, 1989.
[96] B. Beverskog, I. Puigdomenech, Corros. Sci. 39 (1997) 43.
[97] B. Beverskog, I. Puigdomenech, Corros. Sci. 38 (1996) 2121.
[98] D.M. Bartels, J. Henshaw, H.E. Sims, Radiat. Phys. Chem. 82 (2013) 16.
[99] R.E. Donders, A.J. Elliot, (2009).
[100] Stretch Power License Amendment Request, FPL Energy Seabrook, 2003.
[101] MCNP — A General Monte Carlo N-Particle Transport Code, Version 5 Volume II: User's Guide, Los Alamos National Laboratory, 2008.
[102] H. Christensen, Nucl. Technol. 109 (1995) 373.
[103] CASMO-4E: A Fuel Assembly Burnup Program User's Manual, Studsvik, UK, 2009.
[104] N. Horelik, B. Herman, B. Forget, K. Smith, in:, Proc Int Conf Math. Comput. Methods Appl. Nuc Sci Eng, Sun Valley, Idaho, 2013.

[105] H. TAKIGUCHI, M. ULLBERG, S. UCHIDA, J. Nucl. Sci. Technol. 41 (2004) 601.
[106] I. ul Haq, N. Cinosi, M. Bluck, G. Hewitt, S. Walker, Nucl. Eng. Des. 241 (2011) 155.
[107] L. Zou, H. Zhang, J. Gehin, B. Kochunas, Nucl. Technol. 183 (2013) 535.
[108] Berger, M.J., Coursey, J.S., Zucker, M.A., Chang, J., ESTAR, PSTAR, and ASTAR: Computer Programs for Calculating Stopping-Power and Range Tables for Electrons, Protons, and Helium Ions, NIST, Gaithersburg, MD, 2005.
[109] J. Henshaw, J.C. McGurk, H.E. Sims, A. Tuson, S. Dickinson, J. Deshon, J. Nucl. Mater. 353 (2006) 1.
[110] D.S. Sholl, J.A. Steckel, Density Functional Theory: A Practical Introduction, John Wiley & Sons, Inc., 2009.
[111] M.W. Chase, National Institute of Standards and Technology (U.S.), NIST-JANAF Thermochemical Tables, American Chemical Society ; American Institute of Physics for the National Institute of Standards and Technology, [Washington, D.C.]; Woodbury, N.Y., 1998.
[112] S.R. Morrison, Electrochemistry at Semiconductor and Oxidized Metal Electrodes, Plenum Press, New York, 1980.
[113] N.W. Ashcroft, N.D. Mermin, Solid State Physics, Holt, Rinehart and Winston, New York, 1976.
[114] R. Memming, Semiconductor Electrochemistry, Wiley-VCH Verlag GmbH, 2007.
[115] N. Sato, (1998).
[116] P. Cohen, American Society of Mechanical Engineers., The ASME Handbook on Water Technology for Thermal Power Systems, American Society of Mechanical Engineers, New York, NY, 1989.
[117] O. Madelung, U. Rössler, M. Schulz, eds., in:, SpringerMaterials - Landolt-Börnstein Database, n.d.
[118] O. Madelung, U. Rössler, M. Schulz, eds., in:, SpringerMaterials - Landolt-Börnstein Database, n.d.
[119] O. Madelung, U. Rössler, M. Schulz, eds., in:, SpringerMaterials - Landolt-Börnstein Database, n.d.
[120] X. Zhao, D. Vanderbilt, Phys Rev B 65 (2002) 075105.
[121] E. Santos, W. Schmickler, Angew. Chem. Int. Ed. 46 (2007) 8262.
[122] Y. Xu, M.A.A. Schoonen, Am. Mineral. 85 (2000) 543.
[123] M.J. Carmezim, A.M. Simões, M.O. Figueiredo, M. Da Cunha Belo, Corros. Sci. 44 (2002) 451.
[124] A. Rohrbach, J. Hafner, G. Kresse, Phys. Rev. B 70 (2004) 125426.
[125] G. Rollmann, A. Rohrbach, P. Entel, J. Hafner, Phys Rev B 69 (2004) 165107.
[126] N.J. Mosey, E.A. Carter, Phys. Rev. B 76 (2007) 155123.
[127] N.J. Mosey, E.A. Carter, J. Mech. Phys. Solids 57 (2009) 287.
[128] N.J. Mosey, P. Liao, E.A. Carter, J. Chem. Phys. 129 (2008).
[129] S.M.O. Souvi, M. Badawi, J.-F. Paul, S. Cristol, L. Cantrel, Surf. Sci. 610 (2013) 7.

[130] K.N. Nigussa, K.L. Nielsen, Ø. Borck, J.A. Støvneng, Corros. Sci. 53 (2011) 3612.
[131] D. Costa, K. Sharkas, M.M. Islam, P. Marcus, Surf. Sci. 603 (2009) 2484.
[132] A. Kiejna, T. Pabisiak, J. Phys. Chem. C 117 (2013) 24339.
[133] T.P. Trainor, A.M. Chaka, P.J. Eng, M. Newville, G.A. Waychunas, J.G. Catalano, G.E. Brown Jr., Surf. Sci. 573 (2004) 204.
[134] S. Yin, X. Ma, D.E. Ellis, Surf. Sci. 601 (2007) 2426.
[135] M.-T. Nguyen, N. Seriani, R. Gebauer, J. Chem. Phys. 138 (2013).
[136] A. Hellman, R.G.S. Pala, J. Phys. Chem. C 115 (2011) 12901.
[137] D. Costa, P. Marcus, Surf. Sci. 604 (2010) 932.
[138] C. Chen, H. Yu, S. Zheng, Sci. China Technol. Sci. 54 (2011) 88.
[139] B. Malki, O. Le Bacq, A. Pasturel, B. Baroux, J. Electrochem. Soc. 161 (2014) C486.
[140] M.I. Aroyo, A. Kirov, C. Capillas, J.M. Perez-Mato, H. Wondratschek, Acta Crystallogr. Sect. A 62 (2006) 115.
[141] Aroyo Mois Ilia, Perez-Mato Juan Manuel, Capillas Cesar, Kroumova Eli, Ivantchev Svetoslav, Madariaga Gotzon, Kirov Asen, Wondratschek Hans, Z. Für Krist. 221 (2009) 15.
[142] M.I. Aroyo, J.M. Perez-Mato, D. Orobengoa, E. Tasci, G. De La Flor, A. Kirov, Bulg. Chem. Commun. 43 (2011) 183.
[143] G. Kresse, J. Hafner, Phys. Rev. B 47 (1993) 558.
[144] G. Kresse, J. Hafner, Phys. Rev. B 49 (1994) 14251.
[145] G. Kresse, J. Furthmüller, Comput. Mater. Sci. 6 (1996) 15.
[146] G. Kresse, J. Furthmüller, Phys. Rev. B 54 (1996) 11169.
[147] P.E. Blöchl, Phys Rev B 50 (1994) 17953.
[148] G. Kresse, D. Joubert, Phys Rev B 59 (1999) 1758.
[149] J.P. Perdew, K. Burke, M. Ernzerhof, Phys. Rev. Lett. 77 (1996) 3865.
[150] J.P. Perdew, K. Burke, M. Ernzerhof, Phys. Rev. Lett. 78 (1997) 1396.
[151] S.L. Dudarev, G.A. Botton, S.Y. Savrasov, C.J. Humphreys, A.P. Sutton, Phys. Rev. B 57 (1998) 1505.
[152] P.E. Blöchl, O. Jepsen, O.K. Andersen, Phys Rev B 49 (1994) 16223.
[153] G. Henkelman, A. Arnaldsson, H. Jónsson, Comput. Mater. Sci. 36 (2006) 354.
[154] E. Sanville, S.D. Kenny, R. Smith, G. Henkelman, J. Comput. Chem. 28 (2007) 899.
[155] W. Tang, E. Sanville, G. Henkelman, J. Phys. Condens. Matter 21 (2009) 084204.
[156] K. Momma, F. Izumi, J. Appl. Crystallogr. 41 (2008) 653.
[157] K. Momma, F. Izumi, J. Appl. Crystallogr. 44 (2011) 1272.
[158] Y. Wang, H. Fang, C.L. Zacherl, Z. Mei, S. Shang, L.-Q. Chen, P.D. Jablonski, Z.-K. Liu, Surf. Sci. 606 (2012) 1422.
[159] S. Shi, A.L. Wysocki, K.D. Belashchenko, Phys. Rev. B 79 (2009) 104404.
[160] Y. Sato, S. Akimoto, J. Appl. Phys. 50 (1979) 5285.
[161] L.W. Finger, R.M. Hazen, J. Appl. Phys. 51 (1980) 5362.
[162] R.E. Newnham, Y.M. de Haan, Z. Für Krist. Krist. Krist. Krist. 117 (1962) 235.
[163] D. Adler, in:, D.T. and H.E. Frederick Seitz (Ed.), Solid State Phys., Academic Press, 1968, pp. 1–113.

[164] P.J. Brown, J.B. Forsyth, E. Lelièvre-Berna, F. Tasset, J. Phys. Condens. Matter 14 (2002) 1957.
[165] L.M. Corliss, J.M. Hastings, R. Nathans, G. Shirane, J. Appl. Phys. 36 (1965) 1099.
[166] R.A. Lefever, in:, K.-H. Hellwege, A.M. Hellwege (Eds.), 11 Fe Oxides, n.d.
[167] B. Gilbert, C. Frandsen, E. Maxey, D. Sherman, Phys Rev B 79 (2009) 035108.
[168] J.A. Cline, A.A. Rigos, T.A. Arias, J. Phys. Chem. B 104 (2000) 6195.
[169] M. Lübbe, W. Moritz, J. Phys. Condens. Matter 21 (2009) 134010.
[170] A. Barbier, A. Stierle, N. Kasper, M.-J. Guittet, J. Jupille, Phys Rev B 75 (2007) 233406.
[171] A. Hofmann, S.J. Clark, M. Oppel, I. Hahndorf, Phys Chem Chem Phys 4 (2002) 3500.
[172] U. Aschauer, A. Selloni, Phys Chem Chem Phys 14 (2012) 16595.
[173] G. Zhang, X. Wang, Y. Xiong, Y. Shi, J. Song, D. Luo, Int. J. Hydrog. Energy 38 (2013) 1157.
[174] E. Skúlason, V. Tripkovic, M.E. Björketun, S. Gudmundsdóttir, G. Karlberg, J. Rossmeisl, T. Bligaard, H. Jónsson, J.K. Nørskov, J. Phys. Chem. C 114 (2010) 18182.
[175] C.E. Cava, L.S. Roman, C. Persson, Phys Rev B 88 (2013) 045136.
[176] E. Ibe, M. Sakagami, S. Uchida, J. Nucl. Sci. Technol. 23 (1986) 11.
[177] E. Ibe, S. Uchida, Nucl. Sci. Eng. 90 (1985) 140.
[178] N.E. Todreas, M.S. Kazimi, Nuclear Systems Volume 1: Thermal Hydraulic Fundamentals, Taylor and Francis, New York, New York, 1990.

Appendix A: RADICAL Derivation and Models

A.1 Concentration Equation Derivation

The differential equations for the concentration of chemical species are derived with respect to space rather than time, because in two-phase flow, the vapor and liquid velocities are unequal resulting in slip between the two phases. If the differential equations are taken with respect to time, they will be more complex because the respective masses of the two phases will be in different locations at the same time interval. To solve for the concentration of chemical species in the fluid, a mass balance is developed for the control volume shown below in Figure A-1.

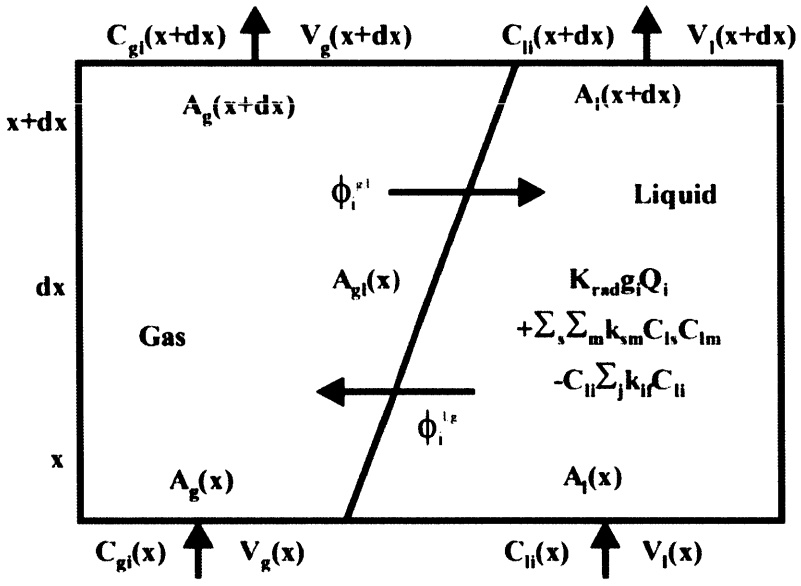

Figure A-1. Differential control volume element for a Two-Phase fluid [77]

The mass balance for the liquid phase of the differential control volume is given by the following equation:

$$\frac{d[C_{li}A_{l(x)}dx]}{dt} = A_l(x)dx\left[K_{rad}G_iQ_i + \sum_s\sum_m k_{sm}C_{ls}C_{lm} - C_{li}\sum_j k_{ij}C_{lj}\right] + V_l(x)A_l(x)C_{li}(x) - V_l(x+dx)A_l(x+dx)C_{li}(x+dx) + A_{gl}(x)[\phi_i^{g,l} - \phi_i^{l,g}] \quad \text{(A-1)}$$

where:

i, j, m are indices for different species

l, g refer to the liquid phase and gas phase respectively

C is the concentration of the given species [mol/L]

A is the cross sectional area [cm^2]

V is velocity [cm/s]

k_{rad} is a conversion factor for g-values from [# / 100 eV] to [mol/L-Rad]

G is the g-value of the given species [# / 100 eV]

Q is the dose rate [Rad/s]

k is the rate constant for chemical reactions

$KOEFF_{ji}$ is a tally for the number of species i created or destroyed in a reaction

Φ is the concentration flux across the gas liquid interface

Similarly, the mass balance for the gas phase is given by the following equation:

$$\frac{d[C_{gi}A_{g(x)}dx]}{dt} = V_g(x)A_g(x)C_{gi}(x) - V_g(x+dx)A_g(x+dx)C_{gi}(x+dx) + A_{gl}(x)[\phi_i^{l,g} - \phi_i^{g,l}] \quad \text{(A-2)}$$

The following subsections will address the terms in Equations (A-1) and (A-2).

A.1.1 Cross Sectional Area of the Liquid and Vapor Phases

The relationship between the cross-sectional area of the phases, the total cross-sectional area and the void fraction must be characterized to obtain the final concentration differential equations.

Cross-sectional area and void fraction relationships are used to eliminate the liquid and vapor cross-sectional areas that cannot be adequately characterized otherwise. The area occupied by the vapor phase can be represented as the product of the void fraction and the total cross-sectional area as in Equation (A-3). Similarly, the product of the total cross-sectional area and the compliment of the void fraction can represent the area occupied by the liquid phases as in Equation (A-4). Differentiating these equations yields Equation (A-5) and Equation (A-6):

$$A_g = \alpha(x)A_T(x) \quad \text{(A-3)}$$

$$A_l = [1-\alpha(x)]A_T(x) \quad \text{(A-4)}$$

$$\frac{\partial A_g(x)}{\partial x} = A_T(x)\frac{\partial \alpha(x)}{\partial x} + \alpha(x)\frac{\partial A_T(x)}{\partial x} \quad \text{(A-5)}$$

$$\frac{\partial A_L(x)}{\partial x} = -A_T(x)\frac{\partial \alpha(x)}{\partial x} + [1-\alpha(x)]\frac{\partial A_T(x)}{\partial x} \quad \text{(A-6)}$$

A.1.2 Radiolysis

Radiolysis is the production of chemical species from the destruction of other chemical species by ionizing radiation. When gamma rays, fast neutrons, alpha particles, and beta particles irradiate water, it will dissociate into various radicals, ions, and stable species. In this model only water is considered to undergo radiolysis with the following species being produced:

$$H_2O \rightarrow e_{aq}^-, H^+, H, OH, HO_2, H_2, H_2O_2 \quad \text{(A-7)}$$

The rate of production of these species is proportional to the amount of energy deposited in the water due to radiation dose. The number of species produced per 100 eV of adsorbed radiation energy is defined as the g-value of the radiation and is determined experimentally for each type of radiation. G-values on both the type of radiation and the temperature of water. G-values for stable species (O_2, H_2, and H_2O_2) can be directly measured, but those for short-lived chemical radicals (e_{aq}^-, H^+, H , OH, and HO_2) must be calculated using a mass balance. The g-value sets used in RADICAL can be found in Appendix B:.

The production rate of a species can be calculated from g-values and the dose rates in the control volume. In RADICAL, radiolysis is not considered in the vapor phase because the density is quite low.

A.1.3 Chemical Reactions

The following example indicates how reaction kinetics are determined for a first order reaction. For a chemical reaction with two reactants and two products:

$$A + B \rightarrow C + D \tag{A-8}$$

The kinetics for the generation of species C is given by:

$$\frac{d[C]}{dt} = k[A][B] \tag{A-9}$$

The kinetics for the annihilation of species A is given by:

$$\frac{d[A]}{dt} = -k[A][B] \tag{A-10}$$

These equations differ only in the sign of the rate constant, which depends on whether it is a reactant or a product. Therefore, the same rate constant, KOEF, is used for both generation and annihilation of chemical species. [76]

With this notation, the two terms in Equation (A-1) which account for production and annihilation by chemical reaction are replaced with:

$$\sum_{s}\sum_{m} k_{sm}C_{ls}C_{lm} - C_{li}\sum_{j} k_{ij}C_{lj} = \sum_{j=1}^{NRx}\left(KOEF_{ji}k_j\prod_{m=1}^{3} C_{l,mi}\right) \tag{A-11}$$

On the right hand side of the above equation, the product of the right The product on the right hand side is carried out over all reactions inputted in the reaction set matrix and the species is summed over all the reactions.

The reaction set must include reactions for all species initially found in the coolant and for chemical species produced by radiolysis. Each reaction input into RADICAL includes a symbolic representation of the chemical reaction occurring, a designation for the temperature treatment of the rate constant, and coefficients required to

calculate the rate constant. The rate constants can be very sensitive to water temperature, and in some cases a simple Arrhenius treatment is insufficient to adjust for temperature. There are many different water reaction sets available, and the set previously used was determined by the MIT radiolysis workshop in 1992. [78] In RADICAL, up to three reactants and four products are accepted for each reaction and only up to second-order kinetics are considered. The reaction sets used in RADICAL can be found in Appendix B:.

A.1.4 Convection

In Equations (A-1) and (A-2), convection is represented by the following terms respect to liquid or gas phase:

$$V_l\,(x)A_l(x)C_{li}(x) - V_l(x+dx)A_l(x+dx)\,C_{li}(x+dx) \tag{A-12}$$

Expanding the convection term at x+dx using a Taylor series, and neglecting second and higher order terms,

$$\begin{aligned} V_l(x+dx)A_l(x+dx)\,C_{li}(x+dx) \\ &\approx \left[C_{li}(x)+\frac{\partial C_{li}}{\partial x}dx\right]\left[V_l(x)+\frac{\partial V_l}{\partial x}dx\right]\left[A_l(x)+\frac{\partial A_l}{\partial x}dx\right] \\ &\approx V_l(x)A_l(x)C_{li}(x) + V_l(x)C_{li}(x)\frac{\partial A_l}{\partial x}dx \\ &+ A_l(x)C_{li}(x)\frac{\partial V_l}{\partial x}dx \quad + V_l(x)A_l(x)\frac{\partial C_{li}}{\partial x}dx \end{aligned} \tag{A-13}$$

A.1.5 Mass transfer between liquid and vapor phases

The flux of chemical species between the gas and liquid phases can be represented by the following relationships for the interfacial area between the vapor and liquid, and the flux between the liquid and vapor phases: [176]

$$A_{gl}(x) = \frac{6\alpha}{d_b} A_T(x)dx \tag{A-14}$$

$$\phi_i^{g,l} = k_i^{g,l}(C_{gi} - aC_{gi}) \tag{A-15}$$

$$\phi_i^{l,g} = k_i^{l,g}(C_{li} - bC_{li}) \tag{A-16}$$

Where A_{gl} is the interfacial area per unit volume, and $\phi_i^{g,l}$ and $\phi_i^{l,g}$ are the flux of species "i" from the vapor into the liquid and the liquid into the vapor respectively. The constants a and b are proportionality constants to describe the concentration gradient between the bulk fluid and the fluid at the bubble surface. The constant, 6, divided by the bubble diameter is constant at a given pressure; this is incorporated along with a and b into new constants:

$$\mu_i^{l,g} = \frac{6k_i^{l,g}}{d_b}(1 - \alpha) \tag{A-17}$$

$$\mu_i^{g,l} = \frac{6k_i^{g,l}}{d_b}(1 - \beta) \tag{A-18}$$

These are referred to as the mass transfer constants, with the values used in the model given in Table A-1. Thus the mass transfer is given by:

$$\phi_i^{l,g} A_{gl}(x) = \mu_i^{l,g} \alpha(x) A_T C_{li}(x) \tag{A-19}$$

Table A-1. Mass transfer constant values for use in radiolysis models [177]

	H_2	O_2
$\mu_i^{l,g}$, gas release factor	30	23
$\mu_i^{g,l}$, gas absorption factor	9.9	12.4

A.2 Thermal Hydraulics Models

In addition to the two concentration equations, Equations (3-1) and (3-2), additional equations describing the properties of the fluid are required. In the two phase regime, thermal-hydraulic effects are determined using either Bankoff's correlation or the Chexal-Lellouche correlation. [78]

A.2.1 Bankoff Correlation

The void fraction and fluid velocities are calculated using Bankoff's correlation: [178]

$$\alpha(x) = \frac{1}{C_o} \times \frac{1}{1 + \left[\frac{1-\chi(x)}{\chi(x)}\right]\frac{\rho_v}{\rho_l}} \tag{A-20}$$

Where:

$$\frac{1}{C_o} = 0.71 + 0.0001 \times P(in\ psi)$$

χ is the fluid quality
ρ is the density of the phases

The quality of the fluid is a function of the power dissipated in the reactor core:

$$\chi(x) = \begin{cases} 0 & (x < x_b) \\ \frac{q_f}{2h_{fg}} - \frac{h_f - h_i}{h_{fg}} - \frac{q_t}{2h_{fg}} \cos\left(\frac{\pi x}{h_L}\right) & (x \geq x_b) \end{cases} \quad \text{(A-21)}$$

$$q_t = h_f + \chi_e h_{fg} - h_i \quad \text{(A-22)}$$

where:

i is the value at the core inlet

e is the value at the core outlet

x_b is the position in the reactor where boiling initiates

h is the enthalpy

In addition to solving for the void fraction in terms of operational parameters of the primary system, the expressions that give the gas and liquid velocities in terms of the operating parameters are determined by defining the slip ratio:

$$S(x) = \frac{V_g}{V_l} = \frac{1 - \alpha(x)}{\frac{1}{C_o} - \alpha(x)} \quad \text{(A-23)}$$

The gas and liquid velocities are calculated from the fluid average velocity using the following equations:

$$\alpha \rho_g V_g + (1 - \alpha)\rho_l V_l = \rho_l V_o \quad \text{(A-24)}$$

$$V_l = \frac{\rho_l V_o}{\rho_g \alpha S + \rho_l (1 - \alpha)} \quad \text{(A-25)}$$

$$V_g = S V_l \quad \text{(A-26)}$$

The fluid average velocity can be calculated from the mass flow rate:

$$V_o = \frac{\dot{m}}{A_T \rho_l} \tag{A-27}$$

A.2.2 Chexal-Lellouche Correlation

The Chexal-Lellouche correlations [78] use the following equations to represent fluid velocities.

$$V_l = \frac{\dot{m}}{A_T(x)\rho_l(x)}\left[\frac{1-\chi(x)}{1-\alpha(x)}\right] \tag{A-28}$$

$$V_g = \frac{\dot{m}\chi(x)}{A_T(x\rho_g(x)\alpha(x)} \tag{A-29}$$

The thermodynamic quantities are calculated using the Chexal-Lellouche thermodynamic subroutines, and require the initial temperature, pressure, and power as input.

1.3 Lin Empirical Correlation for ECP in BWRs

An ECP model by Lin can be used in RADICAL calculate the electrochemical corrosion potential or ECP in BWRs. This ECP model was developed by measuring ECP under simulated BWR coolant chemistry conditions using a rotating cylinder electrode (RCE). The model developed accounts for fluid velocity, hydrogen concentration, and either oxygen or hydrogen peroxide concentration. There are two ECP values calculated, one for oxygen the other for hydrogen peroxide. The ECP correlation is given by the following equation and is valid for both oxidants: [79]

$$ECP = C_1 \tanh\left[\frac{\log_{10}(Conc) - C_2}{C_3}\right] + C_4 \log_{10}(Conc) + C_5 \tag{A-30}$$

where

Conc is the oxidant concentration, O_2 or H_2O_2, in ppb

ECP is relative to the given oxidant in mV (SHE)

The five constants determine the shape of the curve using different constants for oxygen and hydrogen peroxide. The constants for the hydrogen peroxide relationship are:

$$C_1 = C_5 + 510 \tag{A-31}$$

$$C_2 = 0.00574\left[Conc_{H_2}\right]^{0.772} - 0.00754\sqrt{V_{RCE}} + 0.811 \tag{A-32}$$

$$C_3 = 0.569 \tag{A-33}$$

$$C_4 = 25.33 \tag{A-34}$$

$$C_5 = \frac{-4.62\left[Conc_{H_2}\right]^{0.808}}{\exp\left(0.002280\left[Conc_{H_2}\right]\right)} + 1.50\sqrt{V_{RCE}} - 192.0 \tag{A-35}$$

and the constants for the oxygen relationship are:

$$C_1 = C_5 + 510 \tag{A-36}$$

$$C_2 = 0.00531\left[Conc_{H_2}\right]^{0.772} - 0.0111\sqrt{V_{RCE}} + 1.78 \tag{A-37}$$

$$C_3 = 1.02 \tag{A-38}$$

$$C_4 = 18.7 \tag{A-39}$$

$$C_5 = -18.6\left[Conc_{H_2}\right]^{0.264} - 177.0 \tag{A-40}$$

where

$Conc_{H2}$ is the hydrogen concentration in ppb

V_{RCE} is the velocity of the rotating cylinder electrode

The linear velocity in the BWR primary coolant path is converted to RCE by the following equation:

$$V_{RCE} = 3.01 \exp\left[0.425 + 1.25\, ln\left(V_{pipe}\right) - 1.79\, ln\left(d_{pipe}\right)\right] \quad \text{(A-41)}$$

Once the ECP is calculated for both oxygen and hydrogen peroxide the two are combined to yield one ECP value for the region modeled. This is done by comparing the values for each oxidant and selecting the larger. This value is then used to determine an equivalent concentration of the other oxidant necessary to produce this ECP value (using the other set of constants). Since the ECP model is not an easily invertible function, the equivalent concentration is determined iteratively. The equivalent concentration is then added to the original concentration that yielded the lower ECP value. This new oxidant concentration is then used to calculate a final ECP for the region.

Appendix B: Water Reaction Sets and G-Values

This appendix contains the reaction sets and g-values used in the RADICAL code:

- Table B-1 compares all G-values sets. Note that only the Christensen set includes values for alpha radiation.
- Table B-2 contains the RADICAL reaction set.
- The AECL water reaction set:
  - Table B-3 contains forward reaction rate constants
  - Table B-4 contains the acid/base equilibrium constants
- Table B-5 contains rate constants for equilibrium reactions. These reactions require the acid/base equilibrium constants listed in Table B-4.
- Table B-6 lists the Notre Dame iron and nickel impurity reactions.

Table B-1. G-Values. Units: # Species per 100 eV. [78,84,93]

Species	Gamma			Fast neutron			Alpha
	Christensen	AECL	Radical	Christensen	AECL	Radical	Christensen
H_2	0.6	0.63905	0.8	1.17	0.9906	0.88	1.4
H_2O_2	0.55	0.266	0.28	0.65	0.404	0.99	1.18
e-	3.54	3.43438	3.76	0.65	1.287	0.93	0.17
H	0.87	1.56001	0.7	0.46	0.4978	0.5	0.29
H^+	3.54	3.43438	3.76	0.65	1.287	0.93	0.17
OH	4.51	5.73941	5.5	2	2.868	1.09	0.39
HO_2	0	0	0	0.05	0.03	0.04	0.17

Table B-2. Rate Constants for the RADICAL Water Reaction Set [78]

Rxn #	Reaction	k @ 298K (L/mol-s)	E_a (kJ/mol-K)
F3	$e^- + H_2O \rightarrow H + OH^-$	16	12.55
F4	$e^- + H^+ \rightarrow H$	3.50E+11	0
F5	$e^- + OH \rightarrow OH^-$	2.00E+10	12.55
F6	$e^- + H_2O_2 \rightarrow OH + OH^-$	1.30E+11	0
F7	$H + H \rightarrow H_2$	8.50E+10	0
F8	$e^- + HO_2 \rightarrow HO_2^-$	2.00E+10	12.55
F9	$e^- + O_2 \rightarrow O_2^-$	2.60E+09	0
F10	$e^- + e^- \rightarrow OH^- + OH^- + H_2$	5.00E+09	12.55
F11	$OH + OH \rightarrow H_2O_2$	1.70E+10	0
F12	$H + OH^- \rightarrow e^- + H_2O$	2.00E+07	18.83
F13	$H + e^- \rightarrow H_2 + OH^-$	2.50E+10	12.55
F14	$HO_2^- + e^- \rightarrow OH + OH^- + OH^-$	3.50E+09	12.55
F15	$H + OH \rightarrow H_2O$	5.50E+10	0
F16	$H_2 + OH \rightarrow H + H_2O$	4.00E+07	18.0163
R16	$H + H_2O \rightarrow OH + H_2$	0.000104	85.1695
F17	$H + O_2 \rightarrow HO_2$	8.60E+10	0
F18	$H + HO_2 \rightarrow H_2O_2$	2.00E+10	12.55
F19	$H + O_2^- \rightarrow HO_2^-$	2.00E+10	12.55
F20	$O_2^- + e^- \rightarrow HO_2^- + OH^-$	1.30E+08	18.83
F21	$H + H_2O_2 \rightarrow OH + H_2O$	9.00E+07	16.6147
F22	$H_2O_2 + OH \rightarrow H_2O + HO_2$	3.00E+07	13.0122
F23	$HO_2 + OH \rightarrow O_2 + H_2O$	8.60E+10	0
F24	$H_2O_2 + OH^- \rightarrow HO_2^- + H_2O$	1.80E+10	12.55
R24	$HO_2^- \rightarrow H_2O_2 + OH^-$	570000	18.83
F25	$HO_2 + HO_2 \rightarrow O_2 + H_2O_2$	850000	22.8237
F26	$HO_2 \rightarrow H^+ + O_2^-$	25700	12.55
R26	$O_2^- + H^+ \rightarrow HO_2$	5.00E+10	12.55
F27	$HO_2 + O_2^- \rightarrow HO_2^- + O_2$	5.00E+09	0
F29	$H^+ + OH^- \rightarrow H_2O$	1.44E+11	12.55
R29	$\rightarrow H^+ + OH^-$	0.792427	12.55
F30	$OH + O_2^- \rightarrow O_2 + OH^-$	8.60E+10	0
tif	$\frac{1}{2}O_2 + \frac{1}{2}O_2 \rightarrow O_2$	1.00E+15	0
w32	$H_2O_2 \rightarrow OH + OH$	0.200	0
ss	$H_2O_2 \rightarrow \frac{1}{2}O_2 + H_2O$	0.124	0

Table B-3. Rate Constants for the AECL Water Reaction Set [84]

Rxn #	Reaction	Rate Constant Rate constants are (L/mol-s) Activation energies are (kJ/mol-K)
R2	$e^- + e^- \rightarrow H_2 + OH^- + OH^-$	$Log_{10}k_{R2} = -47.530 + \frac{4.92\times10^4}{T} - \frac{1.036\times10^7}{T^2}$
R3	$H + H \rightarrow H_2$	$k_{R3}(298K) = 5.1x10^9$ $E_A = 15.5$
R4	$OH + OH \rightarrow H_2O_2$	$Log_{10}k_{R4} = 8.054 + \frac{2.193\times10^3}{T} - \frac{7.395\times10^5}{T^2} + \frac{6.870\times10^7}{T^3}$
R5	$e^- + H \rightarrow H_2 + OH^-$	$k_{R5}(298K) = 2.76x10^{10}$ $E_A = 14.9$
R6	$e^- + OH \rightarrow OH^-$	$Log_{10}k_{R6} = 13.12 - 1.023 * \frac{10^3}{T} + 7.624 * \frac{10^4}{T^2}$
R7	$H + OH \rightarrow H_2O$	$k_{R7}(298K) = 1.10x10^{10}$; $E_A = 9.1$
R8	$e^- + H_2O_2 \rightarrow OH + OH^-$	$k_{R8}(298K) = 1.40x10^{10}$; $E_A = 15.7$
R9	$e^- + O_2 \rightarrow O_2^-$	$k_{R9}(298K) = 2.30x10^{10}$; $E_A = 11.6$
R10	$e^- + O_2^- \rightarrow H_2O_2 + OH^- + OH^-$	$k_{R10}(298K) = 1.30x10^{10}$; $E_A = 13.0$
R11	$e^- + HO_2 \rightarrow HO_2^-$	$k_{R11}(298K) = 1.30x10^{10}$; $E_A = 13.0$
R12	$H + H_2O_2 \rightarrow OH + H_2O$	$k_{R12}(298K) = 3.6x10^7$ $E_A = 21.1$
R13	$H + O_2 \rightarrow HO_2$	$Log_{10}k_{R13} = 10.704 + \frac{2.840\times10^2}{T} - \frac{1.369\times10^5}{T^2}$
A14	$H + HO_2 \rightarrow OH + OH$	$k_{A14}(298K) = 1.13x10^{10}$; $E_A = 15.2$
R15	$H + O_2^- \rightarrow HO_2^-$	$k_{R15}(298K) = 1.13x10^{10}$; $E_A = 15.2$
R16	$OH + H_2O_2 \rightarrow HO_2 + H_2O$	$k_{R16}(298K) = 2.90x10^7$; $E_A = 13.8$
R17	$OH + O_2^- \rightarrow O_2 + OH^-$	$k_{R17}(298K) = 1.10x10^{10}$; $E_A = 10.9$
R18	$OH + HO_2 \rightarrow O_2 + H_2O$	$k_{R18}(298K) = 8.80x10^9$; $E_A = 6.6$
R19	$HO_2 + HO_2 \rightarrow H_2O_2 + O_2$	$k_{R19}(298K) = 8.4x10^5$; $E_A = 20.1$
A22*	$H_2O_2 \rightarrow O + H_2O$	$k_{A22}(298K) = 1.30x10^{-7}$; $E_A = 65.0$
tif *	$O + O \rightarrow O_2$	$k_{tif}(298K) = 1.00x10^{15}$; $E_A = 0.0$

*The AECL set offers two pathways for hydrogen peroxide decomposition: to H_2O and O, or to 2 OH. The report does not include a recombination rate for $O + O \rightarrow O_2$, so the reaction rate was taken from the RADICAL reaction set. We found no difference between using the mechanism in reaction A14 and tif or the alternate OH decomposition pathway.

Table B-4. Acid/Base equilibrium constants of H_2O, H_2O_2, OH,HO_2 and H. Units: mol/L

Acid/Base Equilibrium Constants
$pK_{H2O} = 16.690 - 4.262 \times 10^{-2}\,t + 2.071 \times 10^{-4}\,t^2 - 5.594 \times 10^{-7}\,t^3 + t\,7.161 \times 10^{-10}t^4$
$pK_{H2O2} = 12.383 - 3.020 \times 10^{-2}\,t + 1.700 \times 10^{-4}\,t^2 - 5.151 \times 10^{-7}\,t^3 + 6.960 \times 10^{-10}t^4$
pK_{OH}=12.383 – 3.020× 10^{-2} t + 1.700×× 10^{-4} t^2 – 5.151× 10^{-7} t^3 + 6.960× $10^{-10}$$t^4$
pK_{HO2}=4.943 – 6.230× 10^{-3} t + 4.125× 10^{-5} t^2 – 8.182× 10^{-9} t^3
pK_H=10.551 – 4.430× 10^{-2} t + 1.902× 10^{-4} t^2 – 4.661×× 10^{-7} t^3 + 5.980× $10^{-10}$$t^4$

* t = Temperature in °C

Table B-5. Equilibrium Rate Constants for the AECL Water Reaction Set [84]

Rxn #	Reaction	Rate Constant Rate constants are (L/mol-s) activation energies are (kJ/mol-K)
f23	$H_2O \rightarrow H^+ + OH^-$	$k_{f23} = k_{b23} * K_{H2O}$
b23	$H^+ + OH^- \rightarrow H_2O$	$Log_{10}k_{b23} = 20.93 - \frac{1.236\times10^4}{T} + \frac{6.36\times10^6}{T^2} - \frac{1.48\times10^9}{T^3} + \frac{1.24\times10^{11}}{T^4}$
f24	$H_2O_2 \rightarrow H^+ + HO_2^-$	$k_{f24} = k_{b24} * K_{H2O2}$
b24	$H + HO_2^- \rightarrow H_2O_2$	$Log_{10}k_{b24} = 16.41 - \frac{4.888\times10^3}{T} + \frac{1.62\times10^6}{T^2} - \frac{2\times10^8}{T^3}$
f25	$H_2O_2 + OH^- \rightarrow HO_2^- + H_2O$	$Log_{10}k_{f25} = 13.34 - \frac{2.22\times10^3}{T} + \frac{7.33\times10^5}{T^2} - \frac{1.07\times10^8}{T^3}$
b25	$HO_2^- + H_2O \rightarrow H_2O_2 + OH^-$	$k_{b25} = k_{f25} \times K_{H2O}/K_{H2O2}$
f26	$OH \rightarrow H^+ + O^-$	$k_{f26} = k_{b26} * K_{OH}$
b26	$H^+ + O^- \rightarrow OH$	$Log_{10}k_{b26} = 16.41 - \frac{4.888\times10^3}{T} + \frac{1.62\times10^6}{T^2} - \frac{2\times10^8}{T^3}$
f27	$OH + OH^- \rightarrow O^- + H_2O$	$Log_{10}k_{f27} = 13.34 - \frac{2.22\times10^3}{T} + \frac{7.33\times10^5}{T^2} - \frac{1.07\times10^8}{T^3}$
b27	$O^- + H_2O \rightarrow OH + OH^-$	$k_{b27} = k_{f27} \times K_{H2O}/K_{OH}$
f28	$HO_2 \rightarrow H^+ + O_2^-$	$k_{f28} = k_{b28} \times K_{HO2}$
b28	$H^+ + O_2^- \rightarrow HO_2$	$Log_{10}k_{b28} = 16.41 - \frac{4.888\times10^3}{T} + \frac{1.62\times10^6}{T^2} - \frac{2\times10^8}{T^3}$
f29	$HO_2 + OH^- \rightarrow O_2^- + H_2O$	$Log_{10}k_{f29} = 13.34 - \frac{2.22\times10^3}{T} + \frac{7.33\times10^5}{T^2} - \frac{1.07\times10^8}{T^3}$
b29	$O_2^- + H_2O \rightarrow HO_2 + OH^-$	$k_{b29} = k_{f29} \times K_{H2O}/K_{HO2}$
f30	$H \rightarrow H^+ + e^-$	$k_{f30} = k_{b30} \times K_H$
b30	$H^+ + e^- \rightarrow H$	$Log_{10}k_{b30} = 39.13 - \frac{3.888\times10^4}{T} + \frac{2.05\times10^7}{T^2} - \frac{4.90\times10^9}{T^3} + \frac{4.38\times10^{11}}{T^4}$
f31	$H + OH^- \rightarrow e^- + H_2O$	$Log_{10}k_{f31} = 22.97 - \frac{1.971\times10^4}{T} + \frac{1.14\times10^7}{T^2} - \frac{2.99\times10^9}{T^3} + \frac{2.80\times10^{11}}{T^4}$
b31	$e^- + H_2O \rightarrow H + OH^-$	$k_{b31} = k_{f31} * K_{H2O}/K_H$
f32	$H + H_2O \rightarrow H_2 + OH$	$Log_{10}k_{f32} = 9.408 - \frac{2.827\times10^3}{T} - \frac{3.792\times10^5}{T^2}$
b32	$H_2 + OH \rightarrow H + H_2O$	$Log_{10}k_{b32} = -11.56 + \frac{3.255\times10^4}{T} - \frac{1.86\times10^7}{T^2} + \frac{4.55\times10^9}{T^3} - \frac{4.14\times10^{11}}{T^4}$

Table B-6. Notre Dame Iron and Ni Reaction Set [77]

Rxn #	Reaction	k @ 298K (L/mol-s)	E_a (kJ/mol-K)
F1	$Fe^{2+} + OH \rightarrow Fe^{3+} + OH^-$	5.7E+08	13
F2	$Fe^{2+} + e^- \rightarrow Fe^+$	5.5E+10	13
F3	$Fe^+ + OH \rightarrow FeOH^+$	7.0E+08	13
F4	$Fe^+ + H_2O_2 \rightarrow Fe^{2+} + OH^- + OH$	1.3E+02	13
F5	$Fe^+ + O_2^- + \rightarrow Fe^{2+} + OH^- + OH^- + H_2O_2$	8.8E+08	13
F6	$H + Fe^{2+} \rightarrow FeH^{2+}$	3.4E+06	13
F7	$FeH^{2+} + H^+ \rightarrow Fe^{3+} + H_2$	2.6E+04	13
F8	$Fe^+ + H \rightarrow FeH^+$	3.0E+06	13
F9	$FeH^+ + H^+ \rightarrow Fe^{2+} + H_2$	2.3E+04	13
F10	$Fe^{2+} + H_2O_2 \rightarrow Fe^{3+} + OH^- + OH$	1.5E+02	13
F11	$Fe^{2+} + O_2^- \rightarrow Fe^{3+} + OH^- + OH^- + H_2O_2$	9.9E+08	13
F12	$Fe^{3+} + e^- \rightarrow Fe^{2+}$	5.0E+10	13
F13	$Fe^{3+} + O_2^- \rightarrow Fe^{2+} + O_2$	9.9E+08	13
F14	$Fe^{3+} + H \rightarrow Fe^{2+} + H^+$	6.5E+06	13
F15	$Fe^{3+} \rightarrow FeOH^{2+} + H^+$	7.5E+07	13
F16	$FeOH^{2+} + H^+ \rightarrow Fe^{3+}$	1.2E+10	13
F17	$FeOH^{2+} \rightarrow Fe(OH)_2^+ + H^+$	1.5E+05	13
F18	$Fe(OH)_2^+ + H^+ \rightarrow FeOH^{2+}$	2.0E+10	13
F19	$Fe(OH)_2^+ + Fe(OH)_2^+ \rightarrow FeOOH + FeOH^{2+}$	1.2E+03	13
F20	$H^+ + FeOH^+ \rightarrow Fe^{2+}$	1.0E+10	0
F21	$Fe^{2+} \rightarrow FeOH^+ + H^+$	4.0E+02	0
F22	$FeOH^{2+} + H^+ \rightarrow Fe^{3+}$	1.0E+10	0
F23	$Fe^{3+} \rightarrow FeOH^{2+} + H^+$	1.3E+09	0
F24	$Ni^{2+} + e^- \rightarrow Ni^+$	5.5E+10	13
F25	$Ni^{2+} + H \rightarrow Ni^+ + H^+$	5.0E+05	13
F26	$Ni^+ + H_2O_2 \rightarrow Ni^{2+} + OH^- + OH$	9.9E+07	13
F27	$Ni^+ + OH \rightarrow Ni^{2+} + OH^-$	5.0E+10	13
F28	$Ni^+ + O_2 \rightarrow Ni^{2+} + O_2^-$	5.5E+10	13
F29	$H^+ + NiOH^+ \rightarrow Ni^{2+}$	1.0E+10	0
F30	$Ni^{2+} \rightarrow H^+ + NiOH^+$	1.4E+02	0
F31	$Ni^{2+} + OH^- + OH^- \rightarrow Ni(OH)_2$	1.0E+10	0
F32	$Ni(OH)_2 \rightarrow Ni^{2+} + OH^- + OH^-$	1.0E-07	0

Appendix C: Dose to Power Ratios for a PWR

The following figures show the ratio of dose to linear heat generation rates for clean fuel pins in PWRs from MCNP calculations. These are the "raw" dose ratios: in order to be used, they need to be interpolated for fuel burnup and boron concentration.

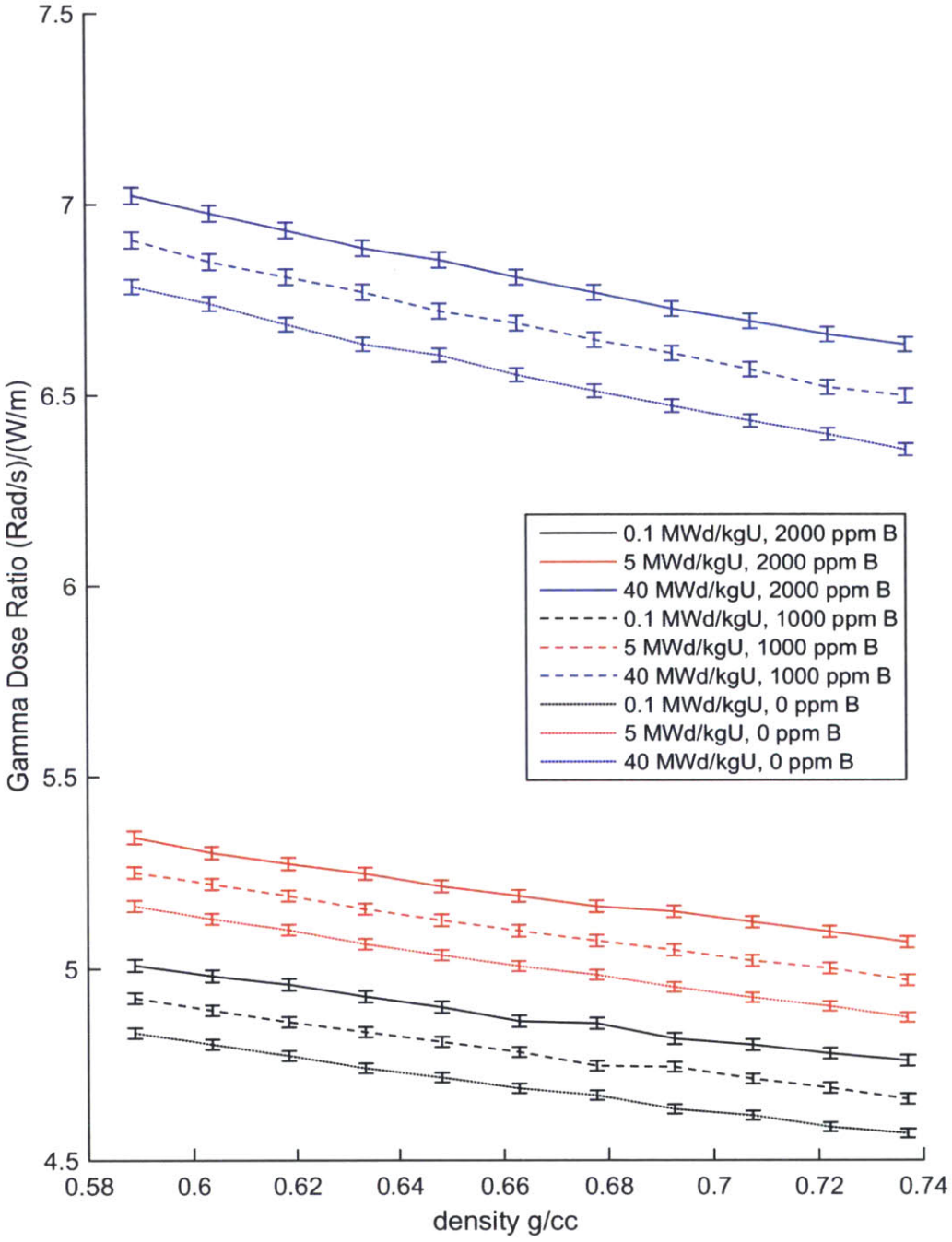

Figure C-1. Ratio of gamma dose rate to power for PWR fuel (units: Rad-m/J)

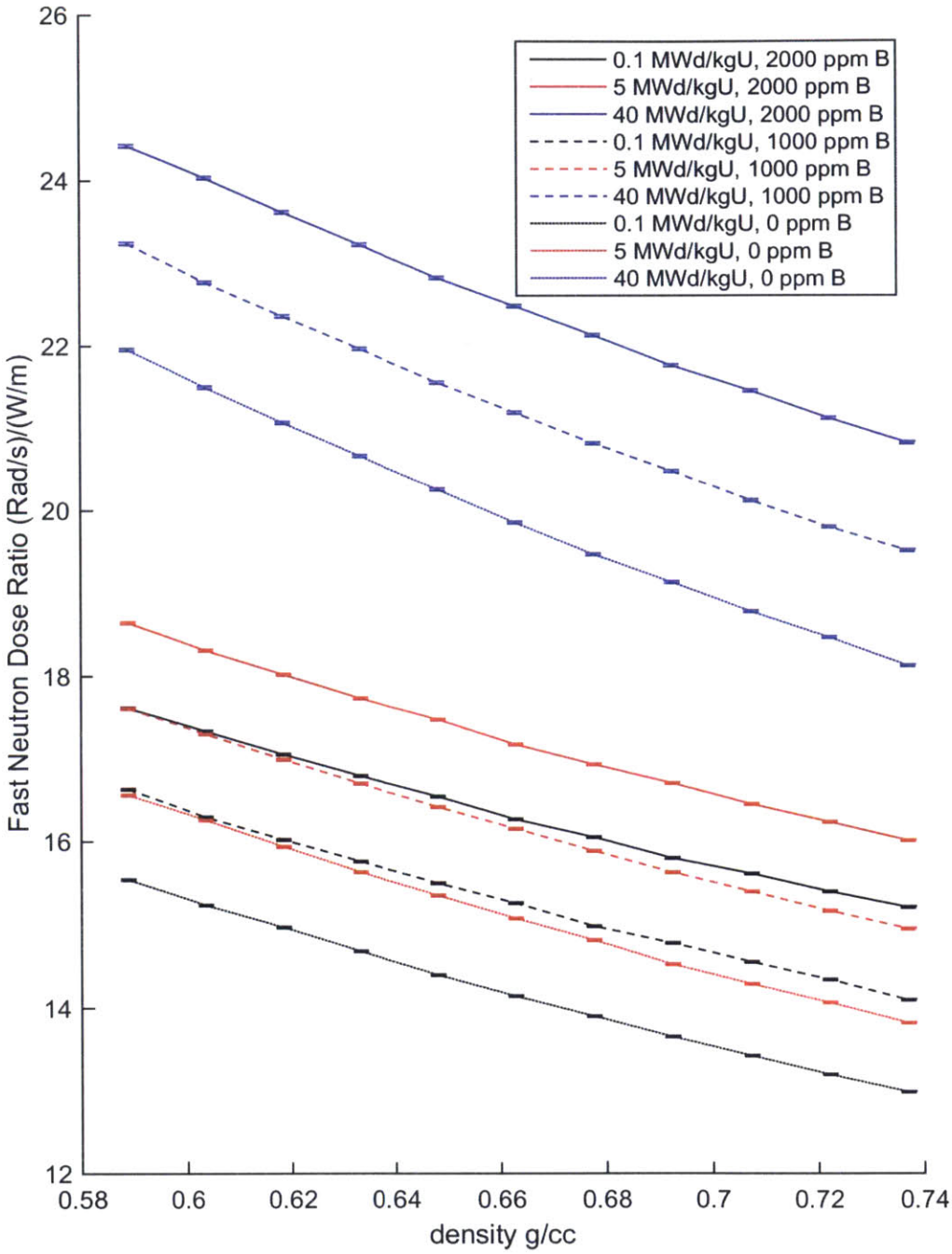

Figure C-2. Ratio of fast neutron dose rate to power for PWR fuel (units: Rad-m/J)

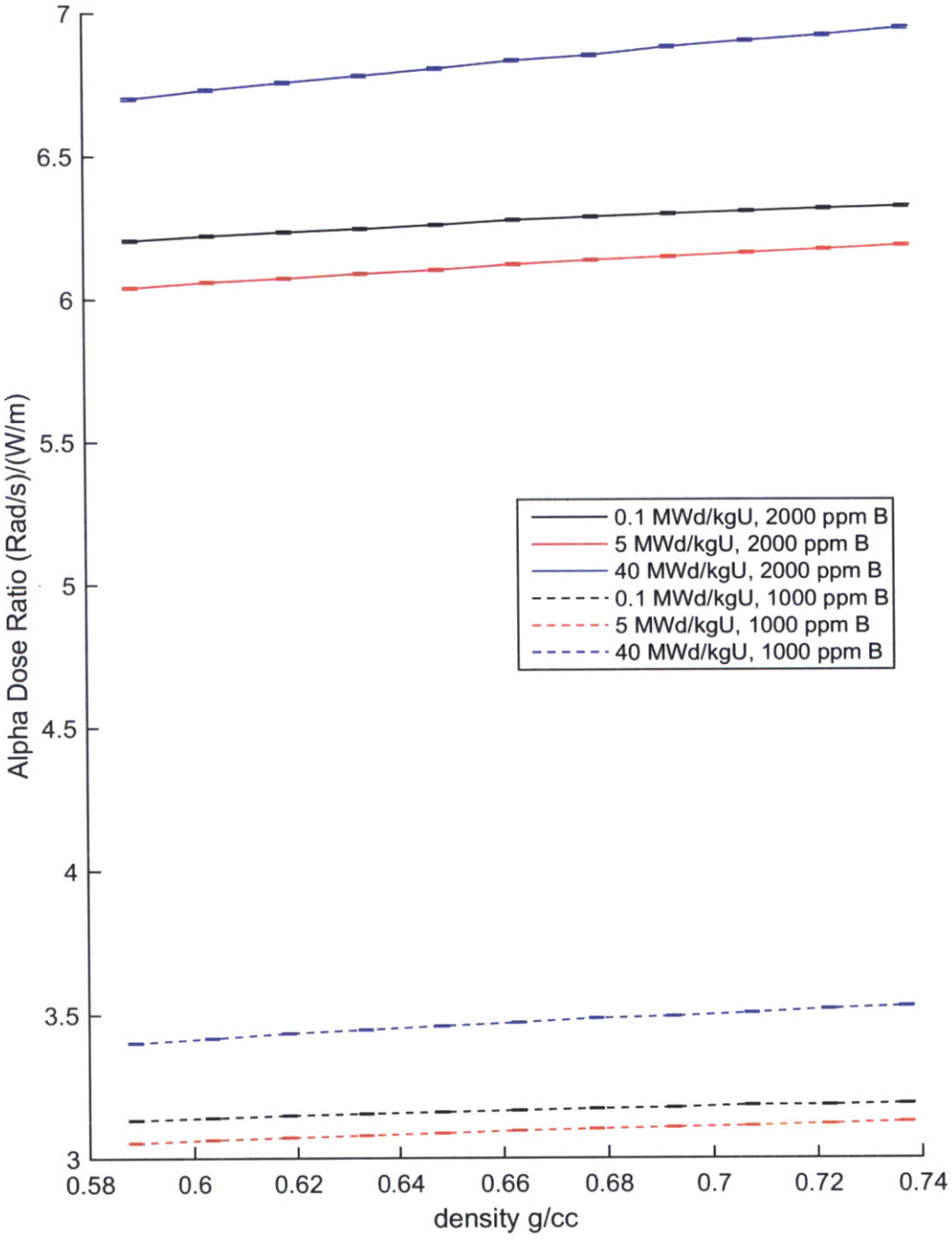

Figure C-3. Ratio of alpha dose rate to power for PWR fuel (units: Rad-m/J)